

**MODELLING, DESIGN AND DEVELOPMENT OF PV  
BASED MICROGRID**

**Thesis submitted to  
DELHI TECHNOLOGICAL UNIVERSITY**

**FOR  
THE AWARD OF THE DEGREE OF  
DOCTOR OF PHILOSOPHY**

**By  
NIKITA GUPTA  
(2K14/Ph.D/EE/10)**

**Under the Supervision of**

**Prof. Rachana Garg  
Department of Electrical Engineering  
Delhi Technological University  
Delhi-110042**



**DEPARTMENT OF ELECTRICAL ENGINEERING  
DELHI TECHNOLOGICAL UNIVERSITY  
DELHI-110042**

**JULY 2018**

## **CERTIFICATE**

This is to certify that the thesis entitled “**Modelling, Design and Development of PV based Microgrid**” being submitted by Ms. Nikita Gupta for the award of degree of Doctor of Philosophy in the Department of Electrical Engineering, Delhi Technological University, Delhi, is the record of student’s own work carried out by her under my supervision. The contents of this research work have not been submitted in part or full to any other university or institute for award of any degree.

Prof. Rachana Garg  
Department of Electrical Engineering  
Delhi Technological University  
Shahbad Daultapur, Delhi-110042, India

*This research work is dedicated to my beloved family,  
My Parents, Shashi Bhushan and Poonam Gupta  
My Sisters, Neha and Ankita Gupta,  
My Husband, Rahul Dogra  
And My Mother-in-Law, Shashi Dogra  
For their endless love, support and encouragement*

## ACKNOWLEDGEMENT

I would like to express my sincere gratitude to my supervisor, Prof. Rachana Garg, for her invaluable guidance and inspiration to carry out this research work. I thank her for the scholarly inputs and consistent inspiration which I received throughout the research work. I express my sincere gratitude and thanks to her, not only for the guidance for research but also for the personal and emotional support she gave me from time to time. Her cooperation, positive attitude and understanding really deserve an everlasting appreciation.

I shall remain indebted to Prof. Parmod Kumar for his help, moral support and encouragement that I receive so spontaneously throughout the tenure of my research work. His vast knowledge of power systems and control systems and quality research publications has been very helpful in carrying out my research work. Without his constant help, support and guidance, this research work would not have been possible.

I would like to express my deepest thanks to Prof. Madhusudan Singh, DRC Chairman and HOD, Electrical Engineering, Delhi Technological University (formerly Delhi College of Engineering) for his immense support and valuable guidance during the entire work of this thesis.

I extend my gratitude to Prof. Yogesh Singh (Vice Chancellor) for his co-operation and support. I would like to convey my thanks to Prof. H.C. Taneja (Dean, PG) and Dr. Anil Kumar (AR, PG) for providing a supportive environment to complete my research at Delhi Technological University. My sincere thanks and deep gratitude are to Prof. Sukumar Mishra and all SRC members for their valuable guidance and consistent support during my research work.

I am also very grateful to Dr. Priya Mahajan for her encouragement and support. I would like to express my gratitude to Prof. Uma Nangia, Dr. Mini Sreejeth, Prof. Pragati Kumar, Prof. Suman Bhowmick, Prof. Mukhtiar Singh and Dr. M. Rizwan and other faculty members of the Electrical Engineering Department, DTU who helped me in numerous ways during various stages of my Ph.D. Thanks are due to



Mr. Mukesh Kumar of Project and Research Lab, Mr. Pradeep Kumar Rana of Workshop Lab, Mr. Vickey Kumar Prasad of UEE Lab and Mr. TPS Rana of Machines Lab, DTU Delhi for providing me with the facilities and assistance during this work. I would like to thank the office staff of EED, Central Library and Central Computer Centre for their valuable co-operation and support.

I would like to thank all my seniors, especially, Shruti Jaiswal, Shagufta Khan, Tausif Ahmad and Ashutosh Trivedi, to motivate and guide me in the starting of my research work. I would like to use this opportunity to thank my fellow researchers and juniors, Priyanka Chaudhary, Imran Quadri, Pallavi Verma, Rupam Singh, Anuj Varshney, Saurabh Gupta, Manoj Kumar, Manita and Urvashi Meena for their co-operation and informal support in pursuing this research work.

I am extremely grateful to my parents, Mr. Shashi Bhushan Gupta, Mrs. Poonam Gupta, my mother in law, Mrs. Shashi Dogra, and my siblings Neha Gupta and Ankita Gupta for their dreams, blessings and constant encouragement. Their trust in my capabilities had been a key factor in all my achievements. I find myself at a loss of words to express my gratitude to my husband, Mr. Rahul Dogra who spent sleepless nights with me during my research work and motivated me to make me believe in myself. He has been always there with his critical review of my work and suggestions.

I am thankful to those who have directly or indirectly helped me to finish my dissertation study. It is not possible to mention all of them; nonetheless, I wish to acknowledge their contribution to this work.

**Nikita Gupta**  
**(2k14/Ph.D/EE/10)**

## ABSTRACT

In recent years, with the exhaustion of fossil fuels and increasing public awareness about the use of green energy, the renewable energy has gained popularity and is emerging as an important source of energy. Also, the electrical power grid is on the threshold of a paradigm shift from centralized power generation, transmission and massive electric grids to distributed generation (DG). DG basically uses small-scale generators, like photovoltaic (PV) panels, wind turbine, fuel cells, small and micro hydropower, diesel generator set, etc., and is confined to small distribution networks to produce power close to the end users. Renewable energy sources (RES) are the important constituents of DG and provide electricity with higher reliability and security and have fewer harmful environmental consequences than traditional power generators.

With increased penetration of DGs into the traditional grid system, it is required to resolve the technical and operational problems viz. power quality, voltage instability, fault identification and clearing, etc. brought by the DG deployment. PV based microgrid may be one of the solutions to meet these challenges. A microgrid is a group of interconnected loads and distributed generators within clearly defined electrical boundaries that acts as a single controllable entity with respect to the grid. It can be connected and disconnected from the grid to enable it to operate either in grid-tied or standalone mode. Grid-tied PV based microgrid can be either single-stage or two-stage depending on the technical requirements. In single stage configuration, PV array is directly connected to a DC/AC converter whereas in two-stage configuration an additional DC/DC converter with maximum power point tracking (MPPT) capability is connected in between the PV array and DC/AC converter and provides the desired DC voltage to the inverter.

This research work aims at modelling, design and development of a two-stage three-phase grid-tied PV based microgrid. In order to predict the behaviour of the designed system under steady state as well as in the dynamic state, modelling of the overall system has been carried out. Steady state response of the PV based microgrid is studied from its mathematical model comprising of the governing equations of the designed

system. Characterization studies viz. sensitivity and reliability analysis are the performance indicators of any system. Accordingly, the sensitivity analysis of the designed system has been performed and the sensitivity functions of the major components, i.e. solar cell and converter have been developed. Also, component and system level reliability analysis have been performed for the system under consideration.

In the present work, the two stages of power conversion consist of boost converter and grid interfacing inverter. The DC-DC converter is used to boost the output voltage of the PV array to the required DC link voltage level along with the functionality of tracking the maximum power obtained from PV array under varying irradiation and temperature. The PV inverter is used to convert the generated DC voltage to AC of required voltage and frequency and to maintain the power balance between DG, load and grid. The interfacing control algorithms are used to control the inverter for its efficient utilization and grid synchronization. Conventional control algorithms use feedback controller like proportional integral (PI) controller for DC-link voltage control. These controllers are not best suited for nonlinear systems like PV based microgrid as the overshoots and long settling time in their response are inevitable. In order to overcome the drawbacks of the conventional algorithms, an intelligent asymmetrical fuzzy logic (AFL) based interfacing control algorithm and feedforward-feedback adaptive interfacing control algorithm are proposed and developed for the PV inverter. The proposed algorithms also improves the utilization of the proposed system by incorporating additional features of active power filter (APF), VAR generation, and load balancing in the inverter.

Grid interconnection of PV based microgrid has the advantage of efficient utilization of generated power. But the technical requirements from the utility grid side need to be satisfied to ensure the safety of the operators and the reliability of the utility grid. According to IEEE Std 1547-2003, one such technical requirement of the grid interconnection is the response of the microgrid to islanding. This research work proposes a novel islanding detection algorithm based on the estimation and analysis of negative sequence components of the voltage ( $V_{neg}$ ) at the point of common coupling (PCC). Wavelet packet transform (WPT) is used for the features extraction from  $V_{neg}$

components. The binary tree classifier is used to discriminate between other disturbances and islanding condition. The proposed algorithm is capable of detecting islanding events even under the worst-case scenario, where the inverter output power is nearly equal to the local load consumption. Also, the proposed method is faster than the existing passive detection methods.

A standalone PV system can be used efficiently and economically to feed household loads, the majority of which works on DC power, such as LED (Light Emitting Diodes) lights, BLDC (Brushless DC) drives, mobile phones, computers, televisions, etc. Standalone PV system feeding DC power directly to loads can be an attractive solution to locally utilize DC electricity with minimum distribution and conversion losses. This concept has recently resulted in a novel grid system known as DC nanogrid. A DC nanogrid supplies the residential and commercial loads which may operate on AC or DC voltage of different utilization levels. Interfacing such variety of loads and controlling power flow between these loads presents an interesting challenge. Multiple dedicated converters can serve the purpose, but they exhibit the problems of power flow coordination, low efficiency, higher component count, and the increased size of the system. The last objective of this research is to develop innovative multi-terminal voltage converters for renewable-energy applications. A PV based multi-terminal DC nanogrid is developed using dual-input single-output (DISO) and single-input dual-output (SIDO) converter configurations with improved reliability and efficiency. The characterization studies of these converters such as sensitivity analysis and reliability analysis have been carried out. Also, the performance of the developed converter configurations are investigated using MATLAB along with Simulink toolbox. The SIDO converter configurations are experimentally validated using a 100W prototype, built and tested in the laboratory of DTU for practical applications.

The research work presented in the thesis is expected to provide good exposure to design, development and control of the grid-tied PV based microgrid and DC nanogrid.

## TABLE OF CONTENTS

COVER PAGE	i	
CERTIFICATE	ii	
ACKNOWLEDGEMENT	iv	
ABSTRACT	vi	
TABLE OF CONTENTS	ix	
LIST OF FIGURES	xiv	
LIST OF TABLES	xix	
LIST OF ABBREVIATIONS	xxi	
LIST OF SYMBOLS	xxiii	
<b>CHAPTER-I</b>	<b>INTRODUCTION</b>	<b>1-10</b>
1.1	Introduction	1
1.2	PV based microgrid	2
1.2.1	Characterization Studies of PV based microgrid	4
1.2.1.1	Sensitivity Analysis	4
1.2.1.2	Reliability Analysis	5
1.3	Islanding Studies for PV based microgrid	6
1.4	DC Nanogrid	6
1.5	Motivation and Research Objectives	7
1.6	Problem Identification	8
1.7	Organization of Thesis	9
1.8	Concluding remarks	10
<b>CHAPTER-II</b>	<b>LITERATURE REVIEW</b>	<b>11-25</b>
2.1	Introduction	11
2.2	PV based microgrid	11
2.2.1	Modelling and design of grid-tied PV based microgrid	12
2.2.2	Control algorithms for grid-tied PV based microgrid	15
2.2.2.1	MPPT control algorithm	15

2.2.2.2	Control algorithm for grid interfacing inverter	17
2.3	Sensitivity and reliability characterization studies	19
2.3.1	Sensitivity analysis	19
2.3.2	Reliability analysis	20
2.4	Islanding Studies for grid-tied PV based microgrid	21
2.5	Multi-terminal voltage converters for DC nanogrid	23
2.6	Identified research gaps	24
2.7	Concluding remarks	25
 <b>CHAPTER-III</b>		
	<b>PV BASED MICROGRID: MODELLING</b>	<b>26-49</b>
	<b>AND CHARACTERIZATION STUDIES</b>	
3.1	Introduction	26
3.2	Engineering Photovoltaics	26
3.2.1	Modelling of PV cell	29
3.2.1.1	Single-Diode Model	29
3.2.1.2	Double-Diode Model	30
3.3	Design of proposed PV based microgrid	31
3.3.1	Design of PV array	32
3.3.2	Design of DC-DC boost converter	33
3.3.3	Maximum Power Point Tracking	34
3.3.4	Design of PV inverter	35
3.3.5	Design of DC link capacitor and interfacing inductors	36
3.4	Characterization Studies of PV based microgrid	37
3.4.1	Sensitivity Analysis	37
3.4.1.1	Numerical results for sensitivity analysis	39
3.4.2	Reliability analysis	40
3.4.2.1	Evaluation of component reliability	41
3.4.2.2	Numerical results for component reliability	41
3.4.2.3	Evaluation of system reliability	44
3.4.2.4	Numerical results for system reliability	45
3.4.2.5	Reliability Improvement	47
3.5	Concluding remarks	49

<b>CHAPTER-IV</b>	<b>PV BASED MICROGRID: INTERFACING CONTROL ALGORITHMS</b>	<b>50-77</b>
4.1	Introduction	50
4.2	System configuration for PV based microgrid	51
4.3	Interfacing control algorithms	52
4.3.1	SRF theory based conventional control algorithm	54
4.3.2	Proposed AFL based intelligent control algorithm	56
4.3.3	Proposed feedforward-feedback adaptive control algorithm	61
4.4	Results and Discussions	63
4.4.1	Performance evaluation of proposed AFL based intelligent control algorithm	63
4.4.1.1	Performance under balanced linear and non- linear loads	64
4.4.1.2	Performance under load unbalancing	66
4.4.1.3	Performance under irradiation variation	67
4.4.2	Performance evaluation of proposed feedforward- feedback adaptive control algorithm	69
4.4.2.1	Performance under balanced linear and non- linear loads	69
4.4.2.2	Performance under load unbalancing	71
4.4.2.3	Performance under irradiation variation	73
4.4.3	Comparison of proposed intelligent and adaptive control algorithm with conventional control algorithm	74
4.5	Concluding remarks	77
<b>CHAPTER-V</b>	<b>PV BASED MICROGRID: ISLANDING STUDIES</b>	<b>78-96</b>
5.1	Introduction	78
5.2	Islanding	78
5.3	Basic Islanding Detection Techniques	81
5.3.1	Remote islanding detection techniques	81

5.3.2	Local islanding detection techniques	82
5.3.2.1	Passive islanding detection methods	82
5.3.2.2	Active islanding detection methods	84
5.4	Limitations of local islanding detection techniques	85
5.5	Proposed algorithm for islanding detection	87
5.5.1	Signal Extraction: Negative sequence voltage ( $V_{neg}$ ) extraction	88
5.5.2	Feature Extraction: Wavelet Packet Transform	88
5.5.3	Decision Making: Binary Tree Classifier	90
5.6	Results and Discussions	91
5.7	Concluding remarks	96

**CHAPTER-VI            MULTI-TERMINAL    DC    NANOGRID:    97-127**  
**DESIGN, DEVELOPMENT, AND**  
**IMPLEMENTATION**

6.1	Introduction	97
6.2	DC Nanogrid	98
6.3	Dual-input single-output converters	99
6.3.1	DISO buck-buck DC converter	100
6.3.1.1	Control Algorithm	100
6.3.1.2	Simulation Results	102
6.3.2	DISO buckboost-buckboost DC converter	103
6.3.2.1	Control Algorithm	104
6.3.2.2	Simulation Results	105
6.3.3	Characterization Studies	107
6.3.3.1	Sensitivity Analysis	107
6.3.3.2	Reliability Analysis	108
6.4	Single-input dual-output converters	112
6.4.1	SIDO with boost DC and buck DC output	112
6.4.1.1	Control Algorithm	113
6.4.1.2	Simulation Results	115
6.4.1.3	Hardware development and implementation	116



6.4.2	SIDO with boost DC and AC output	117
6.4.2.1	Control Algorithm	117
6.4.2.3	Simulation Results	119
6.4.2.4	Hardware development and implementation	120
6.4.3	Characterization Studies	121
6.4.3.1	Sensitivity Analysis	121
6.4.3.2	Reliability Analysis	123
6.5	Concluding remarks	127
<b>CHAPTER-VII CONCLUSIONS AND SCOPE FOR FURTHER WORK</b>		<b>128-132</b>
7.1	Introduction	128
7.2	Main Conclusions	129
7.3	Suggestions for further work	131
REFERENCES		<b>133-151</b>
APPENDICES		<b>152-157</b>
LIST OF PUBLICATIONS		<b>158-159</b>
BIODATA		<b>160</b>

## LIST OF FIGURES

<b>Figure</b>	<b>Description</b>	<b>Page No.</b>
1.1	Classification of grid-tied PV based microgrid	3
1.2	Block diagram of two-stage three-phase grid-tied PV based microgrid	3
1.3	Classification of methods for reliability analysis	5
2.1	Commonly used DC-DC converters (a) buck converter (b) boost converter and (c) buck-boost converter	13
2.2	Commonly used configurations of inverter (a) centralized technology, (b) string technology, (c) multi-string technology, and (d) module technology	14
3.1	I-V curve of a PV cell	27
3.2	I-V and P-V characteristics of a PV cell	28
3.3	Formation of PV array using PV modules	29
3.4	Single-diode model of PV cell	29
3.5	Double-diode model of PV cell	31
3.6	Schematic diagram of the PV based microgrid	31
3.7	I-V and P-V characteristics of PV array used in proposed system for (a) different temperature levels and (b) different irradiation levels	32
3.8	Circuit diagram of boost converter	33
3.9	Flowchart for Perturb and Observe MPPT algorithm	34
3.10	Schematic diagram of three-phase voltage source converter	35
3.11	Sensitivity graphs for (a) photon current and (b) boost converter output voltage	40
3.12	Pareto analysis of the electrical and electronic components	44
3.13	Reliability block diagram and logic gate representation of (a) standalone PV based microgrid, (b) standalone PV based microgrid with battery storage and (c) grid-tied PV based microgrid	46

3.14	Sensitivity graph of various stress factors	47
4.1	Simulink model of two-stage three-phase grid-tied PV based microgrid	51
4.2	Block diagram of closed-loop control of PV inverter	52
4.3	Space vector equivalent of PV inverter	53
4.4	Block diagram of control scheme for SRF theory based conventional control algorithm	55
4.5	Block diagram of control scheme for AFL based intelligent control algorithm	57
4.6	Membership functions for input variable 'error', 'derror' and output variable ' $I_{loss}$ '	59
4.7	Surface plot of rule base for computing ' $I_{loss}$ ' component	60
4.8	Block diagram of control scheme for feedforward-feedback adaptive control algorithm	62
4.9	Simulation results for PV based microgrid with AFL based intelligent control algorithm under balanced linear load	64
4.10	Simulation results for PV based microgrid with AFL based intelligent control algorithm under balanced non-linear load	65
4.11	Simulation results for PV based microgrid with AFL based intelligent control algorithm under unbalancing of non-linear load	67
4.12	Simulation results for PV based microgrid with AFL based intelligent control algorithm under irradiation variation	68
4.13	Simulation results for PV based microgrid with feedforward-feedback adaptive control algorithm under balanced linear load	70
4.14	Simulation results for PV based microgrid with feedforward-feedback adaptive control algorithm under balanced non-linear load	71
4.15	Simulation results for PV based microgrid with feedforward-feedback adaptive control algorithm under unbalancing of non-linear load	72
4.16	Simulation results for PV based microgrid with feedforward-	73

	feedback adaptive control algorithm under irradiation variation	
4.17	Comparison of AFL based intelligent control algorithm with SRF theory based conventional control algorithm for transient condition of sudden load change	75
4.18	Comparison of feedforward-feedback adaptive control algorithm with SRF theory based conventional control algorithm for transient condition of sudden load change	76
4.19	Comparison of performance of the conventional, intelligent and adaptive control algorithm for transient condition of sudden load change	77
5.1	Schematic diagram of IEEE Std 929-2000 based test setup for islanding detection in PV based microgrid	80
5.2	Example of power quality degradation caused by active islanding detection methods	86
5.3	Variation of ROCOF under varying active power mismatch for the designed system	86
5.4	Flowchart of the proposed islanding detection algorithm	87
5.5	Scheme for extraction of negative sequence component of PCC voltage signal	88
5.6	Structure diagram of three level DWT and WPT	89
5.7	Simulation results for Islanding of PV based microgrid with active power mismatch of 40%	92
5.8	Simulation results for Islanding of PV based microgrid with active power mismatch of 0%	93
5.9	Simulation results for sudden load change at PCC	93
5.10	Simulation results for grid side distortions	94
5.11	Results for the variation of islanding detection time of proposed algorithm under varying active and reactive power conditions	95
5.12	Comparison of islanding detection time of proposed and ROCOF algorithm	96
6.1	Schematic diagram of a DC Nanogrid	98
6.2	Circuit diagram of (a) DISO buck-buck DC converter and (b)	99

	DISO buckboost–buckboost DC converter	
6.3	Timing diagram of DISO buck-buck DC converter along with operational circuit during (a) Interval-I, (b) Interval-II, (c) Interval-III and (d) Interval-IV	101
6.4	Simulation results of DISO buck-buck DC converter	103
6.5	Timing diagram of DISO buckboost-buckboost DC converter along with operational circuit during (a) Interval-I, (b) Interval-II and (c) Interval-III	105
6.6	Simulation results of DISO buckboost-buckboost DC converter	106
6.7	Circuit diagram and Markov chain model of (a) Conventional buck converter and (b) Conventional buckboost converter	109
6.8	Circuit diagram and Markov chain model of (a) DISO buck-buck DC converter and (b) DISO buckboost- buckboost DC converter	110
6.9	Reliability curves of (a) Conventional buck converters and DISO buck-buck DC converter and (b) Conventional buckboost converters and DISO buckboost-buckboost DC converter.	111
6.10	Circuit diagram of (a) SIDO converter with buck DC and boost DC output and (b) SIDO converter with AC and boost DC output	112
6.11	Timing diagram of SIDO converter with buck DC and boost DC output along with operational circuit during (a) Interval-I, (b) Interval-II and (c) Interval-III	114
6.12	Simulation results of SIDO converter with buck DC and boost DC output (a) PWM switching waveforms and generated gate pulses $GS_1$ and $GS_2$ (b) Input voltage ( $V_{in}$ ), boost output voltage ( $V_{O1}$ ) and buck output voltage ( $V_{O2}$ ) waveforms	115
6.13	Experimental setup for SIDO converter with buck DC and boost DC output	116
6.14	Experimental results of SIDO converter with buck DC and boost DC output (a) $GS_1$ gate pulse obtained from carrier wave	117

	and reference signal (b) $GS_2$ gate pulse obtained from carrier wave and reference signal (c) Gate pulses $GS_1$ and $GS_2$ (d) $V_{O1}$ measured on Ch. 1, $V_{O2}$ measured on Ch. 2 and $V_{in}$ measured on Ch. 3 obtained	
6.15	Timing diagram of SIDO converter with AC and boost DC, output along with operational circuit during (a) Interval-I, (b) Interval-II, and (c) Interval-III	119
6.16	Simulation results of SIDO converter with AC and boost DC output (a) PWM switching waveforms and generated gate pulses $GS_1$ , $GS_2$ , $GS_3$ , and $GS_4$ (b) Input voltage ( $V_{in}$ ), Boost DC output voltage ( $V_{dcout}$ ) and AC output voltage ( $V_{acout}$ )	120
6.17	Experimental setup for SIDO converter with AC and boost DC output	120
6.18	Experimental results of SIDO converter with AC and boost DC output (a) Carrier wave and DC reference signals: $V_d$ and $-V_d$ (b) Carrier wave and sinusoidal reference signals: $V_m$ and $-V_m$ (c) Gate pulses $GS_1$ , $GS_2$ , $GS_3$ , and $GS_4$ (d) $V_{dcout}$ measured in Ch. 1, $V_{acout}$ measured in Ch. 2 and $V_{in}$ measured in Ch. 3	121
6.19	Circuit diagram and Markov chain model of conventional boost converter	124
6.20	Circuit diagram and Markov chain model of SIDO converter with buck DC and boost DC output	125
6.21	Circuit diagram and Markov chain model of SIDO converter with AC and boost DC output converter	126
6.22	Reliability curves of (a) conventional and SIDO converter with buck DC and boost DC output (b) conventional and SIDO converter with AC and boost DC output	127

## LIST OF TABLES

<b>Table</b>	<b>Description</b>	<b>Page No.</b>
2.1	Performance parameters of basic DC-DC converters	13
3.1	Sensitivity values of PV cell and converter parameters	39
3.2	Failure rate and MTBF of electronic components of a PV system	43
3.3	Failure rate and MTBF of electrical components of a PV system	44
3.4	Reliability values for different configurations of PV based microgrid	45
3.5	Improved failure rate and reliability of components and standalone PV system	48
3.6	Reliability values for different configurations of PV based microgrid with redundancy	49
4.1	Fuzzy rule base for computing $I_{loss}$	60
5.1	Inverter response to abnormal voltage and frequency disturbance	80
5.2	Frequency band of each decomposed level	90
6.1	Switch status and voltage across inductor for DISO buck-buck DC converter during different intervals of time	100
6.2	Switch status and voltage across inductor for DISO buckboost-buckboost DC converter during different intervals of time	104
6.3	Sensitivity functions and normalized sensitivity values of DISO buck-buck DC converter	107
6.4	Sensitivity functions and normalized sensitivity values of DISO buckboost-buckboost DC converter	108
6.5	Voltages and currents of SIDO converter with boost and buck DC output during different intervals of time.	113
6.6	Voltages and currents of SIDO converter with AC and boost DC output during different intervals of time.	118

6.7	Sensitivity functions and normalized sensitivity values of SIDO converter with boost and buck DC output	122
6.8	Sensitivity functions and normalized sensitivity values SIDO converter with AC and boost DC output	123



## LIST OF ABBREVIATIONS

AFD	Active Frequency Drift
AFL	Asymmetrical Fuzzy Logic
ANFIS	Adaptive Neuro-Fuzzy Inference System
ANN	Artificial Neural Network
APF	Active Power Filter
BLDC	Brushless DC
CSC	Current Source Converter
DISO	Double-Input Single-Output
DG	Distributed Generation
DWT	Discrete Wavelet Transform
ESS	Energy Storage System
FLC	Fuzzy Logic Controller
HCC	Hysteresis Current Control
IGBT	Insulated-Gate Bipolar Transistor
LED	Light Emitting Diodes
MIMO	Multiple-Input Multiple-Output
MISO	Multiple-Input Single-Output
MPP	Maximum Power Point
MPPT	Maximum Power Point Tracking
MTBF	Mean Time Between Failures
NDZ	Non-Detection Zone
OFP/UFP	Over Frequency Protection /Under Frequency Protection
OVP/UVF	Over Voltage Protection/Under Voltage Protection
PCC	Point of Common Coupling
PI	Proportional Integral
PLL	Phase-Locked Loop
PV	Photo Voltaic
P&O	Perturb And Observe
PWM	Pulse Width Modulation

RBD	Reliability Block Diagram
RES	Renewable Energy Sources
RMS	Root Mean Square
ROCOF	Rate Of Change Of Frequency
SA	Sensitivity Analysis
SFS	Sandia Frequency Shift
SIDO	Single-Input Double-Output
SIMO	Single-Input Multiple-Output
SMS	Slip Mode Frequency
SRF	Synchronous Reference Frame
STATCOM	Static Synchronous Compensator
SVS	Sandia Voltage Shift
THD	Total Harmonic Distortion
UPF	Unity Power Factor
VSC	Voltage Source Converter
WPT	Wavelet Packet Transform
WT	Wavelet Transform

## LIST OF SYMBOLS

$A$	Diode ideality factor
$C_c$	Capacitance in DC-DC converter
$C_d$	DC link capacitance
$C_L$	Load capacitance
$CF$	Crest factor
$D$	Duty cycle for converters
$D_c$	Diode in DC-DC converter
$e(t)$	Voltage error signal
$E$	PV operating irradiation
$E_{ref}$	PV reference irradiation
$F(x)$	Probability of failure
$f_o$	Resonant frequency
$f_s$	Switching frequency
$G$	Voltage Gain
$GS$	PWM gate signals
$h$	Overload factor
$i_c$	Inverter current
$i_{ca}, i_{cb}, i_{cc}$	Inverter currents in three phase system
$i_l$	Load current
$i_{la}, i_{lb}, i_{lc}$	Load currents in three phase system
$i_s$	Grid current
$i_{sa}, i_{sb}, i_{sc}$	Grid currents in three phase system
$i_{sa}^*, i_{sb}^*, i_{sc}^*$	Reference grid currents in three phase system
$i_d$	$d$ - axis current
$i_q$	$q$ - axis current
$I_{loss}$	Output of DC link voltage controller
$I_{mpp}$	Array current at maximum power point
$I_o$	Diode saturation current of a PV cell

$I_{PV}$	Output current of a PV cell
$I_{ph}$	Photon current of a PV cell
$I_{sc}$	Short circuit current of a PV cell
$I_{sw}$	Current rating of IGBT Switch
$\Delta i_i$	Ripple current in input current of boost converter
$I_{in}$	Input current of DC-DC converter
$I_{out}$	Output current of DC-DC converter
$I_l$	Current through inductor in DC-DC converter
$I_d$	Current through diode in DC-DC converter
$K_i$	Integral gain of controller
$K_p$	Proportional gain of controller
$L_{fa}, L_{fb}, L_{fc}$	Interfacing inductor of PV inverter in three phase system
$L_{sa}, L_{sb}, L_{sc}$	Grid inductor in three phase system
$L_L$	Load inductor
$L_c$	Inductor in DC-DC converter
$m$	Modulation index
$N_s$	Number of solar cells in series
$N_p$	Number of solar cells in parallel
$P(t)$	Probability vector
$P_{PV}$	Power supplied by PV array
$P_{grid}$	Active power supplied by grid
$P_{inv}$	Active power supplied by inverter
$P_{load}$	Active power consumed by load
$\Delta P$	Active power mismatch
$q$	Elementary charge ( $1.602 \times 10^{-19}C$ )
$Q_f$	Quality factor
$Q_{grid}$	Reactive power supplied by grid
$Q_{inv}$	Reactive power supplied by inverter
$Q_{load}$	Reactive power required by load
$\Delta Q$	Reactive power mismatch
$R$	Reliability

$R_f$	Internal resistance of the interfacing inductor
$R_{in}$	Input resistance of DC-DC converter
$R_L$	Load resistance
$R_{out}$	Output resistance of DC-DC converter
$R_{sa}, R_{sb}, R_{sc}$	Grid resistances in three phase system
$R_{mpp}$	Resistance at maximum power point
$R_p$	shunt resistance ( $\Omega$ ) of solar cell
$R_s$	series resistance ( $\Omega$ ) of solar cell
$S$	Switch
$\hat{S}_p^F$	Normalized Sensitivity of function 'F' with respect to 'P'
$T$	Switching time period
$T_{PV}$	PV cell operating temperature, in K
$T_{ref}$	PV cell reference temperature, 278 K
$T(s)$	Transfer function
$v_c$	Inverter output voltage
$v_{ca}, v_{cb}, v_{cc}$	Inverter voltages in three phase system
$v_l$	Load voltage
$v_{la}, v_{lb}, v_{lc}$	Load voltages in three phase system
$v_s$	Grid voltage
$v_{sa}, v_{sb}, v_{sc}$	Grid voltages in three phase system
$V_{dc}$	DC link voltage
$V_{dc}^*$	Reference DC link voltage
$V_{LL}$	RMS value of line to line voltage
$V_{sw}$	Voltage rating of IGBT Switch
$V_{neg}$	Negative sequence voltage
$V_{mpp}$	Array voltage at maximum power point
$V_{PV}$	Output voltage of PV array
$V_{oc}$	Open circuit voltage of PV cell
$V_L$	Voltage across inductor in DC-DC converters
$V_{in}$	Input voltage of DC-DC converter
$V_{out}$	Output voltage of DC-DC converter

$\Delta v$	Voltage ripple in output voltage of boost converter
$V_{carrier}$	Triangular carrier wave signal for SIDO converters
$V_m$	Sinusoidal reference signal for SIDO converter
$V_{ab}$	Output voltage at inverter bridge terminals of SIDO converter
$V_{mod}$	Reference signal for SIDO converter
$V_{sn}$	Switch node voltage for SIDO converter
$V_{o1}$	Boost output voltage for SIDO converter
$V_{o2}$	Buck output voltage for SIDO converter
$V_{in1}$	Input voltage of DISO converter
$V_{in2}$	Input voltage of DISO converter
$x$	Output of DC link fuzzy controller
$\alpha$	Complex operator
$\theta$	Voltage phase angle
$\lambda$	Failure Rate
$\sigma$	Stress factor
$\varphi(x)$	Scaling function
$\psi(x)$	Wavelet function
$\kappa$	Boltzmann constant

# **CHAPTER-I**

## **INTRODUCTION**

### **INTRODUCTION**

In recent years, concerns are raised over traditional power plants in view of their higher initial costs, lower efficiency and harmful environmental effects [1]. Also, the existing conventional transmission and distribution systems have been facing issues such as capacity constraints for bulk power transmission, higher tariff and high losses due to the fact that the loads are located far from generation. Considering the above, it is obvious that the traditional power system no longer guarantees reliable and sustainable electricity supply. Localized power generation, i.e. microgrid with distributed generation (DG) is appearing as an alternate solution to the traditional power system.

DG is an approach that uses small-scale power generation technologies to produce electricity close to the end users. In contrast to large-scale generating stations located far from load centres, DGs use small generation plants and can provide power onsite with least dependence on the transmission system. DGs can yield power ranging from a few kilowatts to megawatts.

Microgrid is a group of DG units, controllable loads and storage devices, all operating together as a single system by using power electronic interfaces and controls for flexibility [2]. With this form of power system, transmission line losses are considerably reduced as the energy sources are usually very close to the consumer. Besides providing cheaper electricity, microgrid have the advantage of providing clean power as they normally have renewable energy sources (RES) viz. solar, wind, fuel cells, hydropower, biomass and geothermal as energy sources. Amongst the several available forms of renewable energy, solar energy is gaining widespread popularity. Solar PV systems, compared to other renewable energy power systems, have abundant solar energy as a source, low maintenance solar panels with no moving parts, no noise and zero emissions, competitive pricing with vast technological advancements and least environmental effects [3]. PV systems range from small, rooftop-mounted or building-

integrated systems with capacities from a few to several tens of kilowatts, to large-scale PV power plant of hundreds of megawatts. More importantly, PV is one of the most suitable RES, especially in remote areas where electricity from the central grid is not available and alternative sources of electricity such as diesel are expensive. Hence, PV based microgrid may be one of the solutions to meet the challenges faced by the conventional grid.

However, with the increased number of microgrid deployed into the traditional grid system, it is necessary to identify the potential technical and operational problems brought about by the microgrid deployment. Also, technically innovative ways have to be introduced for sensing, monitoring, and coordinating future distribution systems in order to facilitate the integration of microgrid without creating reliability and safety problems.

## **1.2. PV BASED MICROGRID**

PV based microgrid can operate in two ways, either in standalone mode or in grid-tied mode. A standalone microgrid is referred to as a grid which is not connected to the utility grid and operates autonomously. Energy storage system (ESS) like batteries are an integral part of PV based standalone microgrid. During the night, or during a period of low solar irradiance, such as a cloudy or rainy day, when the output of PV system is low, batteries are used to supply power to the loads. A grid-tied microgrid is defined as a grid that is connected to the utility grid at the point of common coupling (PCC). It cooperates with the utility grid by adjusting the power balance of the system in terms of facilitating the power flow between the microgrid source, load and grid. Grid-tied PV based microgrid can be connected to a single-phase or three-phase network depending on the configuration at the PCC [4]. It can further be classified on the basis of number of stages: single-stage and two-stage as shown in figure 1.1 [5].

In a single-stage configuration, a grid-interfacing inverter is connected across PV array, which provides AC output of desired voltage and frequency in order to integrate microgrid with the utility grid [5]. In the two-stage configuration, a DC/DC converter with maximum power point tracking (MPPT) capability is usually interposed between



PV array and the grid-interfacing inverter in order to provide the necessary DC voltage at the inverter.

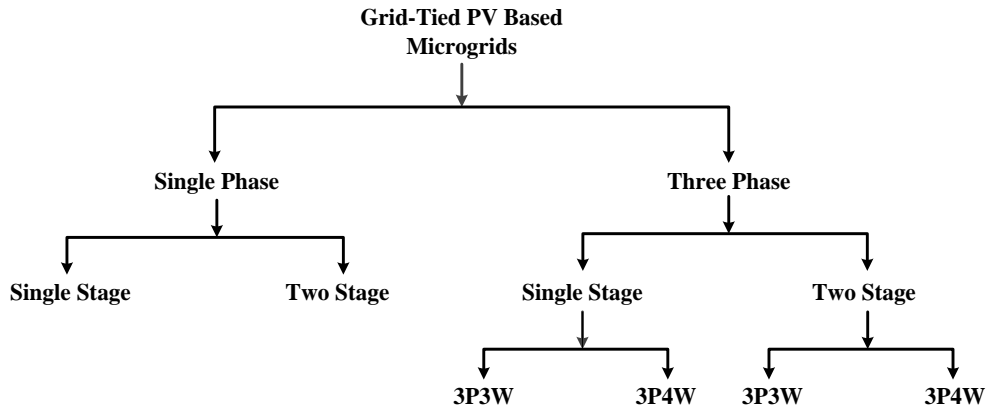


Figure 1.1. Classification of grid-tied PV based microgrid

A two-stage grid-tied PV based microgrid basically requires two control algorithms: (a) algorithm for MPPT, and (b) algorithm for controlling of the grid-interfacing inverter, as shown in figure 1.2.

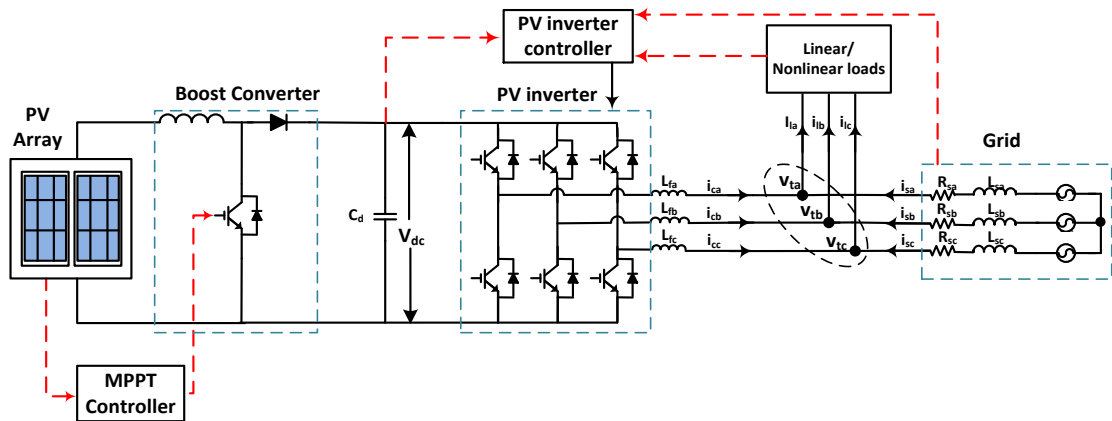


Figure 1.2. Block diagram of two-stage three-phase grid-tied PV based microgrid

MPPT is a widely addressed issue right from the evolution of the PV generating system. The change in irradiance and temperature results in deviation of power from the maximum power. Hence, a control algorithm is required to quickly respond to this change and track the maximum power [6, 7]. The maximum power thus generated is supplied to the load through a grid-interfacing PV inverter, at desired voltage and frequency, maintaining the power balance between DG, load and grid. Generally, the inverter is controlled in a way to maintain DC-link voltage constant, thereby controlling

the flow of active power. The inverter control strategies can be implemented in both stationary as well as rotating (synchronous) reference frame. However, the synchronous reference frame is more suitable, as it converts the sinusoidal signals into DC-signals, which can be easily controlled by simple PI controllers. The synchronous reference frame transformation requires the grid synchronizing angle, which can be easily detected from grid voltage using a phase lock loop (PLL) [8].

### 1.2.1. Characterization Studies of PV based microgrid

Characterization studies viz. sensitivity analysis and reliability analysis are the performance indicators of any system. Sensitivity analysis is carried out for determining the impact of input parameters on the output of a system [9, 10] while the reliability analysis is carried out to ascertain that a system can perform its intended function without failure for a specified interval under stated conditions [11-14]. These studies are intended to give a better insight to the PV system designer and its operator to predict and select the optimal operating point in dynamic situations.

#### 1.2.1.1. Sensitivity Analysis

Sensitivity analysis (SA) is the determination of dependence of a function on the parameters of interest. Partial differentiation type sensitivity analysis gives the normalized sensitivity of a quantity, i.e. the percentage change in the value of the quantity for one per cent change in the value of the parameter of interest. The normalized sensitivity of a function, F with respect to parameter p can be evaluated by,

$$\hat{S}_p^F = \frac{\partial F/F}{\partial p/p} = \left(\frac{p}{F}\right) \left(\frac{\partial F}{\partial p}\right) = \frac{\partial(\log F)}{\partial(\log P)} \quad (1.1)$$

If a number of parameters vary simultaneously, then the sensitivity of the function is computed using the Jacobian matrix given by,

$$J_{0P_i}^F = \begin{bmatrix} \frac{\partial F_1}{\partial P_1} & \frac{\partial F_1}{\partial P_2} & \dots & \frac{\partial F_1}{\partial P_N} \\ \cdot & \cdot & \cdot & \cdot \\ \cdot & \cdot & \cdot & \cdot \\ \frac{\partial F_A}{\partial P_1} & \frac{\partial F_A}{\partial P_2} & \dots & \frac{\partial F_A}{\partial P_N} \end{bmatrix} \quad (1.2)$$

The PV generated power is a function of PV cell characteristics such as PV voltage and current, and associated converter parameters. The PV cell shows nonlinear current-voltage characteristics depending on irradiance level and cell temperature [3]. Also, the output of a converter depends upon its designed parameters. Thus, there is a need to carry out the sensitivity studies of PV cell and converter output related to parameters of interest to analyze their performance under real conditions.

**1.2.1.2. Reliability Analysis**

Reliability is the probability of availability. Availability of a system can be calculated as given by,

$$Availability = \frac{Operational\ Time}{Operational\ Time + Down\ Time} * 100 \tag{1.3}$$

If F(x) is the probability of failure, then reliability can be defined as R(x) = 1- F(x) and is time dependent. Existing methods for reliability evaluation can be classified into further categories as shown in figure 1.3.

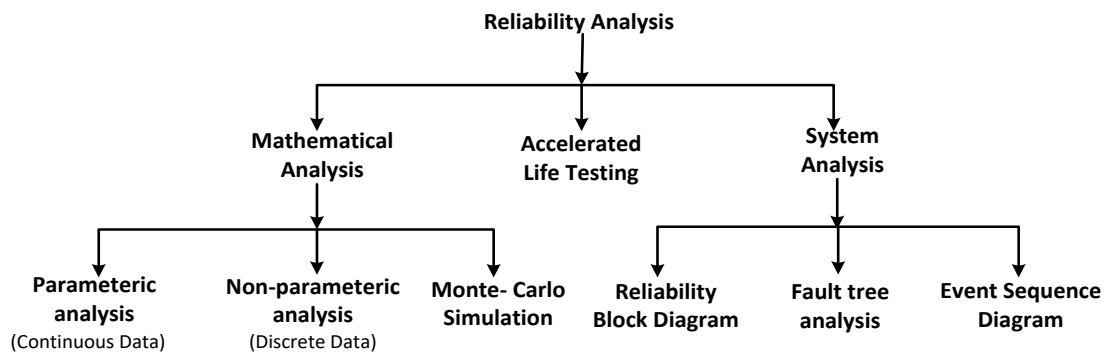


**Figure 1.3. Classification of methods for reliability analysis**

For a system to be reliable, the reliable operation of all its components is also important. Although, PV modules operate reliably for 25–30 years, but the components of the PV system experience stress due to switching operation of devices, environmental parameters, and voltage levels to which devices are subjected. The reliability studies of the components for the stipulated time are equally important for the efficient working of the overall system. Therefore, it is important to assess the impact of adding PV

sources to a power system in terms of its reliability contribution in meeting energy demand.

### **1.3. ISLANDING STUDIES FOR PV BASED MICROGRID**

Islanding can be defined as a condition in which a DG remains energized in a localized area while the remainder of the electric power system loses power due to some faults, etc. This is an undesirable mode of operation, as this results into several negative impacts on utility power system and the DG itself, such as the safety hazards to utility personnel, PQ related problems of electric service to the utility customers, and serious damages to the DG if utility power is wrongly restored. Islanding, therefore, must be detected at the earliest. Each DG unit must be equipped with an islanding detection device, anti-islanding relay, that disconnects the DG as soon as islanding is detected. IEEE standard recommends disconnecting all DGs within 2 s after the formation of unwanted islanding [15-17].

Islanding detection methods are broadly classified into communication-based methods and DG resident methods. Communication-based methods work on the principle of communication between the utility and distributed energy resource. It consists of schemes such as power line carrier communication scheme, transfer trip scheme, etc. Whereas, DG resident methods are based on measuring the variations in system parameters, such as frequency, voltage, impedance, phase angle, active power, reactive power, and harmonic distortion at the DG site. DG resident methods are further sub-grouped as passive and active methods. Over/under voltage protection (OVP/UVP), over/under frequency protection (OFP/UFP), rate of change of frequency and power, and harmonic distortion are some of the passive islanding detection methods, while, slip-mode frequency shift, Sandia frequency and voltage shift, and negative sequence current injection are some active islanding detection methods [18, 19].

### **1.4. DC NANOGRID**

With falling prices of PV cells and associated equipment in recent times, the market has opened up wide opportunities for solar energy technologies throughout the world. There is ample scope for PV based energy generation for regions where the potential for grid extension is likely to remain low. A standalone microgrid generally feeds to

house hold loads, such as LED lights, mobile phones, computers, variable-speed motor based appliances, pumps, etc. with the majority of them being run on DC power. Standalone solar PV based systems such as DC nanogrid is thus, emerging as an attractive solution to locally utilize the DC electricity with minimum distribution and AC/DC and DC/AC conversion losses [20- 25]. Further, AC loads in the standalone microgrid can also be fed through converters. However, with both AC and DC loads at different operating voltage levels, controlling of power flow between them present an interesting challenge. Multiple dedicated converters can solve the purpose, but they exhibit the problems of power flow coordination, low efficiency, higher component count, and the increased size of the system. However, multi-terminal converters can provide different input and output voltages in an integrated architecture with higher efficiency and compactness. Hence, multi-terminal voltage converters are best suited for DC nanogrid.

### **1.5. MOTIVATION AND RESEARCH OBJECTIVES**

Microgrid can be very useful in making use of RES for electricity generation. They can provide reliable electricity in urban areas and electricity at a reasonable price to the remote and isolated communities. PV based microgrid can meet most of the concerns and issues of the energy planners. Today, PV generation cost per unit has come down drastically. In addition to cost reduction, generation from PV modules provide clean energy and high reliability when connected with the utility grid. Further, increased DC voltage dependent domestic loads such as LEDs, BLDC based fans and pumps, etc. and advancement of technologies in the area of real-time control, power electronics and system integration motivated and led to the following research objectives:

1. Developing characterization functions of sensitivity and reliability for the designed PV system and its performance evaluation.
2. Developing interfacing control algorithms for inverters in a grid-tied PV based microgrid.
3. Design and development of intelligent and flexible algorithms for islanding detection in PV based microgrid.
4. Design and development of multi-terminal voltage converters for DC nanogrid.

## 1.6. PROBLEM IDENTIFICATION

For meeting the defined objectives, the following problems are identified:

1. In PV based microgrid, the PV array is interfaced with the power electronic converters. The mathematical model of the system components viz. PV cell, DC-DC converter, PV inverter, DC link capacitor and interfacing inductors need to be developed. The simulation studies using MATLAB software needs to be carried out.
2. The validity of the model for variation in the parameters of interest can be studied using sensitivity analysis. The sensitivity functions of the PV cell and a boost converter, therefore, needs to be developed. The utility of the developed functions may be shown by studying the simulated performance of the PV array. The reliability studies of standalone and grid-tied PV system can be performed. Also, methods to improve system reliability may be discussed.
3. PV inverter control needs intelligent and adaptive algorithms which can take into account the uncertainties and vagueness into consideration. The control algorithm along with active power control, shall also provide additional features of reactive power compensation, harmonics compensation and load balancing. Intelligent and adaptive control algorithms meeting these requirements need to be developed.
4. Anti-islanding studies are a pre-requisite for grid interfacing inverters. Unintentional islanding is undesirable and has to be timely detected to de-energize the inverter from further harming the loads and operators. Thus, islanding detection methods having negligible non-detection zone and run-on time need to be developed. Also, the developed algorithm has to be compared with the existing algorithms to establish the superiority of the developed algorithm.
5. DC Nanogrid is the future of standalone microgrid for providing electricity to the rural and off-grid areas. Multi-terminal voltage converters need to be developed for DC nanogrid that works on DC source like PV and supply power to DC as well as AC loads. Also, studies related to the risk management and parametric variation needs to be performed for such multi-terminal converters. This will help the design engineer to visualize the system performance and risk management under any situation.

## 1.7. ORGANIZATION OF THESIS

Chapter-I presents the introduction, motivation, objectives and problem identification of the research work carried out. The organization of the thesis is also given in this chapter.

Chapter-II includes the literature review of PV based microgrid and its associated areas. Literature review related to sensitivity and reliability analysis of PV based microgrid, control algorithms for MPPT and grid-interfacing PV inverter, islanding detection techniques and multi-terminal converter based DC nanogrid has been presented.

Chapter-III discusses the PV based microgrid modelling and its characterization studies viz. sensitivity and reliability analysis. Design of components in a PV based microgrid has been presented. Differential sensitivity analysis has been used to develop the sensitivity functions of the PV system. Reliability analysis is carried out using Pareto analysis and reliability block diagram, along with logic gate representation model, has been developed and presented for different configurations of PV based microgrid. Reliability improvement methods have also been presented. For reliability evaluation MIL-HDBK-217 military handbook and MTBF calculator software by ALD are referred.

Chapter-IV presents the novel AFL based intelligent and feedforward-feedback adaptive interfacing control algorithms for inverter in a two-stage three phase grid-tied PV system. The proposed algorithms, along with active power control, also provides additional features of reactive power compensation, harmonics compensation and load balancing under linear and nonlinear load conditions to the PV inverter. Also, the performance of the PV inverter with proposed algorithms is investigated using MATLAB along with Simulink toolbox.

Chapter-V proposes a novel WPT signal processing based passive islanding detection algorithm to detect an islanding condition in a PV based microgrid. Binary tree classifier is further used for decision making. Based on IEEE Std. 929-2000 and UL1741 anti-islanding test requirements, extensive simulation studies have been carried out.

Chapter-VI proposes multi-terminal converters viz. dual-input single-output and single-input dual-output converters for PV based DC nanogrid. Further, the steady-state characteristics of developed multi-terminal converters have been validated by extensive simulation studies. Sensitivity functions and Markov reliability model of these converters are also developed and presented in this chapter. Experimental prototype of SIDO converter configurations is developed in the laboratory using my-RIO controller and DSP (dSPACE 1104 R&D) controller.

Chapter-VII summarizes the performance of PV based microgrid and highlights the main conclusions of the proposed work. The scope for further work in this area is also enlisted at the end of this chapter.

At the end of the thesis, the list of references and appendices is provided.

## **1.8. CONCLUDING REMARKS**

This chapter provides an overview of the research work carried out and embedded in this dissertation. The motivation and the objectives of the research work are presented and the research problems have been identified. The overview of the research work carried out is précised chapter wise.



## **CHAPTER-II**

### **LITERATURE REVIEW**

#### **INTRODUCTION**

The introductory chapter-I, defines the objectives, motivation and identification of the research problems. To gain the right perspective of research problems, a literature review has been carried out in the related areas of the research work. This chapter presents the brief review on the (i) PV based microgrid, (ii) PV system modelling, (iii) Sensitivity and reliability characterization of system, (iv) Islanding operation of PV based microgrid, and (v) Multi-terminal voltages converters for DC nanogrid. In the subsequent sections each topic is briefly discussed and reviewed without trying to be exhaustive. The references cited in this chapter are also representative rather than exhaustive.

#### **2.2. PV BASED MICROGRID**

Microgrid are electricity distribution systems containing DG, loads and storage devices that can be operated in a controlled, coordinated way while connected to the grid or islanded. The DGs are near to customers sites and are equipped with power electronic interfaces to provide the control and flexibility required by the microgrid. Appropriately designed power electronics and controls ensure that the microgrid meets the needs of its customers as well as the utility [2].

Robust and sustainable power generation system needs to be environment-friendly and reliable. PV offers an alternative source of electric power generation which is pollution free, environment-friendly and sustainable. Grid-tied microgrid enhances the reliability of continuous supply to customers. Such integration introduces many challenges viz. efficiency, reliability, power quality, etc. which need to be addressed before integrating PV based microgrid to the power grid [3-5]. Modelling of the complete system along with control strategies is thus essential to predict the behaviour of the system under steady state as well as dynamic state before making an investment.

### 2.2.1. Modelling and design of grid-tied PV based microgrid

PV cell is the basic unit of a PV generation system and its circuit model is necessary in order to study the system behaviour. Output parameters of a solar cell depend upon the meteorological parameters like solar irradiance and temperature. In literature, different modelling methods of solar PV cell are available. Single-diode and double-diode models are commonly employed for the PV cell performance study [26, 27]. Ahmed et al. [28] had developed a seven-parameter model of PV cell from the generalized five parameters (single-diode model) and studied its performance. Lun et al. [29] developed a new method based on Taylor's series expansion for the single-diode model of solar cells. The developed model gives the entire I–V characteristics and can be used to compute current directly corresponding to different voltage. K. Ishaque et al. [30] presented a double diode model of the PV cell. The proposed model gives satisfactory accuracy at low values of solar irradiance and allows to predict solar PV system performance more accurately. The authors also estimated the values of series and shunt resistance so that the input parameter was reduced to four and hence, computational time was reduced.

As compared to double diode model, single diode is preferred because of simplicity of model, less parameter identification and satisfactory performance at normal conditions [31]. The output power produced by the solar cell is not sufficient for use. They are grouped in series and parallel to make solar module and arrays. N. Pandiarajan et al. [32] presented the procedure for the simulation of PV modules with MATLAB/Simulink. Authors had used single-diode model of PV cell to simulate a 36W PV module with its I-V and P-V characteristics.

Advancement in semiconductor and power electronic technologies has made a remarkable improvement in power extraction from PV modules. The output voltage/power of PV system is low and needs to be enhanced for the applications like water pumping system, grid-tied PV system, etc. Therefore, DC-DC converter plays a significant role in the architecture of two-stage grid-tied PV system. Basic DC-DC converters are of three types [33, 34] viz. buck converter, boost converter and buck-boost converter shown in figure 2.1.

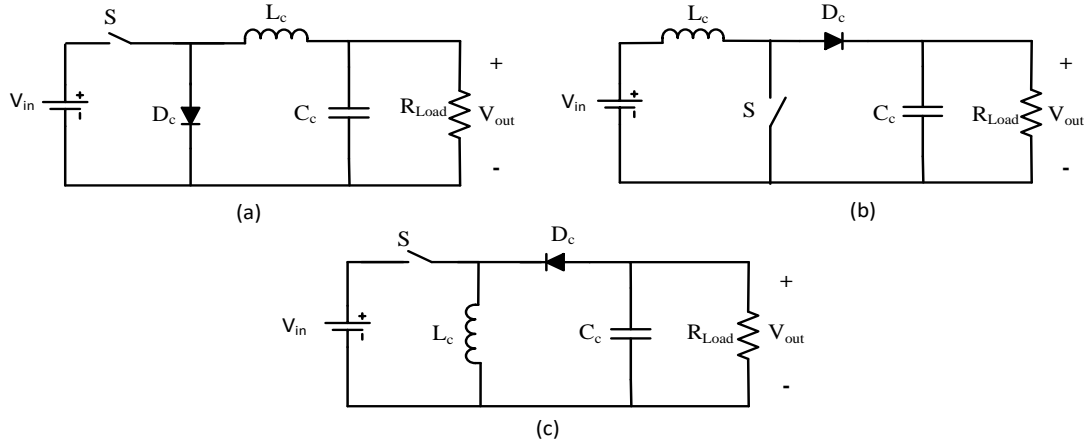


**Figure 2.1. Commonly used DC-DC converters (a) buck converter (b) boost converter and (c) buck-boost converter**

The performance parameters for all the basic DC-DC converters are tabulated in table 2.1 [33-35]. The designing of converter depends heavily on these parameters.

**Table 2.1. Performance parameters of basic DC-DC converters**

Types of Converter	Parameters				
	$A_v = V_{out}/V_{in}$	$A_i = I_{out}/I_{in}$	$R_{in} = V_{in}/I_{in}$	$L_c$	$C_c$
Buck	$D$	$\frac{1}{D}$	$\frac{R_{Load}}{D^2}$	$\frac{V_{out}(1-D)}{\Delta i_i f_s}$	$\frac{\Delta i_i}{8\Delta v f_s}$
Boost	$\frac{1}{1-D}$	$1-D$	$(1-D)^2 R_{Load}$	$\frac{V_{in} D}{\Delta i_i f_s}$	$\frac{I_{out} D}{\Delta v f_s}$
Buck-Boost	$\frac{D}{1-D}$	$\frac{1-D}{D}$	$\frac{(1-D)^2}{D^2} R_{Load}$	$\frac{V_{out}(1-D)}{\Delta i_i f_s}$	$\frac{I_{out} D}{\Delta v f_s}$

The boost converter topology has cheaper implementations and better dynamic response when compared to the buck converter. Hence they are widely used in MPP tracking applications of PV system [36].

In a microgrid, inverter is used for interfacing the microgrid with the main grid. Various topologies for grid-tied PV systems are categorized on the basis of number of power processing stages, whether utilizes a transformers or not, and types of grid interface [37-46]. Based on structural configuration, grid-tied inverters are classified as: central type, string type, multi-string type and module type as shown in figure 2.2. In central type configuration, all the PV strings are connected to the DC side of the inverter and the single AC output is connected to the utility grid [37]. In string type configuration, each PV string is connected to an inverter at the DC side, and AC outputs of all inverters

are combined and connected to the utility grid. Multi-string configuration is a further development of string inverter, where several strings are interfaced with their own DC-DC converter to a common DC-AC inverter. In module type configuration, each module has one dedicated inverter connected on the back of the module [38]. The module DC terminals are connected to the DC side of the inverter and then AC wires of all terminals are combined and connected to the utility interconnection point. Central type inverter is widely used for low voltage applications because of its simplicity and better control. Multi-string inverter can be used in high power applications with higher efficiency.

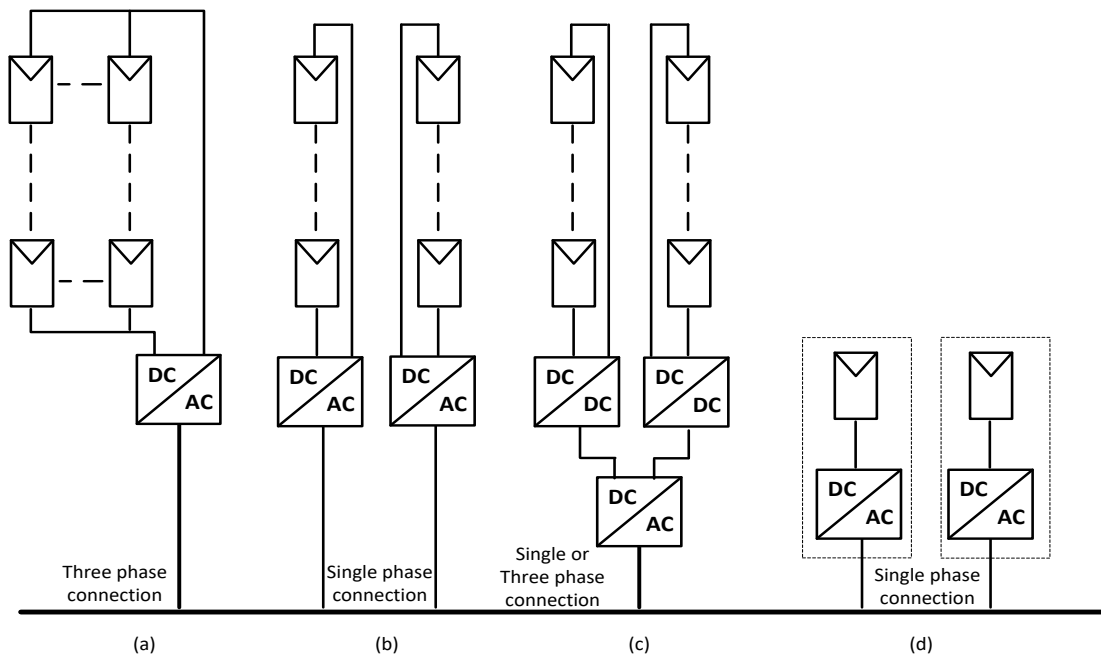


**Figure 2.2. Commonly used configuration of inverter (a) centralized technology, (b) string technology, (c) multi-string technology, and (d) module technology [47]**

Another classification of inverters is based on power processing stages [47]. Accordingly the inverters are classified as,

- (a) Single stage inverter: It has single power processing stage that handles the MPPT, voltage amplification, and grid current control.
- (b) Two stage inverter: It is a dual power processing inverter where the DC-DC converter is responsible for the MPPT and the DC-AC inverter controls the grid current. Voltage amplification can be included in both stages.

L. G. Junior et al. [48] presented the evaluation of different inverters for solar PV

applications. According to the authors, the most suitable topology uses a boost stage and one inverter stage cascaded. Transformer integrated topologies have low efficiency and high-frequency transformer. This paper presented the comparative simulated result for various topologies. F. Schimpf et al. [49] presented a review for low and medium level grid-connected solar PV inverters, especially for rooftop applications. Again the authors classified the inverters according to the configuration of power stages, use of transformer and type of PV system. According to this review transformerless topologies are advantageous over the other topologies in terms of cost, weight etc. S. K. Khardem et al. [50] presented a technical review of power quality problems associated with the renewable energy based DG system. This review paper also described the role of custom power devices like STATCOM (Static Synchronous Compensator), etc. in power quality improvement. Authors explained that output of PV panel depends on the solar intensity and atmospheric conditions and power quality issues are not only because of solar irradiance but also depend upon the inverters, filters, controlling mechanism, etc. According to the authors, special attention is required to maintain the voltage profile and power flow. Custom power devices are found to be very capable for integration of renewable energy based generating plants into the grid.

### **2.2.2. Control algorithms for grid-tied PV based microgrid**

Two basic control algorithms are needed in a grid-tied PV based microgrid: (a) algorithm for MPPT and (b) algorithm for controlling of grid interfacing inverter.

#### **2.2.2.1. MPPT control algorithm**

MPPT is the widely addressed issue right from the evolution of the PV generating system. There are numerous MPPT techniques, and they vary on the basis of complexity, convergence speed, parameters, cost and ability to detect local maxima and minima. These MPPT techniques are based on the reference voltage or reference current signal of the PV system which is adjusted in order to achieve Maximum Power Point (MPP). T. Eshram et al. [51] and B. Subudhi et al. [52] reviewed different MPPT techniques evolved from 1968 to 2002.

R. Faranda et al. [53] presented a comparative and analytical study of ten MPPT algorithms using MATLAB/Simulink. Authors compared the ten most commonly used

techniques namely incremental conductance method, open voltage method, short-circuited pulse method, Perturb and Observe (P & O), constant voltage method, and a few more. According to the author's conclusion, open voltage and short circuit pulse techniques provide low energy output in comparison with P & O and incremental conductance algorithms. Authors analyzed that the constant voltage technique is worst among the all ten MPPT methods. X. Liu et al. [54] developed the conventional P&O method, however it is not efficient. To improve the efficiency of P&O MPPT algorithm, authors had developed an enhanced P&O technique. In this new method the maximum power is recorded and when its difference with the present power reaches zero duty cycle at that instant is considered as the optimal signal. The simulation is done using Powersim and the algorithm is implemented on a 3 kW grid-connected power system. B. Masood et al. [55] had studied P&O and incremental conductance techniques and their significance under different weather conditions are listed. Authors suggested that P&O and incremental conductance method are cheap techniques with remarkable efficiency but are not suitable for rapidly changing weather conditions. A better technique to track MPP which is hybrid of both P&O and incremental conductance is presented. Authors had measured the value of irradiation in real time to decide the suitability of these which techniques for a particular time period. A. Ramasamy et al. [56] suggested a new MPPT technique by using fractional open circuit voltage based fractional order incremental conductance method. This combined approach deals with the measurement of current and voltage and overcomes the disadvantages of incremental conductance and P&O as it is able to track MPP quickly even in changing weather conditions and does not oscillate near MPP. W. Xiao et al. [57] categorised the MPPT algorithms as: real-time identification method, extremum seeking control, particle swarm optimization, direct search algorithm and adaptive step size method. Shortcomings of P&O and incremental conductance are mentioned in terms of stability and accuracy. To overcome these disadvantages recursive and adaptive control strategies are suggested. However, direct control strategies are complex in nature and require the knowledge of uncertain parameters to calculate MPP. Extremum control strategies overcome the disadvantages of direct control method.

M. Abdulkadir et al. [58] presented the design and simulation for tracking the MPP with a highly efficient DC-DC boost converter and had modified the incremental

conductance algorithm. This adaptive solution is called integral regulator which improves the incremental conductance convergence, reduces ripple oscillations and minimizes the error. F. Kazan et al. [59] developed a new method for tracking of the MPP in a system consisting of a PV generator, a controller, and a boost converter whose gate pulses are controlled with the help of the control technique. The authors of the paper have explained the concept of MPP and its control and tracking. They have implemented a proportional–integral–derivative controller for MPPT. This proposed controller tracked the MPP under various conditions effectively and efficiently. Y. Xiong et al.[60] proposed a unique method on the basis of constant voltage and incremental conductance method. The aim was to overcome the disadvantage of the low efficiency of constant voltage method and the difficulty in choosing the iterative step size of incremental conductance method. Simulation results were presented to validate the effectiveness of proposed method.

#### **2.2.2.2. Control algorithm for grid interfacing inverter**

The performance of the grid interfacing inverter mainly depends on the generation of reference or compensating signal so, selection of the reference generation scheme is an important feature of grid-interfacing inverter control [61]. Many reference generation schemes either in the frequency domain or in the time domain are presented in literature for generating appropriate compensating signals [62]. In the frequency domain compensation technique, Fourier transformation of distorted voltage or current signal is done, and the compensating harmonic component is extracted to generate appropriate compensating signals. High computation time is required for online application of Fourier transformation, which further increases with the increase of the harmonic order to be eliminated. The large response time is the main disadvantage of the frequency domain technique. While in the case of time domain compensation technique, instantaneous derivation of compensating signals is done from the harmonic polluted current or voltage signals. The time domain techniques are easy to implement and requires less computation time compared to the frequency domain compensation methods. Some important time domain algorithms are Synchronous Reference Frame (SRF) theory, instantaneous reactive power theory, conductance fryze, etc. [63-68].

A. Sinha et al.[69] proposed the control strategy for minimizing the frequency

fluctuation for the various loads with and without transient disturbance or faults. The significance of the optimum value of droop coefficient in frequency control and phase feedback was also discussed for the better working of the controller. B. Singh et al.[70] presented the grid integration of a two-stage solar PV power generating system using two-quadrature PLL based control, which also mitigates power quality problems in three phase, three wire distribution system. It has been observed that the quadrature PLL based control algorithm is robust in nature and worked well for mitigating power quality problems. C. Jain et al.[71] presented a single stage grid-tied PV system with a simple unit vector-based control which also ensures improved power quality at PCC. The PV system compensates for linear and nonlinear loads which are connected at PCC. The unit vector is used to estimate the fundamental active power component of load currents which along with PV power feed-forward loop improves the dynamic response of the system with reduced settling time.

Conventional voltage controllers use a proportional-integral (PI) controller to control the active power through the inverter. Normally a PV inverter works under uncertain solar irradiation, load requirements and dynamic grid side operating conditions. It may not be easy to set optimal gains of the PI controller and this may lead to inappropriate inverter operation. For this purpose, the intelligent and adaptive controllers are required where the conventional PI controller may fail due to change in operating conditions. Some of the intelligent controllers are fuzzy logic controller (FLC), neural network, adaptive neuro-fuzzy inference system (ANFIS), etc. [72-75]. N.G.M Thao et al. [76] showed the detailed application of FLC in converter as well as inverter control in a grid-connected PV system. Authors demonstrated a simple single-level control method suitable for a small PV plant and also coordinated control strategy for a large-scale PV farm. They have focused on frequency and power flow control of grid-connected PV system. M. Yatak et al.[77] presented fuzzy logic control of a grid-connected two stage three-phase PV system. The FLC regulates the d - q axis currents for the inverter control. The simulation results show that the system achieved better performance in terms of dynamic responses, the axes currents follow the reference currents without overshoots and the settling time was very short.



### **2.3. SENSITIVITY AND RELIABILITY CHARACTERIZATION STUDIES**

The deviation or discrepancy between design and actual operation can result in serious effects on the overall system performance. Characterization studies viz. sensitivity and reliability characterizations are, thus, important aspects of system modelling [9-14].

#### **2.3.1. Sensitivity analysis**

Sensitivity model helps to reduce parameter uncertainty and increases the system accuracy. It provides a powerful tool for validating a designed system by studying the change in the response of the system with 1% change in any of its parameters. Notable contributions in the field of sensitivity studies are made by R. Kasturi and P. Doraraju, M. D'Amore, S. Cristina, R.G. Wasley and J. Momoh [78- 82]. P. Kumar et al. [83] have carried out the sensitivity analysis to determine the effect of parameters which concern the generation of corona noise. Taylor's first derivative is used for developing sensitivity functions. With the help of this model, a greater insight into the electrical design aspect of overhead lines could be obtained. L. Guo et al. [84] have proposed cat swarm optimization algorithm to estimate the unknown parameters of PV cell for sensitivity analysis. Cat swarm optimization algorithm was found to be most effective in identifying parameters of solar cell models. H. Andrei et al. [85] used a sensitivity study to analyze the performances of PV cells related to the different temperature and irradiance levels. The model parameters for the equivalent circuit of PV cell were derived. The accuracy of the proposed method was validated with numerical values obtained from real case studies. M. Ito et al. [86] conducted sensitivity analysis of very large-scale PV systems from economic and environmental viewpoints. The authors concluded that the generation cost was affected by degradation, interest ratio, depreciation period and labour cost. D. J. Pannell [87] presents a selective review and overview of theoretical and methodological issues in the sensitivity analysis (SA). There are many possible uses of SA, described within the categories of decision support, communication, increased understanding or quantification of the system, and model development. Also, a system for reporting and discussing SA results is recommended. L. Shu et al. [88] presented track sensitivity analysis method for analyzing the parameters of inverter and filter, which influence the PV system. Studies showed that parameters of the outer voltage loop control and filter parameter have

higher sensitivity than other inverter control parameters on the active and reactive power. Q. Li-nan et al. [89] discussed the use of SA methods, including static sensitivity and trajectory sensitivity, for parameter identification of grid-tied PV inverter. X. Zhu et al. [90] presented a systematic solution method to obtain the five-parameter model of the PV solar cells that can be used in the case when only a few data are available from the manufacturers. The basic ranges of parameters are defined, and the sensitivities of parameters are graphically obtained.

### **2.3.2. Reliability Analysis**

Reliability of a system is the probability that the system will give satisfactory performance for a given period of time when used in the manner and for the purpose intended. Researchers have suggested several methods to improve the reliability of a system or component, for reducing cost and failure time, etc. [91-95]. R. Billinton [96] in his book covers the application of reliability theory to the computations of reliability indices of power systems. A. Rueda et al. [97], provided a summary of reliability theories and methods. The reliability analysis includes representation of reliability parameters, renewal theory, coherent structure, diagram-based models, theoretical methods, and other miscellaneous techniques that cannot be classified in any of the categories. M. Ahmad et al. [98] presented a new methodology for estimating hardware and software reliability under uncertain use conditions and derived probabilistic estimates for overall system reliability. Numerical finite element models were combined with statistical techniques and Monte Carlo simulations to develop a reliability prediction framework/approach. P. Wang et al. [99] developed a new method to evaluate the impacts of PV power on customer reliability and system reserve deployment. They proposed a method based on the pseudo-sequential Monte Carlo simulation technique. The proposed method can effectively model the chronological aspects and stochastic characteristics of PV power and system operation with high computation efficiency.

S. V. Dhople et al. [100] presented the performance of Markov reward model-based framework to evaluate PV system reliability. The framework allows the computation of performance metrics such as capacity and energy yield, and reliability metrics such as availability. They also provided an analytical method to compute the sensitivity of

performance metrics to Markov reward model parameter variations. P. Venemans et al. [101] described a method for the quantitative assessment of the reliability of Smart Grids. The method proposed here make use of (1) Analytical calculations by means of fault tree analysis, (2) Partial state space evaluation and (3) Simulation of semi-stationary fault scenarios. The proposed combination of these three seems to be very promising and can be an important validation tool during the design of smart grids. P. Zhang et al. [102] had carried out studies for improvement of reliability so that maintenance cost can be reduced. High reliability is achieved by selecting suitable converter topology of a PV system. F. Chan et al. [103] analyzed and compared the reliability of three inverter configurations of PV system, such as integrated topology, two-stage, and three-stage configuration. They calculated the failure rate using MIL-HDBK 217 [104] and established that the reducing the stress factors with the highest contribution to failure rate helps in improving the reliability.

Researchers have also assessed and shown with experiments that improvement in even a single component of a device connected to a PV system can improve the overall reliability of that device. S.E. Aldaco et al. [105] had assessed the reliability of push-pull DC-DC converter by derating its power transistors. F. Obeidat et al. [106] discussed the reliability of 250W PV microinverter through failure rate calculated using MIL-HDBK-217F. Variation in the failure rate of different configurations of microinverter was observed for over a wide variation of temperature stress factor and voltage ratio stress factor.

#### **2.4. ISLANDING STUDIES FOR GRID-TIED PV BASED MICROGRID**

The current injected into the utility must obey the regulations, such as the IEEE Std. 519, which states the maximum allowable amount of injected current harmonics. Besides these regulations, interfacing inverters must have islanding detection feature. Islanding is the continued operation of the inverter when the grid has been removed on purpose, by accident, or by damage. The available detection schemes are normally divided into two groups: communication-based methods and DG resident methods. DG resident methods are sub-grouped as active and passive. Commonly used active islanding detection methods are slip mode frequency shift method (SMS) [107, 108], Active frequency drift (AFD) [109, 110], Sandia frequency shift (SFS) [111], Sandia

voltage shift (SVS) [112], high frequency signal injection [113, 114], negative sequence current injection [115], etc. The active schemes introduce a disturbance into the grid and monitor the effect. This may affect the power quality, and problems with multiple inverters in parallel with the grid are also known to exist [116]. Commonly used passive islanding detection methods are over/under voltage protection and over/under frequency protection [117], rate of change of frequency (ROCOF) [118], rate of change of power, rate of change of frequency over power, rate of change of voltage and change in power factor [119-120], voltage unbalance [121], change of impedance [122], phase jump detection [123], etc. The passive methods do not have any influence on the power quality since they just monitor grid parameters. However, they suffer from significant non-detection zone (NDZ) and threshold selection problem [116].

The large NDZ drawback of passive techniques can be overcome by using modern signal processing techniques like Fast Fourier Transform, Short Time Fourier Transform, Kalman filter, Wavelet Transform (WT), and S-transform [124-129]. K. Jay-Hyung et al. [130] used Goertzel algorithm to reduce the islanding detection time in single-phase two-stage PV system. The Wavelet transform is based on the scaling and shifting of window whereas the window size and position is fixed. The use of wavelets allows the decomposition of a signal into components as a function of time and frequency, providing a more precise time location of a transient than other signal processing techniques. H. K. Kazemi et al. [131] presented method based on wavelet transforms for the islanding detection of wind turbines having run on the time of less than 0.2 sec. M. Hanif et al. [132] proposed scheme that operates on the PCC voltage measurement and setting thresholds using third-level wavelet coefficients and is able to avoid nuisance tripping and detect the islanding condition within an average of 0.05 sec. M. Heidari et al. [133] compared the performance of discrete WT and WT and other passive islanding techniques. The main drawback of WT is that it only extracts the low-frequency band and ignores some useful properties of the high-frequency band, which has significant values to reveal islanding condition. To overcome this drawback of WT, the Wavelet Packet Transform (WPT) was developed which divides the whole time-frequency plane, instead of an only low-frequency band providing better results. S. A. Saleh et al. [134] had employed WPT for feature extraction of the direct and quadrature (d-q axis) components of the instantaneous three-phase apparent powers.

The performance of passive techniques can be improved by selecting optimum threshold values. Intelligent classifiers along with signal processing techniques can be used for this purpose. Intelligent classifiers commonly used in signal processing are decision tree, random forest, support vector machine, fuzzy logic control, artificial neural network (ANN) and adaptive neuro-fuzzy inference system (ANFIS) [135, 136].

## **2.5. MULTI-TERMINAL VOLTAGE CONVERTERS FOR DC NANOGRID**

A DC nanogrid is an evolutionary concept derived from the development of material science and power electronics and are emerging as an attractive solution to locally utilize DC electricity with minimum distribution and conversion losses. It can feed household loads, majority of which works on DC power such as LED lights, BLDC drives, mobile phones, computers, televisions, etc. [137-139].

M. R. Khan et al. [140] proposed the concept of DC nanogrid highlighting its technical advantages and some of the economic and social considerations involved in their development. The solar PV irrigation energy cost was presented and it is found to be lower than diesel-based irrigation costs in Bangladesh. K. Engelen et al. [141] discussed the topological design, buffering of the DC bus, interfacing distributed generators, efficiency analysis, and safety measures. They concluded that it is generally not efficient to implement a DC distribution system exclusively at the level of the end-user and further research should focus on the extension of DC power delivery to higher levels of the grid. D. Palit et al. [142] attempted to examine nuances of solar DC microgrid development in India with special focus on Uttar Pradesh. Author discusses the solar DC microgrid programs for rural electrification drawing from literature reviews, interview with key stakeholders and field survey to selected sites. P. R. Mishra et al. [143] describes the concept of storage integrated DC grid along with system design for a petrol pump station. Economic analysis in terms of total cost of ownership, cumulative savings over the years is presented. Authors concluded that though the initial investment of solar system is high, the total cost of ownership is much less than diesel generator set if considered for period of 3 years or more with significant cumulative savings. B. Nordman et al. [144] emphasized the need for further research into local power distribution with a focus on nanogrid. Authors illustrate the operation and controlling of a simple nanogrid and load behaviour in response to varying electricity

availability from a renewable source.

In a DC nanogrid, loads having different voltage levels are connected to a common bus through multiple DC/DC and DC/AC converters. Multiple dedicated converters, exhibits the problem of power flow coordination, low efficiency, higher component count, and the size of the system. On the other hand, multi-terminal converters, have been able to provide an integrated architecture with higher efficiency and compactness [145-155]. S. K. Mishra et al. [156] proposes switched boost inverter as a power electronic interface in DC nanogrid. He has discussed the structure and advantages of the proposed inverter based nanogrid and tested the control system of inverter experimentally using a 0.5 kW laboratory prototype, supplying both DC and AC loads simultaneously. These experimental results confirm the suitability of the inverter and its closed-loop control strategy for dc nanogrid applications. P. Lee et al. [157] explained the topology known as interleaved boost converter consisting of interleaved and intercoupled boost converter. By interleaving method the converters are modulated such that each switch operates at same switching frequency with a phase shift of  $180^\circ$ . Interleaving also requires additional inductors, diode and switching devices. This will increase the cost of the converter. The efficiency, size and transient response are improved. K. Tattiwong et al. [158] introduced a converter known as quadratic boost converter consisting of a single switch, one capacitor, two diodes and two inductors. The merits of this topology are it has high gain and reduced voltage stress and current stress. However, presence of more number of components leads to decrease in efficiency. It is mainly used in high power application. These converters are best suited for solar PV applications.

## **2.6. IDENTIFIED RESEARCH GAPS**

PV based microgrid are gaining importance since last few years due to the exhaustion of fossil fuels and increase in greenhouse gases and in order to select their optimum operating parameters, characterization studies need to be performed. Sensitivity analysis and reliability analysis are the important characterizations studies of any system that helps to reduce parameter uncertainty and to ascertain that a system can perform its intended function without failure. Although vast literature exists regarding these studies for other systems, there is still a wide scope for applying them in emerging

field of PV based microgrid. Power converter is the important component in a microgrid. As, solar irradiation is not available for almost two third period of the day, power converter used in a grid interfaced PV system is not utilized during this period and is normally switched off to reduce its losses leading to poor utilization of the power converters. To improve their utilization, additional features of filtering, load balancing, etc. have to be incorporated in the grid interfacing inverter which needs advanced control algorithms. Hence, algorithms with multi-functionality features have to be developed for the controlling of grid interfacing inverters. Also, from protection point of view, interfacing inverter is required to have an anti-islanding feature and should be able to detect islanding condition at the earliest. Existing islanding detection algorithms face issues of PQ problems, large NDZ, threshold selection, etc. which needs to be addressed. To overcome the disadvantage of the existing algorithms, advanced islanding detection algorithms need to be developed.

The RES viz. PV, fuel cells, etc. are mostly DC sources. Also, the load profile of household is changing drastically and is having a mix of both DC as well AC loads operating at different voltage levels. This has resulted in a novel grid system, DC nanogrid with multiple dedicated converters. But such system exhibits the problems of power flow coordination, low efficiency, higher component count and increased size of the system. To overcome these limitations of multiple converter based structure of DC nanogrid, multi-terminal converters need to be developed.

## **2.7. CONCLUDING REMARKS**

In this chapter, the literature review on PV based microgrid and associated areas have been carried out. Work of the researchers in the area of design and modelling of grid-tied PV based microgrid along with required control algorithms are presented. A survey of the sensitivity and reliability analysis of PV system and relevant areas has been brought out. The works related to islanding issues and required detection algorithms carried out by various researchers have been presented. The evolution of DC nanogrid and the application of multi-terminal voltage converters for DC nanogrid are also briefed. The research gaps in the PV based microgrid from literature survey are identified

# **CHAPTER-III**

## **PV BASED MICROGRID: MODELLING AND CHARACTERIZATION STUDIES**

### **INTRODUCTION**

Design and development of PV based microgrid need mathematical modelling of associated components such as PV cell/ array, DC-DC converter, PV inverter, DC link capacitor and interfacing inductors. The design of a system is influenced by its characterization features such as sensitivity, reliability, etc. The study of these characterization features is important as they can predict the behaviour of the system and can be used to modify it as per requirement. In order to check the validity of parametric variation, sensitivity analysis is carried out, while risk management verification is done by using reliability analysis. This chapter deals with the modelling and design of PV based microgrid and to validate the design of the developed PV system; characterization studies have been carried out. The sensitivity functions of the PV cell and boost converter have been developed, and the numerical values have been computed for the system developed. The performance of the PV array has been examined and is mapped with the sensitivity results. The component reliability study using Pareto analysis is carried out. System reliability analysis for PV standalone and grid-tied microgrid have been performed using reliability block diagram (RBD) method and logic gate representation model. Reliability improvement methods also have been discussed with respect to the designed system.

### **3.2. ENGINEERING PHOTOVOLTAICS**

PV directly convert light energy into electrical energy at the atomic level. The photoelectric effect was first noted by a French physicist, Edmund Becquerel, in 1839 [159-160]. He found that certain materials would produce small amounts of electric

---

This chapter is based on the paper - (i) "Sensitivity and Reliability Models of a PV System Connected to Grid," Renewable and Sustainable Energy Reviews. Elsevier. Volume 69, March 2017, Pages 188-196. DOI:10.1016/j.rser.2016.11.031.



current when exposed to light, an electromagnetic wave. Light energy contains many photons, that moves at different frequencies within the spectrum of the light, having a specific energy  $E = h\nu$ . When PV cell, made of semiconductor material, is exposed to light, some photons are reflected on the PV surface, and remaining photons are absorbed by the PV material. The absorbed photons, which have energy greater than band gap energy of the semiconductor material (for Si energy gap is 1.12eV), generate free charge carriers. Due to band bending in p-n junction semiconductor, electrons try to move to lower energy level (n region), and holes try to move to higher energy level (p region). This results in the creation of a potential difference between p and n region. The potential difference across p-n junction circulates current inside the cell (diode forward bias) called dark current (since it is not directly related to irradiance). Figure 3.1 shows the operating region of PV p-n junction semiconductor devices and it can be observed that the PV cell has a non-linear I-V characteristic.

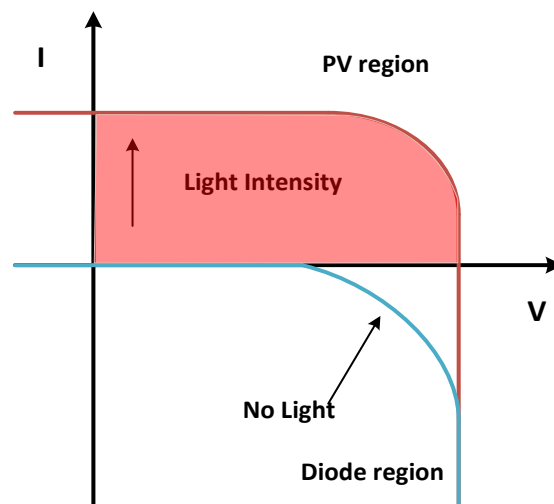


**Figure 3.1. I-V curve of a PV cell**

Figure 3.2 shows the I-V and P-V characteristics of a PV cell operating under standard test conditions. When the solar cell is open-circuited, that is not connected to any load, the current will be at its minimum (zero), and the voltage across the cell is at its maximum, known as the solar cell's open circuit voltage ( $V_{oc}$ ). When the solar cell is short-circuited, the voltage across the cell is at its minimum (zero), but the current flowing out of the cell reaches its maximum, known as the solar cell's short circuit

current ( $I_{sc}$ ). Thus, the span of the solar cell I-V characteristic curve ranges from the short-circuit current to zero current at the full open circuit voltage.

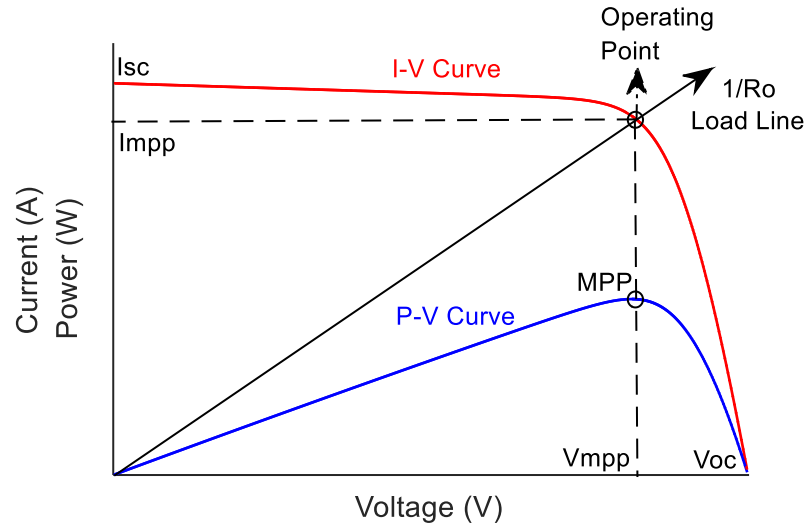


**Figure 3.2. I-V and P-V Characteristics of PV cell**

Also, there is one particular combination of current ( $I_{mpp}$ ) and voltage ( $V_{mpp}$ ) for which the power reaches its maximum value,  $P_{mpp}$ . The point at which the cell generates maximum electrical power is known as the maximum power point (MPP). If the load line crosses the characteristic curve precisely at this point, then the maximum power can be transferred to this load (expected operating point). But if the load line cuts the curve at any other point, the power transferred will be less than the maximum power. The value of this load resistance would be given by:

$$R_{mpp} = \frac{V_{mpp}}{I_{mpp}} \quad (3.1)$$

A solar cell when exposed to sunlight, produces a  $V_{oc}$  of about 0.4 to 0.6 V DC, which is very low. To produce higher voltages and power, PV cells are connected electrically in series and/or parallel circuits. PV modules consist of PV cell circuits sealed in an environmentally protective laminate and are the fundamental building blocks of PV systems. A PV array is the complete power-generating unit, consisting of any number of PV modules as shown in figure 3.3 [3].

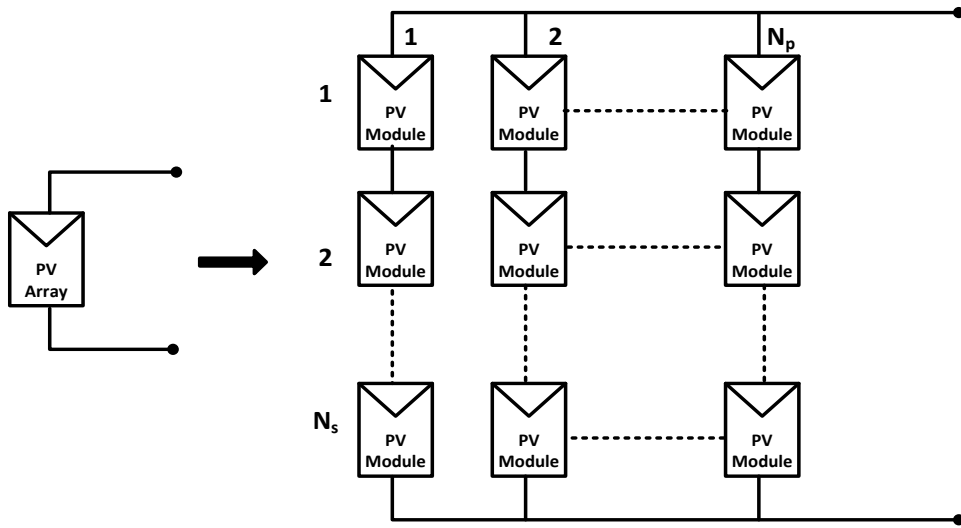


Figure 3.3. Formation of PV array using PV modules

### 3.2.1. Modelling of PV cell

PV cell modelling is very important for the analysis of the PV system. There are currently two main lumped circuit models in use [26-31]:

- (i) Single-Diode Model
- (i) Double-Diode Model

#### 3.2.1.1. Single-Diode Model

The Single-Diode Model is described by the modified Shockley diode equation and is modelled as a current source parallel with a diode as shown in figure 3.4.

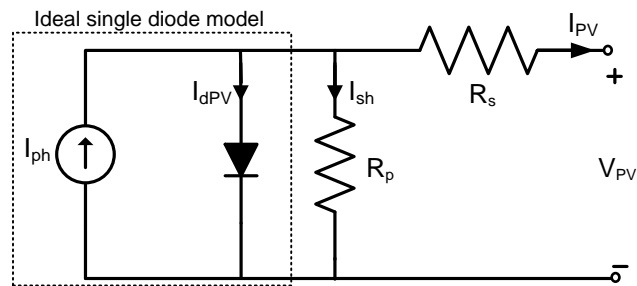


Figure 3.4. Single-diode model of PV cell

When exposed to sunlight (or another intense light source), a solar cell produces almost constant open circuit voltage depending upon the cell material while the current ( $I_{PV}$ ) flow to connected load is proportional to light energy (photons) and is given by [3, 161],

$$I_{PV} = I_{ph} - I_0 \left[ \exp \left\{ \frac{q(V_{PV} + I_{PV}R_s)}{A\kappa T} \right\} - 1 \right] - \frac{V_{PV} + I_{PV}R_s}{R_p} \quad (3.2)$$

Where,  $\kappa$  is the Boltzmann constant,  $q$  is the elementary charge ( $1.602 \times 10^{-19}\text{C}$ ),  $I_0$  is the diode saturation current,  $A$  is the diode ideality factor,  $R_s$  is the series resistance ( $\Omega$ ) and  $R_p$  is the shunt resistance ( $\Omega$ ) of the solar cell. The photocurrent  $I_{ph}$ , depends upon parameters, such as temperature and solar irradiance, and is defined by,

$$I_{ph} = I_{sc} \frac{E}{E_{ref}} \left[ 1 + (T_{PV} - T_{ref}) * \kappa_i \right] \quad (3.3)$$

Where  $E$  is operating irradiance,  $E_{ref}$  is PV cell reference irradiance,  $T_{PV}$  is the PV cell operating temperature,  $T_{ref}$  is PV cell reference temperature of 278 K, and  $\kappa_i$  is constant related to temperature co-efficient of  $I_{sc}$  taken as 0.004 %/°C.

The single-diode model is not very accurate in describing cell behaviour at low illuminations as the effect of nonohmic losses, due to recombination in the space charge region of the solar cell is not considered. Also, this circuit model is based on assumptions of linearity, i.e. the current flowing through the cell is a superposition of two currents, one due to junction bias and the other due to illumination. These assumptions may not be accurate, but this model do generally fit experimental I-V characteristics fairly accurately and can provide a very useful tool in assessing cell performance provided the model parameters are obtainable.

### 3.2.1.2. Double-Diode Model

Some of the limitations of single diode model has been overcome in the double diode model. The effect of non-ohmic losses can be represented in the equivalent circuit by a second diode term with a saturation current  $I_{02}$ , which is different from the saturation current ( $I_0$ ) of the ideal solar cell diode.

$$I_{PV} = I_{ph} - I_{01} \left[ \exp \left\{ \frac{q(V_{PV} + I_{PV}R_s)}{A_1 k T} \right\} - 1 \right] - I_{02} \left[ \exp \left\{ \frac{q(V_{PV} + I_{PV}R_s)}{A_2 k T} \right\} - 1 \right] - \frac{V_{PV} + I_{PV}R_s}{R_p} \quad (3.4)$$

In figure 3.5, the first diode with ideality factor  $A_1$  accounts for dark current and second diode with an ideality factor of  $A_2$  accounts for non ohmic shunt losses in the PV cell.

The double-diode model introduces itself as a proper solution to the problem of weather variation effects. However, the increased number of unknown parameters and the computational time hinder this model from being widely used compared to the single diode model.

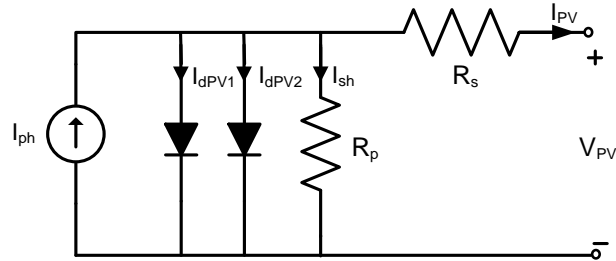


Figure 3.5. Double-diode model of PV cell

### 3.3. DESIGN OF PROPOSED PV BASED MICROGRID

A solar PV plant of 10 kW rating is considered for the study of PV based microgrid.

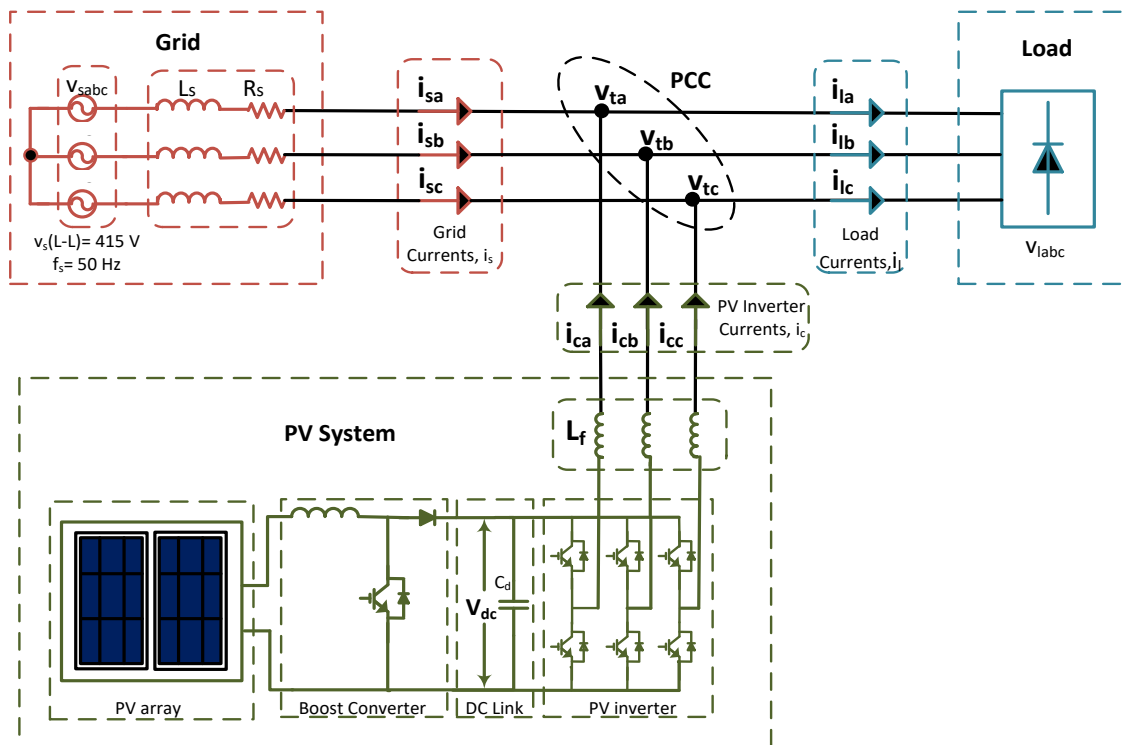


Figure 3.6. Schematic diagram of the PV based microgrid

The schematic diagram shown in figure 3.6 comprises of main sections of a PV based microgrid system: (1) PV array, (2) Boost converter with MPPT algorithm, (3) PV

inverter along with DC link capacitor and interfacing inductors. The detailed design of these sections are presented below [33, 34, 62]:

### 3.3.1. Design of PV array

Single-diode model is considered in the present work. The model for the PV array is obtained by modifying the PV cell equation (3.2) by inserting the indices  $N_s$  and  $N_p$  where  $N_s$  and  $N_p$  are number of cells in series and parallel respectively, and is given by,

$$I_{PV(array)} = N_p I_{ph} - N_p I_o \left[ \exp \left\{ \frac{q \left( V_{PV(array)} + I_{PV(array)} R_s \left( \frac{N_s}{N_p} \right) \right)}{N_s A k T} \right\} - 1 \right] - \frac{V_{PV(array)} + I_{PV(array)} R_s \left( \frac{N_s}{N_p} \right)}{R_p \left( \frac{N_s}{N_p} \right)} \quad (3.5)$$

As per the datasheet of solar module used [Appendix-A], the simulated cell has  $V_{oc}$  of 0.612 V, and  $I_{sc}$  of 8.72 A. Each module has 60 cells in series thus,  $V_{oc}$  of module is 36.7 V. Maximum voltage, and current through the modules is around 80%-85% of  $V_{oc}$  and  $I_{sc}$ , i.e.  $V_{mpp}$  is 29.7 V, and  $I_{mpp}$  is 7.74 A. To obtain the desired 10 kW power from the PV modules, 11 modules are connected in series per string, and 4 such strings are connected in parallel. Figure 3.7 depicts I-V and P-V characteristics of the designed 10 kW PV array, at different temperature and irradiation levels.

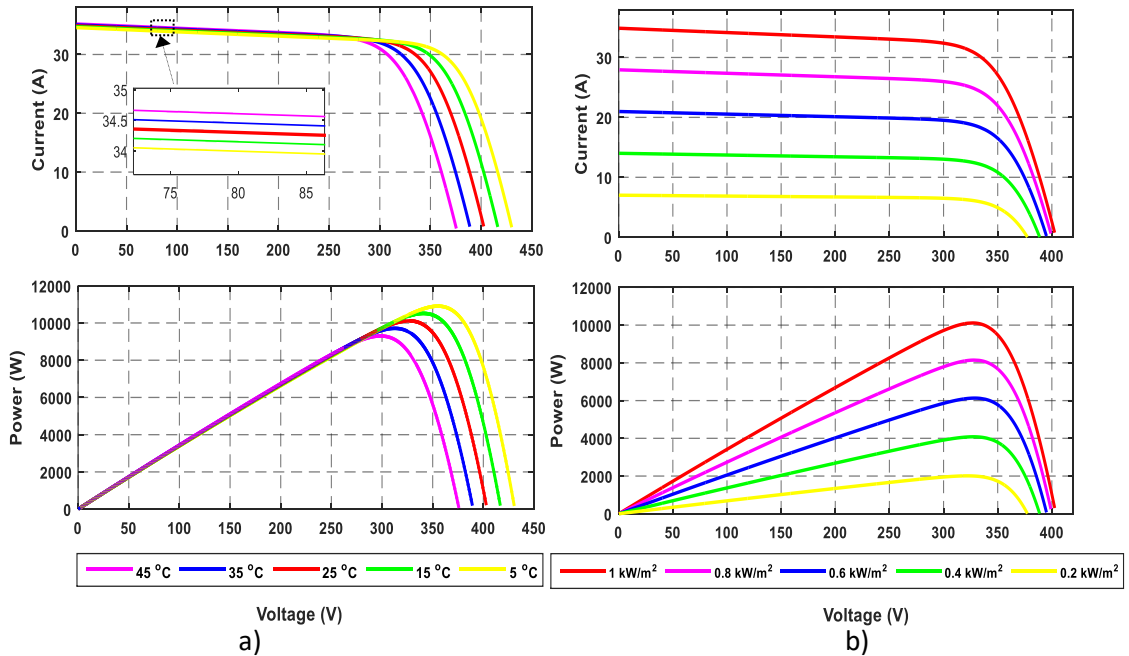


Figure 3.7. I-V and P-V characteristics of PV array used in proposed system for (a) different temperature levels and (b) different irradiation levels

### 3.3.2. Design of DC-DC boost converter

DC-DC converters are basically of three types: buck converter, boost converter and buck-boost converter. In the designed system, the boost converter, as shown in figure 3.8, is used.

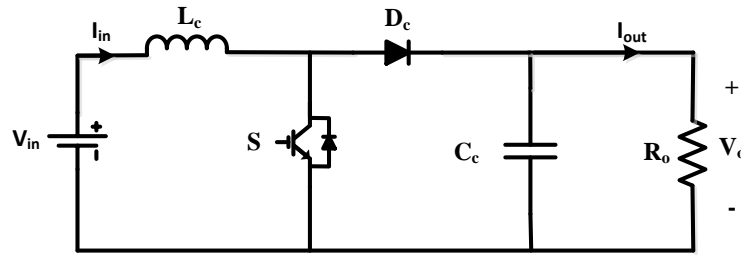


Figure 3.8. Circuit diagram of boost converter

The boost converter is used to obtain and regulate the required DC link voltage and to track the MPP. The converter is designed using inductor, capacitor, and Insulated-Gate Bipolar Transistor (IGBT) as a switch. The passive elements of converter viz. inductor ( $L_c$ ) and capacitor ( $C_c$ ) are calculated by [33, 34],

$$L_c = V_{in} (V_{out} - V_{in}) / \Delta i_i f_s V_{out} \quad (3.6)$$

$$C_c = I_{out} D / \Delta v f_s \quad (3.7)$$

Where,  $D$  is the duty cycle and can be calculated as,

$$D = 1 - (V_{in} / V_{out}) \quad (3.8)$$

Further,  $V_{in}$  is the input voltage,  $V_{out}$  is the output voltage,  $\Delta i_i$  is input current ripple taken as 10% of input current,  $f_s$  is the switching frequency,  $\Delta v$  is ripple in output voltage taken as 3% of the boost converter output voltage and  $I_{out}$  is the output current of the boost converter.

In the present work, the converter is designed to boost the PV array output voltage to 800 V.  $\Delta i_i$  is taken as 3.1 A, (10 % of input current 31 A) and  $\Delta v$  is taken as 24 V (3% of output voltage 800 V).

From the above parameters, the value of the inductor is calculated as 8.31mH and capacitor as 255  $\mu$ F. The reference duty ratio of the converter is obtained using the

MPPT algorithm. It is then compared with the saw-tooth waveform of frequency 10 kHz, to generate switching for the IGBT switch,  $S$ , of the boost converter.

### 3.3.3. Maximum power point tracking

In order to extract the maximum power, the PV system must be capable of tracking the solar panel unique MPP that varies with irradiance and temperature. In the present work, Perturb and Observe (P&O) algorithm is implemented to track the MPP [51]. Figure 3.9 gives the flowchart for P&O algorithm

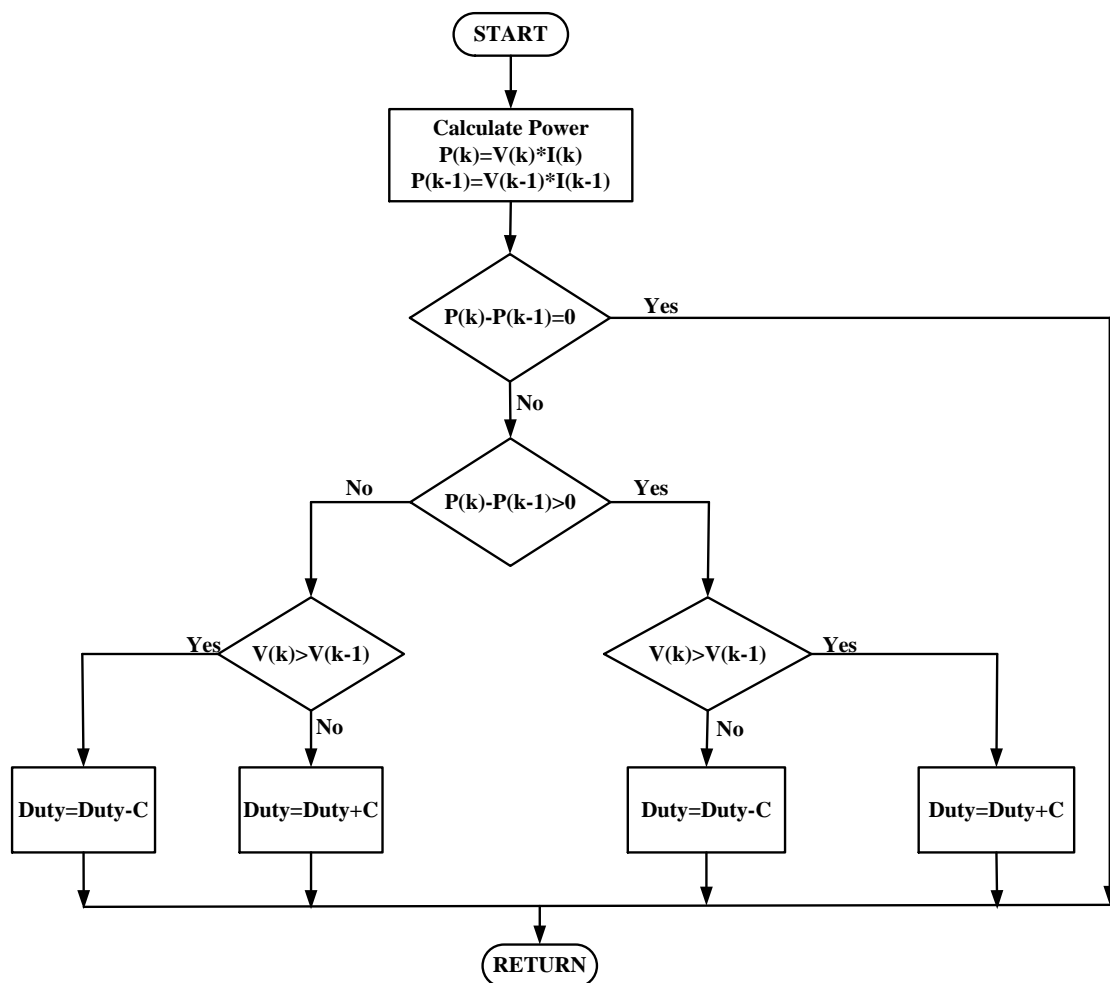


Figure 3.9. Flowchart for Perturb and Observe MPPT algorithm

The P&O algorithm is like climbing a hill in which the DC voltage is changed in steps ( $=\Delta V$ ) to operate around the MPP. After each step, the change in power is observed. If the power increases, the next voltage change (increase/ decrease) should have the same sign as the previous one and if the power reduces, that is, the change in power is



negative, the next perturbation is done contrary to the previous. It can be mathematically related to the sign of ratio of change in power to change in voltage, that is, the voltage change in the next perturbation should have the same sign as that of the ratio of change in power to change in voltage in the current step. As the PV's output DC voltage, taken as a reference, changes after each time step, the reference voltage always oscillates around the MPP voltage. This causes a power loss that increases with the step size of the perturbation. If this step width is large, the MPPT algorithm responds quickly to sudden changes in operating conditions. On the other hand, if the step size is small, the losses under stable or slowly changing conditions will be lower, but the system will not respond quickly to rapid changes in temperature or irradiance. There is always a tradeoff between speed and steady-state loss.

**3.3.4. Design of PV inverter**

A PV inverter is used to convert generated DC voltage to AC voltage. The DC/AC converters can be broadly classified into two types: voltage source converter (VSC) and current source converter (CSC) [162-164]. In a VSC the direction of power flow is determined by the polarity of DC- side current. A large capacitor is connected in parallel to the DC side terminals of VSC, resembling a voltage source. In the present work, VSC is used as a PV inverter. The two-level three-phase PV inverter consisting of six IGBTs with antiparallel diodes and DC link capacitor  $C_d$  at DC side used is shown in figure 3.10 [165].

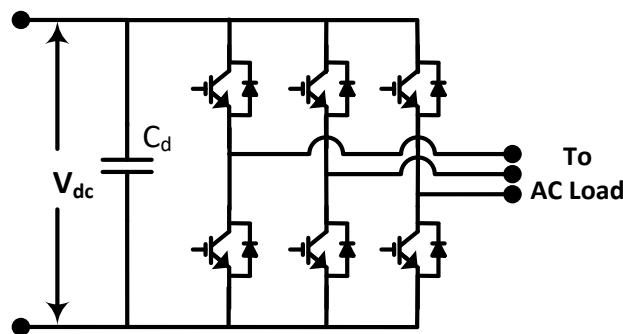


**Figure 3.10. Schematic diagram of three-phase voltage source converter**

In the present study, a 10 kW three phase 415 V inverter is designed. IGBT's voltage and current are calculated as,

$$I_{sw} = CF * I_{rms} = CF * \frac{P_{load}}{3 * pf * V_{load}} \quad (3.9)$$

$$V_{sw} = \sqrt{2} * V_{rms} \quad (3.10)$$

Where CF is the crest factor taken as 3 [62]. By considering the safety factor of 2, the ratings of the IGBTs for the inverter are selected as 1200V, 60A.

### 3.3.5. Design of DC link capacitor and interfacing inductors

The design of a DC link capacitor depends on the energy storage capacity needed during transient conditions. The value of DC link capacitance,  $C_d$  is calculated as,

$$0.5C_d(V_{dc}^2 - V_{dc1}^2) = 3k_1hV_{ph}I_{ph}t_c \quad (3.11)$$

where  $V_{dc}$  is nominal DC link voltage taken as reference DC voltage and is always greater than PCC voltage [62],  $V_{dc1}$  is minimum voltage level of the DC link voltage,  $h$  overloading factor selected to be 1.2 [62], the constant  $k_1$  is selected 0.1,  $V_{ph}$  is phase voltage,  $I_{ph}$  is phase current ( $I_{ph}=P/3V_{ph}$ ) and  $t_c$  is the time taken to regain DC link voltage, its value is considered as 30 $\mu$ s.

The DC link voltage can be obtained by [62],

$$V_{dc} = \frac{2\sqrt{2}V_{LL}}{\sqrt{3}m} \quad (3.12)$$

where  $m$  is the modulation index and its value is considered as 0.9, and  $V_{LL}$  is the AC line voltage of PV inverter and its value is 415 V. The  $V_{dc}$  obtained is 753 V. So, in the present work the DC link voltage is selected as 800 V. Accordingly, DC link capacitance ( $C_{dc}$ ) is calculated as 1806  $\mu$ F and is selected as 2000  $\mu$ F for design consideration.

Interfacing inductors,  $L_f$  are used at the AC side of PV inverter, which couple the inverter to the grid. The design of the interfacing inductors is carried out to limit the ripple in the currents and voltages. The interfacing inductors are designed using [62],

$$L_f = \frac{\sqrt{3}mV_{dc}}{12hf_s\Delta i} \quad (3.13)$$

Where  $\Delta i$  is the current ripple taken as 10 % of inverter current,  $f_s$  is the switching frequency taken as 10 kHz in the present work,  $m$  is the modulation index taken as 0.9 and  $h$  is the overload factor taken as 1.2. The value of interfacing inductor is calculated to be 3 mH.

### **3.4. CHARACTERIZATION STUDIES OF PV BASED MICROGRID**

Sensitivity and reliability analysis are the two characterizations studies carried out in the present work.

Sensitivity analysis is the determination of dependence of a function on the parameters of interest [9, 10]. Sensitivity analysis as a tool gives an insight into the problems associated with a model under consideration. The designer gets an insight about the sensitiveness of the designed model for the changes in the input values of one or more parameters. There are basically two types of sensitivity analysis approaches: local sensitivity analysis and global sensitivity analysis. Local sensitivity analysis is an analytical approach based on derivatives taken at a single point such as differential sensitivity analysis, correlation analysis, etc. Global sensitivity analysis is implemented using Monte Carlo technique that uses a global set of samples to explore the designed system. In the present work differential sensitivity analysis method is used.

Reliability is the probability of various components performing their functions satisfactorily for the period under consideration and at their designed operating parameters [11-14]. Reliability evaluation techniques can be subdivided into three categories- Mathematical analysis, system analysis, and accelerated life testing as shown in figure 1.3. Mathematical analysis can be further divided parametric analysis, non-parametric analysis and Monte Carlo simulation while system analysis may be further classified as reliability block diagram (RBD), fault tree analysis and event sequence diagram. In the present work, the RBD analysis is used.

#### **3.4.1. Sensitivity analysis**

The differential sensitivity analysis, used to determine the sensitivity of the PV system, includes solving the partial derivatives with respect to parameters of interest.

The normalized sensitivity of function  $F$ , with respect to parameter  $p$ , can be obtained from the partial derivatives as,

$$\hat{S}_p^F = \frac{\partial F/F}{\partial p/p} = \left(\frac{p}{F}\right) \left(\frac{\partial F}{\partial p}\right) \quad (3.14)$$

In the present work, sensitivity functions for PV cell and DC-DC converters are developed.

### Evaluation of sensitivity functions for PV cell

The sensitivity functions of photon current ( $I_{ph}$ ), open circuit voltage ( $V_{oc}$ ), short circuit current ( $I_{sc}$ ) of a PV cell have been developed with respect to irradiation ( $E$ ) and temperature ( $T_{PV}$ ) and are given by equations (3.15) - (3.20),

$$\hat{S}_E^{I_{ph}} = \frac{E}{I_{ph}} S_E^{I_{ph}} = \frac{E}{I_{ph}} * \left(\frac{\partial I_{ph}}{\partial E}\right) = \frac{E}{I_{ph}} * ([1 + (T_{PV} - T_{ref}) * k] * \frac{I_{sc}}{E_{ref}}) \quad (3.15)$$

$$\hat{S}_{T_{PV}}^{I_{ph}} = \frac{T_{PV}}{I_{ph}} S_{T_{PV}}^{I_{ph}} = \frac{T_{PV}}{I_{ph}} * \left(\frac{\partial I_{ph}}{\partial T_{PV}}\right) = \frac{T_{PV}}{I_{ph}} * \left(\frac{I_{sc} * k * E}{E_{ref}}\right) \quad (3.16)$$

$$\hat{S}_E^{V_{oc}} = \frac{E}{V_{oc}} S_E^{V_{oc}} = \frac{E}{V_{oc}} * \left(\frac{\partial V_{oc}}{\partial E}\right) = \frac{E}{V_{oc}} * \left(\frac{1}{\alpha * (I_{ph} + I_0)} * \frac{\partial I_{ph}}{\partial E}\right) \quad (3.17)$$

$$\hat{S}_{T_{PV}}^{V_{oc}} = \frac{T_{PV}}{V_{oc}} S_{T_{PV}}^{V_{oc}} = \frac{T_{PV}}{V_{oc}} * \left(\frac{\partial V_{oc}}{\partial T_{PV}}\right) = \frac{T_{PV}}{V_{oc}} * \left(\frac{1}{\alpha * (I_{ph} + I_0)} * \frac{\partial I_{ph}}{\partial T_{PV}}\right) \quad (3.18)$$

$$\hat{S}_E^{I_{sc}} = \frac{E}{I_{sc}} S_E^{I_{sc}} = \frac{E}{I_{sc}} * \left(\frac{\partial I_{sc}}{\partial E}\right) = \frac{E}{I_{sc}} * \left(\frac{1}{1 + \frac{R_s}{R_{sh}}} * \frac{\partial I_{ph}}{\partial E}\right) \quad (3.19)$$

$$\hat{S}_{T_{PV}}^{I_{sc}} = \frac{T_{PV}}{I_{sc}} S_{T_{PV}}^{I_{sc}} = \frac{T_{PV}}{I_{sc}} * \left(\frac{\partial I_{sc}}{\partial T_{PV}}\right) = \frac{T_{PV}}{I_{sc}} * \frac{\partial}{\partial T} \left(\frac{1}{1 + \frac{R_s}{R_{sh}}} * \frac{\partial I_{ph}}{\partial T_{PV}}\right) \quad (3.20)$$

### Evaluation of sensitivity functions for converter

The sensitivity functions of the output voltage ( $V_{out}$ ) of the boost converter have been developed with respect to duty cycle ( $D$ ), inductance ( $L_c$ ), frequency ( $f_s$ ) and capacitance ( $C_c$ ) and are given by equations (3.21) - (3.24),

$$\hat{S}_D^{V_{out}} = \frac{D}{V_{out}} S_D^{V_{out}} = \frac{D}{V_{out}} * \left(\frac{\partial V_{out}}{\partial D}\right) = \frac{D}{V_{out}} * \left(\frac{V_{in}}{(1-D)^2}\right) \quad (3.21)$$

$$\hat{S}_{L_c}^{V_{out}} = \frac{L_c}{V_{out}} S_{L_c}^{V_{out}} = \frac{L_c}{V_{out}} * \left( \frac{\partial V_{out}}{\partial L_c} \right) = \frac{L_c}{V_{out}} * \left( \frac{\Delta i * f_s * V_{out}^2}{V_{in}^2} \right) \quad (3.22)$$

$$\hat{S}_{f_s}^{V_{out}} = \frac{f_s}{V_{out}} S_{f_s}^{V_{out}} = \frac{f_s}{V_{out}} * \left( \frac{\partial V_{out}}{\partial f} \right) = \frac{f_s}{V_{out}} * \left( \frac{\Delta i * L_c * V_{out}^2}{V_{in}^2} \right) \quad (3.23)$$

$$\hat{S}_{C_c}^{V_{out}} = \frac{C_c}{V_{out}} S_{C_c}^{V_{out}} = \frac{C_c}{V_{out}} * \left( \frac{\partial V_{out}}{\partial C_c} \right) = \frac{C_c}{V_{out}} * \left( \frac{f_s * V_{out} * \Delta v}{I_0 - 2 * f_s * C_c * \Delta v} \right) \quad (3.24)$$

### 3.4.1.1. Numerical results for sensitivity analysis

Table 3.1 shows the numerical values of sensitivity obtained corresponding to the developed sensitivity functions using the data presented in Appendix-B. The values obtained from sensitivity functions are validated with the values obtained from the difference equation by changing the parametric value by 1% and 2% respectively.

**Table 3.1. Sensitivity values of PV cell and converter**

Sensitivity functions developed	Sensitivity Values Using		
	Sensitivity function	Difference equation (Parametric variation of 1 %.)	Difference equation (Parametric variation of 2 %.)
$\hat{S}_E^{I_{ph}}$	1.000	1.032	1.000
$\hat{S}_{T_{PV}}^{I_{ph}}$	0.100	0.100	0.100
$\hat{S}_E^{V_{oc}}$	0.024	0.024	0.023
$\hat{S}_{T_{PV}}^{V_{oc}}$	-1.143	-1.143	-1.142
$\hat{S}_E^{I_{sc}}$	0.993	0.993	0.9967
$\hat{S}_{T_{PV}}^{I_{sc}}$	0.099	0.099	0.0993
$\hat{S}_{L_c}^{V_{out}}$	0.972	0.973	0.969
$\hat{S}_{f_s}^{V_{out}}$	0.972	0.972	0.969
$\hat{S}_{C_c}^{V_{out}}$	0.556	0.550	0.550
$\hat{S}_D^{V_{out}}$	0.960	0.960	0.960

From table 3.1, it can be seen that the sensitivity value obtained from sensitivity functions and difference equation conform. Also, it can be seen that the  $I_{sc}$  increases with increase in irradiation level and temperature while  $V_{oc}$  increases with increase in

irradiation level but decreases with the increase in temperature. The same findings have been obtained from figure 3.7 also which further validates the results of sensitivity analysis.

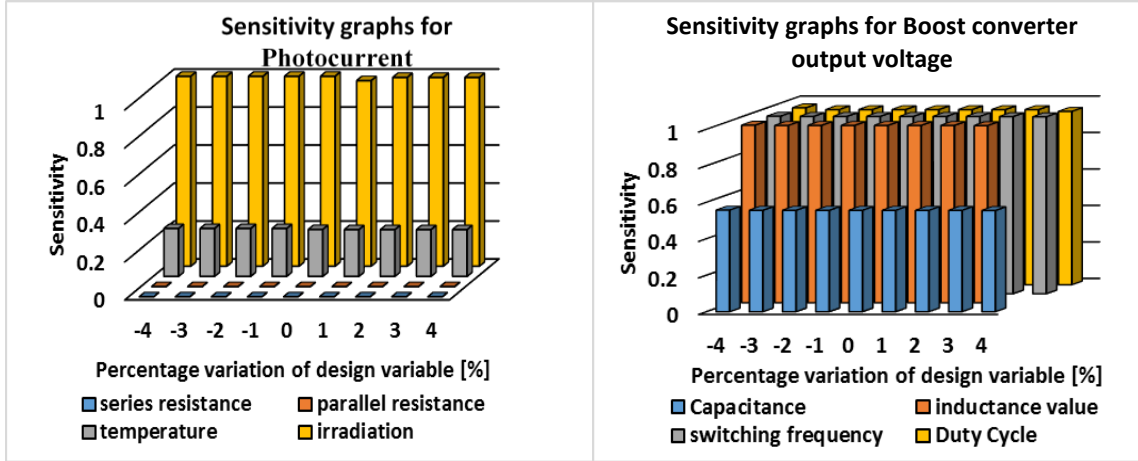


Figure 3.11. Sensitivity graphs for (a) photon current and (b) boost converter output voltage

Table 3.1 also shows that photocurrent is most sensitive to irradiation level. The output voltage of the converter, on the other hand, is equally sensitive to inductor value and switching frequency and least sensitive to capacitor value. The same deductions can be made from sensitivity graphs shown in figure 3.11. Sensitivity graphs shown in figure 3.11 (a) and 3.11 (b) shows the calculated sensitivity values by changing each design variable from - 4% to + 4% in steps of 1%.

### 3.4.2. Reliability analysis

Reliability is the ability of a system to perform a required function under stated conditions for a stated period of time. Additionally, the reliability can also be defined as the probability of the system’s availability [11-14]. The availability can further be defined as,

$$Availability = \frac{Operational\ time\ of\ PV-system}{Operational\ time\ of\ PV-system + Down\ Time} * 100 = \frac{MTBF}{Mean\ cycle\ time} \quad (3.25)$$

Where, MTBF is mean time between failure and is related to failure rate ( $\lambda_p$ ) as,

$$MTBF = \lambda_p^{-1} \quad (3.26)$$

Finally, the reliability is calculated by,

$$Reliability = e^{-\lambda_p t} \quad (3.27)$$

In the present work, the reliability analysis of components used in PV based microgrid is presented. Also, the reliability analysis of the different configurations of PV based microgrid has been presented. In the following subsection, the reliability evaluation of the system components is presented.

### 3.4.2.1. Evaluation of component reliability

The components experience stresses due to switching operation of devices, environmental parameters and voltage levels to which devices are subjected. The reliability of a component depends on its failure rate which is affected by these stresses. The manufacturer provides the data for the failure rate,  $\lambda_b$  of a component based on the ideal conditions. The actual failure rate,  $\lambda_p$  is obtained by multiplying manufacturer listed failure rate ( $\lambda_b$ ) with the associated stress factor  $\sigma_i$ . Thus,

$$\lambda_p = \lambda_b (\prod_{i=1}^n \sigma_i) \quad (3.28)$$

where,  $\sigma_i$  denotes the stress factors applicable to a particular component of PV system. The different stress factors are  $\sigma_a, \sigma_c, \sigma_e, \sigma_q, \sigma_s, \sigma_t$  and  $\sigma_v$  which corresponds to device power rating, the capacitance value, operational environment, quality of component, reverse voltage index factor of diode, temperature and capacitor voltage index factor, respectively. Total failure rate of a series system,  $\lambda_{system}$  can be computed by the summation of the failure rate of all the individual components given by,

$$\lambda_{system} = \sum \lambda_{p(components)} \quad (3.29)$$

### 3.4.2.2. Numerical results for component reliability

In order to compute the reliability of standalone PV microgrid, the failure rate of the system's components due to various stress factors is considered. The stress factors are computed using MIL-HDBK-217 [104] and MTBF calculator software by ALD [166]. Failure rate and MTBF of various components are then computed using data in Appendix-B.

i. Capacitor: In MIL-HDBK-217, the actual failure rate of the capacitor is determined from,

$$\lambda_p = \lambda_b(\sigma_C * \sigma_E * \sigma_Q * \sigma_T * \sigma_V) \quad (3.30)$$

$\sigma_T$  is temperature factor that is calculated from,

$$\sigma_T = \exp\left(-\frac{0.35}{8.617*10^{-5}}\left\{\frac{1}{T_j+273} - \frac{1}{298}\right\}\right) = 15.33 \quad (3.31)$$

$\sigma_C$  is the capacitance value factor given by,

$$\sigma_C = C^{0.23} = 1.3 \quad (3.32)$$

$\sigma_V$  is capacitor voltage index factor calculated from,

$$\sigma_V = \left(\frac{(\text{applied voltage}/\text{rated voltage})}{0.6}\right)^5 + 1 = 5.21 \quad (3.33)$$

$\sigma_e$  is the operational environment stress factor taken as 1 and  $\sigma_q$  quality of component factor taken as 10 in case of capacitor.

ii. Inductor/ Transformer: In MIL-HDBK-217, the actual failure rate of inductor/ transformer is determined from,

$$\lambda_p = \lambda_b(\sigma_e * \sigma_q * \sigma_t) \quad (3.34)$$

$\sigma_T$  is temperature factor expressed as,

$$\sigma_T = \exp\left(-\frac{0.11}{8.617*10^{-5}}\left\{\frac{1}{T_j+273} - \frac{1}{298}\right\}\right) = 2.36 \quad (3.35)$$

$\sigma_e$  is the operational environment stress factor taken as 1 and  $\sigma_q$  quality of component factor taken as 20 in case of Inductor/ Transformer.

iii. MOSFET: In MIL-HDBK-217, the actual failure rate of MOSFET is determined from,

$$\lambda_p = \lambda_b(\sigma_a * \sigma_e * \sigma_q * \sigma_t) \quad (3.36)$$

$\sigma_T$  is temperature factor expressed as,



$$\sigma_T = \exp\left(-1925\left\{\frac{1}{T_j+273} - \frac{1}{298}\right\}\right) = 3.63 \quad (3.37)$$

$\sigma_e$  is the device power rating stress factor taken as 10,  $\sigma_e$  is the operational environment stress factor taken as 1 and  $\sigma_q$  quality of component factor taken as 8 in case of MOSFET.

iv. Diode: In MIL-HDBK-217, the actual failure rate of diode is determined from,

$$\lambda_p = \lambda_b(\sigma_e * \sigma_q * \sigma_t * \sigma_s) \quad (3.38)$$

$\sigma_T$  is temperature factor calculated from,

$$\sigma_T = \exp\left(-3091\left\{\frac{1}{T_j+273} - \frac{1}{298}\right\}\right) = 8.004 \quad (3.39)$$

$\sigma_s$  is the reverse voltage index factor of diode give by,

$$\sigma_s = V_s^{2.43} = 0.29 \quad (3.40)$$

$\sigma_e$  is the operational environment stress factor taken as 1 and  $\sigma_q$  quality of component factor taken as 8 in case of Diode.

The computed values of failure rate and MTBF of the considered components are shown in table 3.2.

**Table 3.2. Failure rate and MTBF of electronic components of a PV system**

COMPONENTS	LISTED FAILURE RATE ( $\lambda_b$ ) (PER MILLION HOURS)	ACTUAL FAILURE RATE ( $\lambda_p$ ) (PER MILLION HOURS)	MTBF (HOURS)
Capacitor	0.0007	0.1245	8.032x10 <sup>6</sup>
Inductor/Transformer	0.0000324	0.00152	6.578x10 <sup>8</sup>
MOSFET	0.012	3.48	0.287x10 <sup>6</sup>
Diode	0.030	0.271	3.690x10 <sup>6</sup>

The failure rates of various electrical components are computed from the MTBF of these components using equation (3.26) and are presented in table 3.3 [167].

**Table 3.3. Failure rate and MTBF of electrical components of a PV system**

COMPONENTS	FAILURE RATE (PER MILLION HOURS)	MTBF (HOURS)
Solar Array	33.3	3.00 x10 <sup>4</sup>
Batteries	22.83	4.38 x10 <sup>4</sup>
Battery Charge Controller	57.07	1.75 x10 <sup>4</sup>
Motor	10	1.00x10 <sup>5</sup>
Controller	53.33	1.87 x10 <sup>4</sup>

It can be deduced from table 3.2 and table 3.3 that MOSFET and battery charge controllers have the highest failure rate. The same can be validated by performing the Pareto analysis of electrical and electronic components as shown in figure 3.12.

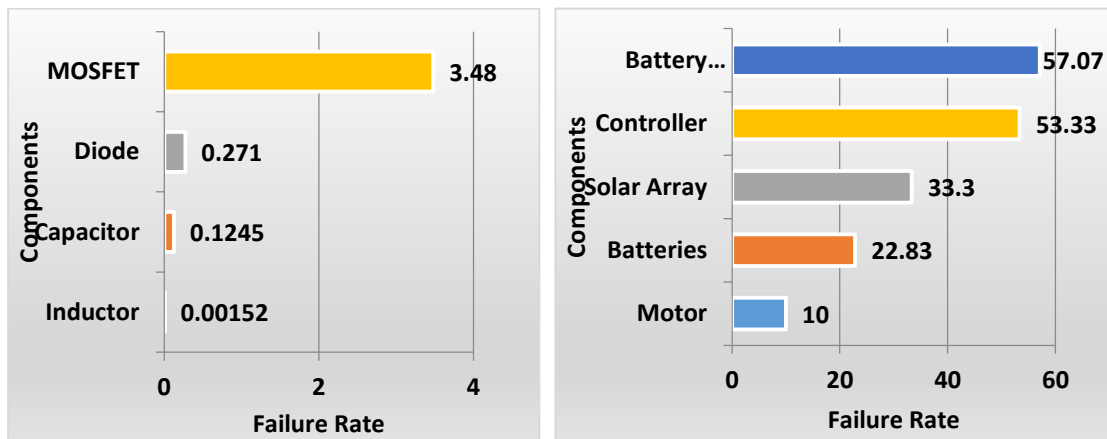


**Figure 3.12. Pareto analysis of the electrical and electronic components**

**3.4.2.3. Evaluation of system reliability**

System approach model using a RBD and logic gate representation is used to obtain reliability of the PV systems. RBD is used for mathematical modelling to express the reliability of the system in terms of the individual component’s reliability. System may have only series components, only parallel components or a combination of both. Reliability of a series system,  $R_s(t)$  is computed as,

$$R_s(t) = \prod_{i=1}^k [R_i(t)] ; i = 1, \dots, n \tag{3.41}$$

Where,  $R(t)$  reliability of the system/ components.

Further, the reliability of the parallel system,  $R_p(t)$  is defined by,

$$R_p(t) = 1 - \prod [1 - R_i(t)]; \quad i = 1, \dots, n \quad (3.42)$$

The reliability of a system having components in series and parallel both may be computed by using equations (3.41) and (3.42) simultaneously.

### 3.4.2.4. Numerical results for system reliability

The reliability analysis is of three different configurations of PV based microgrid, namely (i) standalone system, (ii) standalone system with battery storage and (iii) grid-tied system has been performed. Reliability of these different configurations is evaluated using equations (3.43) and (3.44). The RBD and logic gate representation of these configurations are shown in figure 3.13.

The standalone PV microgrid is the simplest of all, can be represented as shown in figure 3.13 (a) and its reliability is computed by multiplying the reliability of individual components, as given by equation (3.41).

The standalone PV system with battery storage can be represented as figure 3.13 (b), and its reliability,  $R_X$  can be calculated by,

$$R_X = (\{1 - (1 - R_1 * R_2)(1 - R_3 * R_4)\} * R_5 * R_6 * R_{10}) \quad (3.43)$$

Further, the reliability of the grid-tied PV microgrid,  $R_Y$  is calculated by,

$$R_Y = [1 - (1 - \{1 - (1 - R_1 * R_2)(1 - R_3 * R_4)\} * R_5 * R_6)(1 - R_8 * R_7)(1 - R_9)] * R_{10} \quad (3.44)$$

Where,  $R_1, R_2, R_3, R_4, R_5, R_6, R_7, R_8, R_9$  and  $R_{10}$  are the reliability values of PV array, chopper, battery, battery charger, capacitor, inverter, switch, synchronizer, grid and load respectively. The reliability values of these configurations are computed on the basis of data given in Appendix-C and are presented in table 3.4.

**Table 3.4. Reliability values for different configurations of PV based microgrid**

Configuration	Reliability
Standalone System	0.568
Standalone system with battery storage	0.675
Grid-tied system	0.899

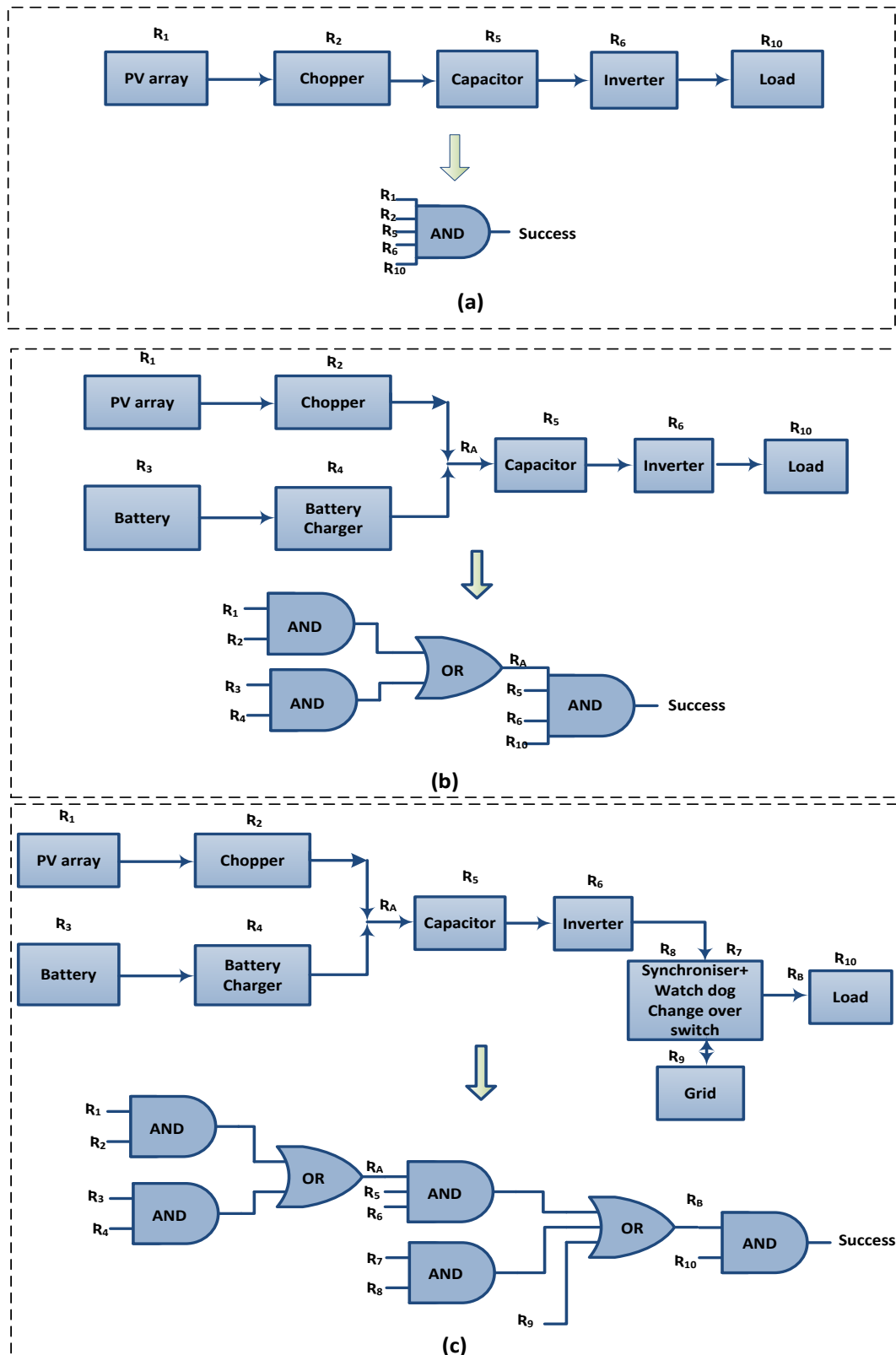


Figure 3.13. Reliability block diagram and logic gate representation of (a) standalone PV based microgrid, (b) standalone PV based microgrid with battery storage and (c) grid-tied PV based microgrid

It can be inferred from table 3.4 that the grid-tied PV microgrid has the highest reliability followed by standalone PV microgrid with battery storage while standalone PV microgrid is least reliable. Hence, grid-tied PV microgrid should be preferred for higher reliability.

**3.4.2.5. Reliability Improvement**

As can be seen from table 3.4, standalone PV system has low reliability. Hence measures should be taken to improve its reliability. There are two main ways by which the reliability can be improved. The first relates to quality and the second to redundancy. Improving quality or redundancy requires additional investment [12, 104].

The first attribute, quality, concerns the quality of component manufacturing, testing, calibration, transportation and operation. These quality concerns depend on the stress to which the components are exposed and the ergonomics and environment of the workplace. Various stress factors have to be identified and minimized to improve the quality and in turn reliability of the components. In order to identify the critical stress factors, sensitivity analysis of failure rate of components with respect to the stress factors is performed. Effect of stress factors on failure rate is obtained by varying one stress factor at a time. Figure 3.14, shows the sensitivity graph of various stress factors.

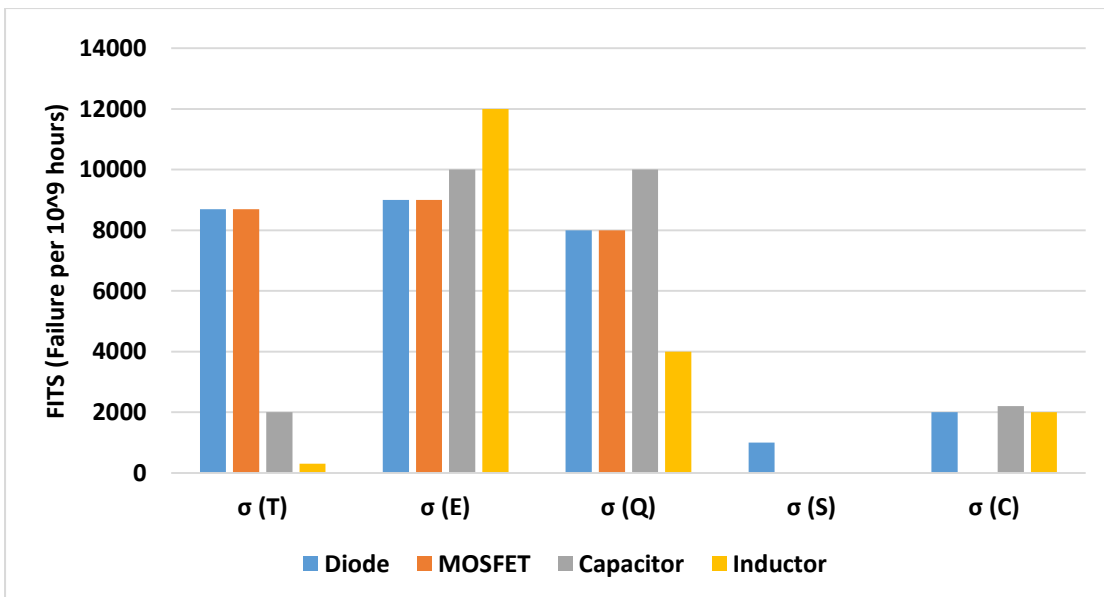


Figure 3.14. Sensitivity graph of various stress factors

It can be observed that that capacitor is most sensitive to quality stress factor while the diode is most sensitive to temperature stress factor. Table 3.5 shows the improved failure rate and reliability of the components and the system under consideration.

**Table 3.5. Improved failure rate and reliability of components and standalone PV system**

Component	Stress Factors		Failure Rate (PER MILLION HOURS)		Reliability	
	Initial	Improved	Initial	Improved	Initial	Improved
<b>Capacitor</b>	$\sigma_v = 5.21$	$\sigma_v = 2.68$	0.124	0.064	0.9989	0.9994
<b>MOSFET</b>	$\sigma_T = 3.63$	$\sigma_T = 2$	3.480	1.917	0.9699	0.9833
<b>Diode</b>	$\sigma_S = 0.29$	$\sigma_S = 0.11$	0.271	0.103	0.9976	0.9990
<b>System (standalone)</b>	-		68.174	52.63	0.55	0.63

The second attribute accepts that components will always fail from time to time and that there should be sufficient 'back-up' in the system so that the function of a failed component is absorbed by another. This backup status is known as redundancy. Redundancy is of two types: active and standby [12]. Active redundancy exists when the components share the function between them and the activity is automatically absorbed by the remaining components if one or more fail. This is also known as parallel redundancy. Standby redundancy exists when the redundant components remain in a standby state and are only switched into the system when the main operating component(s) fail.

The redundancy,  $R_u$  in active standby system is given by,

$$R_u = 2 \prod_{i=1}^n p(a_i) - [\prod_{i=1}^n p(a_i)]^2 = \prod_{i=1}^n p(a_i) [2 - \prod_{i=1}^n p(a_i)] \tag{3.45}$$

where  $p(a_i)$  is the probability of the system under consideration. The redundancy can be computed for the system under consideration using equation (3.45). The computed values are presented in table 3.6.

**Table 3.6. Reliability values for different configurations of PV based microgrid with redundancy**

<b>Configuration</b>	<b>Reliability with Redundancy</b>
Standalone System	0.813
Standalone system with battery storage	0.894
Grid-tied system	0.989

From the table 3.6 it is noted that system reliability has increased when redundant standby system is considered.

### **3.5. CONCLUDING REMARKS**

In this chapter, the modelling and design of PV based microgrid have been presented. The characterization studies for the designed system have been performed. The sensitivity functions of the PV cell and boost converter have been developed, and the numerical values have been computed for the system considered. It is found that PV cell output is most sensitive to irradiation level and converter output is most sensitive to inductor value and switching frequency. The performance of the PV array has been examined and is mapped with the sensitivity results. The reliability analysis of PV standalone and grid-tied microgrid have been carried out using Pareto analysis and logic gate representation model. Pareto analysis has been used as a tool to identify the component with the highest failure rate. Further, Reliability Block Diagram method of system reliability analysis has been used along with the development of logic gate representation models to study the reliability of both standalone and grid-tied PV based microgrid, and it has been observed that grid-tied microgrid are the most reliable. Lastly, component and system level reliability improvement methods have been discussed for the system under consideration. To improve component reliability, sensitivity analysis of stress factors is performed and critical stress factors are identified. To improve the system reliability, redundancy approach has been discussed. These studies are intended to give a better insight to the PV system designer and its operator to predict and select the optimal operating point in dynamic situations.

# **CHAPTER-IV**

## **PV BASED MICROGRID: INTERFACING CONTROL ALGORITHMS**

### **INTRODUCTION**

In the previous chapter, the PV based microgrid considered for the studies has been designed and modelled and the characterization studies have been carried out. In the present chapter, interfacing control algorithms have been developed for the two-stage three-phase grid-tied PV based microgrid and their performance is evaluated and analysed. In the two-stage configuration, the first stage consists of a DC-DC converter for converting the PV output voltage to the required DC link voltage. The switching of the DC-DC converter is controlled by the MPPT algorithm to track the maximum power that can be obtained from the PV module. The second stage interfaces the PV source to the grid using an inverter, controlled by interfacing algorithm. The interfacing control algorithms are used to control the inverter for its efficient utilization and are designed to convert DC voltage obtained from DC-DC converter to AC of required voltage and frequency and of correct phase sequence for grid synchronization along with providing reactive power compensation, harmonics compensation and load balancing. In this chapter, novel AFL based intelligent interfacing control algorithm and feedforward-feedback adaptive interfacing control algorithm are proposed and developed for the PV based microgrid

---

This chapter is based on the papers - (i) Tuning of Asymmetrical Fuzzy Logic Control Algorithm for PV system connected to Grid. *International Journal of Hydrogen Energy*. Volume 42, Issue 26, June 2017, Pages 16375–16385. (ii) Study of Conventional Control Algorithms for PV-Based Grid-Connected Microgrid. *Proceeding of International Conference on Intelligent communication, Control and Devices*. Series: *Advances in Intelligent systems and computing*. Volume no 479. ISBN: 978-981-10-1707-0. (iii) Characterization Study of PV module Connected to Microgrid. *IEEE India International Conference (INDICON 2015) Dec 17-20, 2015, JMI, India*. (iv) Asymmetrical Fuzzy logic control to PV Module Connected micro-grid. *IEEE India International Conference (INDICON 2015) Dec 17-20, 2015, JMI, India*.



**4.2. SYSTEM CONFIGURATION FOR PV BASED MICROGRID**

In chapter three, section 3.4 presented the design and selection of various components the system under consideration. In the present chapter, interfacing control algorithms have been developed for a two-stage three-phase configuration of the grid-tied microgrid. Figure 4.1 shows the MATLAB Simulink model for the system considered. It consists of PV array, DC-DC converter and DC-AC converter, fed by common DC-link capacitor ( $C_d$ ). The DC-DC converter is used to boost the output voltage of the PV array to the required DC link voltage level along with the functionality of tracking the maximum power obtained from PV array under varying irradiation and temperature. The DC-AC conversion and load compensation are performed by using a three-phase PV inverter controlled by interfacing control algorithms. Interfacing inductors ( $L_f$ ) are used for interfacing the inverter with the grid to suppress the injected current harmonics. The performance of the system has been validated for various types of loads. A combination of three series R-L branches connected in a star is selected as a linear load representation and for nonlinear load, an uncontrolled bridge rectifier with series R-L branch is selected. The PV based microgrid is tied to the three-phase AC source through the grid impedance (series  $R_s-L_s$  branch). Data for the designed system is given in appendix-B.

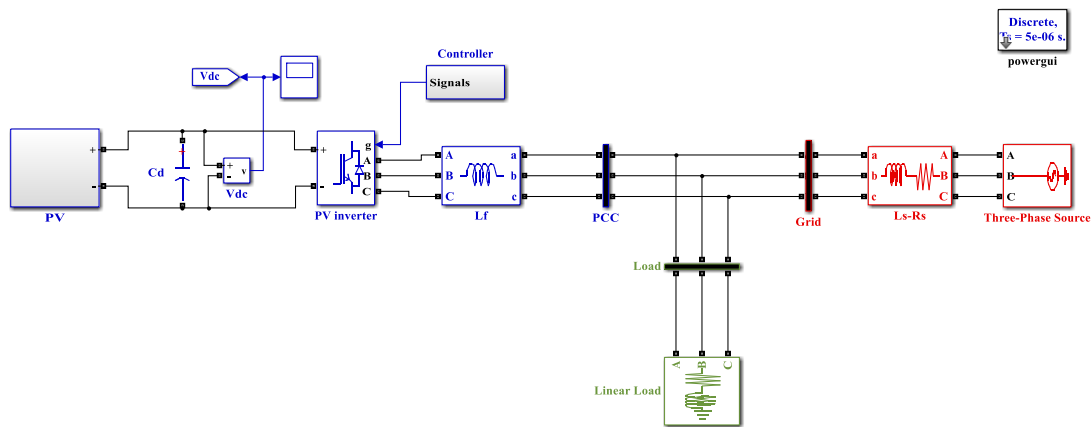


**Figure 4.1. Simulink model of two-stage three-phase grid-tied PV based microgrid**

Interfacing control algorithm for PV inverter is used to convert generated DC power into AC of required voltage and frequency for grid synchronization and also provides load compensation by regulating the DC link voltage using a voltage controller. Some

important interfacing algorithms for controlling PV inverter are Synchronous Reference Frame (SRF) theory, unit template, Instantaneous Reactive Power theory, conductance fryze, etc. In the present work, novel AFL based intelligent control algorithm and feedforward-feedback adaptive control algorithm are proposed and their performance is compared with SRF theory based conventional control algorithm.

### 4.3. INTERFACING CONTROL ALGORITHMS

Interfacing control algorithm in a PV based microgrid plays a vital role for control and synchronization of generated power with the grid. Performance of the grid-interfacing inverter depends on interfacing control algorithm used for generation of reference currents which in turn are used to generate the gate pulses for the inverter.

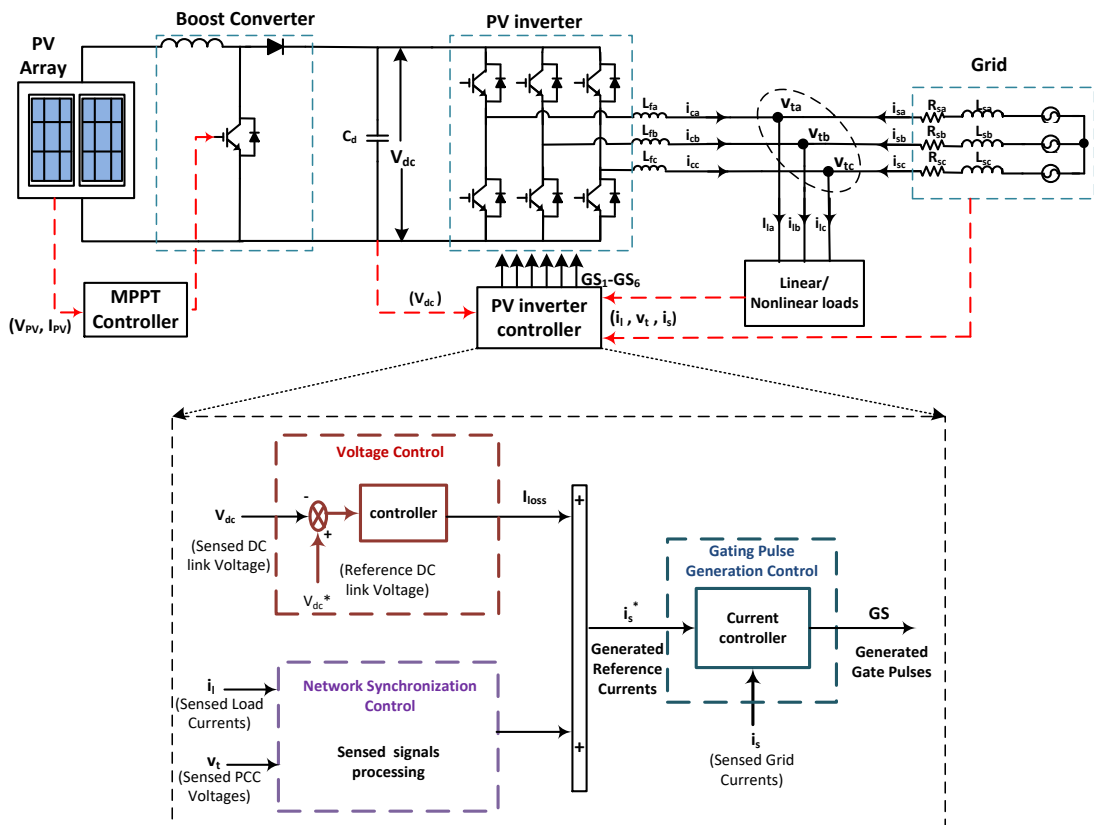
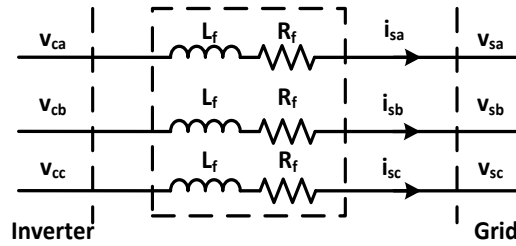


Figure. 4.2. Block diagram of closed-loop control of PV inverter

The inverter can be made to operate in two control modes: (a) unity power factor mode and (b) zero voltage regulation mode. The choice of control strategy for PV inverter is determined by the type of control intended, systems' stability and power quality requirement. A generalized block diagram of the closed-loop control of PV inverter is

shown in figure 4.2. It comprises of three main sub-controls namely (i) network synchronization control, (ii) voltage control, and (iii) gating pulse generation control.

Network synchronization control block is a basic current controller block in which signal processing is carried out and the fundamental component of the control signal is extracted. The inverter output voltage is the vector sum of the AC grid voltage and the series drop of the filter as shown in figure 4.3. Therefore, the network synchronization control block estimates the converter output voltage for a given power reference accounting the filter drop and maintains the power flow to follow the reference.



**Figure 4.3. Space vector equivalent of PV inverter**

Various reference frames can be adapted for the current control viz. natural reference frame, stationary reference frame, and synchronously rotating reference frame. The voltage equation of the equivalent PV inverter model in the stationary and rotating frame can be written as shown in equations (4.1) and (4.2), respectively.

$$v_c = R_f i_s + L_f \frac{d(i_s)}{dt} + v_s \quad (4.1)$$

$$v_{cdq} = R_f i_{sdq} + L_f \frac{d(i_{sdq})}{dt} + j\omega L_f i_{sdq} + v_{sdq} \quad (4.2)$$

where  $L_f$  is the interfacing inductor and  $R_f$  is the internal resistance of the inductor.  $i_s$ ,  $v_s$  and  $v_c$  are grid currents, grid voltages and inverter voltages, respectively in stationary frame and  $i_{sdq}$ ,  $v_{sdq}$  and  $v_{cdq}$  are grid currents, grid voltages and inverter voltages, respectively in synchronously rotating frame. Taking Laplace transform of equation (4.2), the transfer function  $T(s)$  is derived as,

$$T(s) = \frac{i_{sdq}(s)}{V_{cdq}(s) - V_{sdq}(s)} = \frac{1}{(s + j\omega)L_f + R_f} \quad (4.3)$$

The grid voltage ( $v_{sdq}$ ), is subtracted from the inverter voltage ( $v_{cdq}$ ), for obtaining the

required output current. PV inverter supplies the desired voltage,  $v_c$  with low harmonic distortion.

The voltage control block is responsible for voltage control of the DC- link capacitor to reduce output ripple and to ensure balanced inverter output. Voltage control loop uses feedback controllers for forcing the actual quantities to follow the reference quantities. The controller processes the error signal ( $V_{dc}^* - V_{dc}$ ) to generate a current component  $I_{loss}$  that adds to the reference current signals for any energy imbalance in DC bus bar.

Fundamental components obtained from network synchronization control block along with output of voltage control block ( $I_{loss}$ ) are used to calculate the reference current signals. Reference current signals, thus obtained along with corresponding sensed current signals are used to generate the gating pulse signals for switching devices (IGBTs) of PV inverter in the gating pulse generation control. Pulse Width Modulation (PWM) or Hysteresis Current Control (HCC) technique can be used for gating pulse generation.

The main contribution of this work is the development of novel intelligent and adaptive control algorithms. The following section explains the conventional SRF theory based conventional interfacing control algorithm along with the two proposed interfacing control algorithms viz. AFL based intelligent control algorithm and feedforward-feedback adaptive control algorithm.

#### 4.3.1. SRF theory based conventional control algorithm

Block diagram of the control algorithm is shown in figure 4.4. In the SRF theory based intelligent control algorithm, sensed signals  $i_{la}$ ,  $i_{lb}$  and  $i_{lc}$ ;  $v_{ta}$ ,  $v_{tb}$  and  $v_{tc}$ ; and  $V_{dc}$  are fed to controller for extracting the reference currents [62].

SRF theory algorithm uses Park's transformation to reduce three-phase AC quantities to two DC quantities for simplified calculations, given by,

$$I_d = \frac{2}{3} (i_{la} \text{Re}\{e^{i\alpha}\} + i_{lb} \text{Re}\{e^{i\beta}\} + i_{lc} \text{Re}\{e^{i\gamma}\}) \quad (4.4)$$

$$I_q = \frac{2}{3} (i_{la} \text{Im}\{e^{i\alpha}\} + i_{lb} \text{Im}\{e^{i\beta}\} + i_{lc} \text{Im}\{e^{i\gamma}\}) \quad (4.5)$$

where  $\alpha$  is  $(\omega t)$ ,  $\beta$  is  $(\alpha - 2\pi/3)$  and  $\gamma$  is  $(\alpha + 2\pi/3)$ .

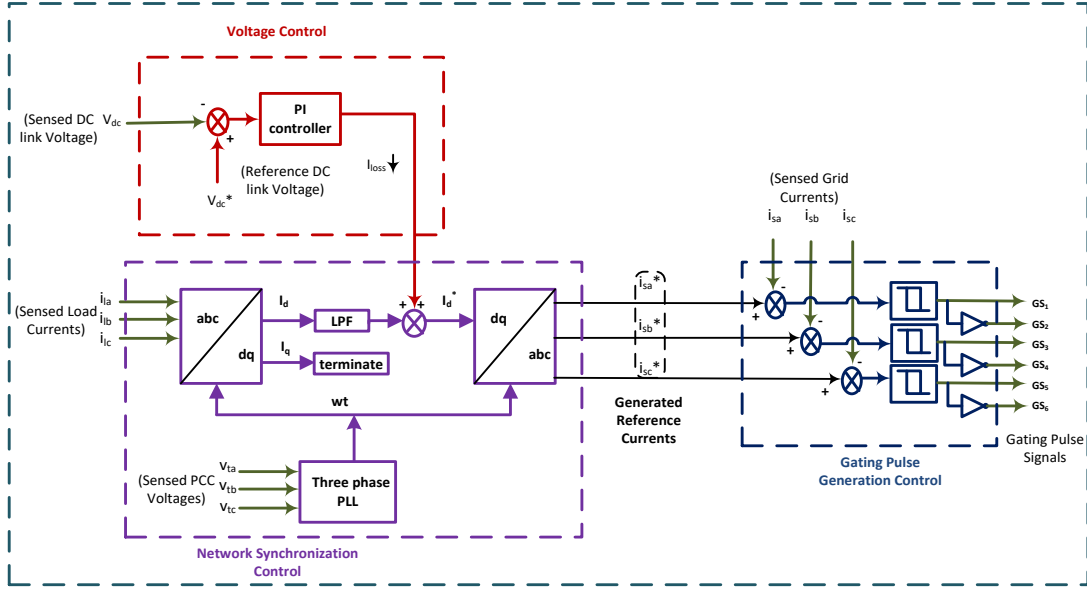


**Figure 4.4. Block diagram of control scheme for SRF theory based conventional control algorithm**

The two DC quantities,  $I_d$  ( $d$ - axis) current and  $I_q$  ( $q$ - axis) current are used to control the real and reactive power respectively. In this study, grid voltage vector is aligned towards  $d$ - axis. So aligning of the vector to the grid  $d$ -axis ensures a unity power factor operation. For interfacing PV inverter with the grid, its output has to be synchronized with the grid. Phase-locked loop (PLL) is used for synchronization of inverter with the grid.

Conventionally Proportional–Integral (PI) controller is used for the DC bus voltage regulation. PI controller consists of two basic coefficients; proportional and integral, which are varied to get an optimal response. The proportional action increases the loop gain and makes the system less sensitive to the parameter variation of system parameters. The integral term accelerates the movement of the process towards setpoint and eliminates the residual steady-state error. The proportional plus integral controller produces an output value which is proportional to voltage error value and also proportional to the integral of the error value. The output of the PI controller in the voltage control loop of the PV inverter control algorithm is given by,

$$I_{loss}(k) = I_{loss}(k - 1) + K_p\{v_e(k) - v_e(k - 1)\} + K_i v_e(k) \quad (4.6)$$

where,  $K_p$  = proportional gain,  $K_i$  = integral gain,  $e(t)$  is the voltage error signal, and

$I_{loss}$  is the output of PI controller considered as the loss component of PV inverter.

The reference active component of supply current ( $I_d^*$ ) is estimated from output of DC bus PI controller ( $I_{loss}$ ) and fundamental DC current component of load current ( $I_d$ ) given by,

$$I_d^* = (I_d + I_{loss}) \quad (4.7)$$

To generate the reference currents inverse Park's transformation is carried,

$$i_{sa}^* = (I_d^* \text{Re}\{e^{i\alpha}\} + I_q^* \text{Im}\{e^{i\alpha}\}) \quad (4.8)$$

$$i_{sb}^* = (I_d^* \text{Re}\{e^{i\beta}\} + I_q^* \text{Im}\{e^{i\beta}\}) \quad (4.9)$$

$$i_{sc}^* = (I_d^* \text{Re}\{e^{i\gamma}\} + I_q^* \text{Im}\{e^{i\gamma}\}) \quad (4.10)$$

The measured currents ( $i_{sa}$ ,  $i_{sb}$ ,  $i_{sc}$ ) and reference currents ( $i_{sa}^*$ ,  $i_{sb}^*$ ,  $i_{sc}^*$ ) signals are processed by HCC which generates the gating pulses for the PV inverter. Source current is controlled within a band. If source current exceeds the upper hysteresis limit, it turns on a negative voltage switching function and cause source current to decrease. If current exceeds the lower hysteresis limit, it turns on a positive voltage switching function to increase the source current. The generated six gate pulses are send to the three-phase PV inverter.

#### 4.3.2. Proposed AFL based intelligent control algorithm

The conventional algorithms are based on hard technology whereas asymmetrical fuzzy logic (AFL) control is based on soft computing techniques. Block diagram of the control scheme for the proposed AFL based intelligent control algorithm is shown in figure 4.5. In the proposed algorithm, sensed signals  $i_{la}$ ,  $i_{lb}$  and  $i_{lc}$ ;  $v_{ta}$ ,  $v_{tb}$  and  $v_{tc}$ ; and  $V_{dc}$  are fed to controller for extracting the reference currents. AFL based intelligent control algorithm process the sensed load current signal similar to SRF theory based conventional control algorithm but uses intelligent fuzzy logic control with asymmetric membership functions for DC voltage control as shown in figure 4.5. Intelligent controller helps in improving dynamic response of algorithm.

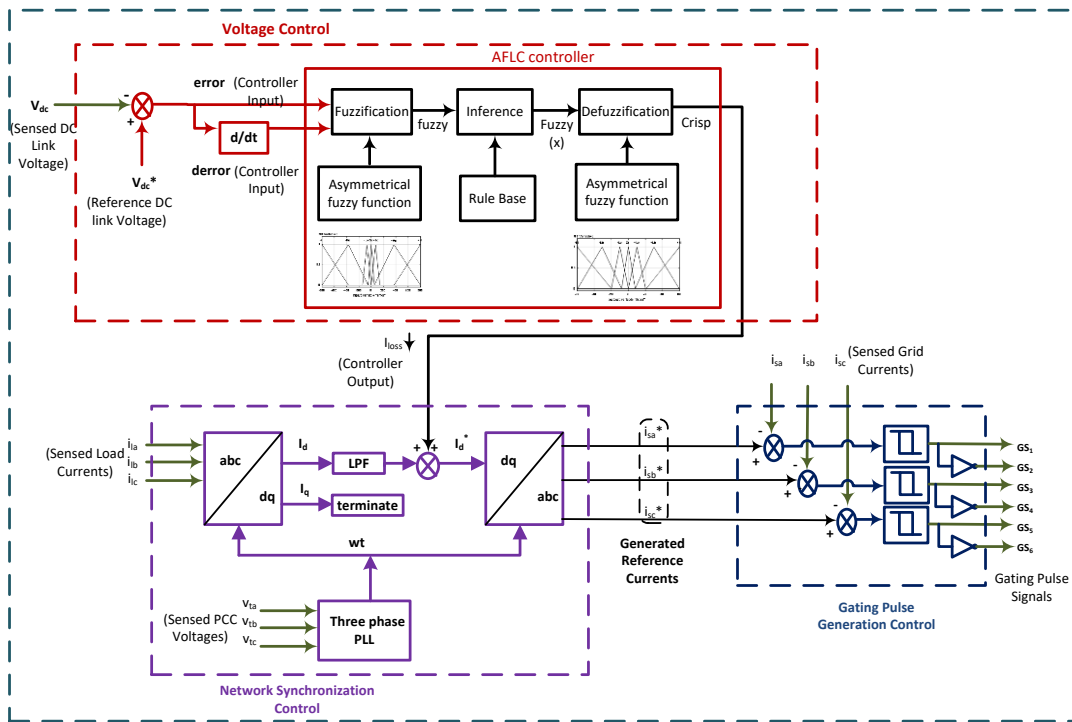


**Figure 4.5. Block diagram of control scheme with proposed AFL based intelligent control algorithm**

Fuzzy logic intelligent controller based on symmetrical membership functions gives a satisfactory solution for nonlinear systems with uncertainties. Unlike Boolean logic, it deals with problems that have fuzziness or vagueness. The methodology of reasoning in fuzzy logic uses “IF... THEN...”statements or rules. In general, membership functions are assigned to the input and output variables.

The configuration of fuzzy logic membership functions can be of two types-

- (i) Symmetrical, and
- (ii) Asymmetrical

Symmetrical fuzzy functions can take into account the uncertainty and vagueness for the uniform signal frequency but deliver unsatisfactory results for variable frequency signal. For such variable frequency signal, wavelet transformation or asymmetrical fuzzy functions needs to be considered. However, the wavelet transformation does not take into account the vagueness and uncertainties in the signal whereas the asymmetric fuzzy functions take into account these factors. In the present studies, asymmetrical membership functions are proposed since the parameters associated with PV systems such as photon energy and the load are uncertain and random in nature. In the proposed

AFL based intelligent algorithm, the input membership functions of FLC are further fine-tuned by the heuristic approach using fine tuning and coarse tuning features that can provide better controlling and stability. The membership functions are denser at the centre to provide greater sensitivity in the region of large DC-link voltage variation and become less dense gradually. Input membership functions are normalized, and suitable tuning gains are used. The inference method and defuzzification remain the same as in symmetric FLC.

Design of AFL based intelligent control algorithm is explained in the following subsections:

### **Fuzzification**

The proposed AFL based algorithm is used to regulate the DC link voltage across the capacitor,  $C_d$ . The sensed DC voltage,  $V_{dc}$  is compared with a reference value,  $V_{dc}^*$  (=800 V) which generates the  $I_{loss}$  factor used for regulating active power component of current [62]. The controller consists of two input variables: *error* and *derror* (change in error), and one output variable  $I_{loss}$ .

$$error(N) = V_{dc}^* - V_{dc}(N) \quad (4.11)$$

$$derror(N) = error(N) - error(N - 1) \quad (4.12)$$

where  $error(N)$  is the error and  $derror(N)$  is the change in error in the  $N^{th}$  iteration.  $V_{dc}^*$  is the reference dc link voltage and  $V_{dc}(N)$  is the sensed dc linked voltage in  $N^{th}$  iteration.

Fuzzy sets of input and output variables consist of seven sets of triangular membership functions as shown in figure 4.6.

The membership functions are *-Hi*: negative high, *-Me*: negative medium, *-Lo*: negative low, *Ze*: zero, *+Lo*: positive low, *+Me*: positive medium and *+Hi*: positive high. In the asymmetrical fuzzy functions, wide span functions are considered for *-Hi*, *-Me*, *+Me*, and *+Hi* for coarse tuning of respected variables. The narrow span functions (*-Lo*, *Z*, *+Lo*) are considered near zero for *error* and  $I_{loss}$  factor for the fine-tuning of respected variables.



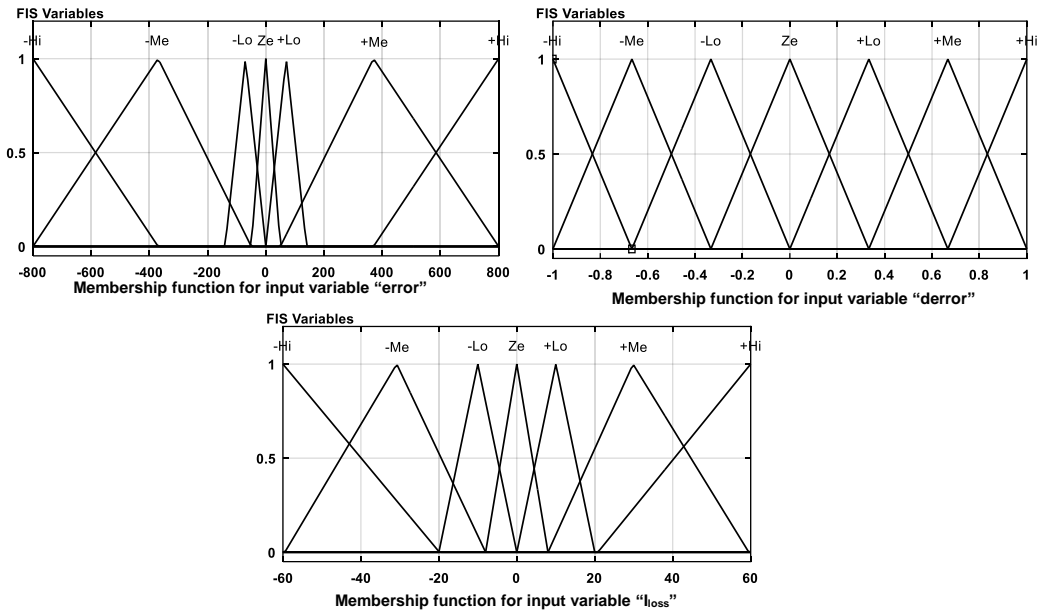


Figure 4.6. Membership functions for input variable ‘error’, ‘derror’ and output variable ‘I<sub>loss</sub>.’

Each membership function has a membership value belonging to {0 1}. Study of the PI controller operation of the system is used to set the span of the input and output membership functions to train the FLC system. Initially,  $V_{dc}$  the voltage across the DC link capacitor may be zero, whereas,  $V_{dc}^*$  the reference voltage is 800 V, so, the maximum error can be  $\pm 800$  V. Thus, the span of *error* functions considered is  $\{-800\ 800\}$  V for the DC-link voltage error. Also, for the DC-link voltage, the simulation results shows that the error value varies between the ranges of  $\{-150\ 150\}$  during transient situation. Hence, near zero error i.e. in the range  $\{-150\ 150\}$ , the frequency of error considered is high. Similarly, the span for the *derror* is set as  $\{-1\ 1\}$  and for the output  $I_{loss}$  is set as  $\{-60\ 60\}$  A.

**Inference Method**

The main function of the inference mechanism is to process the fuzzy values of input according to the rules drawn by experts and based on the active membership functions in *error* and *derror* inputs. In AFL based algorithm there are total 49 rules. An example of a rule is shown as:

IF  
 “error”                    is            +Lo (Positive Low)  
 “derror”                   is            –Lo (Negative Low)  
 THEN

$$“I_{loss}” \quad \text{is} \quad Ze \text{ (Zero)} \tag{4.13}$$

Table 4.1 shows the rule base of the proposed AFL based algorithm for calculating  $I_{loss}$ . Figure 4.7 the surface plot of the rule base.

**TABLE 4.1. Fuzzy rule base for computing  $I_{loss}$**

<b>derror error</b>	<b>-Hi</b>	<b>-Me</b>	<b>-Lo</b>	<b>Ze</b>	<b>+Lo</b>	<b>+Me</b>	<b>+Hi</b>
<b>-Hi</b>	-Hi	-Hi	-Hi	-Me	-Me	-Lo	Ze
<b>-Me</b>	-Hi	-Hi	-Me	-Me	-Lo	Ze	+Lo
<b>-Lo</b>	-Hi	-Me	-Me	-Lo	Ze	+Lo	+Me
<b>Ze</b>	-Me	-Me	-Lo	Ze	+Lo	+Me	+Me
<b>+Lo</b>	-Me	-Lo	Ze	+Lo	+Me	+Me	+Hi
<b>+Me</b>	-Lo	Ze	+Lo	+Me	+Me	+Hi	+Hi
<b>+Hi</b>	Ze	+Lo	+Me	+Me	+Hi	+Hi	+Hi

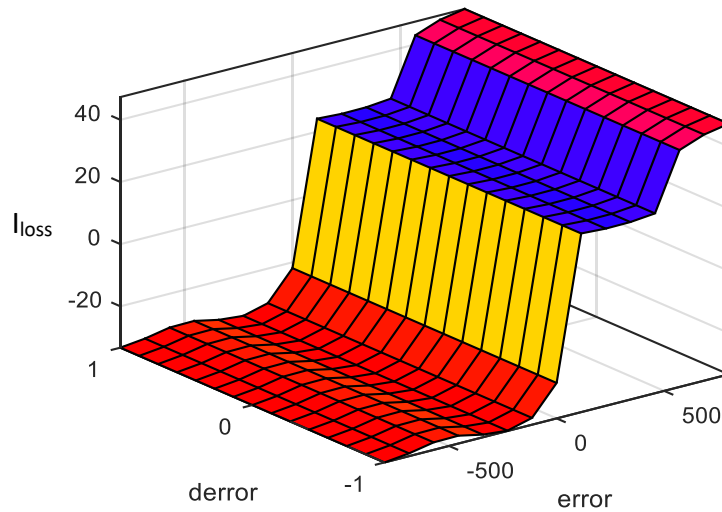


**Figure 4.7. Surface plot of rule base for computing ‘ $I_{loss}$ ’ component**

The rule base matrix provides rules for all possible combinations of the membership functions for *error* and *derror* in line with equation (4.9). Thus, using information from the rule base, the rule, and its certainty is determined by the inference mechanism. In the present work, Mamdani’s MAX-MIN [75] method is used for inference of proposed AFL based algorithm. The output membership function of each rule is given by minimum operator whereas collective fuzzy output ( $x$ ) is provided by maximum operator.

### Defuzzification

The output of the inference method is a fuzzy set. Defuzzification is used to obtain the required crisp control output  $z_o (= i_{loss})$  and is defined by,

$$z_o = defuzzifier(x) \quad (4.14)$$

where  $x$  is aggregate output and *defuzzifier* is defined as defuzzification operator. In the present work center of the area is used as defuzzification operator and is given by,

$$x = \frac{\sum_{i=1}^n \mu(x_i)x_i}{\sum_{i=1}^n \mu x_i} \quad (4.15)$$

where  $\mu x_i$  is the activation degree on rule  $i$ ,  $x_i$  is the center of the Max-Min composition of the output membership functions and  $x$  is the required output  $I_{loss}$ .

The reference active component of supply current ( $i_d^*$ ) is estimated from output of AFL controller ( $I_{loss}$ ) and fundamental DC current component of load current ( $I_d$ ). Further, the measured currents ( $i_{sa}$ ,  $i_{sb}$ ,  $i_{sc}$ ) and reference currents ( $i_{sa}^*$ ,  $i_{sb}^*$ ,  $i_{sc}^*$ ) signals are processed by HCC which generates the gating pulses for the PV inverter.

#### 4.3.3. Proposed feedforward-feedback adaptive control algorithm

As discussed in the previous sections, feedback controllers are used in the interfacing control algorithm. These controllers respond only after they detect a deviation in the value of the controlled output from its desired set point. On the other hand, a feedforward controller can detect the disturbance directly and takes an appropriate control action in order to eliminate its effect on the process output [168]. Any controller in feedforward configuration would act according to the disturbance for which it is designed. Thus, the feedforward controller makes the microgrid adaptive to disturbances occurring in the overall system.

To improve the dynamic response of AFL based control algorithm, feedforward control is added to the voltage control loop and a novel feedforward-feedback adaptive control algorithm is proposed. It can significantly improve performance over simple feedback control whenever there is a major disturbance that can be measured before it affects the system output. Figure 4.8 shows the block diagram of the control scheme for the

proposed feedforward-feedback adaptive control algorithm for the PV inverter. In the algorithm, sensed signals  $i_{la}$ ,  $i_{lb}$  and  $i_{lc}$ ;  $v_{ta}$ ,  $v_{tb}$  and  $v_{tc}$ ; and  $V_{dc}$  are fed to controller for extracting the reference currents. Proposed algorithm process the sensed load current signal similar to SRF theory based conventional control algorithm but uses adaptive feedforward-feedback controller for DC voltage control.

The adaptive controller consists of feedback and feedforward control loops. Feedback control loop consists of AFL based control to maintain the dc bus voltage of PV inverter to reference value. The output of the AFL controller ( $I_{loss}$ ) in a steady state condition is considered as the loss component of the PV inverter. The AFL controller adjusts  $I_{loss}$  continuously in order to maintain the dc link voltage. The loss component is estimated as given in equation (4.14).

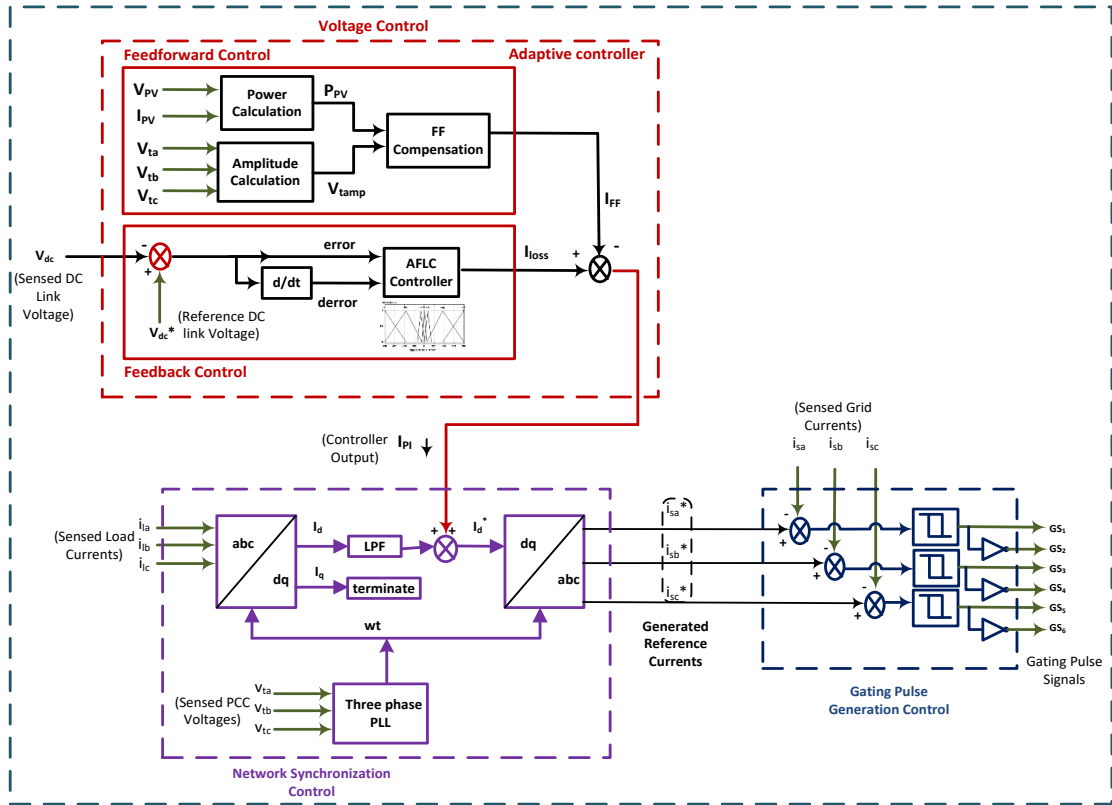


**Figure 4.8. Block diagram of control scheme for proposed feedforward-feedback adaptive control algorithm**

Feedforward control loop estimates the feed-forward current given by

$$I_{FF} = (2P_{PV}) / (3V_{tamp}) \quad (4.16)$$

where  $P_{PV}$  is the power obtained from PV array and  $V_{tamp}$  is the amplitude of PCC voltage and can be estimated as,

$$V_{tamp} = \sqrt{\frac{2(v_{ta}^2 + v_{tb}^2 + v_{tc}^2)}{3}} \quad (4.17)$$

Feedforward control is used to estimate the PV array contribution to the reference grid currents used for switching of the inverter. It can easily be observed that feedforward quantities are directly proportional to PV power and inversely proportional to the grid voltage magnitude. The  $P_{PV}$  term helps during changing atmospheric conditions, whereas the  $V_{tamp}$  helps in fast dynamic response during a sudden voltage sag or swell.

The controller output is estimated from the  $I_{FF}$  and  $I_{Loss}$  components. The grid currents are assumed coming out from equivalent voltage source, and hence considering the direction of grid currents, the losses are drawn from the grid, whereas the PV contribution is fed into the grid. Hence, considering this the peak value of grid current, for overall UPF operation is estimated as,

$$I_{PI} = I_{loss} - I_{FF} \quad (4.18)$$

The reference active component of supply current ( $i_d^*$ ) is estimated from output of adaptive controller ( $I_{PI}$ ) and fundamental DC current component of load current. Further, the measured currents ( $i_{sa}, i_{sb}, i_{sc}$ ) and reference currents ( $i_{sa}^*, i_{sb}^*, i_{sc}^*$ ) signals are processed by HCC which generates the gating pulses for the PV inverter.

#### 4.4. RESULTS AND DISCUSSIONS

This section presents simulation performances and the analysis of the proposed AFL based intelligent control algorithm and feedforward-feedback adaptive control algorithm for two-stage three-phase three-wire PV based microgrid.

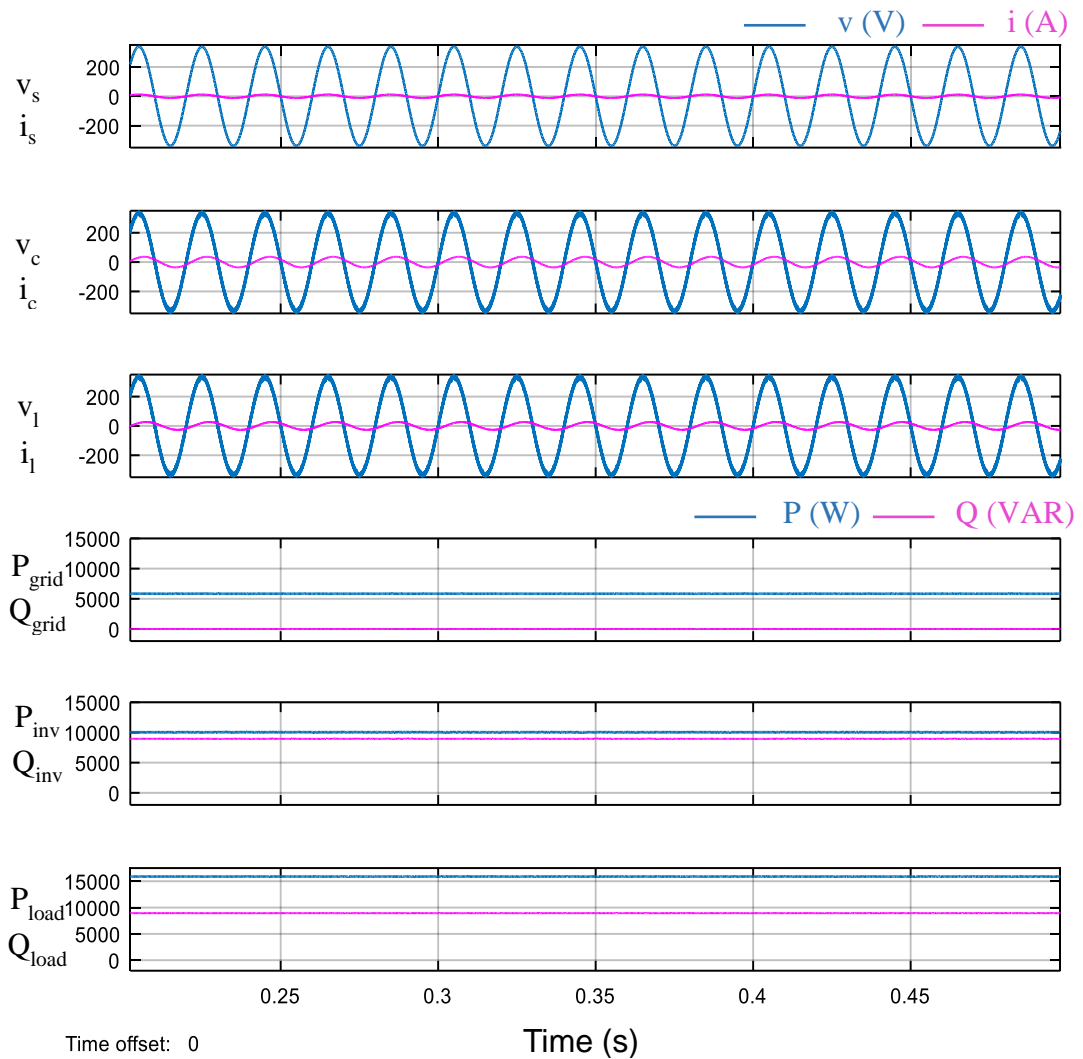
##### 4.4.1. Performance evaluation of proposed AFL based intelligent control algorithm

To evaluate the performance of AFL based intelligent control algorithm operating under steady-state and dynamic conditions with the linear and nonlinear load, simulation studies have been carried out. All the related waveforms are shown on the same time

base for complete characterization of the system. The system parameters and load data used for simulation are given in appendix-B.

**4.4.1.1. Performance under balanced linear and non-linear loads**

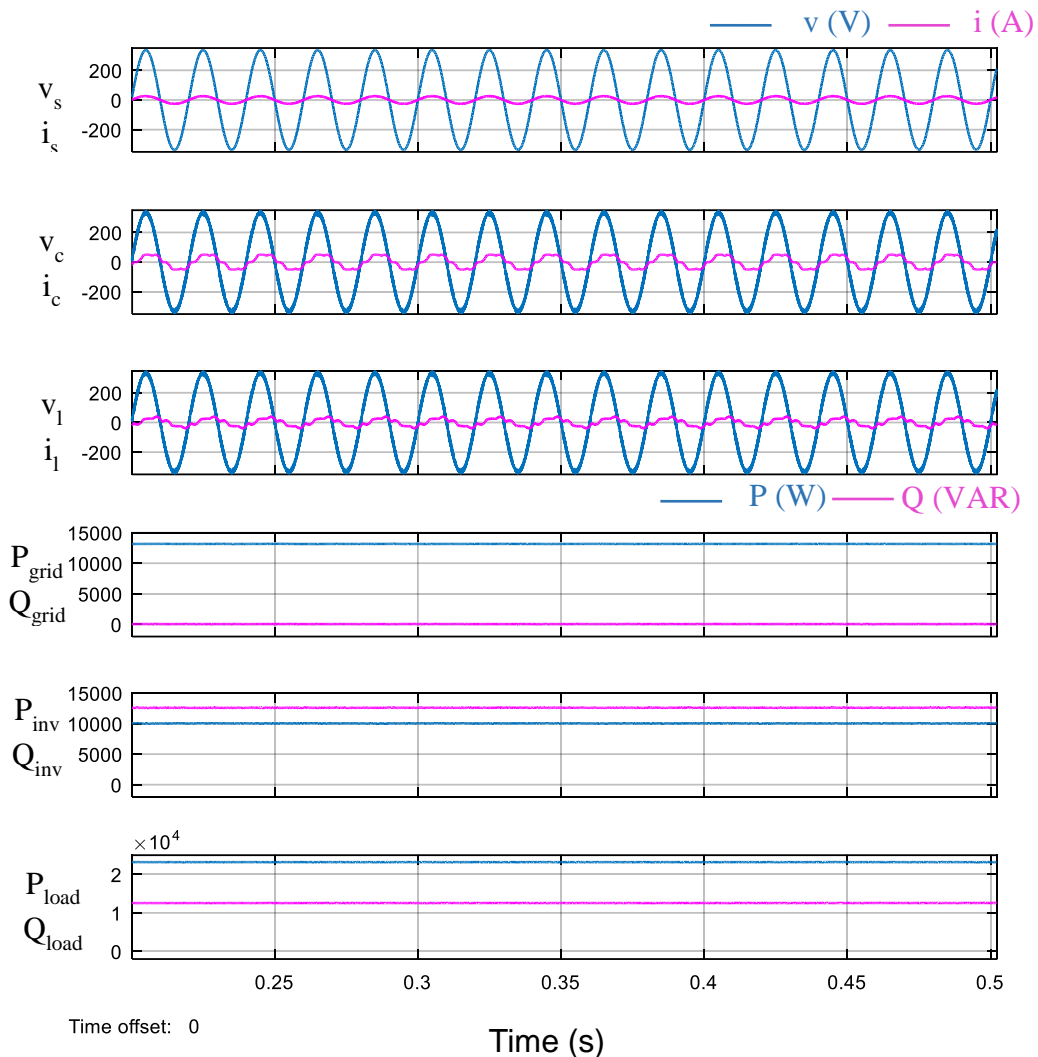
Figure 4.9 shows simulation results under balanced linear load conditions. A three-phase linear load of 32 kVA, 0.5 power factor lagging (highly inductive) is taken for testing the UPF control of proposed algorithm.



**Figure 4.9. Simulation results for PV based microgrid with AFL based intelligent control algorithm under balanced linear load**

Figure 4.9 shows the waveforms of voltage ( $v_{sa}$ ) and current ( $i_{sa}$ ) of phase ‘a’ of grid, voltage ( $v_{ca}$ ) and current ( $i_{ca}$ ) of phase ‘a’ of inverter, voltage ( $v_{la}$ ) and current ( $i_{la}$ ) of phase ‘a’ of load, active ( $P_{grid}$ ) and reactive power ( $Q_{grid}$ ) from grid, active ( $P_{inv}$ ) and reactive power ( $Q_{inv}$ ) from inverter, and active ( $P_{load}$ ) and reactive power ( $Q_{load}$ ) to the

load. It can be seen from the figure; the grid current remains in phase with grid voltage. Also, total THD in grid current is noted to be 3.04 %, which is well within IEEE 519-2014 standard. During steady-state, the active and reactive power demand of load is 16 kW and 9 kVAR (lagging) respectively. The PV array provides the active power of 10 kW, and the grid supplies the rest 6 kW. From the figure it can be seen that complete reactive power demand of load is supplied by the PV inverter locally, thereby, reducing reactive power supplied by the grid to zero. Thus, PV inverter is maintaining unity power factor mode of operation along with power flow balance in a grid-tied PV based microgrid.



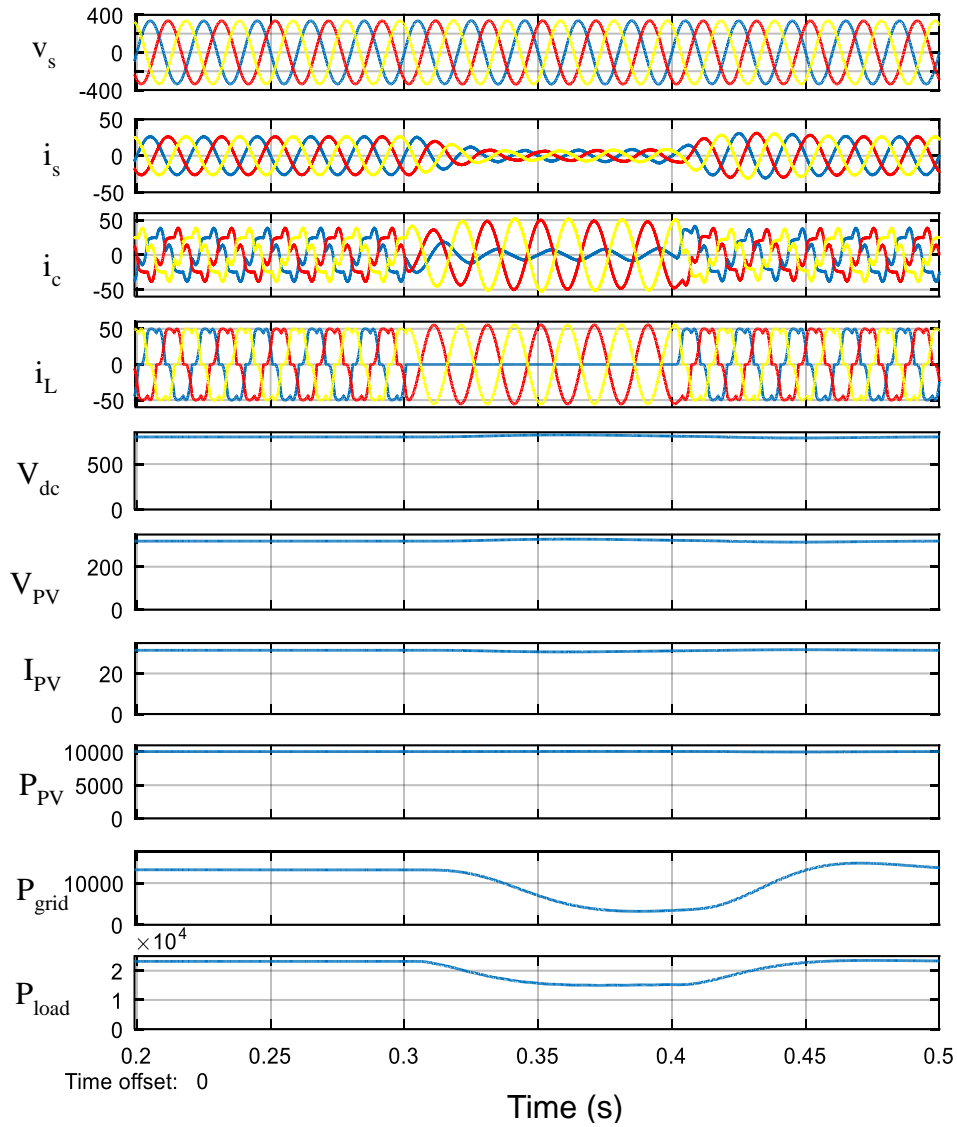
**Figure 4.10. Simulation results for PV based microgrid with AFL based intelligent control algorithm under balanced non-linear load**

Figure 4.10 shows simulation results under balanced non-linear load conditions. A three-phase diode bridge rectifier with RL load ( $10 \Omega$ ,  $0.8 \text{ mH}$ ) is connected at the PCC. Figure 4.10 shows the waveforms of voltage ( $v_{sa}$ ) and current ( $i_{sa}$ ) of phase 'a' of grid, voltage ( $v_{ca}$ ) and current ( $i_{ca}$ ) of phase 'a' of inverter, voltage ( $v_{la}$ ) and current ( $i_{la}$ ) of phase 'a' of load, active ( $P_{grid}$ ) and reactive power ( $Q_{grid}$ ) from grid, active ( $P_{inv}$ ) and reactive power ( $Q_{inv}$ ) from inverter, and active ( $P_{load}$ ) and reactive power ( $Q_{load}$ ) to the load. PV inverter is able to perform active filtering by maintain THD of grid current at 1.07 % (well within the IEEE 519-2014 Std.), even when THD of the connected load is 16.34 %. Thus, the PV inverter supplies the active power generated by PV source along with the reactive power demand and harmonic contents of the load.

#### 4.4.1.2. Performance under load unbalancing

Figure 4.11 shows the response of AFL based intelligent control algorithm based PV inverter under load unbalancing. A three-phase diode bridge rectifier with RL load ( $10 \Omega$ ,  $0.8 \text{ mH}$ ) is connected at the PCC. The load currents are unbalanced between  $t = 0.3 \text{ s}$  to  $0.4 \text{ s}$  as the load is removed from phase 'a'. PV inverter takes appropriate action and grid current in all three phases is settled down to the new value of  $8.4 \text{ A (RMS)}$ /phase from its old value  $26.5 \text{ A (RMS)}$ /phase. The PV inverter current for the phase 'a' is found to be equal and opposite to the grid current, as the load is zero in this phase. The PV inverter draws current  $i_{sa}$  from the grid. Hence, grid sees a combination of load and PV inverter as a three-phase balanced load and remains balanced sinusoid. Also,  $i_{sa}$  is in phase with  $v_{sa}$ , which is the requirement of UPF operation. The DC link voltage of the inverter is well regulated at  $800 \text{ V}$ . Thus, PV inverter controlled by AFL based intelligent control algorithm effectively carries out load balancing and harmonic compensation.





**Figure 4.11. Simulation results for PV based microgrid with AFL based intelligent control algorithm under unbalancing of non-linear load**

**4.4.1.3. Performance under irradiation variation**

Figure 4.12 shows the simulation results of the system for change in irradiation. Figure 4.12 shows the waveforms of grid side voltage ( $v_s$ ) and current ( $i_s$ ), Inverter current ( $i_c$ ), Load current ( $i_L$ ), DC link voltage ( $V_{DC}$ ), and voltage ( $V_{PV}$ ), current ( $I_{PV}$ ), power ( $P_{PV}$ ) from PV array, power ( $P_{grid}$ ) from/ to grid and power ( $P_{load}$ ) to the load. A three-phase diode bridge rectifier with RL load ( $35 \Omega$ ,  $0.8 \text{ mH}$ ) is connected at the PCC. The load is consuming  $7.5 \text{ kW}$  of active power, so the PV is supplying the excess power grid. It can be easily seen by  $180^\circ$  phase shift of grid current ( $i_s$ ) and voltage ( $v_s$ ). The load

currents are constant throughout. At  $t = 0.3$  s, the irradiation is changed from  $1000 \text{ W/m}^2$  to  $500 \text{ W/m}^2$ . With the decrease in the irradiation level, the active power generated from the PV decreases. Hence, power is demanded from the grid. With change in irradiation reactive power generated by the PV inverter remains the same. The grid currents remain balanced and sinusoidal irrespective of change in irradiation.

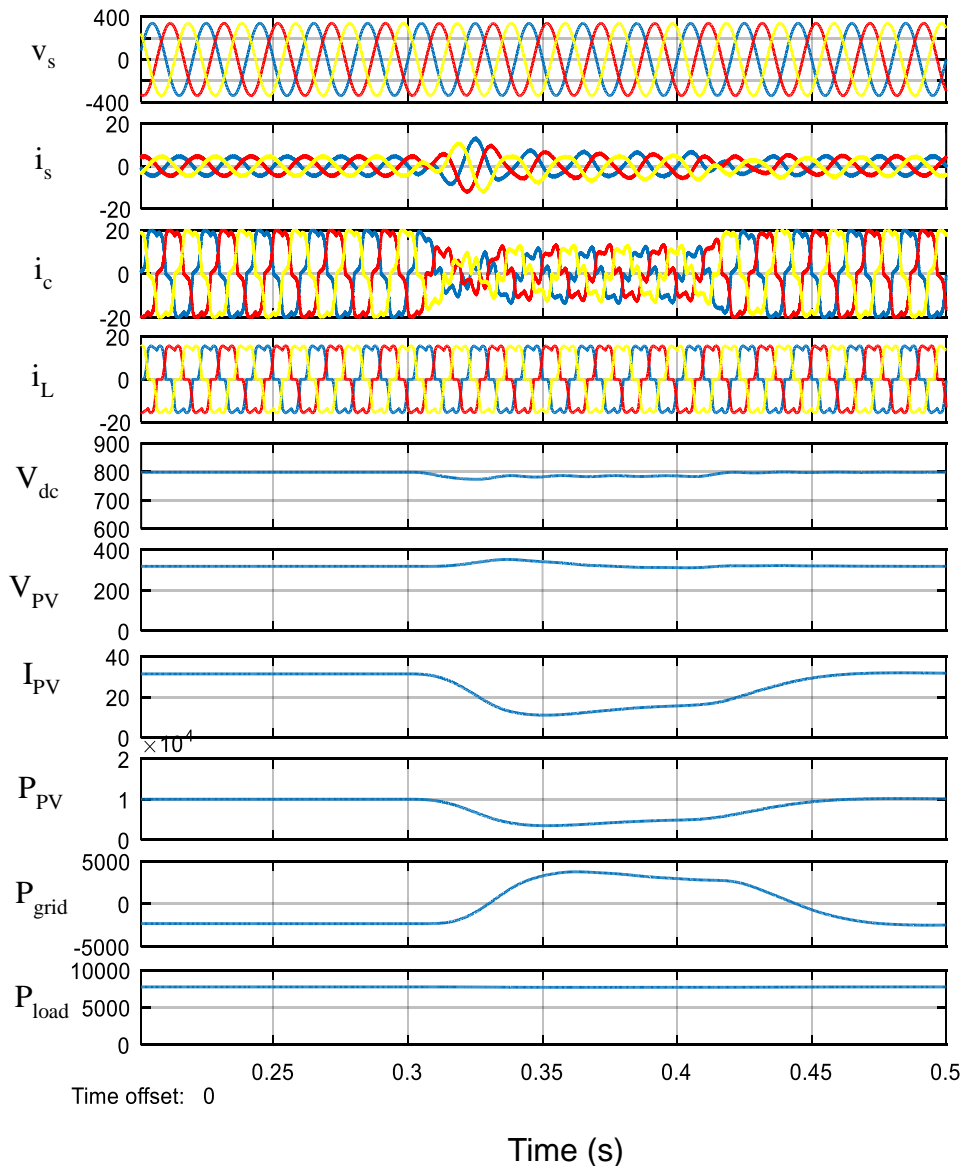


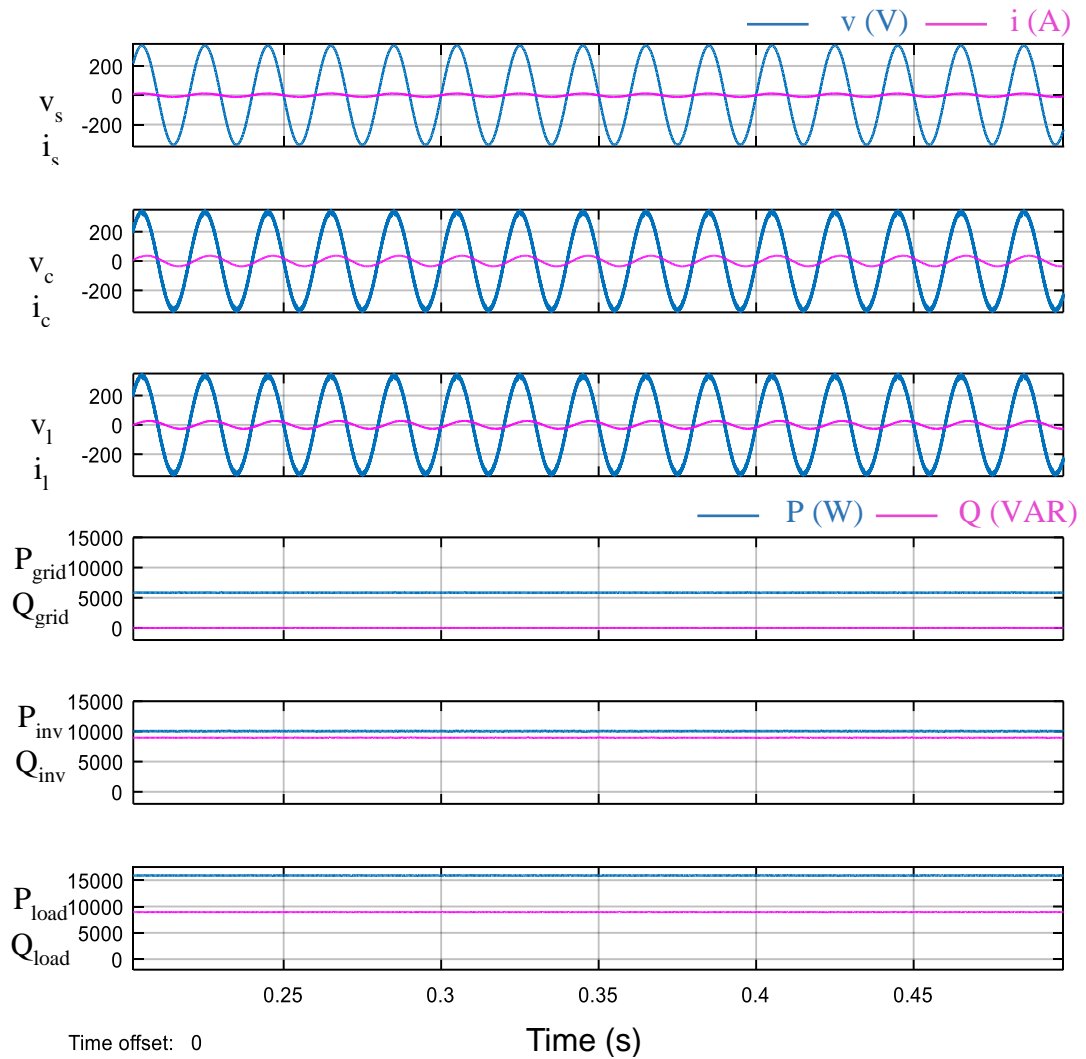
**Figure 4.12. Simulation results for PV based microgrid with AFL based intelligent control algorithm under irradiation variation**

#### 4.4.2. Performance evaluation of proposed feedforward-feedback adaptive control algorithm

To evaluate the performance of feedforward-feedback adaptive control algorithm operating under steady-state and dynamic conditions with the linear and nonlinear load, simulation studies have been carried out. All the related waveforms are shown on the same time base for complete characterization of the system. The system parameters used for simulation are given in appendix-B.

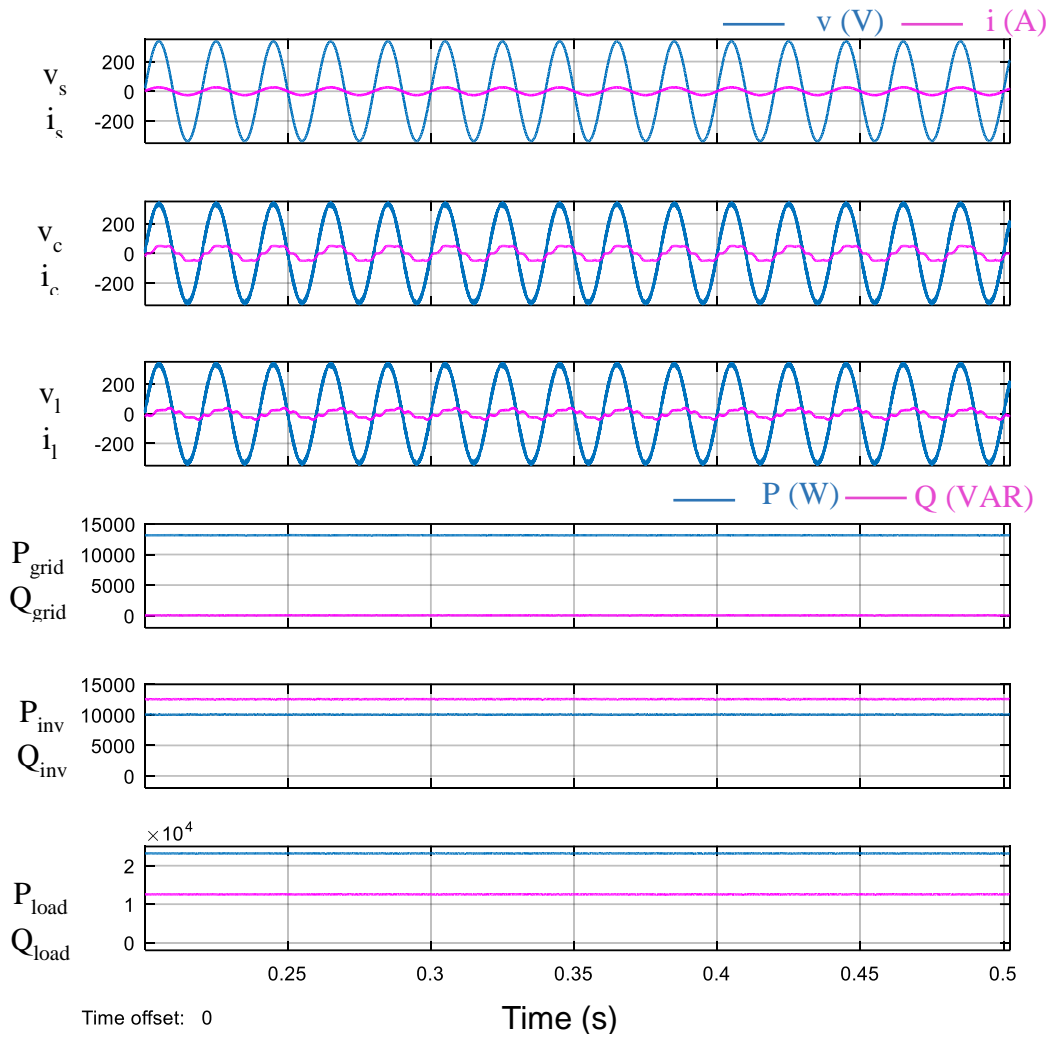
##### 4.4.2.1. Performance under linear and non-linear load

Figure 4.13 shows simulation results under balanced linear load conditions. A three-phase linear load of 32 kVA, 0.5 power factor lagging (highly inductive) is taken for testing the UPF control of proposed algorithm. Figure 4.13 shows the waveforms of voltage ( $v_{sa}$ ) and current ( $i_{sa}$ ) of phase 'a' of grid, voltage ( $v_{ca}$ ) and current ( $i_{ca}$ ) of phase 'a' of inverter, voltage ( $v_{la}$ ) and current ( $i_{la}$ ) of phase 'a' of load, active ( $P_{grid}$ ) and reactive power ( $Q_{grid}$ ) from grid, active ( $P_{inv}$ ) and reactive power ( $Q_{inv}$ ) from inverter, and active ( $P_{load}$ ) and reactive power ( $Q_{load}$ ) to the load. It can be seen from the figure; the grid current remains in phase with grid voltage. Also, total THD in grid current is noted to be 2.90 %, which is well within IEEE 519-2014 standard [64]. During steady-state, the active and reactive power demand of load is 16 kW and 9 kVAR (lagging) respectively. The PV array provides the active power of 10 kW, and the grid supplies the rest 6 kW. From the figure it can be seen that complete reactive power demand of load is supplied by the PV inverter locally, thereby, reducing reactive power supplied by the grid to zero. Thus, PV inverter is maintaining unity power factor mode of operation along with power flow balance in a grid-tied PV based microgrid.



**Figure 4.13. Simulation results for PV based microgrid with feedforward-feedback adaptive control algorithm under balanced near load**

Figure 4.14 shows simulation results under balanced non-linear load conditions. A three-phase diode bridge rectifier with RL load ( $10 \Omega$ ,  $0.8 \text{ mH}$ ) is connected at the PCC. Figure 4.14 shows the waveforms of voltage ( $v_{sa}$ ) and current ( $i_{sa}$ ) of phase ‘a’ of grid, voltage ( $v_{ca}$ ) and current ( $i_{ca}$ ) of phase ‘a’ of inverter, voltage ( $v_{la}$ ) and current ( $i_{la}$ ) of phase ‘a’ of load, active ( $P_{grid}$ ) and reactive power ( $Q_{grid}$ ) from grid, active ( $P_{inv}$ ) and reactive power ( $Q_{inv}$ ) from inverter, and active ( $P_{load}$ ) and reactive power ( $Q_{load}$ ) to the load. PV inverter is able to perform active filtering as well by maintaining THD of grid current at 1.05 % (well within the IEEE 519-2014 Std.), even when THD of the connected load is 16.34 %. Thus, the PV inverter supplies the active power generated by PV source along with the reactive power demand and harmonic contents of the load.



**Figure 4.14. Simulation results for PV based microgrid with feedforward-feedback adaptive control algorithm under balanced non-linear load**

**4.4.2.2. Performance under load unbalancing**

Figure 4.15 shows the response of feedforward-feedback adaptive control algorithm based PV inverter under load unbalancing. A three-phase diode bridge rectifier with RL load ( $10 \Omega$ ,  $0.8 \text{ mH}$ ) is connected at the PCC. The load currents are unbalanced between  $t = 0.3 \text{ s}$  to  $0.4 \text{ s}$  as the load is removed from phase ‘a’. PV inverter takes appropriate action and grid current in all three phases is settled down to the new value of  $8.5 \text{ A}$  (RMS)/ phase from its old value  $26.5 \text{ A}$  (RMS)/ phase.

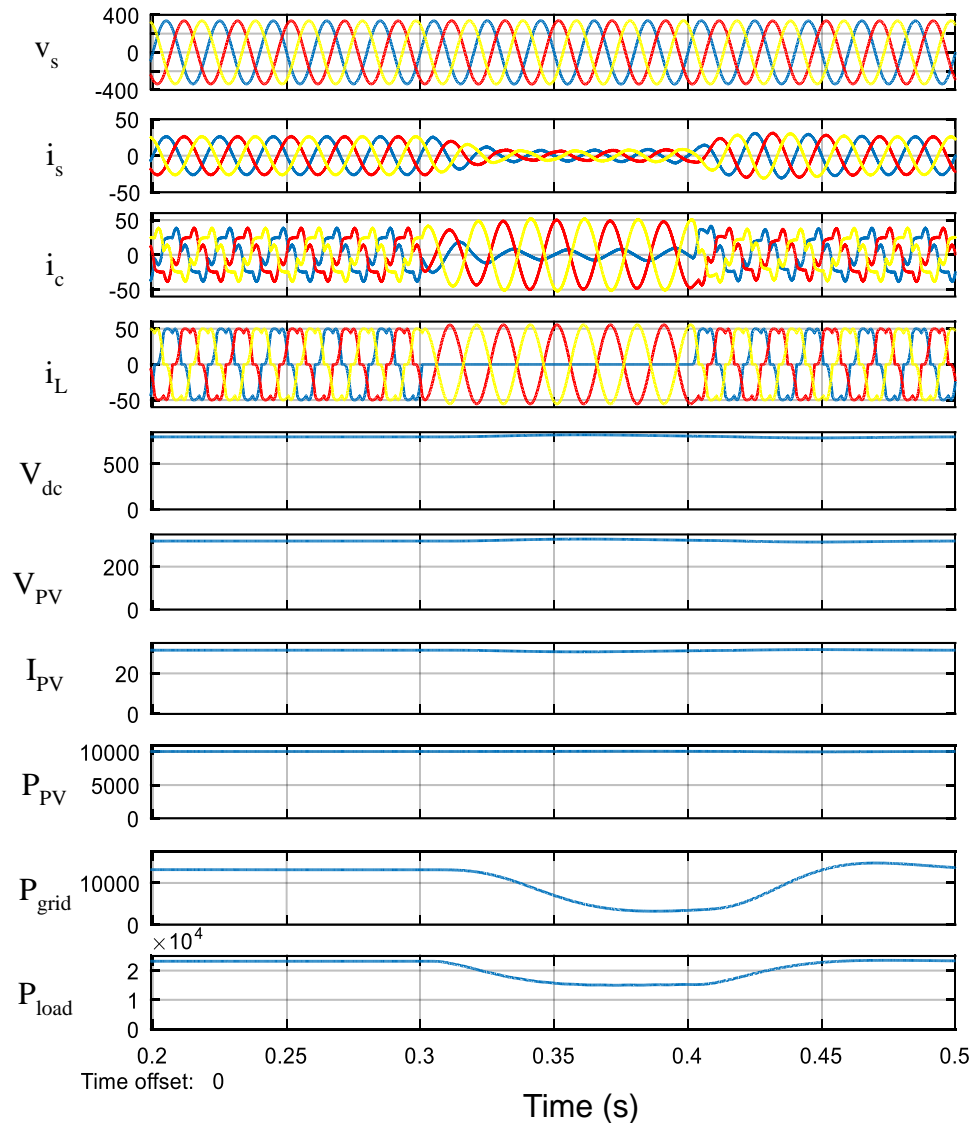


**Figure 4.15. Simulation results for PV based microgrid with feedforward-feedback adaptive control algorithm under unbalancing of non-linear load**

The PV inverter current for the phase ‘a’ is found to be equal and opposite to the grid current, as the load is zero in this phase. The PV inverter draws current  $i_{sa}$  from the grid. Hence, grid sees a combination of load and PV inverter as a three-phase balanced load and remains balanced sinusoid. Also,  $i_{sa}$  is in phase with  $v_{sa}$ , which is the requirement of UPF operation. The DC link voltage of the inverter is well regulated at 800 V. Thus, PV inverter controlled by feedforward-feedback adaptive control algorithm effectively carries out load balancing and harmonic compensation.

**4.4.2.3. Performance under irradiation variation**

Figure 4.16 shows the simulation results of the system for change in irradiation. Figure 4.16 shows the waveforms of grid side voltage ( $v_s$ ) and current ( $i_s$ ), Inverter current ( $i_c$ ), Load current ( $i_L$ ), DC link voltage ( $V_{DC}$ ), and voltage ( $V_{PV}$ ), current ( $I_{PV}$ ) and power ( $P_{PV}$ ) from PV array.

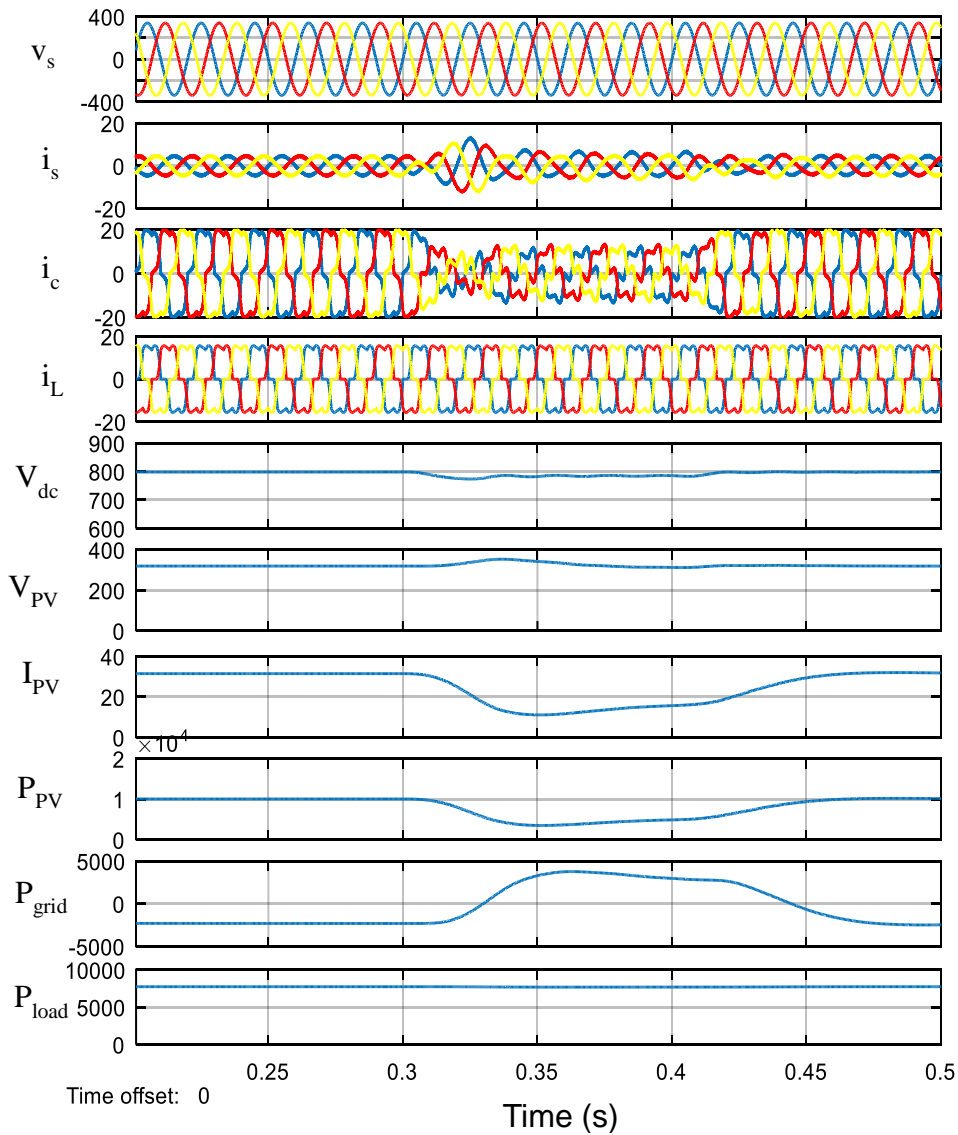


**Figure 4.16. Simulation results for PV based microgrid with feedforward-feedback adaptive control algorithm under irradiation variation**

A three-phase diode bridge rectifier with RL load ( $35 \Omega$ ,  $0.8 \text{ mH}$ ) is connected at the PCC. The load is consuming  $7.5 \text{ kW}$  of active power, so the PV is supplying the excess

power grid. It can be easily seen by  $180^\circ$  phase shift of grid current ( $i_s$ ) and voltage ( $v_s$ ). The load currents are constant throughout. At  $t = 0.3$  s, the irradiation is changed from  $1000 \text{ W/m}^2$  to  $500 \text{ W/m}^2$ . With the decrease in the irradiation level, the power generated from the PV decreases. Hence, power is demanded from the grid. With change in irradiation reactive power generated by the PV inverter remains the same. The grid currents remain balanced and sinusoidal irrespective of change in irradiation.

#### **4.4.3. Comparison of proposed intelligent and adaptive control algorithm with conventional control algorithm**

Figure 4.17 shows the comparison of proposed AFL based intelligent control algorithm and SRF theory based conventional control algorithm. Figure 4.17 (a) shows the simulation result of the designed system with SRF theory based conventional control algorithm, and (b) shows the simulation results with proposed AFL based intelligent control algorithm. A three-phase diode bridge rectifier with RL load ( $10 \Omega$ ,  $0.8 \text{ mH}$ ) is connected at the PCC. Both grid and PV together are feeding the load. Suddenly a load increase of  $20 \text{ kW}$  is applied at  $0.3$  s. It can be observed now that grid current ( $i_s$ ) and voltage ( $v_s$ ) are in phase with each other. Figure 4.17 (c) is the zoomed image of the DC link voltages of the two results. It can be easily observed that the overshoot in the dc-link voltage for load increase at PCC is drastically reduced with the AFL based control algorithm.

Figure 4.18 shows the comparison of proposed feedforward-feedback adaptive control algorithm and SRF theory based conventional control algorithm. Figure 4.18 (a) shows the simulation result of the designed system with SRF theory based conventional control algorithm, and (b) shows the simulation results with proposed feedforward-feedback adaptive control algorithm. A three-phase diode bridge rectifier with RL load ( $10 \Omega$ ,  $0.8 \text{ mH}$ ) is connected at the PCC. Both grid and PV together are feeding the load. Suddenly a load increase of  $20 \text{ kW}$  is applied at  $0.3$  s. It can be observed now that grid current ( $i_s$ ) and voltage ( $v_s$ ) are in phase with each other. Figure 4.18 (c) is the zoomed image of the DC link voltages of the two results. It can be easily observed that the overshoot in the dc-link voltage for load increase at PCC is drastically reduced with the feedforward-feedback adaptive control algorithm.



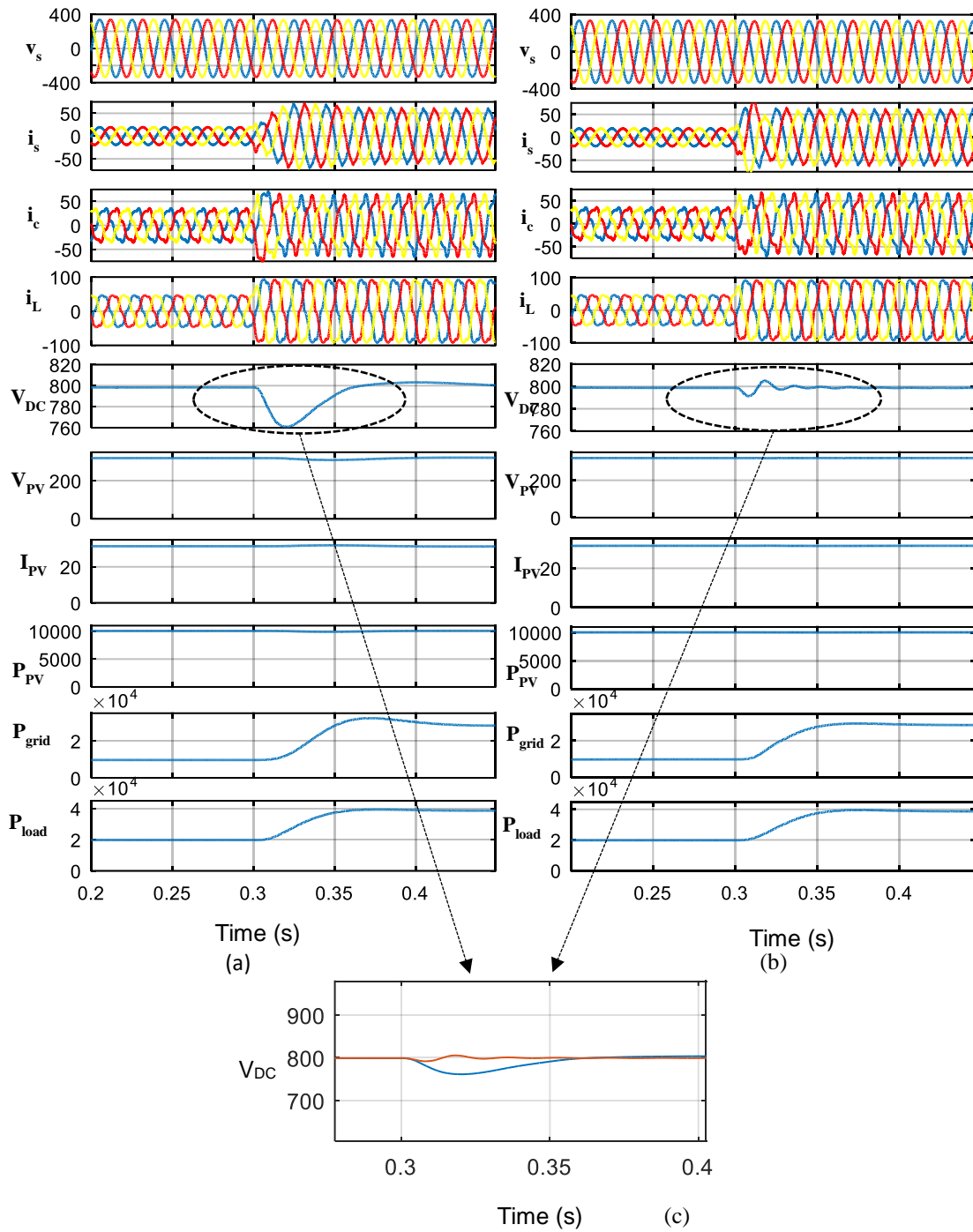
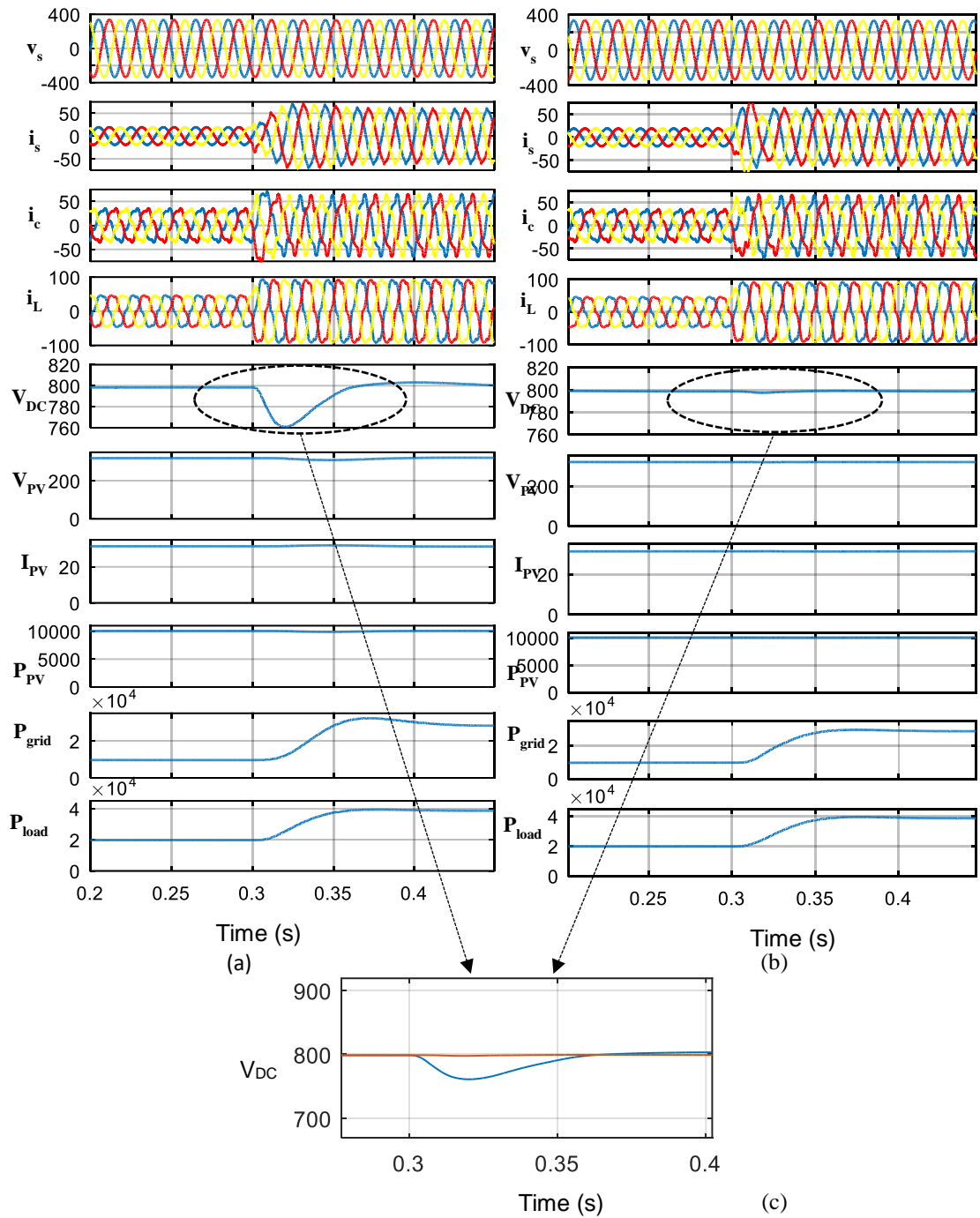


Figure 4.17. Comparison of AFL based intelligent control algorithm with SRF theory based conventional control algorithm for transient condition of sudden load change



**Figure 4.18. Comparison of feedforward-feedback adaptive control algorithm with SRF theory based conventional control algorithm for transient condition of sudden load change**

Figure 4.19 shows the comparison of the DC link voltage variation for the conventional and proposed intelligent and adaptive control algorithms under the transient condition of sudden load change. It can be seen that the feedforward-feedback adaptive control

algorithm has almost constant DC link voltage with negligible settling time, undershoot and overshoots. It can be seen that both the proposed algorithms has better response as compared to the conventional algorithm. The response of proposed feedforward-feedback adaptive algorithm is found to be the best.

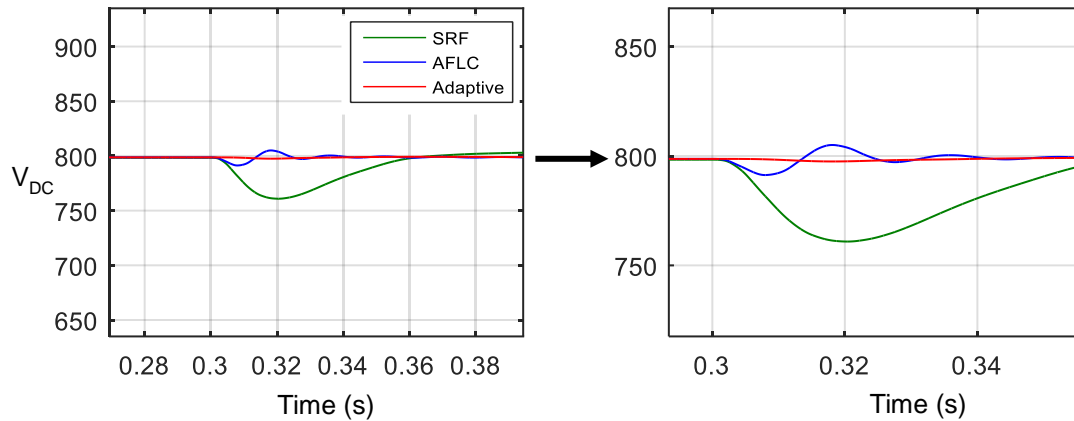


**Figure 4.19. Comparison of the conventional, intelligent and adaptive control algorithm for transient condition of sudden load change**

#### 4.5. CONCLUDING REMARKS

In this chapter, the interfacing control algorithms for multifunctional, two-stage, three-phase PV based microgrid are developed. The simulation studies for the system considered have been carried out using these developed algorithms. The developed control algorithms maintains the power balance and also enable additional functions of active filtering, VAR generation, load balancing and power factor correction. The performance of the developed algorithms have been found satisfactory under different dynamic and steady-state operating conditions. The THD of grid currents is less than 5% (within IEEE-519 standard) even with nonlinear loads. A wide range of simulation results has been shown to demonstrate all the features and to prove the feasibility of the control approaches. Lastly, a comparative study has been presented to validate the superiority of the proposed algorithms.

# **CHAPTER-V**

## **PV BASED MICROGRID: ISLANDING STUDIES**

### **INTRODUCTION**

The modelling, design and control of PV based microgrid are studied in the previous chapters. The PV based microgrid needs to be integrated with the utility grid for effective utilization. This necessitates that the technical requirements of the utility side have to be satisfied for ensuring the safety of the operators and the reliability of the utility grid. The technical specifications and requirements of grid interconnection are response to area power system abnormality, meeting power quality, fast detection of islanding condition, etc. Islanding detection is one of the important technical requirement for grid interconnection of microgrid and requires the attention of the designers for widespread application of PV based microgrid. This chapter deals with the study of islanding detection methods for PV inverters in a grid-tied microgrid. A novel islanding detection algorithm based on the analysis of negative sequence components of the voltage at the PCC, using Wavelet Packet Transform (WPT) has been developed. This algorithm has been integrated with the binary tree classifier for decision-making mechanism. The proposed islanding detection algorithm is tested using MATLAB-Simulink and Sim-Power System toolbox by carrying out simulation studies.

### **5.2. ISLANDING**

Traditionally, the power distribution systems are configured in radial structures. Power and short-circuit currents have unidirectional flow from distribution substations to loads. Most protection, monitoring, and control devices are designed based on this

---

This chapter is based on the papers - (i) "A New Algorithm for Islanding Detection in PV Generator Networks Connected to Low-Voltage Grid," IET Generation, Transmission and Distribution, February 2018, DOI: 10.1049/iet-gtd.2017.1735. (ii) "IED with advanced islanding detection functionality for PV based Microgrid," Proceedings of 5th International Conference on "Computing for Sustainable Global Development", 14th - 16th March 2018, Bharati Vidyapeeth's Institute of Computer Applications and Management (BVICAM), New Delhi (INDIA).

configuration. Recently, RES based microgrid, with bi-directional flow of power, have begun to emerge in the energy market as they provide economic and environmental incentives. However, due to the existing traditional distribution infrastructure and the energy market structure, there are regulatory and technical requirements barring these microgrid from entering the current energy market. Among the technical requirements, some have to be coordinated by the utility system operator, such as voltage regulation, integration with area EPS grounding, etc. Other technical requirements such as low harmonics mitigation, anti-islanding, etc. can be designed at the interconnection interface. This requires that the grid-interfacing inverter control, along with power quality control, must also have an islanding detection feature in it.

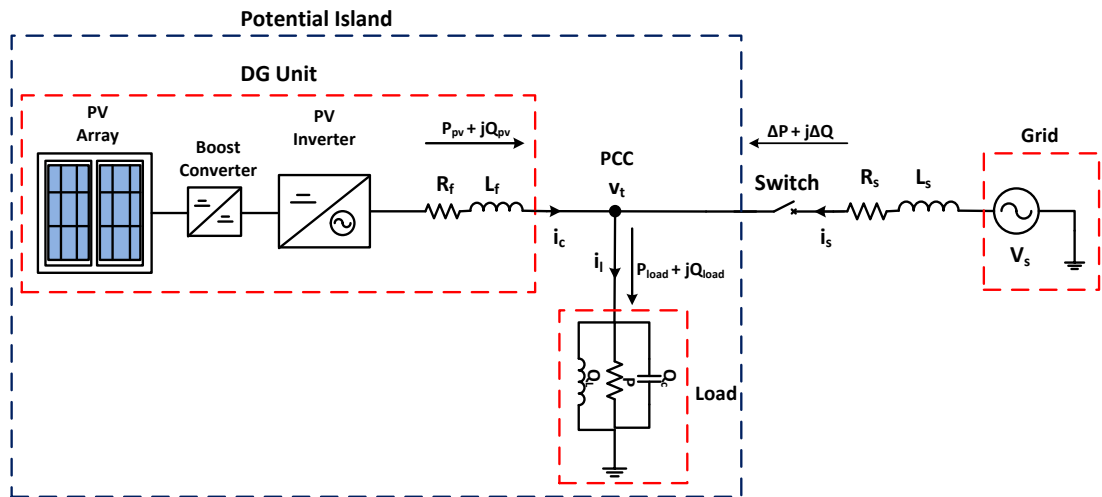
Islanding is a condition in which a portion of the utility system that contains both load and distributed resources remains energized even though they are isolated from the remainder of the utility system [16]. The islanding can be intentional or unintentional. IEEE defines both intentional and unintentional islanding. Intentional islanding may be desirable in some cases, such as in a microgrid designed to run independently during a weather event or unforeseen outage. Unintentional islanding (simply called islanding in this work) is not planned and is considered undesirable as under this condition, grid does not have any control over the voltage and frequency of the islanded area. This may result in excursion of voltage and/or frequency causing power-quality issues, damage to customer's equipment and even personnel safety hazards. Islanding, therefore, must be detected at the earliest, and the DG unit in the islanded area must be disconnected from the rest of the system as soon as possible by shutting down the interfacing inverter.

The IEEE 1547 [15] and IEEE 929-2000 [16], and the UL-1741 [17] are the prominent and the most referenced standards followed across the globe for the interconnection of the microgrid to the grid. The IEEE STD 929-2000 demand the use of an islanding detection feature by PV inverters in a grid-tied microgrid. The standard also suggests test setup and procedures and set the limits for the grid parameters, as shown in table 5.1. As per IEEE STD 929-2000, the voltage and frequency limits are divided into ranges and the trip time for each range is defined. Voltages are in root-mean-square (RMS) values and measured at the PCC and 'trip time' refers to the time between the abnormal condition being applied and the inverter ceasing to energize the utility line.

**Table 5.1. Inverter response to abnormal voltage and frequency disturbance [16]**

Parameter	Limits	Maximum trip time
Voltage	$V < 60$	6 cycles
	$60 \leq V \leq 106$	120 cycles
	$106 \leq V \leq 132$	Normal Operation
	$132 \leq V \leq 165$	120 cycles
	$165 \leq V$	2 cycles
Frequency	59.3-60.5 Hz	Normal operation
	Otherwise	6 cycles

Figure 5.1 shows the schematic diagram of IEEE Std 929-2000 based test setup used for present islanding studies. It consists of the DG unit, represented by Solar PV array, a PV inverter, and a series filter represented by  $R_f$  and  $L_f$  for each phase.


**Figure 5.1. Schematic diagram of IEEE Std 929-2000 based test setup for islanding detection in PV based microgrid**

According to IEEE Std 929-2000, the local load at PCC is RL load with a capacitor reactive power compensation, tuned at the resonance frequency of  $50 \pm 0.1$  Hz, having a quality factor of 2.5. At 50 Hz, the local load appears as a pure resistance,  $R_L$ , which is adjusted to absorb the rated power of the DG unit at the rated PCC voltage. The impedance and the quality factor,  $Q_f$  are expressed as follows,

$$|Z| = \frac{1}{\sqrt{\frac{1}{R_L^2} + \left(\frac{1}{\omega L_L} - \omega C_L\right)^2}} = \frac{R_L}{\sqrt{1 + Q_f^2 \left(\frac{f_0}{f} - \frac{f}{f_0}\right)^2}} \quad (5.1)$$

$$Q_f = R_L \sqrt{\frac{C_L}{L_L}} \quad (5.2)$$

Where  $f$  is the grid frequency and  $f_0$  is the resonance frequency of local RLC load of DG system. In this study, the DG is considered to be operating at unity power factor mode. The relationship between the system powers can be given as,

$$\Delta P = P_{grid} = P_{load} - P_{pv} \quad (5.3)$$

$$\Delta Q = Q_{grid} = Q_{load} - Q_{pv} \quad (5.4)$$

where  $\Delta P$ ,  $\Delta Q$  represent the mismatched power and is supplied by the grid.

If the switch is closed, the system is operating the under grid-tied mode with local load  $P_{load}$  and  $Q_{load}$  supplied from the DG ( $P_{pv}$ ,  $Q_{pv}$ ) and the grid ( $\Delta P$ ,  $\Delta Q$ ). On the other hand, when the switch gets opened, utility grid is disconnected, and the DG unit along with the RLC load forms a potential islanded zone, leading to unsafe operating conditions which could cause major power quality problems.

A PV inverter in a grid-tied microgrid should sense utility conditions and cease to energize the loads when the sensed voltage or frequency lies outside the values stated in table 5.1, i.e. when the potential for a distributed resource island exists.

### 5.3. BASIC ISLANDING DETECTION TECHNIQUES

Islanding detection techniques help to detect the islanding conditions and signals the inverter to cease energizing the loads. They are broadly classified into two groups [107, 108]:

- (i) Remote islanding detection techniques, and
- (ii) Local islanding detection techniques.

#### 5.3.1. Remote islanding detection techniques

Remote islanding detection techniques are based on the principle of communication between DERs and utility. Once islanding occurs, a trip signal is sent to the DER. Remote islanding detection techniques consist of power line carrier communication scheme, transfer trip scheme, etc. The advantages of remote islanding detection

techniques are zero non-detection zone (NDZ), faster response time, no impact on power quality, and effective application in multiple DG systems. However, remote techniques are very expensive for implementation on small-scale systems.

### **Power Line Carrier Communications**

The information of the islanding is carried on the power lines in case of power line carrier communications method. This method includes a signal generator at substation and signal detector equipped at DG. Signal generator continuously broadcast a signal which is received by DG under normal operating conditions. In case of islanding, the transmitted signal is cut off due to substation breaker opening and DG is not able to receive the signal.

### **Transfer Trip**

Transfer trip detection schemes require all circuit breakers which island the DG to be monitored and linked directly to the DG control or through a central substation SCADA system. When a disconnection is detected at the substation, the transfer trip system determines which areas are islanded and sends the appropriate signal to the DGs, to either remain in operation or to discontinue operation.

## **5.3.2. Local islanding detection techniques**

Local detection techniques are based on measurement of the variations in system parameters like voltage, frequency, impedance, phase angle, active power, reactive power, and harmonic distortion. These techniques are further classified into passive and active islanding detection methods.

### **5.3.2.1. Passive islanding detection methods**

Passive islanding detection methods monitor the system parameters, such as voltage, frequency, and harmonics at the PCC, and compare it with a pre-set threshold value for distinguishing between islanding and non-islanding events. The advantages of passive detection methods are fast detection speed, no impact on power quality and cost-effectiveness. Various passive detection methods are the over/under voltage and over/under frequency, the rate of change of frequency, rate of change of voltage,



voltage unbalance, harmonic distortion (voltage and current), etc. [117-123].

### **Over/Under Voltage and Over/Under Frequency**

All the PV inverter in a grid-tied microgrid are required to have over/under voltage protection (OVP/UVP) and over/under frequency protection (OFP/UFP) which ceases the supply to the loads if the frequency or amplitude of the voltage at the PCC varies outside of prescribed limits. The behaviour of the system at the time of utility disconnection will depend on  $\Delta P$  and  $\Delta Q$  at the instant before the switch opens to form the island. The voltage at PCC changes if  $\Delta P \neq 0$  and the OVP/UVP can detect the change while if  $\Delta Q \neq 0$ , the frequency of the voltage will change which can be detected by the OFP/UFP.

### **Rate of Change methods**

These methods include the measurement of the rate of change of frequency (ROCOF), rate of change of voltage, rate of change of power, or a combination of more than one of these methods. If the active and reactive power mismatch is small, there is only a small variation in the magnitude of voltage and frequency at PCC and therefore the islanding condition may not be accurately detected. To overcome this limitation, the rate of change in voltage  $\left(\frac{\partial v}{\partial t}\right)$  or  $\left(\frac{\partial f}{\partial t}\right)$  is used as an index of islanding instead of  $\Delta v$  or  $\Delta f$  respectively. PV inverter will cease to operate if rate of change of these quantities exceeds the specified threshold.

### **Detection of Voltage and/or Current Harmonics**

In this method, PV inverter monitors the total harmonic distortion (THD) of the voltage and/or current and shuts down if this THD exceeds the set threshold. Under normal operating conditions the THD remains less than the threshold values. When an island occurs, PV inverter will produce some current harmonics in its AC output current. Utility disconnection leads to flow of harmonic currents into the load, which generally has much higher impedance than the utility. The harmonic currents interacting with the larger load impedance will produce larger harmonics in voltage. These change in the level of voltage and/ or current harmonics can be detected by the inverter, leading to shut down of PV inverter.

### 5.3.2.2. Active islanding detection methods

In active islanding detection methods, perturbations are induced in either amplitude, frequency or phase of the inverter current or voltage and the detection methods depends on the response of the system to these perturbations. Under normal steady-state conditions, the effect of these perturbations experienced at PCC is very small. But once the microgrid is islanded the impact of these perturbations experienced at PCC is quite large. The advantages of active detection methods are reduced NDZ and a decrease in the detection rate error. Some of the common active islanding detection methods are slip mode frequency shift method (SMS), active frequency drift (AFD), Sandia frequency shift (SFS), Sandia voltage shift (SVS), frequency jump (FJ), etc. [107-115].

#### Slip-mode Frequency Shift

SMS uses positive feedback control to destabilize the source inverter when an island condition occurs. The inverter uses positive feedback of the phase, 'a', to slip the frequency out-of-phase hence leading to the short-term frequency change. SMS is implemented by modifying the PLL filter to be naturally out of phase at the fundamental frequency. Under normal operating conditions without SMS, the PLL tracks phase and frequency changes of the network. With SMS, the strength of the utility source keeps the inverter in phase. However, if the frequency during an island is pushed upwards, due to the out of phase filter, the PLL will see a negative phase error and try to shift the frequency away from the fundamental. Due to the positive feedback, the phase shift will be in the wrong direction and instead of correcting the phase error, will increase it. The frequency eventually will fall out of acceptable limits and the frequency relay will open the breaker.

#### Active Frequency Drift

AFD distorts the frequency output to create a continuous trend to “drift” the frequency away from the fundamental. The method works by altering the frequency by slightly increasing the frequency of each 1/2 cycle followed by a “dead time” where the system waits for the fundamentals to catch up to the biased frequency. Similarly to Slip-Mode Frequency Shift, when the inverter is connected to the utility-fed network, the strong utility keeps the system frequency stable. However, when the network becomes

islanded, the distorted frequency causes the system to seek the system load's resonance frequency, resulting in the inverter eventually drifting up/ down causing the frequency relays to trip.

### **Sandia Frequency Shift and Sandia Voltage Shift**

SFS is an enhancement of the AFD islanding detection method which uses positive feedback. The positive feedback takes the error of the “dead zone,” as an error of the line frequency. When this system is connected to the utility, small frequency changes push the inverter out of the range of the line frequency, but the strength of the utility keeps the system stable. When the utility is disconnected, the errors detected in frequency increase and the dead zone increases. Similarly to SFS, SVS also uses a form of positive feedback to detect islanding. In this case, the inverter decreases its power output and thus its voltage. When the utility is connected, there is little to no change in the output terminal voltage, however when the utility is not connected, the voltage will drop with the reduction of power. The positive feedback control of the voltage reduction is further accelerated downwards until the under voltage protection relay trips.

### **Frequency Jump**

In frequency jump method, “dead zones” are added similarly to the AFD method, but not in every cycle. The frequency is broken into a predefined algorithm, with dead zones added every second or third cycle. When connected to the utility, the inverter only sees a modified current and an unmodified utility linked voltage. When in island state, the voltage and current change as per the inverter programmed wave shape. Therefore, the inverter can detect an island by the modified frequency, or by matching the voltage pattern to the inverter's algorithm.

## **5.4. LIMITATIONS OF LOCAL ISLANDING DETECTION TECHNIQUES**

Both active and passive local islanding detection methods suffer from their limitations [116]. Active islanding detection methods require additional controllers/power electronics equipment to inject perturbations in the power systems. This increases the complexity of the system and reduces the power quality. The injected signals cause waveform distortion, such as the one shown in figure 5.2, where  $v(t)$  is the inverter

output voltage and  $i(t)$  is the inverter output current. Also, additional detection time is required in order to observe the power system response on perturbations. Hence, the system's stability is significantly degraded.

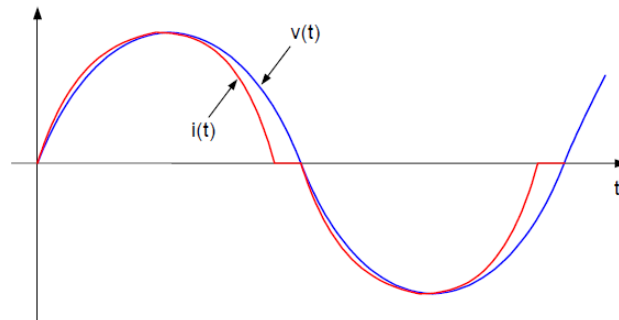


**Figure 5.2. Example of power quality degradation caused by active islanding detection methods**

A major problem with the passive islanding detection methods is that they suffer from large NDZ, and it is very difficult to detect islanding when the DG generated power and load demand in the islanded system are closely matched. Furthermore, the setting of threshold value for the detection involves special consideration as lower threshold setting results in nuisance tripping, and higher threshold setting results in detection failure which results in low detection rates.

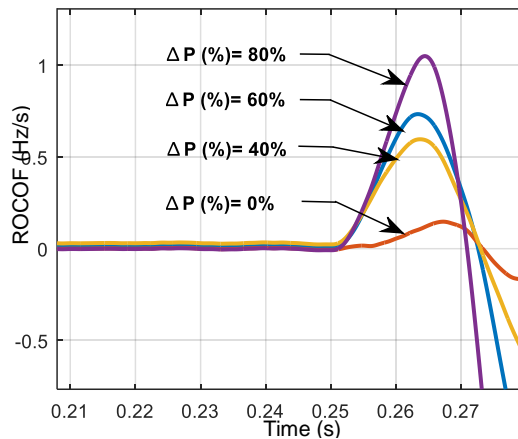


**Figure 5.3. Variation of ROCOF under varying active power mismatch for the designed system**

Figure 5.3 shows that in the performance of ROCOF relay for the designed system. It is observed that the passive actuator- rate of change of frequency (Hz/s) decreases when the active power mismatch decreases during islanding. Setting a threshold in the relay

above 0.5 Hz/s will fail to detect islanding when active power mismatch during islanding is less than 40%. Similar observations can be made with other existing passive islanding detection techniques.

The large NDZ drawback of passive techniques can be overcome by using modern signal processing techniques and the issue of threshold selection of passive techniques can be overcome by using intelligent classifiers along with signal processing techniques [124-136]. In the present work, a novel islanding detection algorithm based on signal processing techniques using intelligent classifiers is proposed.

**5.5. PROPOSED ALGORITHM FOR ISLANDING DETECTION**

Figure 5.4 shows the flowchart of the proposed islanding detection algorithm consisting of three major computational sections: signal extraction, feature extraction, and decision-making.

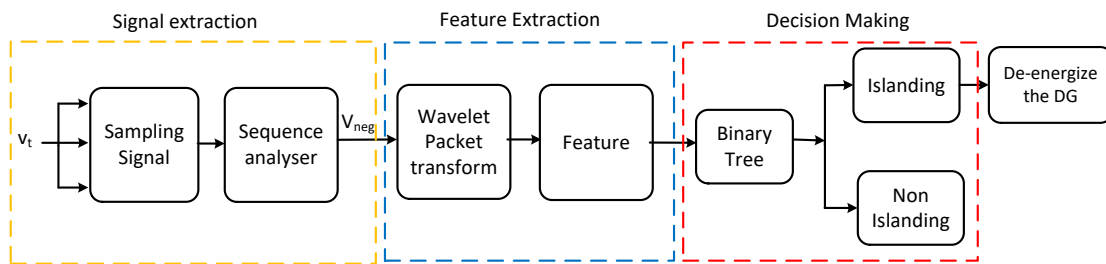


**Figure 5.4. Flowchart of the proposed islanding detection algorithm**

Signal extraction consists of extracting the negative sequence component of the PCC voltage ( $v_t$ ). The voltage signals are sampled, and the non-stationary signals are passed through the sequence analyser to extract the negative sequence voltage signal ( $V_{neg}$ ). The sampling frequency is 10 kHz. Once the  $V_{neg}$  signal components are obtained, they are passed on to the next section, i.e., the feature extraction section. In the present studies, WPT is used for signal processing to extract the desired features from the  $V_{neg}$  signal. Binary Tree classifier is then used in the decision-making section to study the extracted features and decide whether islanding phenomenon has occurred or not. Lastly, the algorithm thus developed sends the signal to inverter for de-energizing the connected DG if there is islanding condition.

### 5.5.1. Signal Extraction: Negative sequence voltage ( $V_{neg}$ ) extraction

Symmetrical components are a useful tool in monitoring and analysing power system disturbances. Positive sequence quantities make up the normal voltages and currents observed on power systems during steady-state conditions. Negative- and zero-sequence quantities, usually present in substantial levels only during unbalanced, faulted conditions on a power system, are used to determine faulted condition in a power system.

The negative sequence component of the voltage signal is extracted from the derived voltage signal at the PCC using the power invariant instantaneous symmetrical components transformation given by [127],

$$V_{neg} = \frac{1}{3} [v_{ta}(\cos\Phi_a + \sin\Phi_a) + \alpha^2 * v_{tb}(\cos\Phi_b + \sin\Phi_b) + \alpha * v_{tc}(\cos\Phi_c + \sin\Phi_c)] \quad (5.5)$$

where  $v_{ta}$ ,  $v_{tb}$ , and  $v_{tc}$  are the a-phase, b-phase, and c-phase, PCC voltage signals and  $\alpha$  is a complex operator defined as,

$$\alpha = e^{j2\pi/3} = 1\angle 120^\circ = -\frac{1}{2} + j\frac{\sqrt{3}}{2} \quad (5.6)$$

Negative sequence voltage magnitude ( $V_{neg}$ ) and voltage phase angle ( $\theta_{vneg}$ ), are evaluated as shown in figure 5.5.

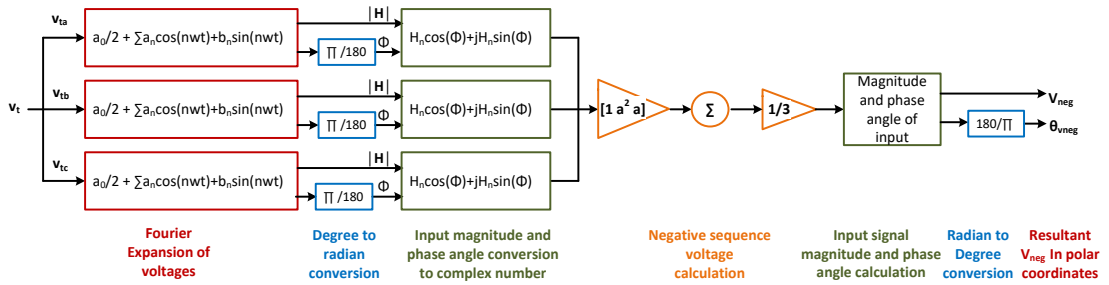


Figure 5.5. Scheme for extraction of negative sequence component of PCC voltage signal

### 5.5.2. Feature Extraction: Wavelet Packet Transform

The wavelet packet method is a type of wavelet decomposition that offers a more productive signal analysis. In the discrete wavelet transform (DWT) decomposition procedure, the generic step splits the approximation coefficients into two parts. After splitting, a vector of approximation coefficients and a vector of detail coefficients are

obtained. The information lost between two successive approximations is captured in the detail coefficients. In the next step, the approximation coefficient vector is further split; successive detail coefficients are never reanalyzed. In the corresponding WPT, each detail coefficient vector is also decomposed into two parts using the same approach as in approximation vector splitting. This offers the richest analysis: the complete wavelet tree is produced.

Figure 5.6 shows the structure diagram of three level and DWT and WPT tree for a 1-D input signal [128].  $\tilde{G}(f)$  is the scaling (low pass) analysis filter and  $\tilde{H}(f)$  represents the wavelet (high pass) analysis filter. The labels at the bottom show the partition of the frequency axis  $[0, 1/2]$  into subbands. The figure shows that subsequent levels of the DWT operate only on the outputs of the low pass (scaling) filter. In the critically-sampled DWT, the outputs of the bandpass filters are down sampled by two at each level.

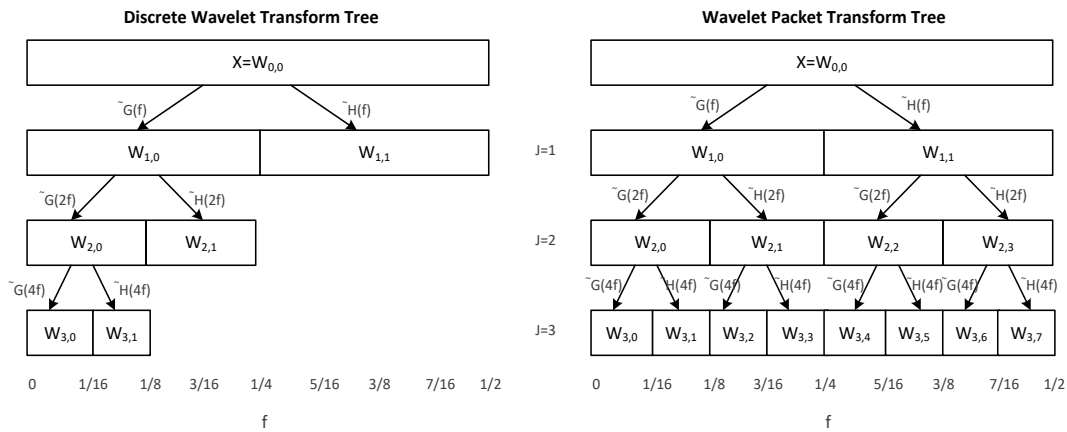


Figure 5.6. Structure diagram of three-level DWT and WPT

In the WPT, the filtering operations are also applied to the wavelet, approximation or detail, coefficients. The result is that wavelet packets provide a subband filtering of the input signal into progressively finer equal-width intervals. At each level,  $j$ , the frequency axis  $[0, 1/2]$  is divided into  $2^j$  subbands. The subbands in hertz at level  $j$  are approximately  $(\frac{nF_s}{2^{j+1}}, \frac{(n+1)F_s}{2^{j+1}})$   $n = 0, 1, \dots, 2^j - 1$  where  $F_s$  is the sampling frequency. Starting with the two filters of length  $2N$ , where  $h(n)$  and  $g(n)$ , correspond to the wavelet. The output of the two filters i.e., high pass and low pass filter constitutes one level of decomposition of the discrete signal. It can be mathematically expressed as,

$$W_n(x), n = 0, 1, 2 \dots \tag{5.7}$$

By

$$W_{2n}(x), n = \sqrt{2} \sum_{k=0}^{2N-1} h(k)W_n(2x - k) \tag{5.8}$$

$$W_{2n+1}(x), n = \sqrt{2} \sum_{k=0}^{2N-1} g(k)W_n(2x - k) \tag{5.9}$$

where  $W_0(x) = \varphi(x)$  is the scaling function and  $W_1(x) = \psi(x)$  is the wavelet function. The WPT shares the valuable energy-preserving property of the DWT while providing superior frequency resolution. Thus, WPT results in equal-width subband filtering of signals as opposed to the coarser octave band filtering found in the DWT [128, 129].

Selection of an appropriate mother wavelet has a vital role in the analysis. Daubechies wavelet family is one of the most suitable wavelet families in analyzing power system transients and islanding detection [126, 133]. In the proposed study, the negative sequence component of the PCC voltage signal is decomposed by WPT which chooses Daubechies 4 (db4), and the layer of decomposition is 3 [133]. Therefore, the negative sequence component of the PCC voltage signal is decomposed into eight frequency bands. Table 5.2 shows the frequency bands of each decomposed level.

**Table 5.2. Frequency band of each decomposed level**

WPD Level	Frequency band (Hz)
1	0-2500, 2500-5000
2	0-625, 625-1250, 1250-2500, 2500-5000
3	0-39.0625, 39.0625-78.125, 78.125-156.25, 156.25-312.5, 312.5-625, 625-1250, 1250-2500, 2500-5000

### 5.5.3. Decision Making: Binary Tree Classifier

Binary tree classifier predicts responses to data in the form of a tree structure. It breaks down a dataset into smaller and smaller subsets while at the same time an associated binary tree is incrementally developed. The final result is a tree with decision nodes and leaf nodes. A decision node has two or more branches. Leaf node represents a classification or decision. The topmost decision node in a tree which corresponds to the best predictor called root node. The depth of a node is the length of the path from the root to the node. In a binary tree for each node  $m$ ,  $N_m$  instances reach  $m$  and  $N_m^i$  of them



belong to  $C_i$  represented by [133],

$$P(C_i | X, m) \equiv p_m^i = \frac{N_m^i}{N_m} \quad (5.10)$$

Node  $m$  is pure if  $p_m^i$  is 0 or 1. If node  $m$  is pure, generate a leaf and stop, otherwise split and continue recursively. The measure of impurity is entropy. The C4.5 algorithm [169] uses the concept of information gain or entropy reduction. Variable  $X$  whose  $k$  possible values have probabilities to  $p_1, p_2 \dots p_k$ . Entropy of variable  $X$  is

$$H(X) = -\sum_j p_j \log_2 p_j \quad (5.11)$$

Candidate split the gain ( $S_g$ ), which partitions training set  $T$  into several subsets,  $T_1, T_2 \dots T_k$ .

$$H_s(T) = \sum_{i=1}^k P_i H_s(T_i) \quad (5.12)$$

Information gain for variable  $S_g$  is  $Gain(S_g) = H(T) - H_s(T)$ . At each decision node, C4.5 chooses the optimal split to be the split that has the greatest information gain,  $Gain(S_g)$ .

## 5.6. RESULTS AND DISCUSSIONS

A two-stage three-phase grid-tied PV based microgrid as shown in figure 5.1 has been simulated to verify the viability of the proposed algorithm. The main parameters used in the simulation are listed in Appendix- B. Four case studies have been considered to prove the effectiveness of the proposed algorithm,

*Case A:* Islanding of PV based microgrid with active power mismatch of 40%

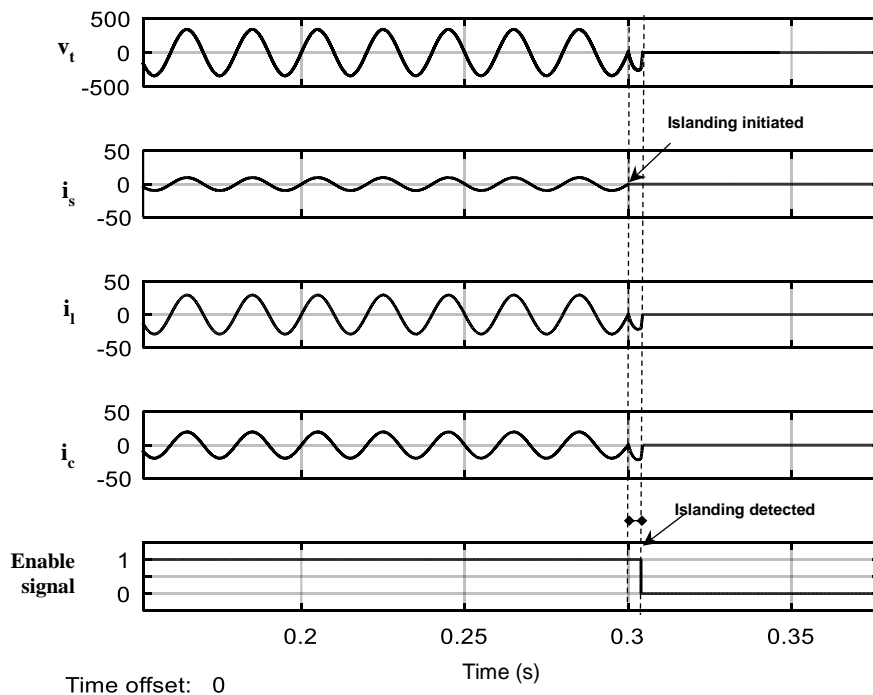
*Case B:* Islanding of PV based microgrid with active power mismatch of 0%

*Case C:* Sudden load change at PCC

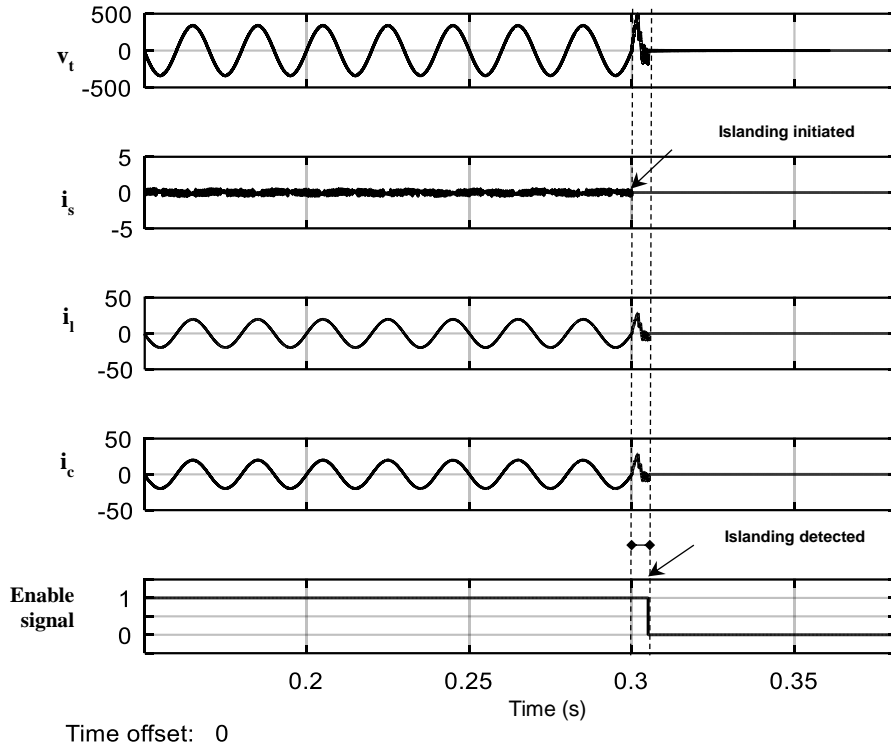
*Case D:* Grid side distortions

Figure 5.7-5.10 shows the simulation results for different cases considered for the studies with the waveforms of the voltage at PCC ( $v_t$ ), grid current ( $i_s$ ), load current ( $i_l$ ), inverter current ( $i_c$ ), and DG enable signal.

Figure 5.7 and 5.8 shows the simulation results for the first two cases i.e. islanding of PV based microgrid with active power mismatch of 40% and 0% respectively. The switch is opened at 0.3 s, and the DG unit along with load is isolated from the grid, and the islanding is initiated. It can be seen that for the first two cases considered in figure 5.7 and 5.8, islanding is successfully detected with a run on the time of approximately 5 ms. In figure 5.8, before the islanding happens, the grid current is close to zero because the inverter’s active power is matched with the active power consumption of the load. It can be seen that grid current becomes zero and there are distortions in PCC voltage as soon as islanding occurs. Therefore, the DG enable signal which was set to ‘1’ (for normal operation) is forced to ‘0’ once islanding is detected within 5 ms even with 0% mismatch. Thus, the proposed algorithm is able to detect the islanding condition and disconnect the DG unit from the rest of the system by shutting down the PV inverter successfully.



**Figure 5.7. Simulation results for Islanding of PV based microgrid with active power mismatch of 40%**



**Figure 5.8. Simulation results for Islanding of PV based microgrid with active power mismatch of 0%**

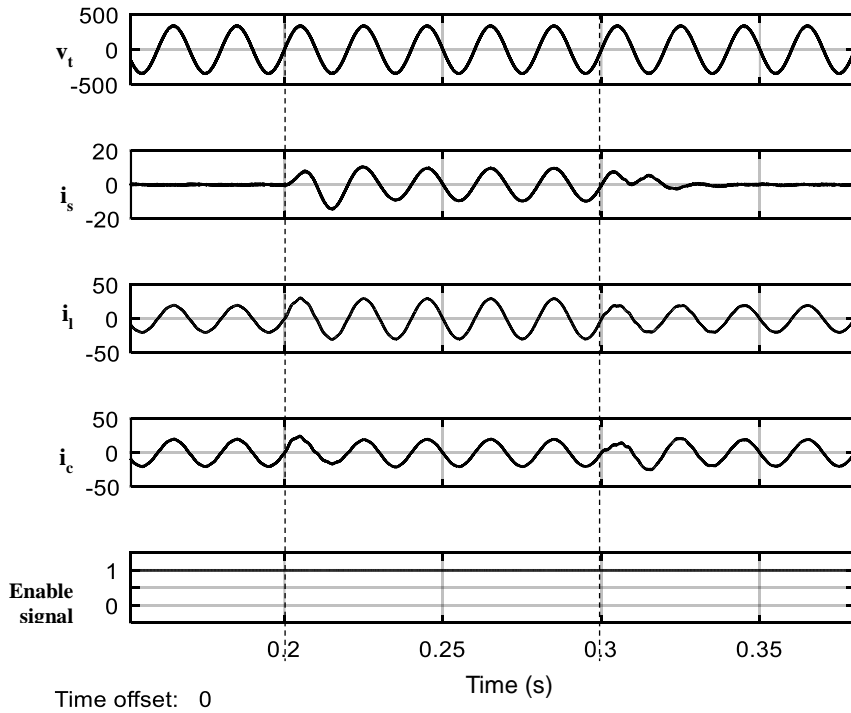


**Figure 5.9. Simulation results for sudden load change at PCC**

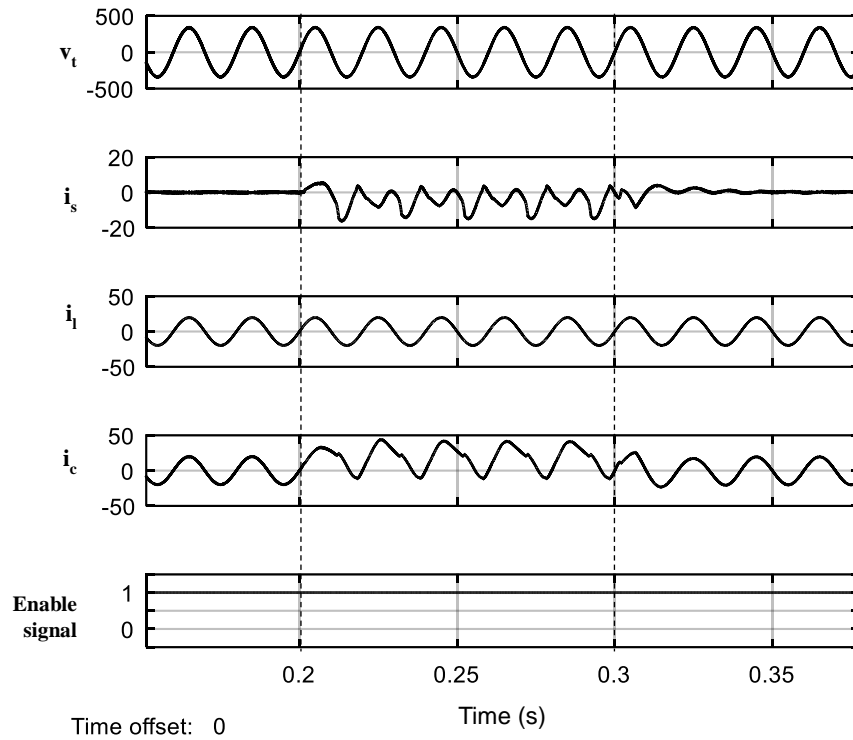


**Figure 5.10. Simulation results for grid side distortions**

The proposed islanding detection method is also tested for non-islanding cases of sudden load change and grid side distortions in the grid-tied operation mode. Figure 5.9 and 5.10 shows the simulation results for the last two cases i.e. sudden load change at PCC and grid side distortions respectively. In figure 5.9, the load is changed at 0.2 seconds and respective changes in the load, grid, and inverter current can be seen. Similarly, in figure 5.10, harmonics are injected in the grid side currents at 0.2 seconds and its effect is noted on the other waveforms. It can be seen from the simulation results that the proposed method accurately identified sudden load change and grid voltage distortion as non-islanding cases, and responded by maintaining its DG enable signal high. Hence, it is demonstrated that the proposed method can correctly recognize these events as non-islanding conditions, which allows the system to continue operating normally.

The performance of islanding detection methods is evaluated by NDZ and run-on time. NDZ is the region under which an anti-islanding technique fails to detect islanding condition, and run-on time is the time difference between the instant at which the

islanding occurs and the islanding is detected. To assess the NDZ region, the performance of the proposed method is investigated concerning active and reactive power mismatches ranging from  $-40\%$  to  $40\%$  during the islanding. The results are presented in the three-dimensional surface graph, as shown in figure 5.11, representing the active power imbalance ( $\% \Delta P$ ), reactive power imbalance ( $\% \Delta Q$ ), and detection time (ms) on the x-, y-, and z-axes of the graph, respectively. It can be seen that the proposed method shows a consistent detection time of 5 ms even in the regions of minimum active and reactive power mismatch. The plateau on the plot represents the NDZ of methods in the PQ plane which shows that the proposed algorithm has a zero NDZ.

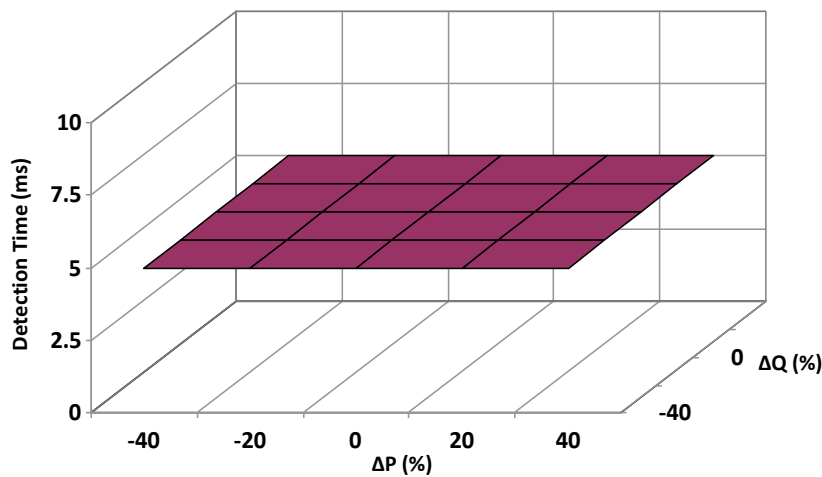


**Figure 5.11. Results for the variation of islanding detection time of proposed algorithm under varying active and reactive power conditions**

Figure 5.12 shows the comparison of the run on time of the proposed method and another passive detection method- ROCOF for active power mismatch. ROCOF shows an inverse relationship between the active power mismatch and detection time. On the other hand, the proposed method shows a constant run on time for different ranges of the active power mismatch. The proposed algorithm can detect islanding even near 0% active power mismatch conditions showing almost negligible NDZ and also the proposed method is faster than existing passive detection methods with having run on the time of 5 ms.

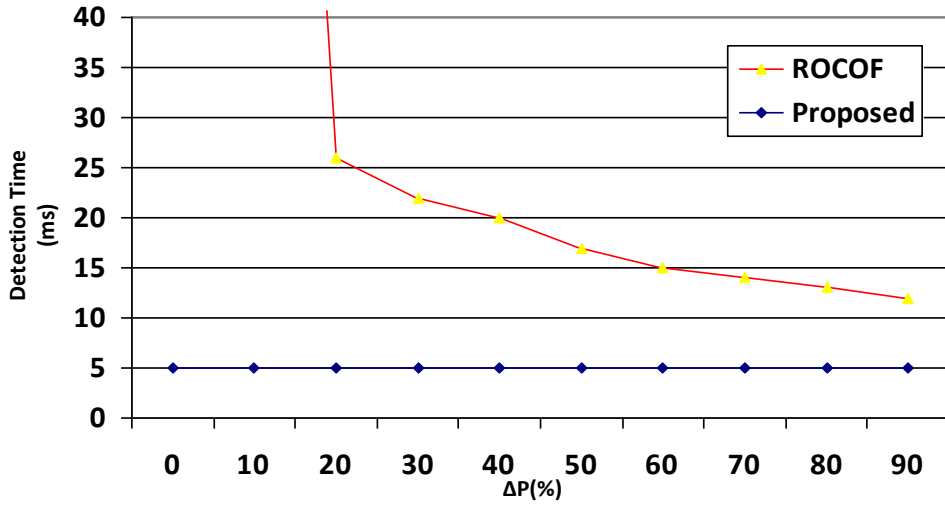


Figure 5.12. Comparison of islanding detection time of the proposed and ROCOF method

**5.7. CONCLUDING REMARKS**

A novel passive islanding detection algorithm is developed in this chapter. The developed algorithm is based on WPT for processing the negative sequence voltage signals at PCC to extract the signal information. Further, binary tree classification has been used to detect and classify an islanding condition for grid-tied PV microgrid. This passive approach for detecting the islanding condition has been found to be fast, independent of load power demands, and has negligible effects on the power quality. The simulation results indicate that the proposed scheme is capable of detecting islanding events even under the worst-case scenario, where the inverter output power is nearly equal to the local load consumption. The proposed method provides the reduction of the NDZ close to zero. The run on time is also reduced to nearly 5 milliseconds. The simulation results show that the proposed method can have accurate discrimination between islanding and non-islanding events.

# **CHAPTER-VI**

## **MULTI-TERMINAL DC NANOGRID: DESIGN, DEVELOPMENT, AND IMPLEMENTATION**

### **INTRODUCTION**

A DC nanogrid is an evolutionary concept derived from the development of material science and power electronics. Here, the power distribution system is built around DC instead of the conventional AC system. A DC nanogrid for the residential and commercial purpose can supply both AC and DC output voltages, using converter/inverter, at different utilization levels to meet the load requirements. Multiple converter poses many problems like coordination of power flow amongst various converters, increased size of the system, more components, etc. A DC nanogrid with multi-terminal converters can overcome these problem. A multi-terminal nanogrid can be designed in MISO (Multiple-Input Single-Output), SIMO (Single-Input Multiple-Output), and MIMO (Multiple-Input Multiple-Output) configurations. In this chapter, design, development and implementation of PV based multi-terminal DC nanogrid using innovative dual-input single-output (type of MISO) and single-input dual-output (type of SIMO) voltage converter configurations has been presented. The developed converter configurations are investigated in detail using MATLAB along with Simulink toolbox. The configurations of SIDO converters are experimentally validated using a 100W prototype, built and tested in the laboratory for practical applications. Further, the performance characterization studies of these converters such as sensitivity and reliability analysis are carried out. Markov reliability models are developed to estimate the mean time to system failure, using military handbook for reliability prediction of electronic equipment (MIL-HDBK-217F).

---

This chapter is based on the paper - (i) Design, Development and Reliability Assessment of Dual Output Converters for PV based DC Nanogrid. *Journal of Renewable and Sustainable Energy*. Volume 10, Issue 2, March 2018. DOI: 10.1063/1.5009570.

**6.2. DC NANOGRID**

A nanogrid is a set of electricity generators and energy storage systems that supply electricity to a localized group of customers like a building while being in isolation from the main grid. These systems have the potential to provide electricity to the people who are without access to electrical connectivity due to geographical constraints or where the costs for grid extension is very high. Nanogrids consisting of diesel and gasoline generators are being used worldwide for a very long time. However, with depletion of fossil fuels, increased environmental concerns, and technological advancement in the green energy system, the RES has emerged as an alternate solution that is cheaper, cleaner, and efficient source of energy. So, nowadays RES based nanogrid are being preferred over diesel or gasoline based nanogrid.

RES like PV, fuel cells, etc. are inherently DC in nature. Further, more and more loads show DC characteristics, for example, LED lightings, computer power supplies, and variable-frequency techniques based household electrical appliances. DC nanogrid are thus, emerging as an attractive solution to locally utilize DC electricity with minimum distribution and conversion losses. Figure 6.1 shows the schematic diagram of a functional DC nanogrid consisting of multiple dedicated converters at source as well as load end [24].

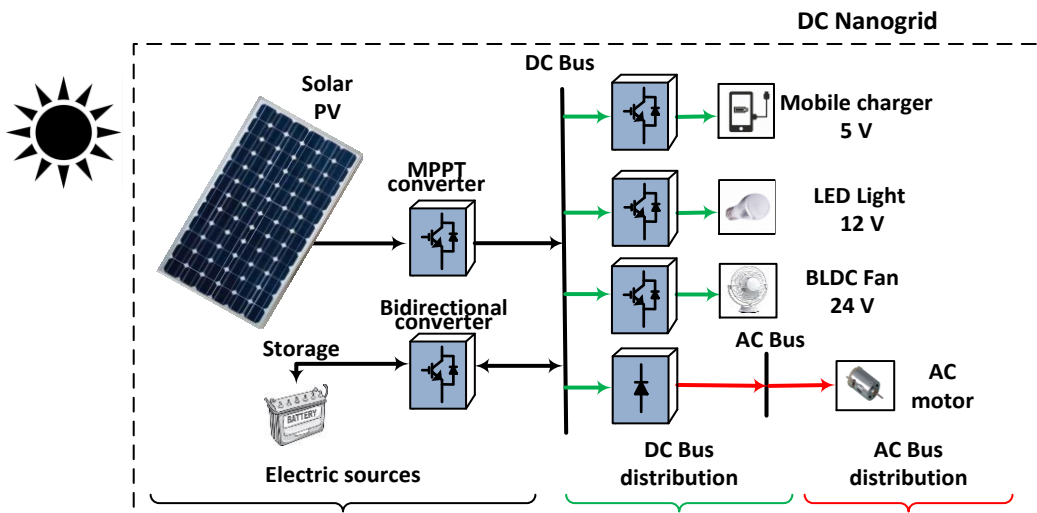


Figure 6.1. Schematic diagram of a DC Nanogrid

Multiple dedicated converters exhibit the problem of power flow coordination, low efficiency, higher component count, and increased size of the system. On the other



hand, multi-terminal converters have been able to provide an integrated architecture with higher efficiency and compactness [145-158]. The multiple-input single-output converters are used in applications where the same load has to be supplied from multiple sources, e.g., in hybrid vehicles, renewable power systems, etc. Similarly, single-input multiple-output converters are used in applications where loads with different voltage requirements have to be supplied from a single source, e.g., household loads like LED bulbs, BLDC drives, etc. The following section presents dual-input single-output (DISO) and single-input dual-output (SIDO) voltage converters proposed for PV based DC nanogrid.

### 6.3. DUAL-INPUT SINGLE-OUTPUT CONVERTERS

Figure 6.2 presents two configurations of DISO converters for PV based DC nanogrid [170, 171].

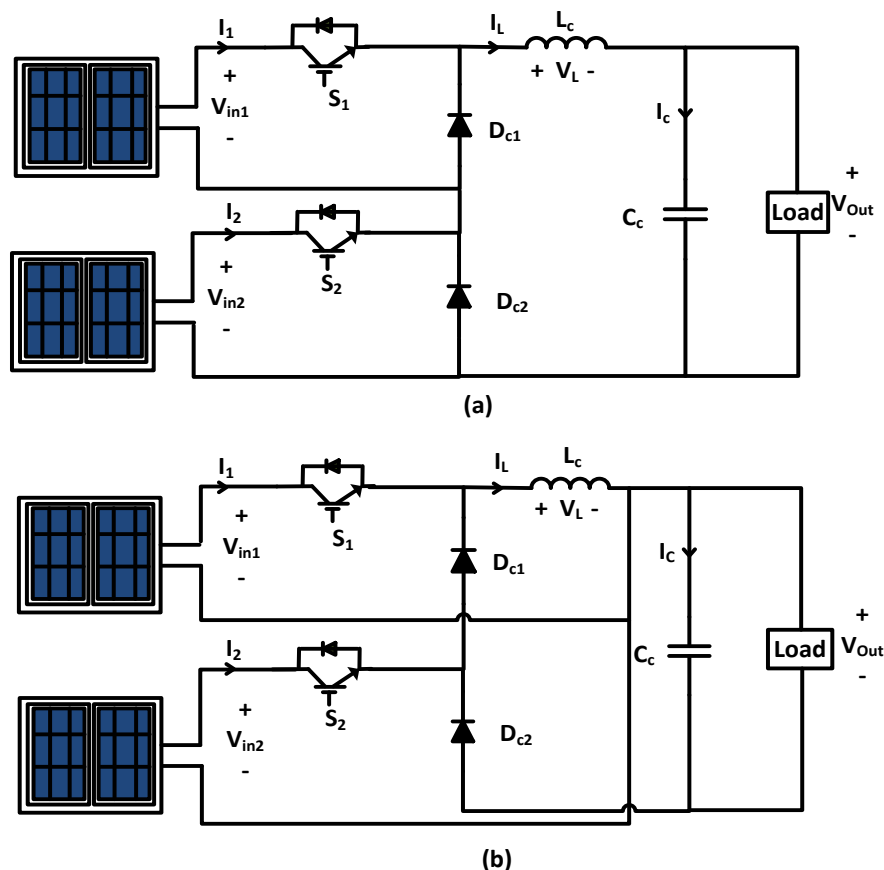


Figure 6.2. Circuit diagram of (a) DISO buck-buck DC converter, and (b) DISO buckboost-buckboost DC converter

These configurations are obtained by extending the concept of two buck converters as shown in figure 6.2(a), and two buck-boost converters as shown in figure 6.2(b) respectively. The following sub-sections explain the design, development and characterization studies of the two configurations of DISO converters.

### 6.3.1. DISO buck-buck DC converter

Figure 6.2 (a) shows the circuit diagram of the DISO buck-buck DC converter. Input voltages ( $V_{in1}$  and  $V_{in2}$ ) are the PV system fed DC bus voltages. The converter is composed of two switches  $S_1$  and  $S_2$ , inductors  $L_c$ , capacitor  $C_c$  and two diodes  $D_{c1}$  and  $D_{c2}$ . PWM signals are used for controlling the switches  $S_1$  and  $S_2$  and they can be derived either from both the inputs individually or simultaneously.

#### 6.3.1.1. Control Algorithm

The control algorithm of the DISO buck-buck DC converter consists of four main intervals of operation in a switching cycle as explained in table 6.1. Duty cycles of the two switches  $S_1$  and  $S_2$  are  $D_1$  and  $D_2$  respectively given by,

$$T_1 + T_2 = D_1 T \tag{6.1}$$

$$T_2 + T_3 = D_2 T \tag{6.2}$$

**Table 6.1 Switch status and voltage across inductor for DISO buck-buck DC converter during different intervals of time**

Interval	Switch Status	Voltage across L ( $V_L$ )	Action
<b>Interval I</b> Time Duration- $T_1$	$S_1$ - ON $S_2$ - OFF	$V_{in1} - V_{out}$	$V_{in1}$ supplies energy
<b>Interval IV</b> Time duration- $T_2$	$S_1$ - ON $S_2$ - ON	$V_{in1} + V_{in2} - V_{out}$	$V_{in1}$ and $V_{in2}$ supplies energy
<b>Interval II</b> Time duration - $T_3$	$S_1$ - OFF $S_2$ - ON	$V_{in2} - V_{out}$	$V_{in2}$ supplies energy
<b>Interval III</b> Time duration- $T_4$	$S_1$ - OFF $S_2$ - OFF	$-V_{out}$	Energy depletion of the inductor

Key waveforms of the DISO buck-buck DC converter are shown in timing diagram of figure 6.3. The operational circuit during different intervals is also shown. The two PWM gate signals,  $GS_1$  and  $GS_2$  are used to control the given converter.  $V_L$  and  $I_L$  are the voltage and current through the inductor respectively, and  $I_1$  and  $I_2$  are the two input currents from the two DC sources.

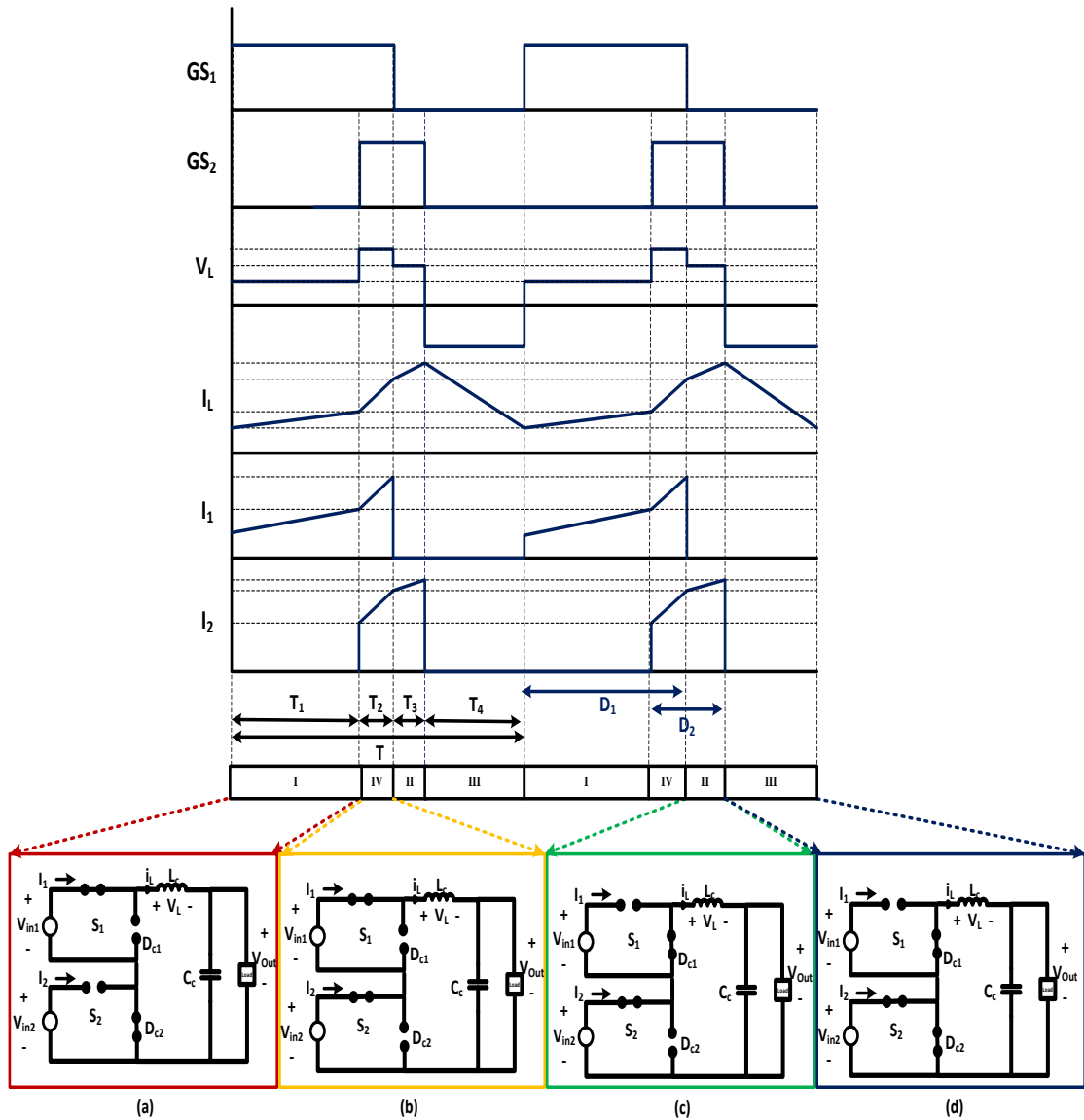


Figure 6.3. Timing diagram of DISO buck-buck DC converter along with operational circuit during (a) Interval-I, (b) Interval-II, (c) Interval-III and (d) Interval-IV

The input-output voltage relationship can be derived from the steady-state volt-second balance analysis [33, 34] of the inductor,  $L_c$ , given by,

$$T_1 + T_2 + T_3 + T_4 = T \quad (6.3)$$

$$T_1(V_{in1} - V_{out}) + T_2(V_{in1} + V_{in2} - V_{out}) + T_3(V_{in2} - V_{out}) + T_4(-V_{out}) = 0 \quad (6.4)$$

The output voltage expression can be obtained as,

$$V_{out} = V_{in1}D_1 + V_{in2}D_2 \quad (6.5)$$

From equation (6.5) it can be concluded that if  $S_2$  is not turned on ( $D_2=0$ ), then the output voltage expression indicates that there is a buck mechanism between  $V_{in1}$  and the output voltage. A similar statement is true for  $V_{in2}$  and  $V_o$  if  $S_1$  is not turned on. Therefore, the name buck–buck converter has been adopted for the proposed configuration.

### 6.3.1.2. Simulation Results

Simulation studies are carried out using MATLAB software along with Simulink toolbox. Parametric values used for the developed converter configuration are given in the Appendix-D. The simulation results of the DISO buck-buck DC converter with two DC voltage sources  $V_{in1} = 24$  V and  $V_{in2} = 12$  V, and the output voltage of  $V_{out} = 18$  V is shown in figure 6.4. Figure 6.4 shows the waveforms of switching commands for  $GS_1$  and  $GS_2$ , inductor voltage ( $V_L$ ), inductor current ( $I_L$ ), input currents from the two sources  $I_1$  and  $I_2$  and current and voltage obtained at the load end  $I_{out}$  and  $V_{out}$  respectively.

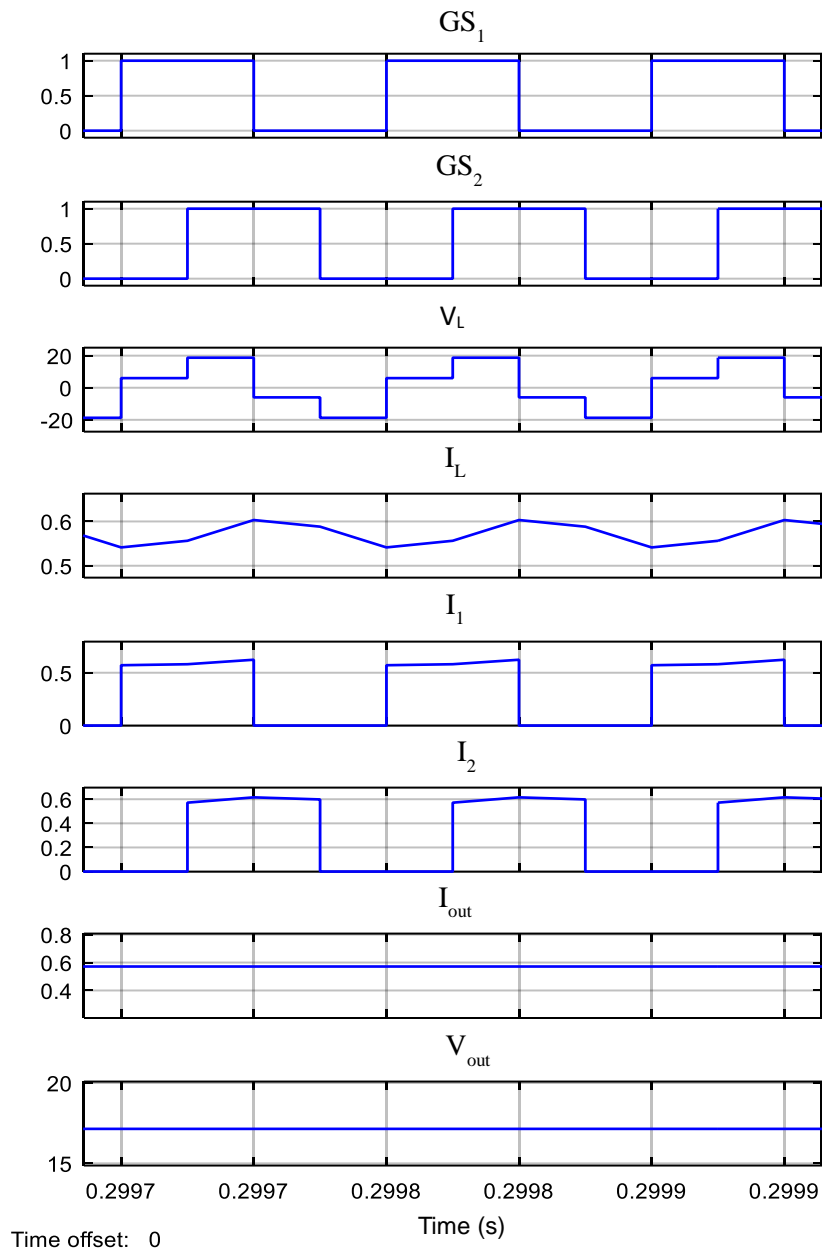


**Figure 6.4. Simulation results of DISO buck-buck DC converter**

### 6.3.2. DISO buckboost-buckboost DC converter

Figure 6.2 (b) shows the circuit diagram of the DISO buckboost-buckboost DC converter. Input voltages ( $V_{in1}$  and  $V_{in2}$ ) are the PV system fed DC bus voltages. The converter is composed of two switches  $S_1$  and  $S_2$ , inductors  $L_c$ , capacitor  $C_c$  and two diodes  $D_{c1}$  and  $D_{c2}$ . PWM signals are used for controlling the switches  $S_1$  and  $S_2$  and they can be derived either from both the inputs individually or simultaneously.

### 6.3.2.1. Control Algorithm

The control algorithm of the DISO buckboost-buckboost DC converter consists of three main intervals of operation in a switching cycle as explained in table 6.2.

**Table 6.2. Switch status and voltage across inductor for DISO buckboost-buckboost DC converter during different intervals of time.**

Interval	Switch Status	Voltage across L ( $V_L$ )	Action
<b>Interval I</b> Time Duration- $T_1$	$S_1$ - ON $S_2$ - OFF	$V_{in1}$	$V_1$ supplies energy
<b>Interval III</b> Time duration - $T_2$	$S_1$ - OFF $S_2$ - OFF	$-V_{out}$	Energy depletion of the inductor
<b>Interval II</b> Time duration- $T_3$	$S_1$ - OFF $S_2$ - ON	$V_{in2}$	$V_2$ supplies energy
<b>Interval III</b> Time duration- $T_4$	$S_1$ - OFF $S_2$ - OFF	$-V_{out}$	Energy depletion of the inductor

Key waveforms of the DISO buckboost-buckboost DC converter are shown in timing diagram of figure 6.5. The operational circuit during different intervals is also shown. The two PWM gate signals,  $GS_1$  and  $GS_2$  are used to control the given converter.  $V_L$  and  $I_L$  are the voltage and current through the inductor respectively, and  $I_1$  and  $I_2$  are the two input currents from the two DC sources.

The input-output voltage relationship can be derived from the steady-state volt-second balance analysis of the inductor,  $L_c$ , given by,

$$T_1 + T_2 + T_3 + T_4 = T \quad (6.6)$$

$$T_1 V_{in1} + T_3 V_{in2} + (T_2 + T_4)(-V_{out}) = 0 \quad (6.7)$$

The output voltage expression can be obtained as,

$$V_{out} = \frac{D_1}{(1-D_1-D_2)} V_{in1} + \frac{D_2}{(1-D_1-D_2)} V_{in2} \quad (6.8)$$

From equation (6.8) it can be concluded that if  $S_2$  is not turned on ( $D_2=0$ ), then the output voltage expression indicates that there is a buckboost mechanism between  $V_{in1}$

and the output voltage. A similar statement is true for  $V_{in2}$  and  $V_{out}$  if  $S_1$  is not turned on. Therefore, the name buckboost–buckboost converter has been adopted for the proposed configuration.

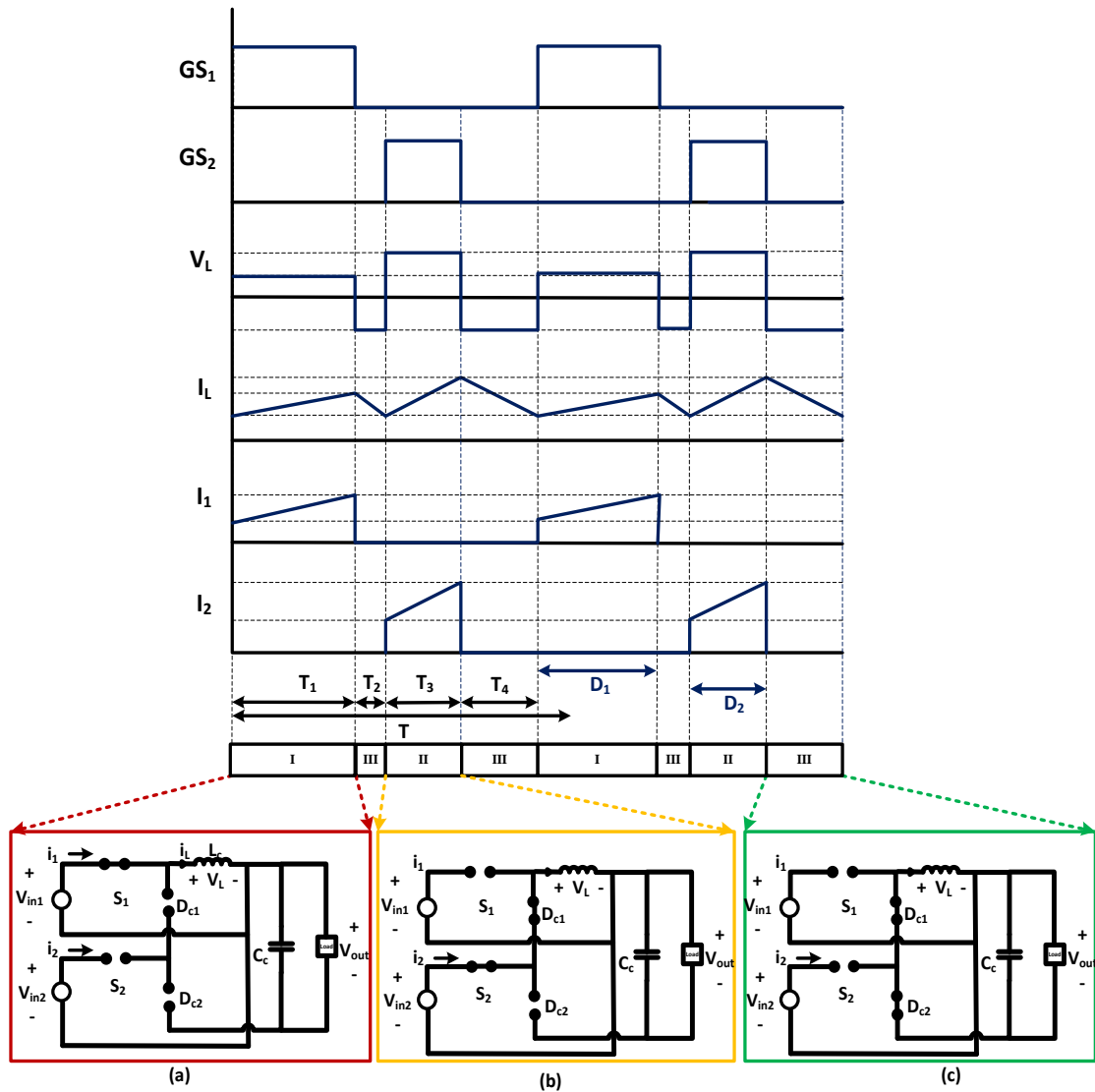
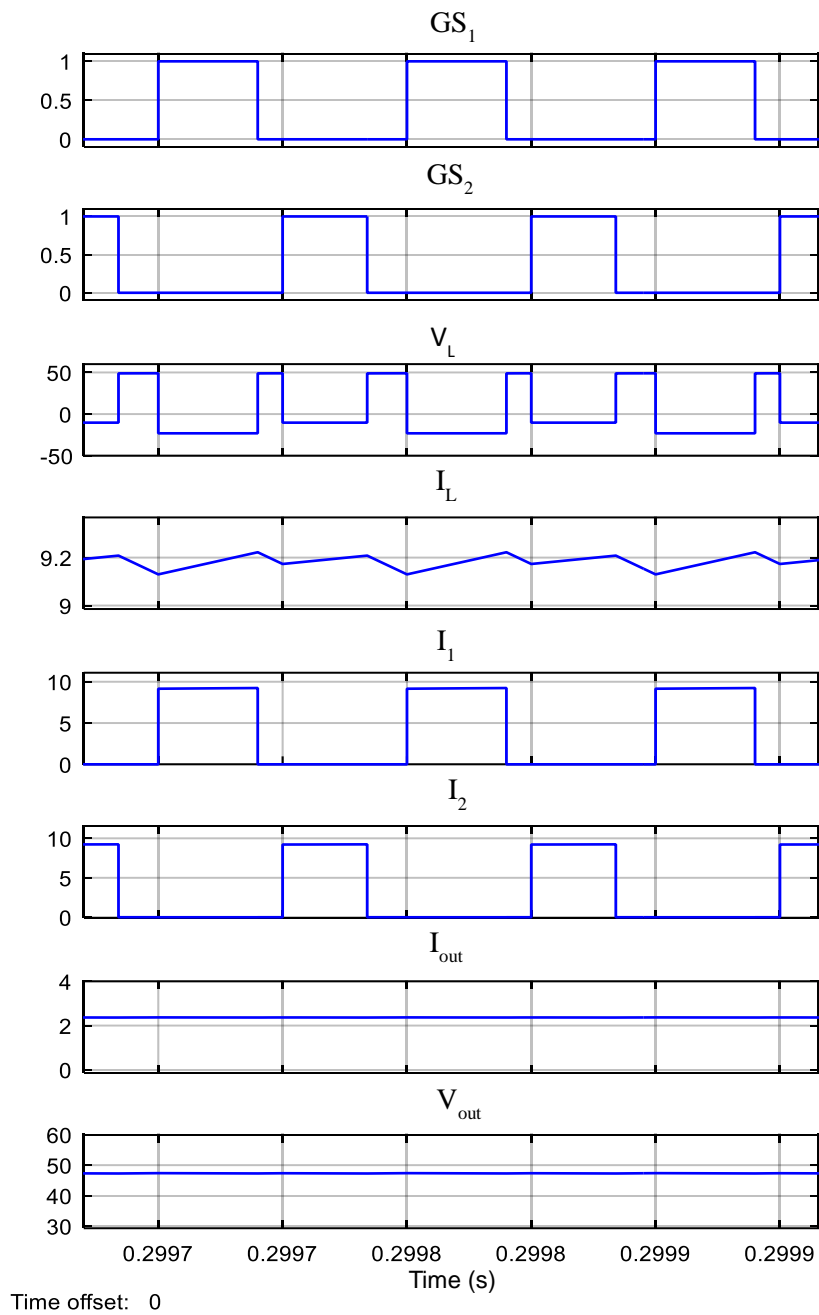


Figure 6.5. Timing diagram of DISO buckboost-buckboost DC converter along with operational circuit during (a) Interval-I, (b) Interval-II and (c) Interval-III

### 6.3.2.2. Simulation Results

Simulation studies are carried out using MATLAB software along with Simulink toolbox. Parametric values used for the developed converter configuration are given in the Appendix-D. The simulation results of the DISO buckboost-buckboost DC converter with two dc voltage sources  $V_{in1} = 24$  V and  $V_{in2} = 12$  V, and the output

voltage of  $V_{out} = 48$  V is shown in figure 6.6.



**Figure 6.6. Simulation results of DISO buckboost-buckboost DC converter**

Figure 6.6 shows the waveforms of switching commands for  $GS_1$  and  $GS_2$ , inductor voltage ( $V_L$ ), inductor current ( $I_L$ ), input currents from the two sources  $I_1$  and  $I_2$  and current and voltage obtained at the load  $I_{out}$  and  $V_{out}$  respectively.



### 6.3.3. Characterization Studies

Sensitivity and reliability analysis are the two characterizations studies carried out in present work for the developed converter configurations.

#### 6.3.3.1. Sensitivity analysis

In this section, sensitivity analysis with respect to parameters of interest for the two configurations of DISO converters is presented and the corresponding sensitivity functions are developed.

##### A. Sensitivity analysis of DISO buck-buck DC converter

The sensitivity analysis of  $V_{out}$  is carried out with respect to  $D_1$  and  $D_2$  to indicate the extent of dependency of  $V_{out}$  on both  $D_1$  and  $D_2$ . Table 6.3 shows corresponding sensitivity functions developed and their normalized sensitivity values computed using the data given in Appendix-D. The sensitivity results show that although  $V_{out}$  increases with the increase in both  $D_1$  and  $D_2$  but is more sensitive to  $D_1$ .

**Table 6.3. Sensitivity functions and normalized sensitivity values of DISO buck-buck DC converter**

Converter Parameter	Sensitivity functions developed	Normalized Sensitivity Values
$V_{out} = V_{in1} * D_1 + V_{in2} * D_2$	$\hat{S}_{D_1}^{V_{out}} = \frac{D_1}{V_{out}} * \frac{\partial V_{out}}{\partial D_1} = \frac{D_1}{V_{out}} * V_{in1}$	0.66
	$\hat{S}_{D_2}^{V_{out}} = \frac{D_2}{V_{out}} * \frac{\partial V_{out}}{\partial D_2} = \frac{D_2}{V_{out}} * V_{in2}$	0.33

##### B. Sensitivity analysis of DISO buckboost-buckboost DC converter

The sensitivity analysis of  $V_{out}$  is carried out with respect to  $D_1$  and  $D_2$  to indicate the extent of dependency of  $V_{out}$  on both  $D_1$  and  $D_2$ . Table 6.4 shows corresponding sensitivity functions developed and their normalized sensitivity values computed using the data given in Appendix-D. The sensitivity results show that although  $V_{out}$  increases with the increase in both  $D_1$  and  $D_2$  but is more sensitive to  $D_1$ .

The inference from sensitivity results helps in the selection of the optimum duty cycles of the two switches to get the desired output.

**Table 6.4. Sensitivity functions and normalized sensitivity values of DISO buckboost-buckboost DC converter**

Converter Parameter	Sensitivity functions developed	Normalized Sensitivity Values
$V_{out} = \frac{D_1}{(1 - D_1 - D_2)} V_{in1} + \frac{D_2}{(1 - D_1 - D_2)} V_{in2}$	$\hat{S}_{D_1}^{V_{out}} = \frac{D_1}{V_{out}} * \frac{\partial V_{out}}{\partial D_1}$ $= \frac{D_1}{V_{out}} * \left[ \frac{(1 - D_1 - D_2)V_{in1} + D_1 V_{in1}}{(1 - D_1 - D_2)^2} \right]$ $+ \left[ \frac{D_2 V_{in2}}{(1 - D_1 - D_2)^2} \right]$ $= \frac{D_1}{V_{out}} * \left[ \frac{(1 - D_2)V_{in1} + D_2 V_{in2}}{(1 - D_1 - D_2)^2} \right]$	2.142
	$\hat{S}_{D_2}^{V_{out}} = \frac{D_2}{V_{out}} * \frac{\partial V_{out}}{\partial D_2}$ $= \frac{D_2}{V_{out}} * \left[ \frac{D_1 V_{in1}}{(1 - D_1 - D_2)^2} \right]$ $+ \left[ \frac{(1 - D_1 - D_2)V_{in2} + D_2 V_{in2}}{(1 - D_1 - D_2)^2} \right]$ $= \frac{D_2}{V_{out}} * \left[ \frac{(1 - D_1)V_{in2} + D_1 V_{in1}}{(1 - D_1 - D_2)^2} \right]$	1.428

### 6.3.3.2. Reliability analysis

In this section, Markov reliability model of two configurations of DISO converters is presented. For any given system, a Markov model consists of a list of that system's possible states, the possible transition paths between those states, and the rate parameters of those transitions (failure rate) [95] as explained in Appendix-E.

#### A. Reliability of conventional buck and conventional buckboost converter

A traditional buck and buck-boost converter simply consist of an inductor, a switch, and a diode. Figure 6.7 (a) and (b) shows the circuit diagram and Markov chain diagram of a conventional buck and buck-boost converter respectively. Two states can be identified: the state in which the converter is healthy (state 1) and the state in which converter fails (state 0). The failure of each element of the buck and buck-boost converter leads to the failure of the complete converter. Therefore, the failure rate and thus, the Markov chain transition from state 1 to 0 is obtained by,

$$\lambda_{total} = \lambda_s + \lambda_L + \lambda_D \quad (6.9)$$

where,  $\lambda_s, \lambda_L, \text{ and } \lambda_D$  are the failure rates of switch, inductor and diode respectively. According to figure 6.7 (a) and (b), the probability of each state is calculated using Chapman–Kolmogorov equation is given by,

$$\frac{d}{dt} \begin{bmatrix} P_0 \\ P_1 \end{bmatrix} = P(t) * Q = \begin{bmatrix} -(\lambda_s + \lambda_L + \lambda_D) & 0 \\ (\lambda_s + \lambda_L + \lambda_D) & 0 \end{bmatrix} \begin{bmatrix} P_0 \\ P_1 \end{bmatrix} \quad (6.10)$$

where,  $P(t)$  is the probability vector and  $Q$  is the transition probability matrix. Assuming that the first state is where the chain begins, the initial condition of the equation above is given by initial state vector  $P_0$ ,

$$P_0 = [1 \quad 0] \quad (6.11)$$

Therefore, the reliability function can be determined by,

$$R_1(t) = P_0(t) = e^{-(\lambda_s + \lambda_L + \lambda_D)t} \quad (6.12)$$

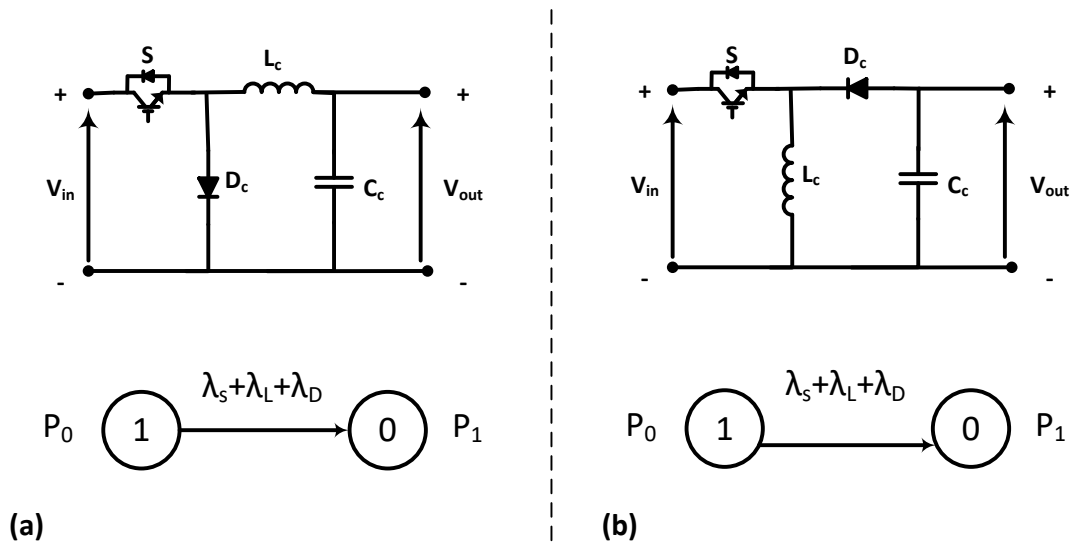
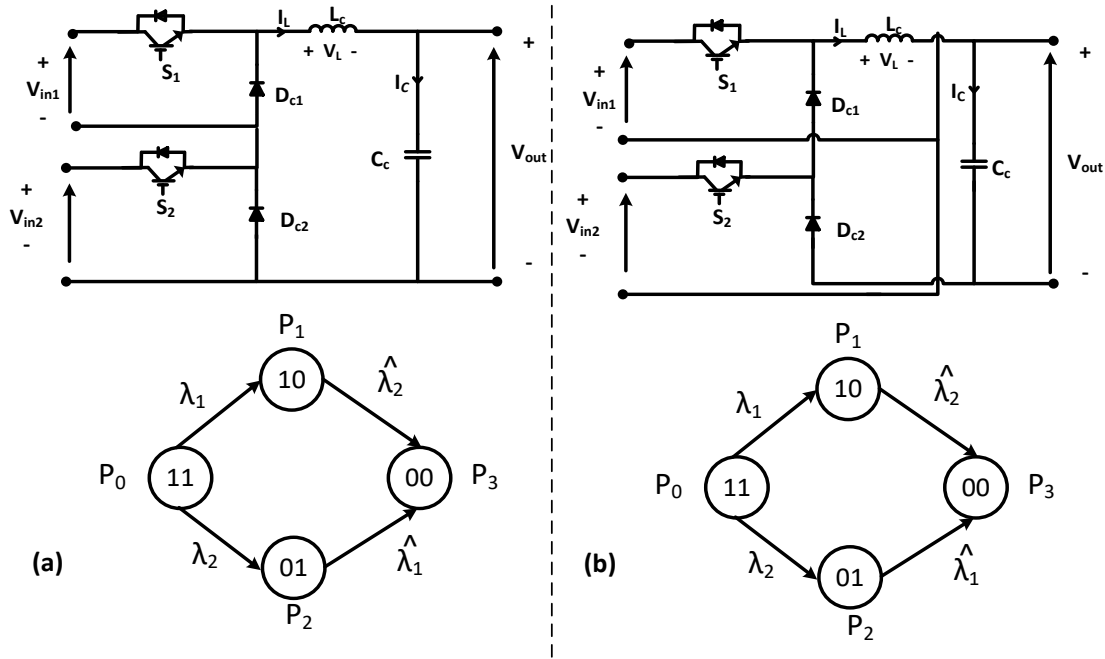


Figure 6.7. Circuit diagram and Markov chain model of (a) conventional buck converter and (b) conventional buckboost converter

**B. Reliability of DISO buck-buck DC converter and DISO buckboost-buckboost DC converter**

DISO buck-buck DC converter and DISO buckboost-buckboost DC converter consists of two switches, one inductor, and a diode. Figure 6.8 (a) and (b) shows the circuit diagram and Markov chain diagram of the two DISO configurations. Four states can be

identified: the state in which both the inputs of the converter are healthy (state 11), a state in which one of the input has failed (state 10), a state in which another input has failed (state 01), and the final state in which the whole configuration has failed (state 00). In the second and third state when a fault occurs, one of the inputs continues to operate. This means that  $\lambda_1 = (\lambda_{s1} + \lambda_{D1})$ ,  $\lambda_2 = (\lambda_{s2} + \lambda_{D2})$ ,  $\hat{\lambda}_1 = (\lambda_{s1} + \lambda_{D1} + \lambda_L)$ , and  $\hat{\lambda}_2 = (\lambda_{s2} + \lambda_{D2} + \lambda_L)$ , where  $\lambda_{s1}$ ,  $\lambda_{s2}$ ,  $\lambda_L$ , and  $\lambda_D$  are the failure rates of two switches, the inductor and diode respectively.



**Figure 6.8. Circuit diagram and Markov chain model of (a) DISO buck-buck DC converter and (b) DISO buckboost- buckboost DC converter**

According to figure 6.8 (a) and (b), the probability of each state is calculated using Chapman–Kolmogorov equation is given by,

$$\frac{d}{dt} \begin{bmatrix} P_0 \\ P_1 \\ P_2 \\ P_3 \end{bmatrix} = P(t) * Q = \begin{bmatrix} -(\lambda_1 + \lambda_2) & 0 & 0 & 0 \\ \lambda_1 & -\hat{\lambda}_2 & 0 & 0 \\ \lambda_2 & 0 & -\hat{\lambda}_1 & 0 \\ 0 & \lambda_2 & \lambda_1 & 0 \end{bmatrix} \begin{bmatrix} P_0 \\ P_1 \\ P_2 \\ P_3 \end{bmatrix} \quad (6.13)$$

where,  $P(t)$  is the probability vector and  $Q$  is the transition probability matrix. Assuming that the first state is where the chain begins, the initial condition of the equation above is given by initial state vector  $P_0$ ,

$$P_0 = [1 \quad 0 \quad 0 \quad 0] \quad (6.14)$$

Therefore, the reliability function can be determined by,

$$R_2(t) = 1 - P_3(t) = e^{-(\lambda_1+\lambda_2)t} + \frac{\lambda_1}{\lambda_1+\lambda_2-\widehat{\lambda}_2} (e^{-(\widehat{\lambda}_2)t} - e^{-(\lambda_1+\lambda_2)t}) + \frac{\lambda_2}{\lambda_1+\lambda_2-\widehat{\lambda}_2} (e^{-(\widehat{\lambda}_1)t} - e^{-(\lambda_1+\lambda_2)t}) \quad (6.15)$$

Precise calculation of  $\lambda$  is necessary for reliability calculation of converters as explained in Chapter-III. The failure rates and MTBF of the inductor, diode and switch required have already been computed and presented in table 3.2.

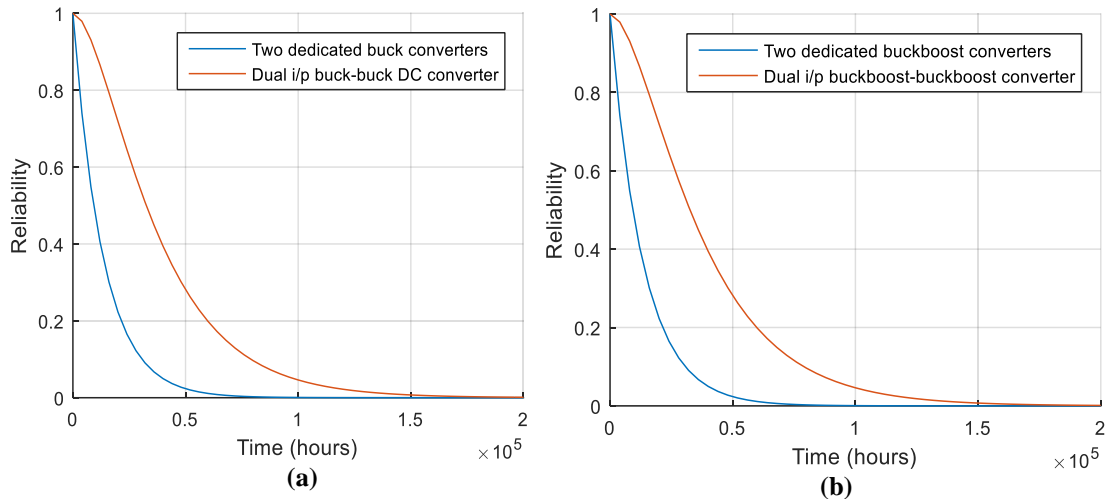


**Figure 6.9. Reliability curves of (a) conventional buck converters and DISO buck-buck DC converter and (b) conventional buckboost converters and DISO buckboost-buckboost DC converter**

Figure 6.9 (a) shows the reliability curves of the proposed DISO buck-buck DC converter plotted using equation (6.15) and reliability of two buck converters. Figure 6.9 (b) shows the reliability curves of the proposed DISO buckboost-buckboost DC converter plotted using equation (6.15) and reliability of two separate buckboost DC converters. The results show that proposed multi-terminal converters are more reliable than their conventional counterparts.

### 6.4. SINGLE-INPUT DUAL-OUTPUT CONVERTERS

Figure 6.10 presents two configurations of single input SIDO converters for PV based DC nanogrid which is developed by replacing the control switch of a conventional boost converter and operating it in continuous conduction mode [151, 154]. In the first configuration as shown in figure 6.10(a), two DC outputs of boost ( $V_{01}$ ) and buck ( $V_{02}$ ) voltage are realized. The second configuration as shown in figure 6.10 (b) is designed for two outputs: AC voltage ( $V_{acout}$ ) of desired frequency and boost DC voltage ( $V_{dcout}$ ).

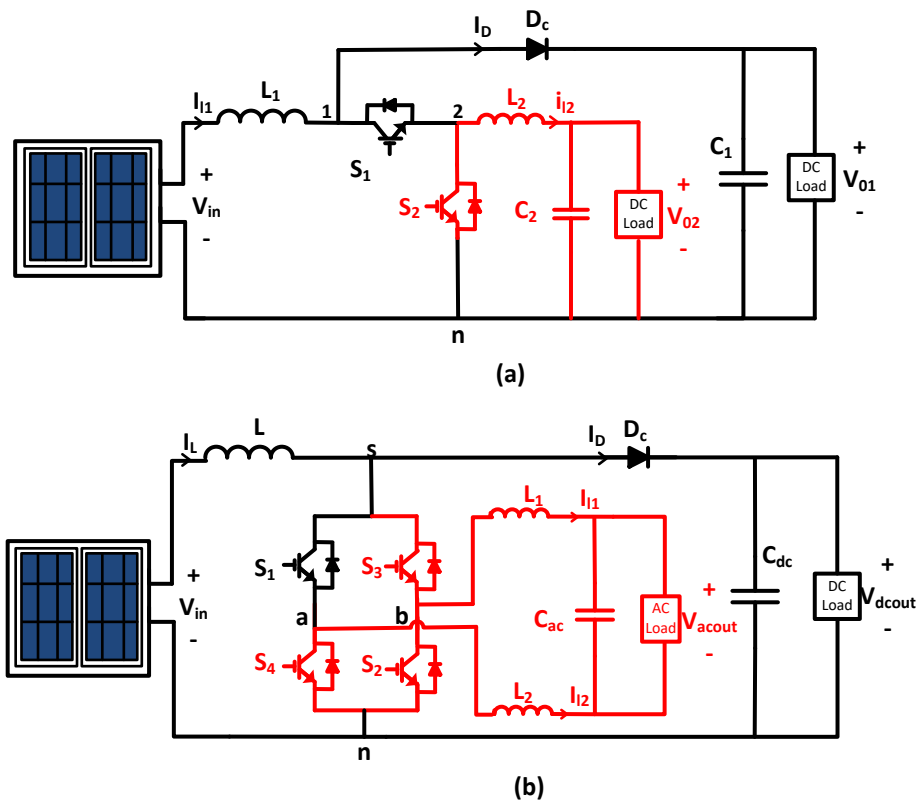


Figure 6.10. Circuit diagram of (a) SIDO converter with buck DC and boost DC output, and (b) SIDO converter with AC and boost DC output

The following section explains the design, implementation and characterization studies of the two configurations of SIDO converters.

#### 6.4.1. SIDO converter with boost DC and buck DC output

The SIDO with boost DC and buck DC output converter is composed of two switches  $S_1$  and  $S_2$ , two inductors  $L_1$  and  $L_2$ , and two capacitors  $C_1$  and  $C_2$  with  $V_{01}$  and  $V_{02}$  as desired buck DC and boost output voltages as shown in figure 6.10. In switching period

$T$ , Switch  $S_1$  is closed for time  $D_1T$  and switch  $S_2$  is closed for time  $D_2T$  where  $D_1$  and  $D_2$  are duty cycles of two switches  $S_1$  and  $S_2$ , respectively.

#### 6.4.1.1. Control Algorithm

The control algorithm of the SIDO converter with buck DC and boost DC output consists of three prime intervals of operation in a switching cycle. The control algorithms for all the intervals have been developed and various voltages and currents are presented in table 6.5.

**Table 6.5. Voltages and currents of SIDO converter with buck DC and boost DC output during different intervals of time.**

Interval	Voltage across $L_1$ ( $V_{L1}$ )	Current Through $L_1$ ( $I_{L1}$ )	Voltage across $L_2$ ( $V_{L2}$ )	Current Through $L_2$ ( $I_{L2}$ )
<b>Interval I</b> Time Duration $-D_2 T$	$V_{L1} = V_{in}$	$I_{L1} = \frac{V_{in}D_2T}{L_1}$	$V_{L2} = -V_{02}$	$I_{L2} = \frac{-V_{02}D_2T}{L_2}$
<b>Interval II</b> Time duration $-(D_1-D_2) T$ .	$V_{L1} = V_{in}$ $-V_{01}$	$I_{L1} = \frac{-(V_{01} - V_{in})(D_1 - D_2)T}{L_1}$	$V_{L2} = V_{01}$ $-V_{02}$	$I_{L2} = \frac{(V_{01} - V_{02})(D_1 - D_2)T}{L_2}$
<b>Interval III</b> Time duration $-(1-D_1) T$	$V_{L1} = V_{in}$ $-V_{01}$	$I_{L1} = \frac{-(V_{01} - V_{in})(1 - D_1)T}{L_1}$	$V_{L2} = -V_{02}$	$I_{L2} = \frac{-V_{02}(1 - D_1)T}{L_2}$

Key waveforms are shown in figure 6.11 along with the equivalent circuit of corresponding modes.  $V_{mod1}$  and  $V_{mod2}$  are the DC reference signal that controls the duty ratios for buck DC and boost output, respectively and  $V_{carrier}$  is the triangular carrier wave signal. The generated gate signals,  $GS_1$  and  $GS_2$ , are provided to the gates of the controlled switches  $S_1$  and  $S_2$ , respectively.  $V_1$  and  $V_2$  are voltages between node 1 and  $n$ , and node 2 and  $n$ , respectively, as shown in figure 6.10 (a).  $I_{L1}$  and  $I_{L2}$  are the currents through the two inductors, and  $\Delta I_{L1}$  and  $\Delta I_{L2}$  are the total range of variation in  $I_{L1}$  and  $I_{L2}$ , respectively.  $I_D$  is current through the diode  $D_c$ .

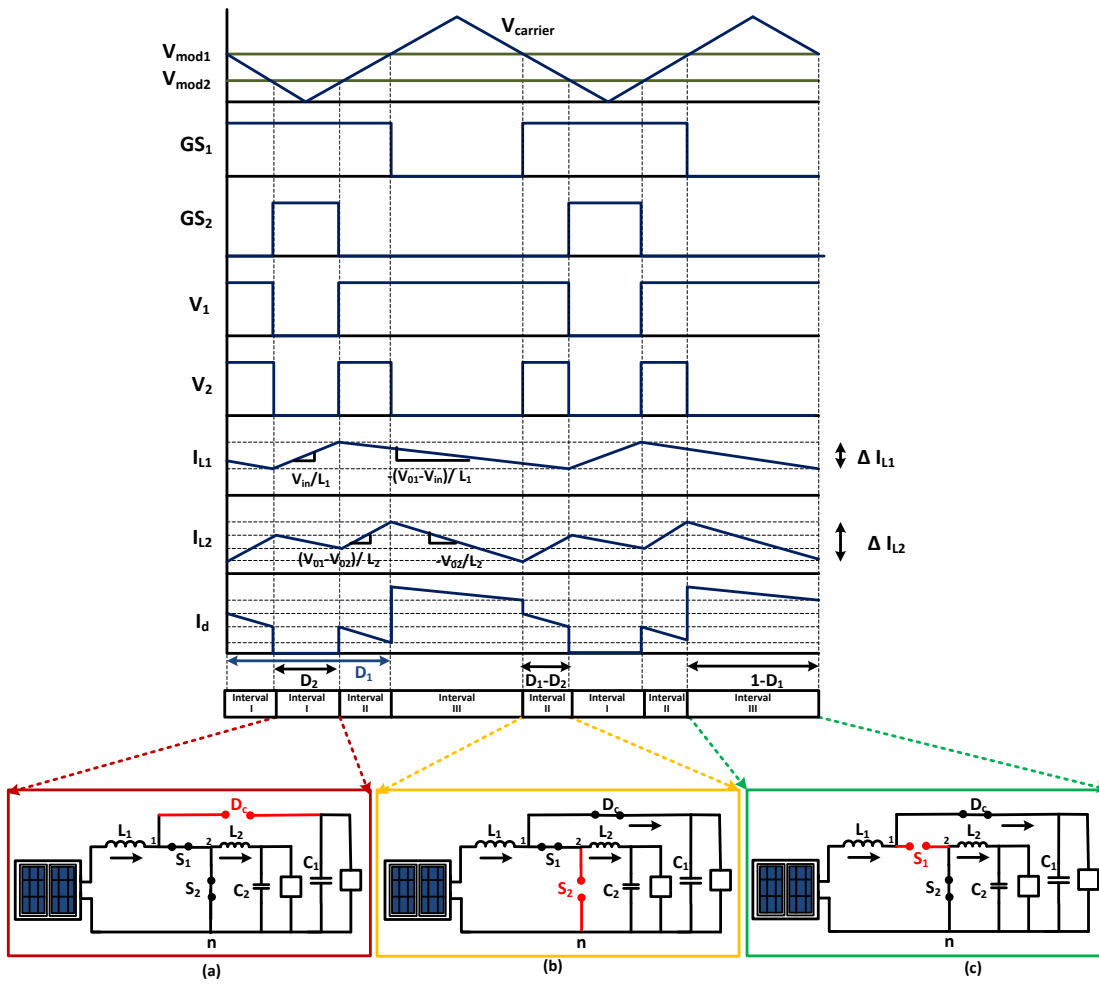


Figure 6.11. Timing diagram of SIDO converter with buck DC and boost DC output along with operational circuit during (a) Interval-I, (b) Interval-II and (c) Interval-III

Steady state operation requires the inductor current to remain same at the end of the switching cycle, i.e., the net change in inductor current over one period is zero. The same can be represented as,

$$I_{L(S-open)} + I_{L(S-closed)} = 0 \quad (6.16)$$

The inductor current  $I_{L1}$  for the complete switching cycle is given by,

$$\frac{V_{in}D_2T}{L_1} + \frac{-(V_{01}-V_{in})(D_1-D_2)T}{L_1} + \frac{(V_{in}-V_{01})(1-D_1)T}{L_1} = 0 \quad (6.17)$$

From equation (6.17), voltage gain ( $V_{01}/V_{in}$ ), known as  $G_{boost}$ , is given as,



$$G_{boost} = \frac{V_{01}}{V_{in}} = \frac{1}{(1-D_2)} \quad (6.18)$$

Similarly, the inductor current  $I_{L2}$ , is given by,

$$\frac{-V_{02}D_2T}{L_2} + \frac{(V_{01}-V_{02})(D_1-D_2)T}{L_2} + \frac{-V_{02}(1-D_1)T}{L_2} = 0 \quad (6.19)$$

Simplifying equation (6.19), gives  $V_{02}$  as,

$$V_{02} = V_{01} (D_1 - D_2) \quad (6.20)$$

From equation (6.18), and (6.20), the voltage gain ( $V_{02}/V_{in}$ ), known as  $G_{buck}$ , is given by,

$$G_{buck} = \frac{V_{02}}{V_{in}} = \frac{(D_1-D_2)}{(1-D_2)} \quad (6.21)$$

From equations (6.18) and (6.21), it can be concluded that the boost DC output depends only on duty cycle  $D_2$  whereas the buck DC output depends on both the duty cycles  $D_1$  and  $D_2$ .

#### 6.4.1.2. Simulation Results

Simulation studies are carried out using MATLAB software along with Simulink toolbox.

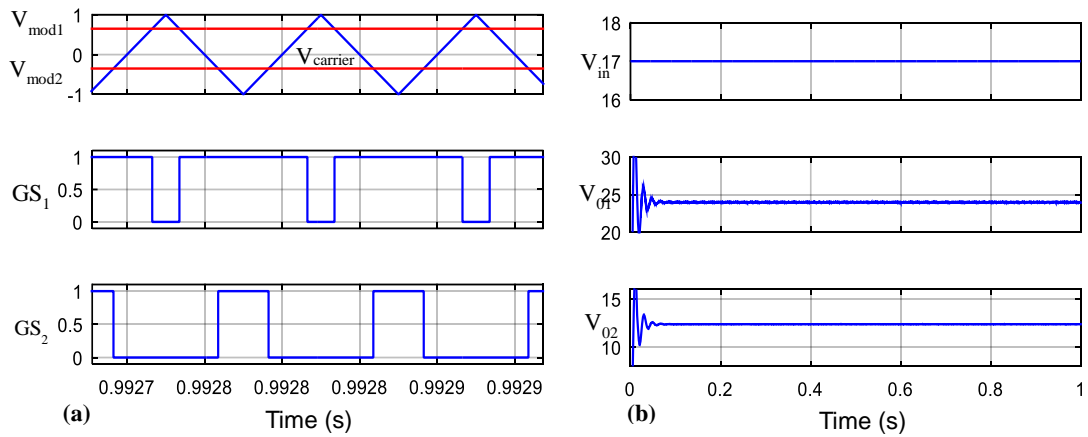


**Figure 6.12. Simulation results of SIDO converter with buck DC and boost DC output (a) PWM switching waveforms and generated gate pulses  $GS_1$  and  $GS_2$  and (b) input voltage ( $V_{in}$ ), boost output voltage ( $V_{01}$ ) and buck output voltage ( $V_{02}$ ) waveforms**

Parametric values for the converter configuration used are given in the Appendix-D. The simulation results of the PV based single input SIDO converter with 17 V input, and two DC output of 24 V and 12 V is shown in figure 6.12. Figure 6.12 (a) shows the PWM Pulse generation for the two switches  $S_1$  and  $S_2$ . Figure 6.12 (b) shows the input voltage of 17 V obtained from the solar panel used, and the two DC outputs, of 24 V ( $V_{o1}$ ) and 12 V ( $V_{o2}$ ) at the boost end and buck end respectively.

#### 6.4.1.3. Hardware development and implementation

Experimental setup of 100 W has been developed and implemented for the DISO converter configuration as shown in figure 6.13. It consists of a 17 V DC input solar panel, designed converter and the loads. The main circuit includes two MOSFET switches  $S_1$  &  $S_2$ , two inductors  $L_1$  &  $L_2$  and two capacitors  $C_1$  &  $C_2$  as described in Figure 6.10 (a). The PWM generated signals for the switches is obtained using My-RIO, an FPGA-based controller. The driver circuit with NPN transistor 2N2222 and Optocoupler IC 6N137 is used to drive the MOSFET switches. Figure 6.14 (a) to 6.14 (c) show PWM generated signal and the gate pulses on Keysight Digital Storage Oscilloscope DSO-X-2024A. The final output obtained is shown in figure 6.14 (d) with the input of 17 V producing boost output voltage of 24 V DC and a buck output voltage of 12 V DC.

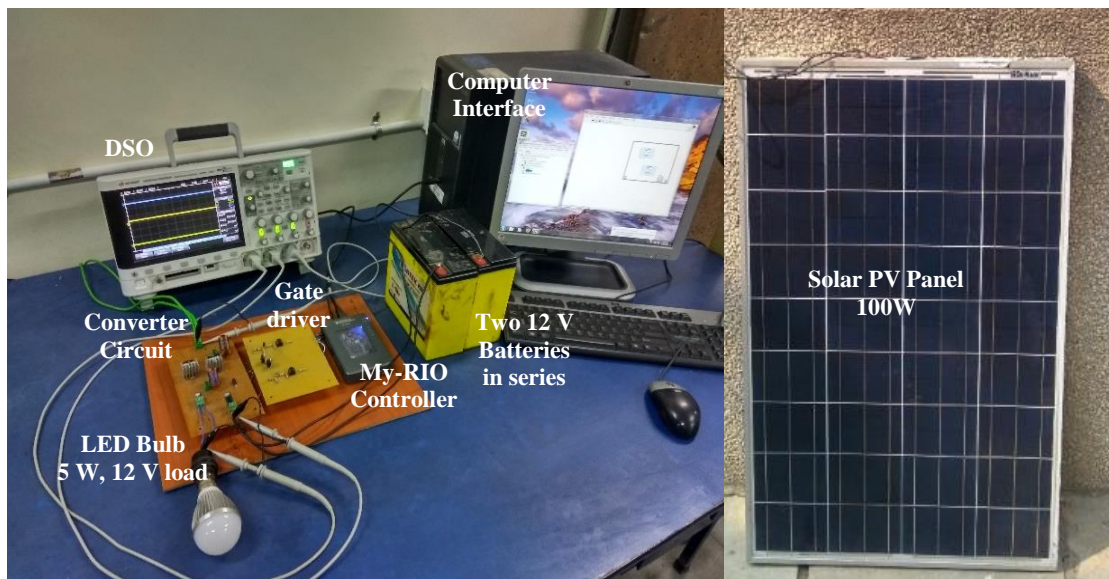
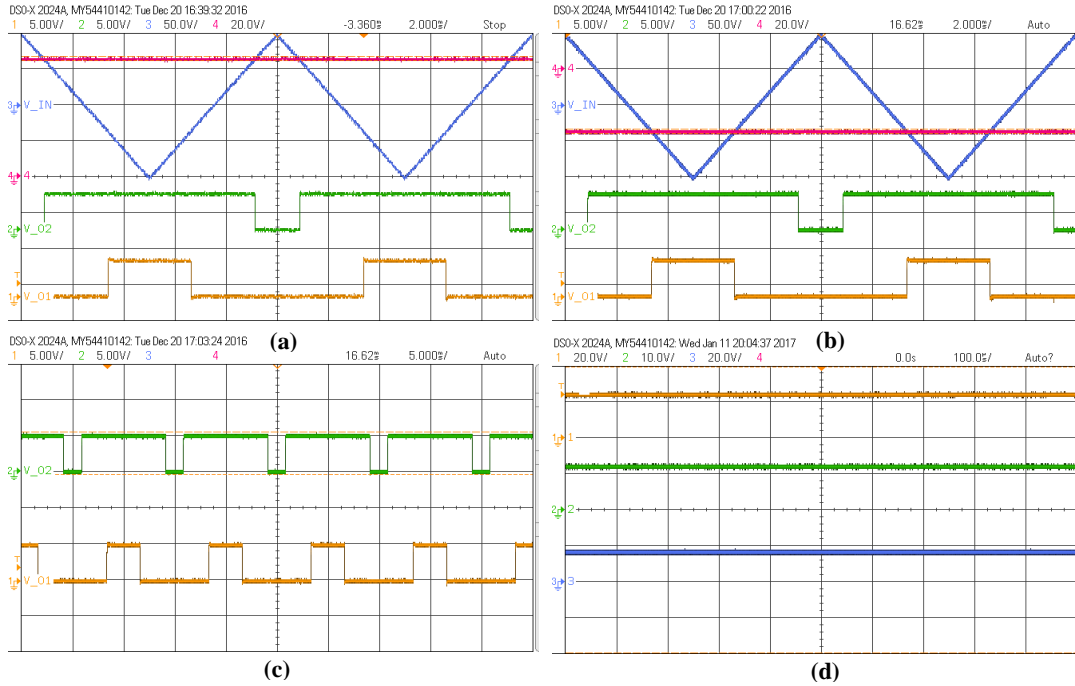


Figure 6.13. Experimental setup for SIDO converter with buck DC and boost DC output



**Figure 6.14. Experimental results of SIDO converter with buck DC and boost DC output (a)  $GS_1$  gate pulse obtained from carrier wave and reference signal, (b)  $GS_2$  gate pulse obtained from carrier wave and reference signal, (c) Gate pulses  $GS_1$  and  $GS_2$  and (d)  $V_{01}$  measured on Ch.1,  $V_{02}$  measured on Ch.2 and  $V_{in}$  measured on Ch.3**

### 6.4.2. SIDO converter with AC and boost DC output

In figure 6.10 (b),  $V_{dcout}$  and  $V_{acout}$  are desired AC and boost DC output voltages respectively, of the SIDO converter. The converter architecture has been derived by replacing controllable switch of a conventional boost converter by the four bidirectional switches ( $S_1$ ,  $S_2$ ,  $S_3$ , and  $S_4$ ), inductors ( $L_1$ ,  $L_2$ ) and capacitor ( $C_{ac}$ ). The voltage across capacitor  $C_{ac}$  gives the AC output whose frequency is determined by the frequency of the reference sinusoidal control signal.

#### 6.4.2.1. Control Algorithm

The control algorithm of the SIDO converter with AC and boost DC output consists of three prime intervals of operation in a switching cycle. The control algorithms for all the intervals have been developed and various voltages and currents are presented in table 6.6.

**Table 6.6 Voltages and currents of SIDO converter with AC and boost DC output during different intervals of time**

Interval	Voltage at Inverter output ( $V_{ab}$ )	Voltage at switch node ( $V_{sn}$ )	Current through diode ( $I_D$ )
Interval I	$V_{ab} = 0$	$V_{sn} = 0$	$I_D = 0$
Interval II	$V_{ab}$ $= \begin{cases} V_{dcout} & \text{if } S_1, S_2 \text{ ON} \\ -V_{dcout} & \text{if } S_3, S_4 \text{ ON} \end{cases}$	$V_{sn} = V_{dcout}$	$I_D = I_L -  I_{ab} $
Interval III	$V_{ab} = 0$	$V_{sn} = V_{dcout}$	$I_D = I_L$

Key waveforms are shown in figure 6.15 along with the equivalent circuit of corresponding modes. The reference signals to the PWM generation circuit are  $V_d(t)$  and  $V_m(t)$ .  $V_d(t)$  is a DC signal that controls the duty ratio of the DC output of the Boost converter, and  $V_m(t)$  is a sinusoidal signal that controls modulation index of the inverter and the frequency of the AC output.  $V_{carrier}$  is the triangular carrier wave signal. The generated gate signals,  $GS_1$  to  $GS_4$  are provided to the gates of the controlled switches  $S_1$  to  $S_4$  respectively.  $V_{ab}$  is the voltage at the inverter output and  $V_{sn}$  is the switch node voltage.  $I_L$  is the current through the inductor  $L$  and  $I_D$  is the current through the diode  $D_c$  as shown in figure 6.10 (b).

Steady-state operation analysis of the control algorithm for different time intervals of converter gives the expression of the voltage gain  $G_{DC}$  and  $G_{AC}$  as,

$$G_{DC} = \frac{V_{dcout}}{V_{in}} = \frac{1}{(1-D)} \quad (6.22)$$

$$G_{AC} = \frac{V_{acout}}{V_{in}} = \frac{M}{(1-D)} \quad (6.23)$$

Where,  $D$  is the duty cycle, and  $M$  is the modulation index. Further,  $M$  is the ratio of the peak magnitudes of the modulating wave ( $V_m$ ) and a carrier wave ( $V_{carrier}$ ), ( $0 \leq M \leq 1$ ) that regulates the AC output voltage.

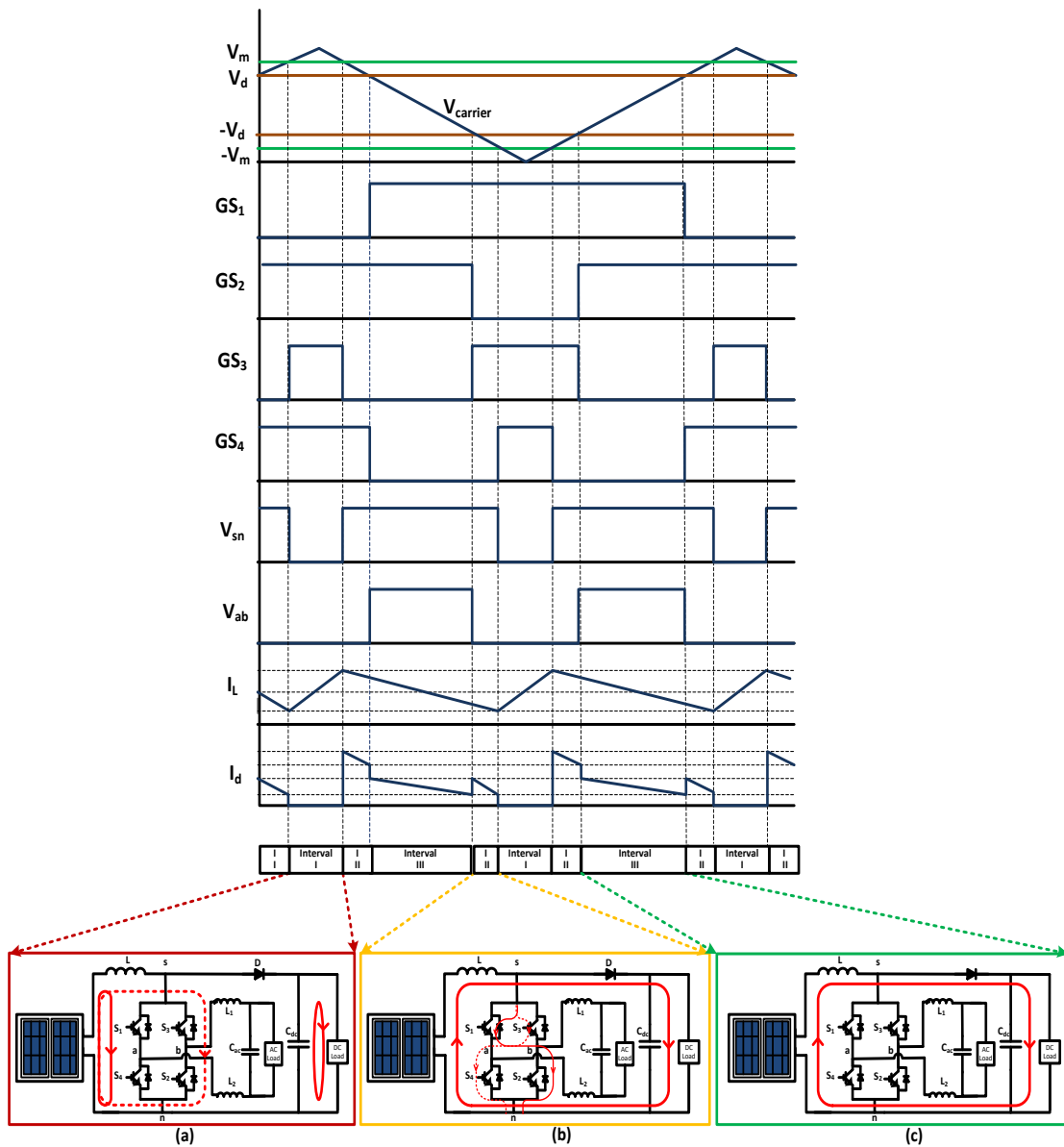
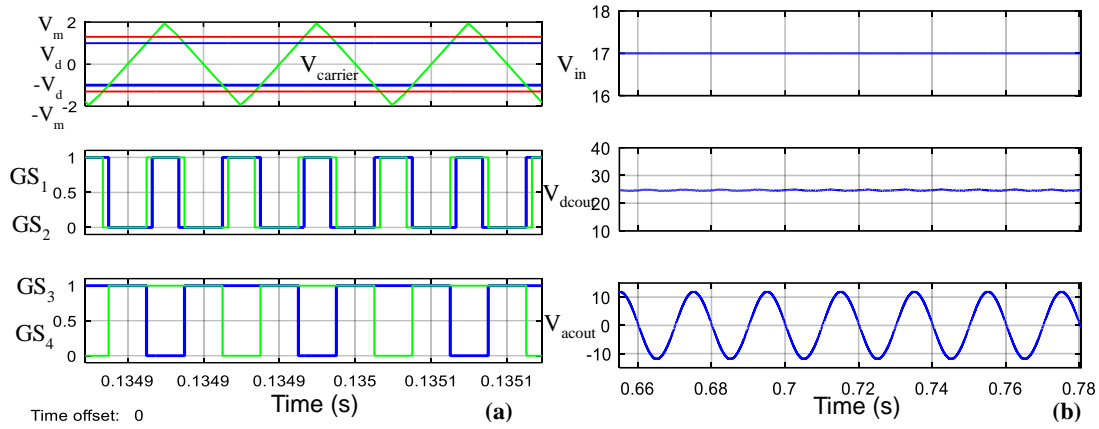


Figure 6.15. Timing diagram of SIDO converter with AC and boost DC output along with operational circuit during (a) Interval-I, (b) Interval-II and (c) Interval-III

### 6.4.2.2. Simulation Results

Simulation studies are carried out using MATLAB software along with Simulink toolbox. Parametric values for the converter configuration used are given in the Appendix-D. The simulation results of the single input SIDO converter with AC and boost DC output is shown in figure 6.16. Figure 6.16 (a) shows the PWM Pulse generation for the four switches  $S_1$ ,  $S_2$ ,  $S_3$ , and  $S_4$ . The figure 6.16 (b) shows the input voltage of 17 V, obtained from the PV panel, the boost DC output of 24 V ( $V_{dcout}$ ) and

AC output of 12 V, 50 Hz ( $V_{acout}$ ).



**Figure 6.16. Simulation results of SIDO converter with AC and boost DC output (a) PWM switching waveforms and generated gate pulses  $GS_1$ ,  $GS_2$ ,  $GS_3$ , and  $GS_4$  and (b) Input voltage ( $V_{in}$ ), Boost DC output voltage ( $V_{dcou}$ ) and AC output voltage ( $V_{acout}$ )**

### 6.4.2.3. Hardware development and implementation

Experimental setup of 100 W has been developed and implemented for the DISO converter configuration is shown in figure 6.17. It consists of a 17 V DC input solar panel, designed converter and the loads. The main circuit includes four MOSFET switches  $S_1$ ,  $S_2$ ,  $S_3$  &  $S_4$ , three inductors  $L$ ,  $L_1$  and  $L_2$  and two capacitors  $C_{dc}$  and  $C_{ac}$  as described in figure 6.10 (b).

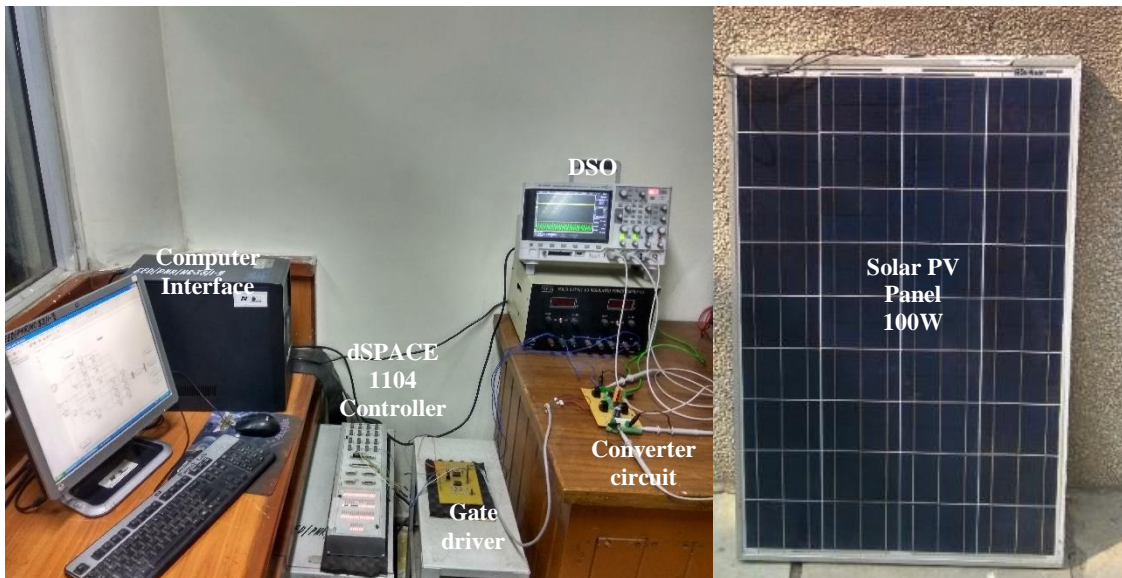


**Figure 6.17. Experimental setup for SIDO converter with AC and boost DC output**



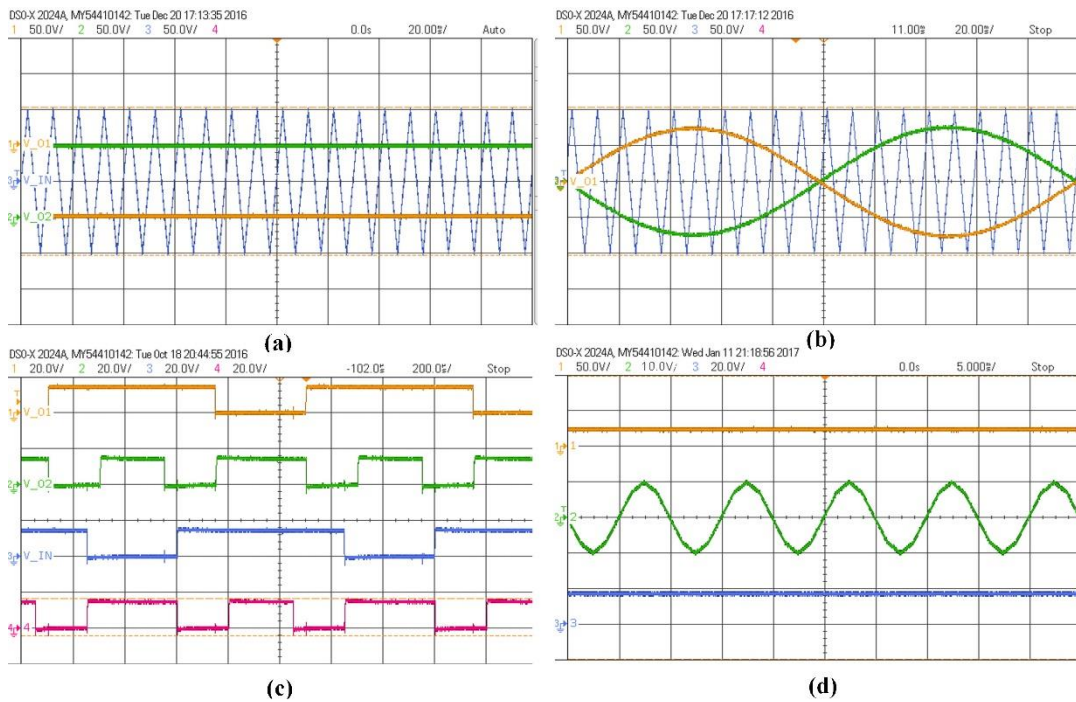


**Figure 6.18.** Experimental results of SIDO converter with AC and boost DC output (a) Carrier wave and DC reference signals:  $V_d$  and  $-V_d$ , (b) Carrier wave and sinusoidal reference signals:  $V_m$  and  $-V_m$ , (c) Gate pulses  $GS_1$ ,  $GS_2$ ,  $GS_3$ , and  $GS_4$  and (d)  $V_{dcout}$  measured on Ch. 1,  $V_{acout}$  measured on Ch. 2 and  $V_{in}$  measured on Ch. 3

The PWM generated signals are obtained using Simulink and dSPACE controller. The driver circuit with NPN transistor 2N2222 and Optocoupler IC 6N137 is used to drive the MOSFET switches. Figure 6.18 (a) to 6.18 (c) show PWM generated signals and gate pulses on Keysight Digital Storage Oscilloscope DSO-X-2024A. Also, the final output generated by the converter is shown in figure 6.18 (d) with an input voltage of 17 V generating an AC output voltage of 10.5 V, 50 Hz and boost DC output voltage of 24 V.

### 6.4.3. Characterization Studies

Sensitivity and reliability analysis are the two characterizations studies carried out in present work for the developed converter configurations.

#### 6.4.3.1. Sensitivity analysis

In this section, sensitivity analysis with respect to parameters of interest for the two configurations of SIDO converters is presented and the corresponding sensitivity functions are developed.

### A. Sensitivity analysis of SIDO converter with buck DC and boost DC output

The sensitivity analysis of  $V_{O1}$  and  $V_{O2}$  is carried out with respect to  $D_1$  and  $D_2$  to indicate the extent of dependency of  $V_{O1}$  and  $V_{O2}$  on both  $D_1$  and  $D_2$ . Table 6.7 shows corresponding sensitivity functions developed and their normalized sensitivity values computed using the data given in Appendix-D. The sensitivity results show that  $V_{O1}$  increases with the increase in  $D_2$  and do not depend on  $D_1$ . Further,  $V_{O2}$  increases with increase in  $D_1$  and decreases with an increase in  $D_2$ .

**Table 6.7 Sensitivity functions and normalized sensitivity values of SIDO converter with boost and buck DC output**

Converter Parameters	Sensitivity functions developed	Normalized Sensitivity Values
<b>Boost Output Voltage</b> $V_{O1} = \frac{V_{in}}{(1 - D_2)}$	$\hat{S}_{D_1}^{V_{O1}} = \frac{D_1}{V_{O1}} * \frac{\partial V_{O1}}{\partial D_1} = 0$	0
	$\hat{S}_{D_2}^{V_{O1}} = \frac{D_2}{V_{O1}} * \frac{\partial V_{O1}}{\partial D_2} = \frac{D_2}{V_{O1}} * \left( \frac{V_{in}}{(1 - D_2)^2} \right)$	0.407
<b>Buck Output Voltage</b> $V_{O2} = \frac{V_{in} * (D_1 - D_2)}{(1 - D_2)}$	$\hat{S}_{D_1}^{V_{O2}} = \frac{D_1}{V_{O2}} * \frac{\partial V_{O2}}{\partial D_1} = \frac{D_1}{V_{O2}} * \left( \frac{V_{in}}{(1 - D_2)} \right)$	1.39
	$\hat{S}_{D_2}^{V_{O2}} = \frac{D_2}{V_{O2}} * \frac{\partial V_{O2}}{\partial D_2} = -\frac{D_2}{V_{O2}} * \left( \frac{V_{in}(1 - D_1)}{(1 - D_2)^2} \right)$	-0.244

### B. Sensitivity analysis of SIDO converter with AC and boost DC output

Table 6.8 shows sensitivity functions developed for the SIDO converter with AC and boost DC outputs with respect to parameters of interest. The numerical values of sensitivity functions are computed using the data presented in Appendix-D. It is observed that DC output voltage increase with an increase in duty cycle  $D$  and remains unaffected by modulation index, whereas the AC voltage increase with an increase in both the duty cycle  $D$  and modulation index  $M$ . Thus, it is possible to get desired DC and AC voltage by the adjustment of the duty cycles and modulation index.

**Table 6.8 Sensitivity functions and normalized sensitivity values of SIDO converter with AC and boost DC output**



Converter Parameters	Sensitivity functions developed	Sensitivity Values
<b>Output Voltage at DC Port</b> $V_{dcout} = \frac{V_{in}}{(1 - D)}$	$\hat{S}_D^{V_{dcout}} = \frac{D}{V_{dcout}} * \frac{\partial V_{dcout}}{\partial D}$ $= \frac{D}{V_{dcout}} * \left( \frac{V_{in}}{(1 - D)^2} \right)$	0.407
<b>Output Voltage at AC Port</b> $V_{acout} = \frac{V_{in} * M}{(1 - D)}$	$\hat{S}_D^{V_{acout}} = \frac{D}{V_{acout}} * \frac{\partial V_{acout}}{\partial D}$ $= \frac{D}{V_{acout}} * \left( \frac{V_{in} * M}{(1 - D)^2} \right)$	0.5085
	$\hat{S}_M^{V_{acout}} = \frac{M}{V_{acout}} * \frac{\partial V_{acout}}{\partial M}$ $= \frac{M}{V_{acout}} * \left( \frac{V_{in}}{(1 - D)} \right)$	1.245

The inference from sensitivity results helps in the selection of the optimum duty cycles of the two switches to get the desired output.

#### 6.4.3.2. Reliability analysis

In this section, Markov reliability model of a two configuration of SIDO converters are presented.

##### A. Reliability of conventional boost DC converter

A traditional boost converter simply consists of an inductor, a switch, and a diode. Figure 6.19 shows the circuit diagram and Markov chain diagram of a conventional boost converter. Two states can be identified: the state in which the converter is healthy (state 1) and the state in which converter fails (state 0). The failure of each element of the boost converter leads to the failure of the complete converter. Therefore the failure rate and thus the Markov chain transition from state 1 to 0 is obtained by,

$$\lambda_{total} = \lambda_s + \lambda_L + \lambda_D \quad (6.24)$$

where,  $\lambda_s$ ,  $\lambda_L$ , and  $\lambda_D$  are the failure rates of switch, inductor and diode respectively.

According to figure 6.19, the probabilities are given by,

$$\frac{d}{dt} \begin{bmatrix} P_0 \\ P_1 \end{bmatrix} = \begin{bmatrix} -(\lambda_s + \lambda_L + \lambda_D) & 0 \\ (\lambda_s + \lambda_L + \lambda_D) & 0 \end{bmatrix} \begin{bmatrix} P_0 \\ P_1 \end{bmatrix} \quad (6.25)$$

Assuming that the first state is where the chain begins, the initial condition of the equation above is,

$$P_0 = [1 \quad 0] \quad (6.26)$$

Therefore, the reliability function of the boost converter configuration can be determined by,

$$R_1(t) = P_0(t) = e^{-(\lambda_s + \lambda_L + \lambda_D)t} \quad (6.27)$$

A similar reliability expression can be obtained for buck converter and single-phase inverter with two stages of Markov model same as that of the boost converter.

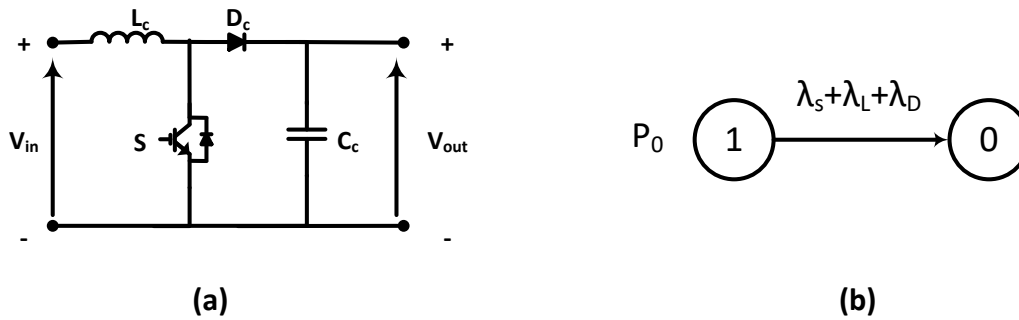


Figure 6.19. Circuit diagram and Markov chain model of conventional boost converter

### B. Reliability of SIDO converter with buck DC and boost DC output

SIDO converter with buck DC and boost DC output converter consists of two inductors, two switches, and a diode. Figure 6.20 shows the circuit diagram and Markov chain diagram of the converter. Three states can be identified: the state in which both the stages of the converter are healthy (state 11), a state in which one of the stages has failed (state 10), and the final state in which the whole configuration has failed (state 00). In the second state when a fault occurs, buck output stage fails and boost output state continues to operate. This means that  $\lambda_1 = \lambda_{s2}$ ,  $\lambda_2 = (\lambda_{s1} + \lambda_{L1} + \lambda_{L2} + \lambda_D)$  and  $\lambda_3 = (\lambda_1 + \lambda_2)$ , where  $\lambda_{s1}$ ,  $\lambda_{s2}$ ,  $\lambda_{L1}$ ,  $\lambda_{L2}$ , and  $\lambda_D$  are the failure rates of two switches, the two inductors and diode respectively. According to figure 6.20, the probabilities are given by,

$$\frac{d}{dt} \begin{bmatrix} P_0 \\ P_1 \\ P_2 \end{bmatrix} = \begin{bmatrix} -(\lambda_1 + \lambda_3) & 0 & 0 \\ \lambda_1 & -\lambda_2 & 0 \\ \lambda_3 & \lambda_2 & 0 \end{bmatrix} \begin{bmatrix} P_0 \\ P_1 \\ P_2 \end{bmatrix} \quad (6.28)$$

Assuming that the first state is where the chain begins, the initial condition of the equation above is,

$$P_0 = [1 \ 0 \ 0] \quad (6.29)$$

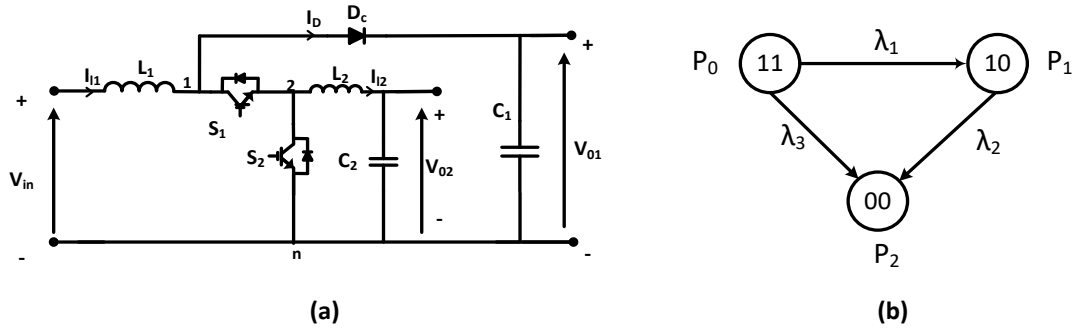


**Figure 6.20. Circuit diagram and Markov chain model of SIDO converter with buck DC and boost DC output**

Therefore, the reliability function of the SIDO converter with buck DC and boost DC output configuration can be determined by,

$$R_2(t) = 1 - P_2(t) = - \frac{(\lambda_2 - \lambda_3)e^{-(\lambda_1 + \lambda_3)t} - \lambda_1 e^{-(\lambda_2)t}}{\lambda_1 + \lambda_3 - \lambda_2} \quad (6.30)$$

### C. Reliability of SIDO converter with AC and boost DC output

SIDO converter with AC and boost DC output converter consists of three inductors, four switches, and a diode. Figure 6.21 shows the circuit diagram and Markov chain diagram of the converter. Three states can be identified: the state in which both the stages of the converter are healthy (state 11), a state in which one of the stages has failed (state 10), and the final state in which the whole configuration has failed (state 00). In the second state when a fault occurs, the buck output stage fails and boost output state continues to operate. This means that  $\lambda_1 = (\lambda_{s3} + \lambda_{s4} + \lambda_{L1} + \lambda_{L2})$ ,  $\lambda_2 = (\lambda_{s1} + \lambda_{s2} + \lambda_L + \lambda_D)$  and  $\lambda_3 = (\lambda_1 + \lambda_2)$ , where  $\lambda_{s1}$ ,  $\lambda_{s2}$ ,  $\lambda_{s3}$ ,  $\lambda_{s4}$ ,  $\lambda_L$ ,  $\lambda_{L1}$ ,  $\lambda_{L2}$ , and  $\lambda_D$  are the failure rates of four switches, the three inductors and diode respectively. According to figure 6.21, the probabilities are given by,

$$\frac{d}{dt} \begin{bmatrix} P_0 \\ P_1 \\ P_2 \end{bmatrix} = \begin{bmatrix} -(\lambda_1 + \lambda_3) & 0 & 0 \\ \lambda_1 & -\lambda_2 & 0 \\ \lambda_3 & \lambda_2 & 0 \end{bmatrix} \begin{bmatrix} P_0 \\ P_1 \\ P_2 \end{bmatrix} \quad (6.31)$$

Assuming that the first state is where the chain begins, the initial condition of the equation above is,

$$P_0 = [1 \quad 0 \quad 0] \quad (6.32)$$

Therefore, the reliability function of the SIDO converter with AC and boost DC output configuration can be determined by

$$R_3(t) = 1 - P_2(t) = - \frac{(\lambda_2 - \lambda_3)e^{-(\lambda_1 + \lambda_3)t} - \lambda_1 e^{-(\lambda_2)t}}{\lambda_1 + \lambda_3 - \lambda_2} \quad (6.33)$$

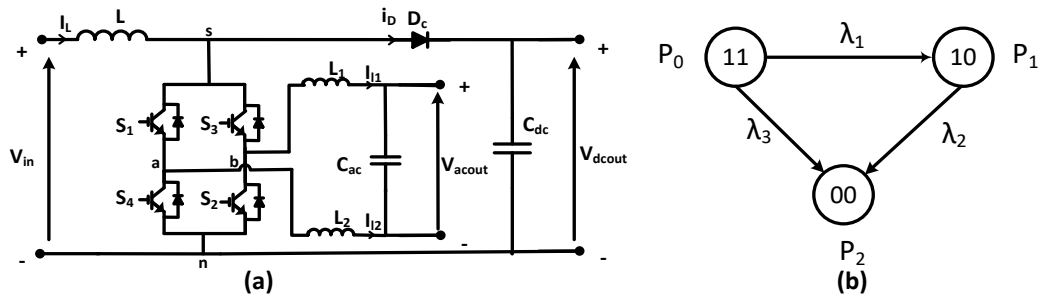
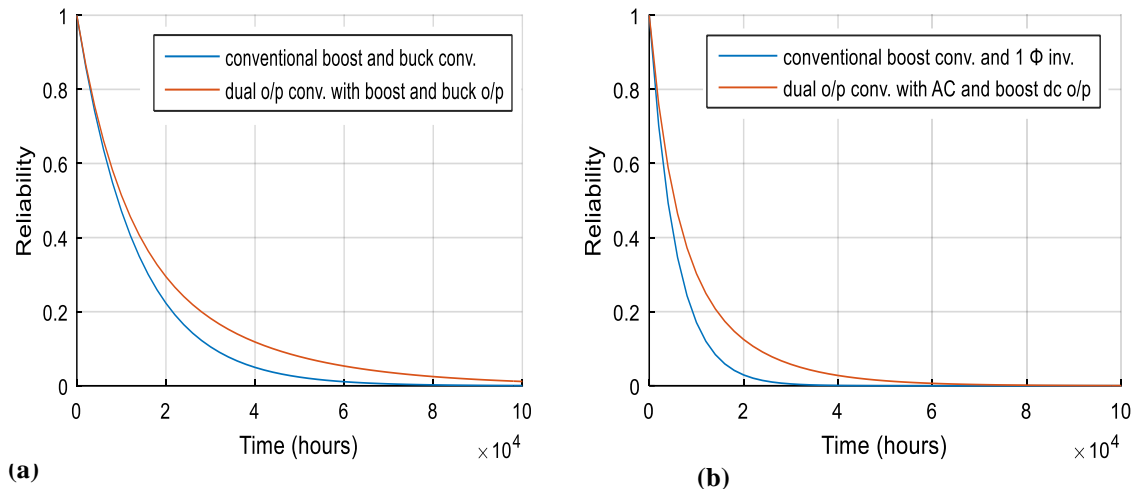


Figure 6.21. Circuit diagram and Markov chain model of SIDO converter with AC and boost DC output

Precise calculation of  $\lambda$  is necessary for reliability calculation of converters as explained in Chapter-III. The failure rates and MTBF of the inductor, diode and switch required have already been computed and presented in table 3.2.

Figure 6.22 (a) shows the reliability curves of the proposed SIDO converter with buck DC and boost DC output plotted using equation (6.30) and reliability of two separate buck DC and boost converter. Figure 6.22 (b) shows the reliability curves of the proposed SIDO converter with AC and boost DC outputs plotted using equation (6.33) and reliability of two separate boost DC converter and 1 phase AC inverter. The results show that proposed multi-terminal converters are more reliable than their conventional counterparts.



**Figure 6.22. Reliability curves of (a) Conventional and SIDO converter with buck DC and boost DC output and (b) Conventional and SIDO converter with AC and boost DC output**

### 6.5. CONCLUDING REMARKS

In this chapter, a PV based multi-terminal DC nanogrid has been presented. The two configurations of each dual-input single-output converters and single-input dual-output converters are designed and their performance is studied. The performance of the single-input dual-output converter configurations have been validated on an experimental setup, and input-output characteristics thus obtained conformed to simulation results. The characterization studies viz. sensitivity analysis and reliability analysis has been carried out. Sensitivity functions of the converter parameters have been developed and the corresponding normalized sensitivity with respect to parameters of interest has been computed. Also, Markov reliability model of the converter configurations has been developed. The reliability studies showed that the proposed multiterminal voltage converters are more reliable than their conventional counterparts of the same rating.

## **CHAPTER-VII**

### **CONCLUSIONS AND SCOPE FOR FURTHER WORK**

#### **INTRODUCTION**

RES based microgrid are gaining importance due to the exhaustion of fossil fuels and increase in greenhouse gases. However, along with numerous advantages they also have some problems associated with them viz. frequency deviation, voltage fluctuation, harmonics, unintentional islanding, etc. The main objective of this research is to model, design and develop PV based microgrid with novel control algorithms for inverter control that can overcome these problems. Characterization studies viz. sensitivity and reliability analysis are presented for the proposed PV based microgrid. The main reference for reliability evaluation is MIL-HDBK-217 military handbook and MTBF calculator software by ALD.

Efficient working and utilization of grid interfacing inverter depend on its control algorithm. Novel intelligent and adaptive interfacing control algorithms are proposed for PV inverter. These control algorithms provide multi-functionalities to the interfacing inverter such as feeding the load at desired voltage and frequency; power balance between DG, load and grid; active filtering; VAR generation and load balancing. The steady-state and transient response of the designed PV based microgrid with the proposed algorithms has been analyzed for linear as well as non-linear loads and balanced and unbalanced conditions using MATLAB along with Simulink toolbox.

It is essential to protect a microgrid against all types of faults. Accidental islanding can occur due to reasons like faults on grid side and needs to be timely detected. A brief review about existing local islanding detection techniques and their limitations are presented. A novel passive islanding detection algorithm based on wavelet packet transform signal processing of negative sequence voltage component of PCC voltage and binary tree classifier is proposed for the designed microgrid.

For the standalone applications of microgrid, novel PV based DC nanogrid structures with multi-terminal voltage converters are proposed. These converters are found to be

more efficient and reliable than their conventional counterparts. Sensitivity functions and Markov reliability models have been developed for the proposed converter configurations. Performance of the proposed multi-terminal converters has been validated using simulation studies. Also, an experimental prototype of single-input dual-output converter configurations is developed in the laboratory using a my-RIO controller and DSP (dSPACE 1104 R&D controller).

## 7.2. MAIN CONCLUSIONS

The research work carried out and reported in this thesis has concentrated on the design, modelling, characterization studies and protection of PV based microgrid. Multi-terminal voltage converters have been proposed, designed and developed for PV based DC nanogrid. The observations and the results reported have justified and fulfilled the objectives laid out for this research work.

The significant conclusions of the work carried out are:

- In the present work, modelling and design of two-stage three phase grid-tied PV based microgrid along with its characterization studies viz. sensitivity and reliability analysis have been carried out. The sensitivity functions of the PV cell and boost converter have been developed, and the corresponding numerical values have been computed for the designed system. Sensitivity results show that the PV cell output is most sensitive to irradiation level and converter output is most sensitive to inductor value and switching frequency. The performance of the PV array has been examined and is compared with the sensitivity results, the two results conform. The component and system level reliability analysis of PV microgrid has been carried out and presented. Pareto analysis, Reliability block diagram and logic gate representation model have been used to calculate the reliability values. Pareto analysis has been used as a tool to identify the component with the highest failure rate. Reliability Block Diagram method of system reliability analysis has been used along with the development of logic gate representation models to study the reliability of both standalone and grid-tied PV based microgrid, and it has been observed that grid-tied microgrid are the most reliable. Also, it has been shown that component reliability can be improved by improving critical stress factors and redundancy approach can

be employed for improving system reliability.

- Inverter control in a grid-tied microgrid plays an important role in bidirectional power flow. Apart from supplying power to the load at desired voltage and frequency, the inverter can be made to have additional features like active filtering and load balancing thus helping the grid in maintaining power quality and voltage profile. Novel interfacing algorithms, AFL based intelligent control algorithm and feedforward-feedback adaptive control algorithm are proposed for the control of inverter in a grid-tied PV based microgrid. Simulation results presented have validated the effectiveness of the proposed algorithms under steady-state as well as transient operating conditions. The THD of grid currents is found to be less than 5% (within IEEE-519 standard) even with nonlinear loads. Further, a comparative analysis of the proposed algorithms with conventional SRF theory based control algorithm is carried out validating the improved transient response of PV inverter with the proposed algorithms.
- Accidental islanding is an undesirable mode of operation which can cause problems to grid operators and customer equipment. Hence, it is mandatory for the grid interfacing inverters to have an added feature of islanding detection so that it can turn off itself once islanding is detected. A novel passive islanding detection algorithm based on negative sequence components ( $V_{neg}$ ) of the voltage at the PCC and WPT signal processing technique has been proposed. The WPT has been employed to extract the features of the  $V_{neg}$  signal and binary tree classifier has been used to discriminate between other disturbances and islanding condition. The proposed method has been found to be faster and has negligible effects on the power quality unlike local islanding detection methods. Simulation results are presented to validate the effectiveness of the proposed method which shows that it provides the reduction of the non-detection zone to nearly zero. The run on time is also reduced to nearly 5 milliseconds. Also, the proposed algorithm has been able to discriminate between events like load perturbation and islanding successfully.
- Standalone microgrid have the potential to provide electricity to people who do not have access to the main grid. A standalone PV based multi-terminal DC nanogrid has been designed, developed and implemented to supply both AC and DC loads at



different utilization levels. Two configurations of each DISO converters and SIDO converters are designed and modelled. Sensitivity and reliability analysis of the proposed configurations are presented. The sensitivity functions of converters have been developed which can help in the selection of the optimum duty cycle and modulation index of the converters for getting the desired output. Markov reliability model of the proposed converter configurations has been developed and compared with the conventional converters of the same ratings. It has been observed that the proposed multi-terminal converters are more reliable than conventional counterparts. The performance of the developed SIDO converter configurations has also been validated on an experimental setup.

### 7.3. SUGGESTIONS FOR FURTHER WORK

There are several important aspects which need to be investigated further, but could not be covered in this research work.

- The present work focuses on the design and control of PV based microgrid under uniform irradiation conditions. PV based microgrid and its algorithms can be developed considering the effect of partial shading also.
- In case of a failure in the utility grid, micro-grid is disconnected from the grid and operates in the islanded mode. Any power shortfall in transferring from the grid tied mode to the islanded mode can be compensated by the energy storage systems. The present work on grid-tied microgrid design can be extended to incorporate efficient ESS.
- The novel intelligent and adaptive interfacing control algorithms proposed in the present work shall be tested on real time systems to verify the improvements that can be achieved using these algorithms.
- The proposed islanding detection algorithm has been used on a single DG microgrid. Some schemes, such as those using impedance measurement, may work for a single DG, but may not work for multiple distributed generators. The proposed scheme shall be tested for multiple DG microgrid for its wider application.
- Standalone PV based DC nanogrid is proposed in the present work for supplying

electricity to the areas which are still not connected to the main grid. The work has proposed multi-terminal voltage converters that will help easy adaption of the DC nanogrid in practical implementation for supplying both AC and DC loads operating at different voltage levels.

## REFERENCES

- [1] O. Ellabban, H. Abu-Rub and F. Blaabjerg, "Renewable energy resources: Current status, future prospects and their enabling technology", *Renewable and Sustainable Energy Reviews*, vol. 39, pp. 748-764, 2014.
- [2] R. Lasseter, "Microgrids", *IEEE Power Engineering Society Winter Meeting*, 2002, pp. 305-308.
- [3] A. McEvoy, T. Markvart and L. Castaner, *Practical Handbook of Photovoltaics-Fundamentals and Applications*, Second Edition, Elsevier, Wyman Street, USA, 2012.
- [4] W. Xiao, M. S. E. Moursi , O. Khan, D. Infield, "Review of grid-tied converter topologies used in photovoltaic systems", *IET Renewable Power Generation*. July 2016, doi: 10.1049/iet-rpg.2015.0521.
- [5] F. Blaabjerg, Z. Chen, and S.B. Kjaer, "Power electronics as an efficient interface in dispersed power generation systems", *IEEE Transaction on Power Electronics*, Vol. 19, No. 5, September 2004, p. 1184-1194.
- [6] P. Mohanty, G. Bhuvaneshwari, R. Balasubramanian and N.K. Dhaliwal, "MATLAB based modeling to study the performance of different MPPT techniques used for solar PV system under various operating conditions", *Renewable and Sustainable Energy Reviews*. Vol. 38, pp. 581–593, 2014.
- [7] K. H. Hussein, I. Muta, T. Hoshino and M. Osakada, "Maximum photovoltaic power tracking: an algorithm for rapidly changing atmospheric conditions", *IEEE proceedings Generation, Transmission and Distribution*, 142, 59-64, 1995.
- [8] S. K. Chung, "Phase-Locked Loop for grid-connected three-phase power conversion systems", *IEEE Proceedings on Electronic Power Applications*, vol. 147, no. 3, pp. 213219, 2000.
- [9] M. D'Amore, "Sensitivity functions of corona loss on HVDC practical power lines: An introduction to optimal design", *In IEEE Transaction PAS*, 98, No. 2, Jan. / Feb 1977, pp 778 – 791. DOI:10.1109/T-PAS.1977.32391

- [10] S. Cristina and M. D'Amore, "Sensitivity analysis of modal quantities for horizontal transmission lines", *In IEEE Canadian communications and Power conference*, October 18-20, 1978, pp 172-175. DOI: 10.1109/TPAS.1979.319511
- [11] W.H. Hines, D.C. Mountgomery and D.M. Goldsman. *Probability and statistics in engineering*. Fourth Edition, John Wiley and Sons Publishers, 2000.
- [12] L. S. Srinath. *Reliability Engineering*. Affiliated East-West Press Pvt. Ltd. 1991.
- [13] C. Singh and R. Billinton. *System reliability, modelling and evaluation*. Hutchinson, 1977.
- [14] C. Singh and A. Lago-Gonzalez, "Reliability modeling of generation systems including unconventional energy sources", *IEEE Transactions on Power Apparatus and Systems*, 1049-1056.
- [15] *IEEE standard conformance test procedures for equipment interconnecting distributed resources with electric power systems*, IEEE Std. 1547.1–2005, 2005, pp. 1–62.
- [16] *IEEE recommended practice for utility interface of PV system*, IEEE standard 929-2000, 2000.
- [17] *Inverters, converters, and controllers for use in independent power systems*, UL STD 1741, 2001.
- [18] Z. Ye, A. Kolwalkar, Y. Zhang, P. Du, and R. Walling, "Evaluation of anti-islanding schemes based on non-detection zone concept", *IEEE Transaction on Power Electronics*, vol. 19, no. 5, pp. 1171–1176, Sep. 2004.
- [19] W. Bower and M. Ropp, *Evaluation of islanding detection methods for utility-interactive inverters in photovoltaic systems*, Sandia Nat. Labs., Albuquerque, NM, USA, Sandia Rep. SAND2002-3591.
- [20] S. Bhattacharyya, *Rural electrification through decentralized off-grid systems in developing countries*, Springer.2013. ISBN: 978-1-4471-4672-8

- [21] M. McHenry and D. Doepel “The ‘low power’ revolution: Rural off-grid consumer technologies and portable micropower systems in non-industrialized regions”, *Renewable Energy*, vol. 78, pp. 679-684, 2015.
- [22] J. M. Guerrero, F. Blaabjerg, T. Zhelev, K. Hemmes, E. Monmasson, S. Jemei, M. P. Comech, R. Granadino, and J. I. Frau, “Distributed Generation: Toward a New Energy Paradigm”, *IEEE Industrial Electronics Magazine*, vol.4, no.1, pp.52-64, March 2010.
- [23] T. Urmee, D. Harries, and H. Holtorf, *Photovoltaics for Rural Electrification in Developing Countries*, 10.1007/978-3-319-03789-9. Springer International Publishing. 2016
- [24] M. Sechilariu and F. Locment, *Urban DC microgrid*, 1st Ed. Cambridge, USA. pp. 14-20. 2016.
- [25] M. Shahidehpour and F. Schwartz, “Don’t let the sun go down on PV”, *IEEE Power Energy Mag.*, vol. 2, no. 3, pp. 40–48, May/Jun. 2004.
- [26] D. S. H. Chan and J. C. H. Phang, "Analytical methods for the extraction of solar-cell single- and double-diode model parameters from I-V characteristics," *IEEE Transactions on Electron Devices*, vol. ED-34, pp. 286-293, 1987.
- [27] R. Chenni, M. Makhlof, T. Kerbache, and A. Bouzid, "A detailed modeling method for photovoltaic cells," *Energy*, vol. 32, pp. 1724-1730, 9// 2007.
- [28] M. T. Ahmed, T. Goncalves and M. Tlemcani, “Single Diode Model Parameters Analysis of Photovoltaic Cell,” *In the proceeding of an international conference on renewable energy research and applications*. 20-23 Nov. 2006. Birmingham, UK.
- [29] S. Lun, S. Wang, G. Yang, and T. Guo, “A new explicit double-diode modelling method based on Lambert W-function for photovoltaic arrays,” *Solar Energy*. 116, 69–82. 2015.
- [30] K. Ishaque, Z. Salam and H. Tahri, “Accurate MATLAB Simulink PV systems simulator based on a two-diode model”, *Journal of power electronics*, vol. 11,

pp. 179- 187, 2011.

- [31] N. A. Shannan, N. Z. Yahaya and B. Singh, “Single-Diode Model and Two-Diode Model of PV Modules: A Comparison,” *IEEE International Conference on Control System, Computing and Engineering*, 29 Nov. - 1 Dec. 2013, Penang, Malaysia.
- [32] N. Pandiarajan and M. Ranganath, “Mathematical modeling of Photovoltaic module with Simulink”, *IEEE*. pp. 258-263, 2011.
- [33] R. Erickson and D. Maksimović, *Fundamentals of power electronics*, 2nd Ed. Secaucus, NJ, USA: Kluwer Academic Publishers. pp. 22-26. 2000.
- [34] D. Hart, *Power Electronics*, 1st Ed. New York: McGraw-Hill. pp. 211-220. 2011.
- [35] J. Zeng, W. Qiao, and L. Qu, “A single-switch isolated DC-DC converter for photovoltaic systems,” in *Proceedings of IEEE Energy Conversion Congress and Exposition*, Fredericton, NB, pp. 3446–3452. 2000.
- [36] W. Xiao, N. Ozog, and W. G. Dunford, “Topology Study of Photovoltaic Interface for Maximum Power Point Tracking,” *IEEE Transactions on Industrial Electronics*, Vol. 54, No. 3, June 2007.
- [37] M. Calais, J. Myrzik, T. Spooner, and V. G. Agelidis, “Inverters for single-phase grid-connected photovoltaic systems—an overview,” in *Proc. IEEE PESC’02*, vol. 2, 2002, pp. 1995–2000.
- [38] M. Meinhardt and G. Cramer, “Past, present and future of grid-connected photovoltaic- and hybrid-power-systems,” in *Proc. IEEE-PES Summer Meeting*, vol. 2, 2000, pp. 1283–1288.
- [39] Y. Xue, L. Chang, S. B. Kjaer, J. Bordonau, and T. Shimizu, “Topologies of single-phase inverters for small distributed power generators: an overview,” *IEEE Trans. Power Electron.*, vol. 19, no. 5, pp. 1305–1314, Sep. 2004.
- [40] M. Calais and V. G. Agelidis, “Multilevel converters for single-phase grid-

- connected photovoltaic systems—an overview,” in *Proc. IEEE ISIE '98*, vol. 1, 1998, pp. 224–229.
- [41] J. M. A. Myrzik and M. Calais, “String and module integrated inverters for single-phase grid-connected photovoltaic systems—A review,” in *Proc. IEEE Bologna PowerTech Conf.*, vol. 2, 2003, pp. 430–437.
- [42] S. B. Kjaer, J. K. Pedersen, and F. Blaabjerg, “Power inverter topologies for photovoltaic modules—A review,” in *Conf. Rec. IEEE-IAS Annu. Meeting*, vol. 2, 2002, pp. 782–788.
- [43] H. Haeberlin, “Evolution of inverters for grid-connected PV-systems from 1989 to 2000,” in *Proc. 17th Eur. Photovoltaic Solar Energy Conf.*, Munich, Germany, Oct. 22–26, 2001, pp. 426–430.
- [44] M. Meinhardt and G. Cramer, “Multi-string-converter: The next step in evolution of string-converter technology,” in *Proc. 9th Eur. Power Electronics and Applications Conf.*, 2001, CD-ROM.
- [45] H. Oldenkamp and I. J. de Jong, “AC modules: past, present and future,” in *Proc. Workshop Installing the Solar Solution*, Hatfield, U.K., 1998.
- [46] B. Lindgren, “Topology for decentralised solar energy inverters with a low voltage ac-bus,” in *Proc. EPE '99*, 1999, CD-ROM.
- [47] S. B. Kjaer, J. K. Pedersen and F. Blaabjerg, “A review of single-phase grid-connected inverters for photovoltaic modules,” *IEEE Transactions on Industry Applications*, vol. 41, pp. 1292-1306, 2005.
- [48] L. G. Junior, M. A. G. de Brito, L. P. Sampaio and C. A. Canesin, “Evaluation of integrated inverter topologies for low power PV systems”, *IEEE International Conference on Clean Electrical Power (ICCEP)*, 2011.
- [49] F. Schimpf and L. E. Norum, “Grid-connected converter for photovoltaic state of art, ideas for improvement of transformer-less inverters”, *Nordic Workshop on Power and Industrial Electronics*, 2008.

- [50] S. K. Khardem, M. Basu and M. F. Conlon, "Power quality in grid-connected renewable energy systems: Role of custom power devices" *International conference on renewable energies and power quality (ICREPQ'10)*, Granada (Spain), March 2010.
- [51] T. Eshram, P.L. Chapman, "Comparison of Photovoltaic Array Maximum Power Point Techniques", *IEEE Transaction on Energy Conversion*, vol.22, no.2, pp. 439-449, June 2007. DOI: 10.1109/TEC.2006.874230
- [52] B. Subudhi, R. A. Pradhan, "Comparative Study on Maximum Power Point Tracking Techniques for Photovoltaic Power Systems", *IEEE Transactions on Sustainable Energy*. Volume: 4, Issue: 1, Jan. 2013.
- [53] R. Faranda, S. Leva and V. Maugeri, "MPPT techniques for PV systems: energetic and cost comparison" *Proceedings of IEEE PES GM 2008*, July 2008.
- [54] X. Liu and L.A.C. Lopes, "An improved perturbation and observation Maximum power point tracking algorithm for PV arrays," *IEEE 35th Annual Power Electronics Specialists Conference*. Volume 3. pp 2005-2010. June 2004, Aachen, Germany.
- [55] B. Masood, M. S. Siddique, R. M. Asif and M. Zia-ul-Haq, "Maximum power point tracking using hybrid perturb & observe and incremental conductance techniques," In the proceeding of *4th International Conference on Engineering Technology and Technopreneuship (ICE2T)*, Kuala Lumpur, Malaysia. 2014.
- [56] A. Ramasamy and N. S. Vanitha, "Maximum power tracking for PV generating system using Novel optimized fractional order open circuit voltage-FOINC method," *International Conference on Computer communication and informatics (ICCCI)*, 2014, pp 1-6.
- [57] W. Xiao, A. Elnosh, V. Khadkikar and H. Zineldin, "Overview of maximum power point tracking technologies for photovoltaic power systems," in the proceeding of *Annual Conference of the IEEE Industrial Electronics Society, (IECON)*, Melbourne, VIC, Australia, pp 3900-3905, 2011.



- [58] M. Abdulkadir, A. S. Samosir, Member and A. H. M. Yatim, “ Modeling and simulation of maximum power point tracking of photovoltaic system in Simulink model” *IEEE International Conference on Power and Energy (PECon)*, Kota Kinabalu Sabah, Malaysia, 2012
- [59] F. Kazan, S. Karaki, R.A Jabr and M. Mansour, “Maximum power point tracking using ripple correlation and incremental conductance” *IEEE Universities Power Engineering Conference*, pp 1-6, 2012.
- [60] Y. Xiong, S. Qian and J. Xu, “Research on Constant Voltage with Incremental Conductance MPPT Method” *IEEE Power and Energy Conference, Asia-Pacific*, pp 1-4, 2012.
- [61] B. Singh, K. A. Haddad, and A. Chandra, "A review of active filters for power quality improvement," *IEEE Transaction on Industrial Electronics*, vol. 46, no.5, pp. 960-971, Oct 1999.
- [62] B. Singh, K. A. Haddad, and A. Chandra. *Power Quality: Problems and Mitigation Techniques*. John Wiley & Sons, 2014.
- [63] *IEEE Standard for interconnecting distributed resources with electric power systems*, IEEE Standard 1547.2-2008, 2008.
- [64] *IEEE Recommended Practices and Requirements for Harmonics Control in Electric Power Systems*, IEEE Standard 519, 2014.
- [65] A. Ghosh and A. Joshi, “A new method for load balancing and power factor correction in power distribution system”, *IEEE Transaction on power delivery*. Volume 15 No. 1. January 2000. pp. 417-422.
- [66] B. Singh and S. Kumar, “Modified Power Balance Theory for Control of DSTATCOM”, *Proceedings of the Joint International Conference on Power Electronics, Drives and Energy Systems (PEDES) & 2010 Power India*, New Delhi (Dec. 2010).
- [67] A. Hirofumi, W. Edson and M. Aredes. *Instantaneous power theory and applications to power conditioning*. 1st Ed. New Jersey: IEEE Press-Wiley Press

Pvt. Ltd. (2007).

- [68] C.N. Rowey, T.J. Summersz, R.E. Betz and D. Cornforth, “A Comparison of Instantaneous and Fryze Power Calculations on P-F and Q-V Droop in Microgrids”, *Proceedings of the 20th Australasian Universities Power Engineering Conference, Christchurch* (Dec. 2010)
- [69] A. Sinha, S. Bhattacharya and S. Mishra, “Phase Angle Restoration in PV-Battery Based Microgrid Including Power Sharing Control”, in *Proc. For the IEEE International Conference on Power Electronics, Drives and Energy Systems*, 16-19 Dec. 2014.
- [70] B. Singh, S. Dwivedi, I. Hussain and A. K. Verma, “Grid Integration of Solar PV Power Generating System Using QPLL Based Control Algorithm”, in *the Proc. of IEEE Power India International Conference*, Dec. 2014.
- [71] B. Singh, C. Jain and S. Goel, “A UVT Based Control for Single-Stage Grid Interfaced SPV System with Improved Power Quality”, in *the Proc. of IEEE Power India International Conference*, Dec. 2014.
- [72] A. Bouafia, F. Krim and J.P. Gaubert, “Design and implementation of high-performance direct power control of three-phase PWM rectifier, via fuzzy and PI controller for output voltage regulation,” *Energy Conversion and Management*, vol. 50, pp. 6-13, 2009.
- [73] M.A. Hannan, Z.A. Ghani, A. Mohamed and M.N. Uddin, “Real-Time Testing of a Fuzzy-Logic-Controller-Based Grid-Connected Photovoltaic Inverter System” *IEEE Transactions on Industry Applications*, Vol. 51, No. 6. 2015. DOI: 10.1109/TIA.2015.2455025.
- [74] H. Suryanarayana and M.K. Mishra, “Fuzzy Logic based Supervision of DC link PI Control in a DSTATCOM”, *Annual IEEE India Conference, INDICON*, 11-13 Dec. 2008. DOI- 10.1109/INDCON.2008.4768766.
- [75] P. Kumar, A. Mahajan, “Soft Computing Techniques for the Control of an Active Power Filter”, *IEEE Transactions on Power Delivery*, Vol. 24, No. 1, January

2009.

- [76] N.G.M. Thao and K. Uchida, "A Two-level Control Strategy with Fuzzy Logic for Large-scale Photovoltaic Farms to Support Grid Frequency Regulation," *Control Engineering Practice*, Vol. 59, pp. 77-99, February 2017. DOI: <http://doi.org/10.1016/j.conengprac.2016.11.006>.
- [77] M. O. Yatak, and O. Faruk, "Fuzzy Control of a Grid Connected Three Phase Two Stage Photovoltaic System", *Proceedings of the International Conference on Power Engineering, Energy and Electrical Drives Torremolinos, Spain*. May 2011.
- [78] R. Kasturi and P. Doraraju, "Sensitivity analysis of power systems," *IEEE Transaction on Power Apparatus and Systems*, vol. 88, no. 10, pp.1521-1524, Oct. 1969.
- [79] M.D' Amore, "Sensitivity functions of corona loss on HVDC practical power lines: An introduction to optimal design," *IEEE Transaction Power Apparatus and Systems*, vol. 98, no. 2, pp. 778-791, Jan/ Feb 1977.
- [80] S. Cristina and M.D' Amore, "Performance sensitivity of power line carrier channel," *IEEE Transaction Power Apparatus and Systems*, vol. 98, no. 4, pp. 1337-1344, July/Aug. 1978.
- [81] S. Cristina and M.D' Amore, "Propagation on polyphase lossy power lines: A new parameter sensitivity model," *IEEE Transaction on Power Apparatus and Systems*, vol. 97, no. 6, pp. 2333-2338, Nov./Dec. 1978.
- [82] R.G. Wasley and J. Momoh, "Distribution power line and its sensitivity to change in circuit height," *IEEE Transaction on Power Apparatus and Systems*, vol. PAS98, no. 1, pp. 35-44, Jan. 1979.
- [83] P. Kumar, R. Garg, and M. S. Thomas, "Some Studies Of Corona Noise Interference Due To EHV Lines", in *the Proc. of International Conference on Electromagnetic Interference and Compatibility*, 6-8 Dec 1995.
- [84] L. Guo, Z. Meng, Z. Sun and L. Wang, "Parameter identification and Sensitivity

- analysis of solar cell models with cat swarm optimization algorithm”, *Energy Conversion and Management*. Volume 108, 15 January 2016, Pages 520–528. doi:10.1016/j.enconman.2015.11.041.
- [85] H. Andrei, T. Ivanovici, E. Diaconu, M.R. Ghita, O. Marin and P.C. Andrei, “Analysis and experimental verification of the Sensitivity of PV cell model parameters”, *In International Conference on Synthesis, Modeling, Analysis and Simulation Methods and Applications to Circuit Design (SMACD)*. Seville. 19-21 Sept. 2012. DOI: 10.1109/SMACD.2012.6339434.
- [86] M. Ito, K. Kato, K. Komoto and T. Kichimi, “A Sensitivity Analysis of Very Large-Scale Photovoltaic Power Generation (VLS-PV) Systems in Deserts”, *In IEEE Conference on Photovoltaic Energy Conference*. Waikoloa. May 2006. DOI: 10.1109/WCPEC.2006.279672.
- [87] D. J. Pannell, *Sensitivity analysis: strategies, methods, concepts, examples*, School of Agricultural and Resource Economics, University of Western Australia, Crawley 6009, Australia.
- [88] L. Shu, “Parameters Sensitivity Analysis of Grid-Connected Photovoltaic Power Generation Model under Different Kinds of Disturbances.” *in the Proc. of IEEE Symposium on Electrical & Electronics Engineering (EEESYM)*, 2012.
- [89] Q. Li-nan, and L. Jing, “Identification of Photovoltaic Power System Based on Sensitivity Analysis” *in the Proc. of IEEE PES Asia-Pacific Power and Energy Engineering Conference*, 8-11 Dec. 2013
- [90] X. Zhu, Z. Fu, X. Long and X. Li, “Sensitivity analysis and more accurate solution of photovoltaic solar cell parameters” *Solar Energy*, 85 (2011), p. 393.
- [91] C. Singh and R. Billinton, *System reliability, modelling and evaluation*. Hutchinson, 1977.
- [92] C. Singh and A. Lago-Gonzalez, “Reliability modeling of generation systems including unconventional energy sources”, *IEEE Transactions on Power Apparatus and Systems*, 1049-1056.

- [93] A. E. Khosroshahi, M. Abapour, and M. Sabahi, “Reliability evaluation of conventional and interleaved DC-DC boost converter,” *IEEE Transaction of Power Electronics*, vol. 30, no. 10, pp. 5821–5828, Oct. 2015.
- [94] H. Calleja, F. Chan and I. Uribe, “Reliability-Oriented Assessment of a DC/DC Converter for Photovoltaic Applications”, *IEEE Power Electronics Specialists Conference*, June 2007. DOI: 10.1109/PESC.2007.4342221.
- [95] R. Billinton and R. N. Allan, *Reliability Evaluation of Engineering Systems*. New York, NY, USA: Springer, 2012.
- [96] R. Billinton, *Power System Reliability Evaluation*, New York: Gordon and Breach, 1970, 229 pp.
- [97] A. Rueda, M. Pawlak, “Pioneers of the reliability theories of the past 50 years”, *in Proc. of Annual Symposium of Reliability and Maintainability – RAMS*, 2004.
- [98] M. Ahmad, “Reliability Models for the Internet of Things: A Paradigm Shift”, *IEEE International Symposium on Software Reliability Engineering Workshops*, 2014.
- [99] P. Wang, L. Goel, and Y. Ding, “Evaluation of nodal reliability risk in a deregulated power system with photovoltaic power penetration Qian Zhao,” *IET Generation, Transmission & Distribution*, October 2012.
- [100] S. V. Dhople and A. D. Domínguez-García, “Estimation of Photovoltaic System Reliability and Performance Metrics”, *IEEE Transactions on Power Systems*, Vol. 27, No. 1, February 2012.
- [101] P. Venemans and M. Schreuder, “A Method for the Quantitative Assessment of Reliability of Smart Grids”, *CIREN Workshop - Lisbon 29-30 May 2012*.
- [102] P. Zhang, W. Li, S. Li, Y. Wang and W. Xiao, “Reliability assessment of photovoltaic power systems: Review of current status and future perspectives”, *Applied Energy*, 104 (2013), pp. 822–833.doi:10.1016/j.apenergy.2012.12.010
- [103] F. Chan and H. Calleja, “Reliability Estimation of Three Single-Phase

- Topologies in Grid-Connected PV Systems,” *IEEE Transactions on Industrial Electronics*, Vol. 58, No. 7, July 2011. DOI: 10.1109/TIE.2010.2060459.
- [104] *Reliability Prediction of Electronic Equipment*, Military Handbook 217-F, Dept. Defence, Arlington, VA, 1991, section 4.
- [105] S.E. De Le´on-Aldaco, H. Calleja, F. Chan and H.R. Jim´enez-Grajales, “Effect of the Mission Profile on the Reliability of a Power Converter Aimed at Photovoltaic Applications—A Case Study”, in *IEEE Transactions on Power Electronics*, Vol. 28. No. 6. June 2013. DOI: 10.1109/TPEL.2012.2222673.
- [106] F. Obeidat and R. Shuttleworth, “Reliability prediction of PV inverters based on MIL-HDBK-217F N2”, In *IEEE Photovoltaic Specialist Conference (PVSC)*. New Orleans, LA. 14-19 June 2015. DOI: 10.1109/PVSC.2015.7356277.
- [107] S.P. Chowdhury, S. Chowdhury and P A. Crossley, “Islanding protection of active distribution networks with renewable distributed generators: a comprehensive survey”, *Electric Power System Research*, 2009; 79:984–92.
- [108] F. De Mango, M. Liserre and A. D. Aquila, “Overview of anti-islanding algorithms for PV systems. Part II: active methods”, in *12th international power electronics and motion control conference (EPE-PEMC)*, 2006. p. 1884–9.
- [109] L.A.C. Lopes and S. Huili, “Performance assessment of active frequency drifting islanding detection method”, *IEEE Transaction on Energy Conversions*, 2006; 21:171–80.
- [110] M.E. Ropp, M. Begovic and A. Rohatgi, “Analysis and performance assessment of the active frequency drift method of islanding prevention”, *IEEE Transaction on Energy Conversions*, 1999; 14:810–6.
- [111] H.H. Zeineldin and S. Kennedy, “Sandia frequency-shift parameter selection to eliminate non-detection zones”, *IEEE Transaction on Power Delivery*, 2009; 24:486–7.
- [112] C.L. Trujillo, D. Velasco, E. Figueres and G. Garcerá, “Analysis of active islanding detection methods for grid-connected micro inverters for renewable

- energy processing”, *Applied Energy* 2010; 87:3591–605.
- [113] D. Reigosa, F. Briz, C. Charro, P. Garcia and J.M. Guerrero, “Active islanding detection using high-frequency signal injection,” *IEEE Transaction on Industrial Applications*. 2012; 48:1588–97.
- [114] D. Reigosa, F. Briz, C. Charro, P. Garcia and J.M. Guerrero, “Active islanding detection for multiple parallel-connected inverter-based distributed generators using high-frequency signal injection,” *IEEE Transaction on Power Electronics*. 2014; 29:1192–9.
- [115] H. Karimi, A. Yazdani and R. Iravani, “Negative-sequence current injection for fast islanding detection of a distributed resource unit,” *IEEE Transaction on Power Electronics*. 2008; 23:298–307.
- [116] S. Raza, H. Mokhlis, H. Arof, J.A. Laghari and L. Wang, “Application of signal processing techniques for islanding detection of distributed generation in distribution network: A review”, *Energy Conversion and Management*, 96, 2015 613–624. <http://dx.doi.org/10.1016/j.enconman.2015.03.029>.
- [117] F. De Mango, M. Liserre, A.D. Aquila and A. Pigazo, “Overview of anti-islanding algorithms for PV systems. Part I: Passive Methods,” *In 12th power electronics and motion control conference (EPE-PEMC)*, 2006. p. 1878–83.
- [118] W. Freitas, X. Wilsun, C.M. Affonso and H. Zhenyu, “Comparative analysis between ROCOF and vector surge relays for distributed generation applications” *IEEE Transaction on Power Delivery*, 2005; 20:1315–24.
- [119] S. K. Salman, D. J. King and G. Weller, “New loss of mains detection algorithm for embedded generation using rate of change of voltage and changes in power factors”, *In 7th international conference on Developments in Power System Protection (IEE)*. August 2002, Amsterdam, Netherlands, 10.1049/cp:20010105.
- [120] F.S. Pai and S. J. Huang, “A detection algorithm for islanding-prevention of dispersed consumer-owned storage and generating units”, *IEEE Transaction on*

*Energy Conversion*, 2001; 16:346–51.

- [121] I. J. Sung and H. K. Kwang, “An islanding detection method for distributed generations using voltage unbalance and total harmonic distortion of current,” *IEEE Transaction on Power Delivery*, 2004; 19:745–52.
- [122] P. O’Kane and B. Fox, “Loss of mains detection for embedded generation by system impedance monitoring,” *In Sixth international conference on developments in power system protection*, 1997. p. 95–8.
- [123] B. Singam and L. Y. Hui, “Assessing SMS and PJD schemes of anti-islanding with varying quality factor,” *In IEEE international power and energy conference (PECon)*, 2006. p. 196–201.
- [124] S. Vyasa, R. Kumara, and R. Kavasseri, “Data analytics and computational methods for anti-islanding of renewable energy based Distributed Generators in power grids”, *Renewable and Sustainable Energy Reviews* 69 (2017) 493–502. <http://dx.doi.org/10.1016/j.rser.2016.11.116>
- [125] I.S. Kim, “Islanding detection technique using grid-harmonic parameters in the photovoltaic system”, *Energy Procedia*, 2012; 14: 137–41.
- [126] P. K. Ray, N. Kishor and S. R. Mohanty, “Islanding and Power Quality Disturbance Detection in Grid-Connected Hybrid Power System Using Wavelet and Transform”, *IEEE Transactions on Smart Grid*, Vol. 3, No. 3, September 2012.
- [127] Available on: [http://nptel.ac.in/courses/Webcourse-contents/IIT-KANPUR/power-system/chapter\\_7/7\\_2.html](http://nptel.ac.in/courses/Webcourse-contents/IIT-KANPUR/power-system/chapter_7/7_2.html).
- [128] Available on: <http://in.mathworks.com/help/wavelet/examples/wavelet-packets-decomposing-the-details.html>.
- [129] H. T. Do, X. Zhang, N. V. Nguyen, S. S. Li, and T.T. Chu, “Passive-Islanding Detection Method Using the Wavelet Packet Transform in Grid-Connected Photovoltaic Systems”, *IEEE Transactions on Power Electronics*, Vol. 31, No. 10, October 2016 6955.



- [130] K. Jay-Hyung, K. Jun-Gu, J. Young-Hyok, J. Yong-Chae and W. Chung-Yuen, “An islanding detection method for a grid-connected system based on the Goertzel algorithm”, *IEEE Transactions on Power Electronics*, 2011; 26: 1049–55.
- [131] H. K. Kazemi and B. Sobhani, “Wavelet transform method for islanding detection of wind turbines”, *Renewable Energy*. 2012, doi:10.1016/j.renene.2011.07.002.
- [132] M. Hanif, M. Basu, and K. Gaughan, “Development of EN50438 compliant wavelet-based islanding detection technique for three-phase static distributed generation systems”, *IET Renewable Power Generation*. Vol. 6, no. 4, pp. 289–301, Jul. 2012.
- [133] M. Heidari, G. Seifossadat and M. Razaz, “Application of decision tree and discrete wavelet transform for an optimized intelligent based islanding detection method in distributed systems with distributed generations”, *Renewable and Sustainable Energy Reviews*. 2013. <http://dx.doi.org/10.1016/j.rser.2013.06.047>.
- [134] S. A. Saleh, A. S. Aljankawey, R. Meng, J. Meng, C. P. Diduch, and L. Chang, “Anti-islanding protection based on signatures extracted from the instantaneous apparent power”, *IEEE Transaction on Power Electronics*. Vol. 29, no. 11, pp. 5872–5891, Nov. 2014.
- [135] S. Mishra, C.N. Bhende, and B. K. Panigrahi, “Detection and Classification of Power Quality Disturbances Using S-Transform and Probabilistic Neural Network,” *IEEE Transactions on Power Delivery*, Vol. 23, No. 1, January 2008.
- [136] H. Shayeghi and B. Sobhani, “Zero NDZ assessment for anti-islanding protection using wavelet analysis and neuro-fuzzy system in an inverter-based distributed generation”, *Energy Conversion and Management*. <http://dx.doi.org/10.1016/j.enconman.2013.12.062>.
- [137] F. Gonzalez-Longatt, B. Rajpurohit, and S. Singh, “Smart multi-terminal DC  $\mu$ -grids for autonomous zero-net-energy buildings: Implicit Concepts,” *IEEE Innovative Smart Grid Technologies - Asia (ISGT ASIA)*, 2015.

- [138] J. Ruutu, J. Nurminen, and K. Rissanen, “Energy Efficiency of Mobile Device Recharging”, *International Journal of Handheld Computing Research*, vol. 4, no. 1, pp. 59-69, 2013.
- [139] D. Boroyevich, I. Cvetkovic, D. Dong, R. Burgos, F. Wang, and F. Lee, “Future electronic power distribution systems—a contemplative view”, *In Proc. 12th Int. Conf. OPTIM Elect. Electron. Equip.*, Brasov, Romania, May 20–22, 2010, pp. 1369–1380.
- [140] M. R. Khan and E. D. Brown, “DC Nanogrids: A Low-Cost PV Based Solution for Livelihood Enhancement for Rural Bangladesh”, *International Conference on the Developments in Renewable Energy Technology (ICDRET)*, 31 May 2014
- [141] K. Engelen, E. L. Shun, P. Vermeyen, I. Pardon, R. D’hulst, J. Driesen and R. Belmans, “The Feasibility of Small-Scale Residential DC Distribution Systems”, *In the Proc. of Annual Conference on IEEE Industrial Electronics, IECON* 6-10 Nov. 2006.
- [142] D. Palit and S. Malhotra, “Energizing rural India using microgrid: The case of solar DC micro-grids in Uttar Pradesh State, India”, *International Conference on the Developments in Renewable Energy Technology (ICDRET)*, 31 May 2014.
- [143] P. R. Mishra, R. B. Panguloori, N. Udupa and D. Mitra, “Economic Evaluation of Solar Hybrid DC Grid for Petrol Pump Stations”, *In the Proc. of Annual IEEE India Conference (INDICON)*, 2013.
- [144] B. Nordman and K. Christensen, “Local Power Distribution with Nanogrids”, *In the Proc. of International Green Computing Conference (IGCC)*, 27-29 June 2013
- [145] R. Wai, and K. Jheng, “High-Efficiency Single-Input Multiple-Output DC-DC Converter”, *IEEE Transactions on Power Electronics*, pp. 886 – 898, Vol. 28, no. 2, Feb. 2013.
- [146] Y. Lin, Y. Luo, K. Chen and W. Hsu, “Liquid Crystal Display (LCD) Supplied by Highly Integrated Dual-Side Dual-Output Switched-Capacitor DC-DC

- Converter with Only Two Flying Capacitors”, *IEEE Transactions on Circuits and Systems*, vol. 59, no. 2, pp. 439-446, 2012.
- [147] C. Huang, Y. Chen, and C. Tsai, “Integrated Single-Inductor Dual-Output DC-DC Converter with Power-Distributive Control”, *IEEE 2nd International Symposium on Next-Generation Electronics (ISNE)* - February 25-26, Kaohsiung, Taiwan.
- [148] J. Dong, G. Chen, Y. Deng, K. Wang, and X. He, “A Family of Integrated Dual-Output DC-DC Converters: Synthesis Methodology and Performance Analysis”, *IEEE 8th International Power Electronics and Motion Control Conference (IPEMC-ECCE Asia)*, 2016.
- [149] Z. Qian, O. Abdel-Rahman, H. Al-Atrash and I. Batarseh, “Modelling and Control of Three-Port DC/DC Converter Interface for Satellite Applications”, *IEEE Transactions on Power Electronics*, vol. 25, no. 3, pp. 637-649, 2010.
- [150] D. Kwon and G. A. Rincon-Mora, “Single-inductor-multiple-output switching DC-DC converter”, *In IEEE Trans. Circuits Syst. II, Exp. Briefs*, vol. 56, no. 8, pp. 614–618, Aug. 2009.
- [151] O. Ray, A. Josyula, S. Mishra and A. Joshi, “Integrated Dual-Output Converter”, *IEEE Transactions on Industrial Electronics*, vol. 62, no. 1, pp. 371-382, 2015.
- [152] P. Patra, A. Patra, and N. Misra, “A Single-Inductor Multiple-Output Switcher with Simultaneous Buck, Boost, and Inverted Outputs”, *IEEE Transactions on Power Electronics*, vol. 27, no. 4, pp. 1936-1951, 2012.
- [153] F. Z. Peng, “Z-source inverter”, *IEEE Transaction on Industrial Applications.*, vol. 39, no. 2, pp. 504–510, Mar ./Apr. 2003.
- [154] O. Ray and S. Mishra, “Boost-Derived Hybrid Converter with Simultaneous DC and AC Outputs”, *IEEE Transactions on Industry Applications*, vol. 50, no. 2, pp. 1082-1093, 2014.
- [155] S. Mishra, R. Adda, and A. Joshi, “Inverse Watkins-Johnson topology based inverter”, *IEEE Transaction of Power Electronics*. vol. 27, no. 3, pp. 1066–

1070, Mar. 2012.

- [156] R. Adda, O. Ray, S. K. Mishra and A. Joshi, “Synchronous-Reference-Frame-Based Control of Switched Boost Inverter for Standalone DC Nanogrid Applications,” *IEEE Transactions on Power Electronics*, Vol. 28, No. 3, March 2013 1219.
- [157] P. Lee, Y. Lee, K.W. Cheng and X. C. Liu, “Steady-state analysis of interleaved boost converter with coupled inductors”, *IEEE Transaction on Industrial Electronics*. 2000 Aug; 47(4):787–95.
- [158] K. Tattiwong and C. Bunlaksananusorn, “Analysis design and experimental verification of quadratic boost converter”, *IEEE Region 10 Conference*; 2014 Oct 22-25; Bangkok. p. 1–6.
- [159] A. E. Becquerel, “Recherches sur les effets de la radiation chimique de la lumiere solaire au moyen des courants electriques”, *Comptes Rendus de L’Academie des Sciences*, vol. 9, pp. 145-149, 1839.
- [160] A. E. Becquerel, “Memoire sur les effects d’electricites produits sous influence des rayons solaires”, *Annalen der Physick und Chemie*, vol. 54, pp. 35-42, 1841.
- [161] J.L Gray, *The Physics of the Solar Cell*, in Handbook of Photovoltaic Science and Engineering, 2011, John Wiley and Sons.
- [162] Y. Amirnaser and R. Iravani. *Voltage-Sourced Converters in Power Systems: Modeling, Control, and Applications*. IEEE Press, 2012 - 451 pages.
- [163] F.W. Fuchs, “Semiconductor losses in voltage source and current source IGBT converters based on analytical derivation,” *IEEE 35th Annual Power Electronics Specialists Conference*, Germany, June 2004.
- [164] Y. W. Li, “Control and Resonance Damping of Voltage-Source and Current-Source Converters with LC Filters,” *IEEE Transactions on Industrial Electronics*. Volume: 56, Issue: 5, May 2009.
- [165] G. Ledwich and A. Ghosh, “A flexible DSTATCOM operating in voltage or

current control mode,” in *IEEE Proceedings Generation, Transmission and Distribution*, vol.149, no.2, pp.215-224, Mar 2002.

- [166] MTBF Calculator user guide by ALD. Available: <http://aldservice.com/FreeMTBFCalculatorUserGuide.html>.
- [167] A.N. Madkor, W.R. Anis and I. Hafez, “The Effect of Numbers of Inverters in Photovoltaic Grid-Connected System on Efficiency, Reliability and Cost,” *International Journal of Scientific & Technology Research*, Volume 4. Issue 09. September 2015. ISSN 2277-8616.
- [168] Available on: <http://nptel.ac.in/courses/103103037/29>.
- [169] J. R. Quinlan. *C4.5: Programs for Machine Learning*. Morgan Kaufmann Publishers, 1993.
- [170] Y. M. Chen, Y. C. Liu and S. H. Lin, “Double-input PWM DC-DC converter for high/ low voltage sources,” *IEEE Transactions on Industrial Electronics*, Vol. 53, NO. 5, October 2006.
- [171] K. P. Yalamanchili , M. Ferdowsi , S. Lu , P. Xiao and K. Corzine, “Derivation of Double-input DC-DC Power Electronic Converters,” *Electric Power Components and Systems*, 39:5, 478-490, DOI: 10.1080/15325008.2010.528540.

## APPENDIX-A

### Manufacturer datasheet of PV module

# Sunmodule<sup>+</sup>™

## SW 230 mono / Version 2.0

SW-02-5005US 07-2012

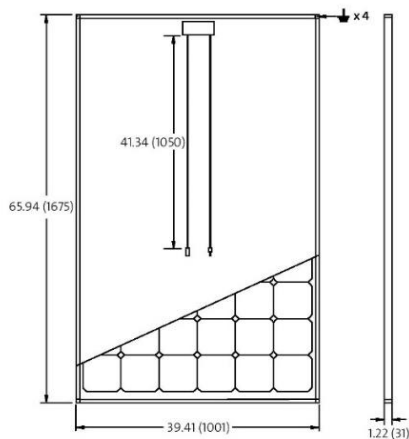
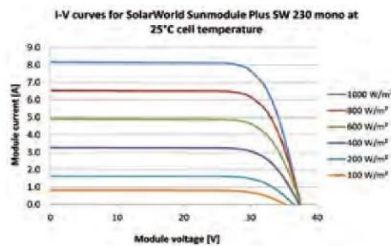
#### PERFORMANCE UNDER STANDARD TEST CONDITIONS (STC)\*

		SW 230
Maximum power	$P_{max}$	230 Wp
Open circuit voltage	$V_{oc}$	37.4 V
Maximum power point voltage	$V_{mpp}$	30.0 V
Short circuit current	$I_{sc}$	8.16 A
Maximum power point current	$I_{mpp}$	7.68 A

\*STC: 1000W/m<sup>2</sup>, 25°C, AM 1.5

#### THERMAL CHARACTERISTICS

NOCT	46 °C
TC $I_{sc}$	0.004 %/K
TC $V_{oc}$	-0.30 %/K
TC P	-0.45 %/K
Operating temperature	-40°C to 85°C



#### PERFORMANCE AT 800 W/m<sup>2</sup>, NOCT, AM 1.5

		SW 230
Maximum power	$P_{max}$	166.9 Wp
Open circuit voltage	$V_{oc}$	33.9 V
Maximum power point voltage	$V_{mpp}$	27.2 V
Short circuit current	$I_{sc}$	6.58 A
Maximum power point current	$I_{mpp}$	6.14 A

Minor reduction in efficiency under partial load conditions at 25°C: at 200W/m<sup>2</sup>, 95% (+/- 3%) of the STC efficiency (1000 W/m<sup>2</sup>) is achieved.

#### COMPONENT MATERIALS

Cells per module	60
Cell type	Mono crystalline
Cell dimensions	6.14 in x 6.14 in (156 mm x 156 mm)
Front	tempered glass (EN 12150)
Frame	Clear anodized aluminum
Weight	46.7 lbs (21.2 kg)

#### SYSTEM INTEGRATION PARAMETERS

Maximum system voltage SC II	1000 V	
Max. system voltage USA NEC	600 V	
Maximum reverse current	16 A	
Number of bypass diodes	3	
UL Design Loads*	Two rail system	113 psf downward 64 psf upward
UL Design Loads*	Three rail system	170 psf downward 64 psf upward
IEC Design Loads*	Two rail system	113 psf downward 50 psf upward

\*Please refer to the Sunmodule installation instructions for the details associated with these load cases.

#### ADDITIONAL DATA

Power tolerance <sup>2)</sup>	-0 Wp / +5 Wp
J-Box	IP65
Connector	MC4
Module efficiency	13.72 %
Fire rating (UL 790)	Class C



#### VERSION 2.0 FRAME

- Compatible with "Top-Down" mounting methods
- ⚡ Grounding Locations:  
4 corners of the frame

1) Sunmodules dedicated for the United States and Canada are tested to UL 1703 Standard and listed by a third party laboratory. The laboratory may vary by product and region. Check with your SolarWorld representative to confirm which laboratory has a listing for the product.

2) Measuring tolerance traceable to TUV Rheinland: +/- 2% (TUV Power Controlled).

3) All units provided are imperial. SI units provided in parentheses.

SolarWorld AG reserves the right to make specification changes without notice.

## APPENDIX-B

### Simulation parameters of grid-tied microgrid

	Parameters	Attributes
<b>PV Sunmodule</b>	Power ( $P_{PV}$ )	10 kW
<b>SW-230</b>	Module Short circuit current ( $I_{sc}$ )	8.72 A
	Module Open circuit voltage ( $V_{oc}$ )	36.7 V
	Module current at MPP ( $I_{mpp}$ )	7.74 A
	Module voltage at MPP ( $V_{mpp}$ )	29.7 V
<b>Boost Converter</b>	Duty Cycle ( $D$ )	0.531- 0.493
	Inductor ( $L_c$ )	8.31 mH
	Capacitor ( $C_c$ )	255 $\mu$ F
	Switching frequency( $f_s$ )	10 kHz
<b>Inverter</b>	Switching frequency ( $f_s$ )	10 kHz
	DC link voltage ( $C_d$ )	800 V
	Interfacing Inductance ( $L_f$ )	7 mH
	Line-to-line voltage, Line-to-neutral voltage	415 V, 220 V
	Rated Power	10 kW
<b>RLC Load</b>	Resistance, Inductance, Capacitance	17.22 $\Omega$ , 21.9 mH, 462 $\mu$ F
<b>(for islanding studies)</b>	Load Quality Factor ( $Q_f$ )	2.5
	Load Resonant Frequency ( $f_o$ )	50 Hz
<b>Grid</b>	Grid frequency (f)	50 Hz
	Line-to-line voltage, Line-to-neutral voltage	415 V, 220 V
	Grid Resistance ( $R_s$ ) Inductance ( $L_s$ )	0.11 $\Omega$ , 0.35 mH

**APPENDIX-C****Data for reliability studies**

<b>Components</b>	<b>Reliability Value</b>
PV Array (R <sub>1</sub> )	0.8
Chopper(R <sub>2</sub> )	0.95
Battery(R <sub>3</sub> )	0.85
Battery Charger(R <sub>4</sub> )	0.7
Capacitor(R <sub>5</sub> )	0.99
Inverter(R <sub>6</sub> )	0.84
Switch(R <sub>7</sub> )	0.95
Synchronizer(R <sub>8</sub> )	0.91
Grid(R <sub>9</sub> )	0.99
Load(R <sub>10</sub> )	0.9



## APPENDIX-D

Design specifications of DISO buck-buck DC converter for simulation studies

<b>Parameter and Component</b>	<b>Attributes</b>
Input voltage	24 V
Input voltage	12 V
Output voltage	18 V
Switching frequency	10 kHz
Duty cycles	$D_1=0.5, D_2=0.5$
Inductor	L=10 mH
Capacitor	C=1000 $\mu$ F

Design specifications of DISO buckboost-buckboost DC converter for simulation studies

<b>Parameter and Component</b>	<b>Attributes</b>
Input voltage	24 V
Input voltage	12 V
Output voltage	48 V
Switching frequency	10 kHz
Duty cycles	$D_1=0.4, D_2=0.32$
Inductor	L=10 mH
Capacitor	C=1000 $\mu$ F

Design specifications of SIDO converter with buck DC and boost DC output for experimental studies

<b>Parameter and Component</b>	<b>Attributes</b>
Power Rating	100 W
Input voltage	17 V
Output voltage	24 V
Output voltage	12 V
Input current	5 A
Switching frequency	10 kHz
Duty cycles	$D_1=0.7, D_2=0.29$
Inductors	$L_1=8\text{mH}, L_2=5\text{mH}$
Capacitors	$C_1=220\mu\text{F}, C_2=220\mu\text{F}$

Design specifications of SIDO converter with AC and boost DC output for experimental studies

<b>Parameter and Component</b>	<b>Attributes</b>
Power Rating	100 W
Input voltage	17 V
Output DC voltage	24 V
Output AC voltage	12 V
Switching frequency	10 kHz
Duty cycles	0.2916
M index	0.6249
Inductors	$L_1=2.4$ mH, $L_2=0.15$ mH
Capacitors	$C_1=220\mu\text{F}$ , $C_2=220\mu\text{F}$

Specifications of Su-Kam PV-module

<b>Parameter and Component</b>	<b>Attributes</b>
Power	100 W
Short circuit current	6.30 A
Open circuit voltage	21.40 V
Module current at MPP	5.70 A
Module voltage at MPP	17.70 V
Tolerance	10 kHz

## APPENDIX-E

### Markov modelling of reliability

Markovian methods are useful tools for evaluating the reliability of a system that has multiple states. In the framework of Markovian models, the transitions between various states are characterized by constant transition rates. Markov reliability model uses a stochastic process to model the system with several states and transitions between states. In the context of reliability modelling, the state-transition diagram associated with the Markov model describes the system status—failed or operational—for each system configuration reached after a unique sequence of component failures. The edges represent transitions between configurations triggered by component failures (or repair procedures). If  $X(t)$  is denoted as a random variable in a Markov process, then  $P_{ij}$  of transitioning probability from the state “i” at  $t=0$  to state “j” at  $t$  is

$$P_{ij} = P[X(t) = j \mid X(0) = i] \quad (\text{E.1})$$

When a random fault occurs, the system transitions from one state to another. The transition rate is the failure rate of the component in which the fault occurred. The probability of each state is calculated using the Chapman–Kolmogorov equation is given by,

$$\frac{dP(t)}{dt} = P(t) * Q \quad (\text{E.2})$$

where,  $P(t)$  is the probability vector and  $Q$  is the transition probability matrix. Solving this differential equation yields the probabilities of transitioning from every state to another as a function of time as given by,

$$P(t) = e^{Qt} * P(0) \quad (\text{E.3})$$

where  $P(0)$  is the initial state vector with  $P(0) = 1$ . Reliability is then given by total probability of not being in the failed state. This can be accomplished easily by adding the entries of  $P(t)$  associated with healthy states.

## LIST OF PUBLICATIONS

### Journal Papers

- [1] N. Gupta and R. Garg, “Design, Development and Reliability Assessment of Dual Output Converters for SPV based DC Nanogrid,” *Journal of Renewable and Sustainable Energy*. Volume 10, Issue 2, March 2018. DOI: 10.1063/1.5009570.
- [2] N. and R. Garg, “Algorithm for Islanding Detection in PV Generator Networks Connected to Low-Voltage Grid,” *IET Generation, Transmission & Distribution*. February 2018, DOI: 10.1049/iet-gtd.2017.1735.
- [3] N. Gupta and R. Garg, “Tuning of Asymmetrical Fuzzy Logic Control Algorithm for PV system connected to Grid” *International Journal of Hydrogen Energy*. Volume 42, Issue 26, June 2017, Pages 16375–16385. Elsevier Publisher. DOI: <http://dx.doi.org/10.1016/j.ijhydene.2017.05.103>.
- [4] N. Gupta, R. Garg, and P. Kumar, “Sensitivity and Reliability Models of a PV System Connected to Grid. *Renewable and Sustainable Energy Reviews*,” Volume 69, March 2017, Pages 188-196. Elsevier Publisher. DOI:10.1016/j.rser.2016.11.031.

### Book Chapters

- [1] N. Gupta, R. Garg, and P. Kumar, “Study of Conventional Control Algorithms for PV-Based Grid-Connected Microgrid,” *Proceeding of International Conference on Intelligent communication, Control and Devices. Series: Advances in Intelligent systems and computing*. Volume no 479. ISBN: 978-981-10-1707-0. Chapter DOI-10.1007/978-981-10-1708-7\_25.

### Proceedings Papers

- [1] N. Gupta, R. Garg, and P. Kumar, “IED with advanced islanding detection functionality for PV based Microgrid,” *5th International Conference on Computing for Sustainable Global Development* 14th - 16th March 2018, Bharati Vidyapeeth's Institute of Computer Applications and Management (BVICAM), New Delhi (INDIA).

- [2] N. Gupta, R. Garg, and P. Kumar, "Characterization Study of PV module Connected to Microgrid," *IEEE India International Conference (INDICON 2015)* Dec 17-20, 2015, JMI, India. DOI- 10.1109/INDICON.2015.7443360.
- [3] N. Gupta, R. Garg, and P. Kumar, "Asymmetrical Fuzzy logic control to PV Module Connected micro-grid," *IEEE India International Conference (INDICON 2015)* Dec 17-20, 2015, JMI, India. DOI- 10.1109/INDICON.2015.7443356.
- [4] N. Gupta, R. Garg, and P. Kumar, "Smart Grid – A Conceptual Design," *National conference on Emerging trends in Electrical and Electronics Engineering (ETEEE-2015)* Feb 02-03, 2015, JMI, Delhi.

## BIO-DATA

<b>Name</b>	Nikita Gupta
<b>Father's Name</b>	Shri. Shashi Bhushan Gupta
<b>Mother's Name</b>	Smt. Poonam Gupta
<b>Date of Birth</b>	8 <sup>th</sup> April 1989
<b>Place of Birth</b>	Hamirpur, Himachal Pradesh
<b>Education Qualification:</b>	
M.Tech 2012-2014	Power System, Delhi Technological University, Delhi
B.Tech 2007-2011	Electrical and Electronics Engineering, National Institute of Technology Hamirpur, Himachal Pradesh
<b>Experience:</b>	
August 2017- till date	Lecturer (Contractual), EED, National Institute of Technology Hamirpur, Himachal Pradesh
July 2011- October 2011	Graduate Engineer Trainee, TATA AutoComp Systems Limited
<b>Area of Interest:</b>	Power system analysis, power electronics applications in renewable energy systems, microgrid and reliability analysis